ISSN 2712-8172

MAGAZINE OF CIVIL ENGINEERING

Magazine of Civil Engineering

ISSN 2712-8172

Online peer-reviewed open-access scientific journal in the field of Civil and Construction Engineering

Founder and Publisher: Peter the Great St. Petersburg Polytechnic University

This journal is registered by the Federal Service for Supervision of Communications, Information Technology, and Mass Media (ROSKOMNADZOR) in 2020. Certificate El No. FS77-77906 issued February 19, 2020.

Periodicity: 8 issues per year

Publication in the journal is open and free for all authors and readers.

Indexing: Scopus, Web of Sceince (ESCI, RSCI), DOAJ, Compendex, Google Academia, Index Copernicus, ProQuest, Ulrich's Serials Analysis System, CNKI

Corresponding address: 29 Polytechnicheskaya st., Saint Petersburg, 195251, Russia

Contacts:
E-mail: mce@spbstu.ru
Web: http://www.engstroy.spbstu.ru

Date of issue: 09.02.2026

Contents

Magazine of Civil Engineering

ISSN 2712-8172

journal homepage: http://engstroy.spbstu.ru/

Research article

UDC 004.02

DOI: 10.34910/MCE.141.1

Electric power system functioning in conditions of extreme weather events in the presence of distributed generation based on renewable energy sources

A.O. Feshin[1], ***M.A. Polyukhovich***[1], ***Yu.V. Logvinova***[1], ***V.G. Burlov***[1] ✉, ***V.V. Barskov***[1], ***J. Arzola-Ruiz***[2], ***M. Castro Fernandez***[2]

[1] *Peter the Great St. Petersburg Polytechnic University, St. Petersburg, Russian Federation*

[2] *Technological University of Havana "José Antonio Echeverría", Havana, Cuba*

✉ *burlov_vg@spbstu.ru*

Keywords: energy efficiency, optimal mode, machine learning, genetic algorithm, objective function, optimal allocation, extreme weather event

Abstract. Significant number of accidents in electric power systems are caused by the effects of extreme weather events. In such conditions, providing consumers with electric energy is especially important. This study is devoted to solving this problem, in which a decision-making model has been developed that takes into account distributed generation based on renewable energy sources. The proposed model is a procedure for optimizing the established electric power mode. Optimization is performed using a genetic algorithm. The regulated parameters are the active capacities of electric power plants, the voltage on the busbars of generators of these stations, and the transformation coefficients. The values of these parameters are determined in case of disconnection of one and two overhead power lines using the example of a modified IEEE-39 circuit. The results show that distributed generation makes it possible to provide full power supply to consumers in a larger number of these emergencies (by 13.2 % and 27.2 %, respectively). With the most optimal location and generation capacity based on renewable energy sources, full power supply to consumers is achieved in 100 % and 98.3 % of emergency situations, respectively. The proposed decision-making model has a high potential to expand its functionality.

Funding: This research was supported by the Ministry of Science and Higher Education of the Russian Federation (agreement № 075-15-2025-673 dated August 20, 2025).

Citation: Feshin, A.O., Polyukhovich, M.A., Logvinova, Yu.V., Burlov, V.G., Barskov, V.V., Arzola-Ruiz, J., Castro Fernandez, M. Electric power system functioning in conditions of extreme weather events in the presence of distributed generation based on renewable energy sources. Magazine of Civil Engineering. 2026. 19(1). Article no. 14101. DOI: 10.34910/MCE.141.1

1. Introduction

Electric power industry occupies a special place in human economic activity, since the supply of electric energy is critically necessary in all areas of the economy: industry, agriculture, transport, healthcare, etc. In addition, a significant part of the total consumption of electric energy is occupied by household consumers.

Extreme weather events have an impact on all areas of human activity [1]. Electric power facilities are also affected by these phenomena [2–4]. Since the main task of the complex is to supply consumers

with electric energy, the issue of ensuring reliable and uninterrupted power supply becomes even more urgent in conditions of extreme events.

Electric power systems (EPS) contain many elements, one of which is overhead power lines (OHPL). Due to the significant length of overhead lines, more than other elements of the EPS are adversely affected by extreme weather events. The impact of these phenomena can lead to an emergency shutdown of one or more overhead lines, which, in turn, may be accompanied by a disruption in the supply of electrical energy to consumers.

Centralized restoration of power supply requires repair of damaged network infrastructure, which, in some cases, may take a long time. Therefore, a common method is the temporary use of backup power circuits and backup sources of electrical energy, which makes it possible to fully or partially restore supply to consumers. At the same time, an important circumstance should be noted: even in an emergency state, the parameters of the electric power mode, as a rule, must be within strictly defined limits.

Based on the information and statistics available to the author's team on the EPS of the Republic of Cuba, an analysis of the threats of power supply disruption was performed. As a result, risk factors have been identified that can lead to emergency disturbances in the operation of the EPS. Extreme weather events are among these factors:

- hurricanes and severe storms; high probability of damage to the electric grid infrastructure, massive power outages, long-term repairs of the EPS infrastructure;
- high ambient temperature; overheating of equipment, increased electrical loads of equipment, damage to OHPL supports due to thermal expansion of materials and reduced structural strength; increased boom sag of OHPL wires;
- heavy rains, which can lead, among other things, to floods and landslides; falling OHPL poles due to soil erosion, damage to underground utilities, flooding of power grid infrastructure, power outages.

From 1980 to 2024, 112 major accidents occurred in the EPS of the Republic of Cuba, disabling more than half of consumers and causing significant economic and technological damage. At the same time, in 97 cases, the interruption in the electricity supply to consumers was more than a day. The causes of these accidents were:

- high ambient temperature – 23 cases (20.5 %);
- thunderstorm events – 19 cases (17 %);
- floods – 9 cases (8 %);
- complex of adverse events (hurricanes/storms and floods) – 34 cases (30.4 %);
- complex of adverse events (thunderstorms and floods) – 2 cases (1.8 %);
- hurricanes/storms – 1 case (0.9 %);
- other reasons (equipment wear, personnel error during repair work, etc.) – 24 cases (21.4 %).

Presented results show that 78.6 % of accidents in the EPS of the Republic of Cuba occurred as a result of exposure to extreme weather events. This resulted in broken wires and falling OHPL supports, flooding of substations, overload of the electrical network due to abnormally high temperatures, and short circuits.

Functioning of EPS in conditions of extreme weather events is characterized by the concept of resilience, which is defined as the ability of EPS to withstand extreme events and recover quickly after these events [5]. Resilience measures can be divided into short-term or operational, which are applied in a relatively short time interval (several days or weeks), including an extreme weather event, and long-term, which are aimed at reducing the vulnerability of EPS to future events [5, 6]. The optimal functioning of EPS in conditions of exposure to extreme weather events is possible if a high level of resilience is ensured and the volume of disconnected electrical energy is reduced among consumers. This issue is of interest among researchers and is considered by them as an optimization problem.

In [7], the solution of the noted problem is performed by determining the optimal composition, capacity, and location of virtual power plants. The virtual station includes generating sources based on renewable energy sources (RES), energy storage systems based on rechargeable batteries and electric vehicles (it is assumed that the latter will operate in the power supply mode in the event of an accident). The problem is solved using the IEEE-118 distribution scheme using the "black widow" optimization

algorithm. The determination of the optimal composition, capacity, and location of virtual power plants is also discussed in [8–11]. The following optimization algorithms are used in these works, the effectiveness of which is tested in IEEE test distribution schemes: the spotted hyena algorithm, IEEE-34 scheme [8]; a hybrid algorithm based on the algorithms "herd of krill" and "pack of gray wolves", IEEE-33 scheme [9]; the hunting prey algorithm, IEEE-85 scheme [10]; hybrid algorithm based on the "krill herd" and "sine-cosine" algorithms, IEEE-69 scheme [11].

Method for increasing the resilience of an electric distribution network, which is formulated as a multi-criteria optimization model, was proposed in [12]. The paper describes in detail the mathematical part of the model, in which the nonlinear components are linearized, and the penalty components are introduced into the objective function. Optimization is performed using the GUROBI software product. The efficiency check was performed in the IEEE-123 test distribution circuit. The developed method is proposed as an assistant to dispatching personnel when making decisions in conditions of extreme weather events.

In [13], it was proposed to optimize the location of charging stations for electric vehicles. A joint solution algorithm is used that combines the Voronoi diagram and the particle swarm optimization algorithm. Testing of the developed algorithm is carried out in the IEEE-39 distribution scheme.

Solution to the optimization problem, taking into account energy storage systems and the individual characteristics of consumer load schedules, is presented in [14]. The particle swarm optimization algorithm is used, testing is performed in the IEEE-33 distribution scheme.

The articles [15, 16] consider the issue of increasing resilience by determining the optimal topology of the electrical network. In [17], in order to increase resilience, it is proposed to determine the optimal composition of power transmission lines that should be laid underground. In these studies, optimization is performed using a genetic algorithm [15], the "Column & Constraint Generation" algorithm based on decomposition [17], and the HiGHS software product [16].

In order to increase resilience in operation [18], a solution is proposed, in which OHPL supports are reinforced and distributed and mobile energy sources are placed. In [19], RES-based sources and battery-based energy storage systems are considered for this purpose. In these studies, the CPLEX software product is used to find the optimal solution. The approaches presented in the papers were tested in IEEE-33 distribution schemes [18, 19] and modified IEEE-118 [19].

In [20], measures such as strengthening OHPL supports and placing distributed energy sources and energy storage systems are considered to solve the optimization problem. The problem is solved using a genetic algorithm. The article [21] uses a particle swarm optimization algorithm and examines the reinforcement of OHPL supports. It is worth noting that [21] additionally takes into account the influence of the state of wind turbines, and in the study [22], when solving the optimization problem, the random nature of power generation by RES-based generating sources is taken into account. The solutions proposed in [20, 21] were tested in the IEEE-69 distribution scheme (a modified scheme is used in [21]).

In the work cycle [23, 24], attention was paid to strengthening and modernizing OHPL supports, pruning bushes and trees, and commissioning backup generating sources. These studies use, among other things, the greedy search algorithm [23] and the "Progressive Hedging" decomposition algorithm [24]. The operation of the proposed models is shown on the test schemes EPRI [23], IEEE-34 [24], and IEEE-123 [24].

It is important to note that the solution of the noted optimization problem is also performed using machine learning algorithms. Increasing the resilience of systems and distribution networks is considered in [25–27]. In [28], a decision support system is presented for managing the demand for electrical energy in distribution networks. In [29], it is predicted that wind power plants will generate power, which has a serious impact on the resilience of the system and the reliability of electricity supply to consumers.

The result of the optimization algorithm is the values of the variables, at which the best value of the objective function is achieved. Based on the analysis of the literature and [30], it can be concluded that researchers use as such variables: reduction or restoration of the load volume (i.e., forced disconnection of electrical energy from some consumers or restoration of their power supply); the capacity of distributed energy sources (including RES-based ones); location and capacity of mobile energy sources, energy storage systems, reactive power compensation systems; the location of electric vehicles and the capacity of their batteries; the condition of devices that change the topology of the electrical network (on or off); variables that characterize the condition of operational repair teams; and some others.

Statistics on accidents in the EPS of the Republic of Cuba and a number of countries (for example, [1–4] and others), as well as the interest of researchers in increasing the resilience of EPS, emphasize the urgency of the problem of optimal functioning of EPS in conditions of extreme weather events. The results obtained in this work are new and complement the above studies. These results include the following. Firstly, the paper considers the EPS scheme, rather than the scheme of the distribution network, that is,

the study was carried out on a larger scale. Secondly, since the EPS scheme is being considered, the work uses a new set of variables for which the best value of the objective function is achieved. Thirdly, the implemented model makes it possible to determine the values of these variables practically for the current electric power mode.

The task of optimizing the current electric power mode can be formulated as follows. It is necessary to determine the values of regulated (independent or optimized) operating and circuit parameters, which will ensure the fullest possible supply of electric energy to consumers. The optimization problem is conditional because it contains constraints in the form of equalities and inequalities.

The noted task was solved by the team of authors, who developed a decision-making model for the optimal functioning of EPS under the influence of extreme weather events. This paper is devoted to the development of this model, which will allow taking into account the availability of distributed energy sources based on RES when making decisions.

Thus, the purpose of this study is to evaluate the effectiveness of integration into EPS of distributed generation based on RES to fully provide consumers with electric energy under the influence of extreme weather events. Such phenomena include high ambient temperature and phenomena that lead to OHPL shutdown (hurricanes, storms, and others). In accordance with the purpose of the study, the following tasks are formulated:

- perform accounting in a distributed generation decision-making model based on RES;
- in the EPS test scheme, determine the optimal RES-based generation capacity and location for various emergency scenarios;
- in the EPS test scheme, consider the uniform distribution of RES-based generation for various emergency scenarios;
- to evaluate the effectiveness of the solutions obtained for the full provision of electric energy to consumers.

2. Methods

The developed decision-making model is a procedure for optimizing the steady-state electric power mode, which makes it possible to determine the values of regulated operating and circuit parameters, at which the minimum value of the objective function is achieved.

The following parameters are accepted as regulated parameters: active capacities of centralized power supply stations, voltage modules on the busbars of generators of these stations, transformation coefficients of step-down transformers.

Optimization task is solved taking into account two types of constraints. Constraints in the form of equalities represent a system of nonlinear equations of the steady-state electric power mode, the solution of which is performed by the Newton method. These equations relate all the operating and circuit parameters of EPS to each other. Restrictions in the form of inequalities are imposed on the regulated variables, as well as on the currents flowing in the OHPL and on the voltages in the EPS nodes.

The dependence of the form is considered as an objective function:

$$F = \sum_{k=1}^{K} I_k + \sum_{m=1}^{M} U_m - \frac{\sum_{n=1}^{N} P_n}{N} \to \min,$$

where K is the number of OHPL that take into account restrictions on the amount of current flowing; M is the number of EPS nodes that take into account restrictions on the amount of voltage; N is the number of EPS nodes that require a full supply of electrical energy to consumers; I_k is the amount of OHPL current exceeding the maximum limit number k; U_m is the amount of if the voltage in the node with the number m exceeds the minimum or maximum limit; P_n is the relative value of the current value of the consumed active power in the node with the number n.

Thus, the objective function takes into account both the current power consumption values and limitations in the form of inequalities. In the optimal mode, OHPL currents and EPS node voltages should be within the specified limits, so the first two components of the objective function will be zero. When consumers are fully supplied with electric energy, $P_n = 1$. Therefore, in this case, the minimum value of

the objective function, regardless of the EPS scheme and the set of optimized parameters, is a constant value and is –1.

Distributed generation based on RES is taken into account in the model when forming a system of nonlinear equations of the steady-state electric power mode. The paper considers two accounting methods. The first one is focused on determining the optimal location (among the consumption nodes) and generation capacity during the current emergency event. In this case, it is assumed that each consumption node has generation capacity (the maximum value of which is 50% of the load capacity), which is included in the list of adjustable parameters. The second method considers the uniform distribution of generation in the consumption nodes.

Let us make an important remark about the above. The lists of regulated parameters and constraints in the form of inequalities adopted in the work are not strictly defined and can be expanded. The lists selected in the work are designed and allow us to show the fundamental possibility of solving the optimization problem. Taking into account additional parameters and restrictions in the algorithm will not lead to significant difficulties.

Optimization of the mode in the developed decision-making model is performed using a genetic algorithm. This algorithm, as follows from the literature review, is used by researchers to solve such problems, since, due to its stochastic nature, it supports a variety of possible solutions and allows for various constraints. This article does not compare the effectiveness of solving the optimization problem using different methods, as this study addresses a different goal. Such a comparison could be performed as part of a continuation and development of this research.

Let us note one more fact. Earlier it was said that the objective function has a known minimum value –1. However, the set of values of the regulated parameters, at which this minimum is achieved, is not the only one. In other words, the minimum of the objective function is not a point, but a certain surface. Due to the stochastic nature of the genetic algorithm, solving the same problem generally leads to different sets of values of the regulated parameters. Thus, among the many solutions, you should choose the one that best suits the current properties and technical characteristics of the equipment. Another possible method, which does not require the marked choice, is to take into account additional components in the expression of the objective function, which will change the form of the function so that it will have obvious extremum points (for example, such a component may be the loss of active power in an electrical network). In this paper, these features are not considered – as noted earlier, the fundamental possibility of solving the optimization problem is shown.

3. *Results and Discussion*

Testing of the new version of the decision-making model was performed in a modified IEEE-39 scheme, in which the structure and values of the parameters were changed. The structural changes are as follows: three transformers that are not connected to generating sources have been replaced by OHPL; a step-down transformer has been added to each consumption node. The EPS diagram obtained in this way is shown in Fig. 1.

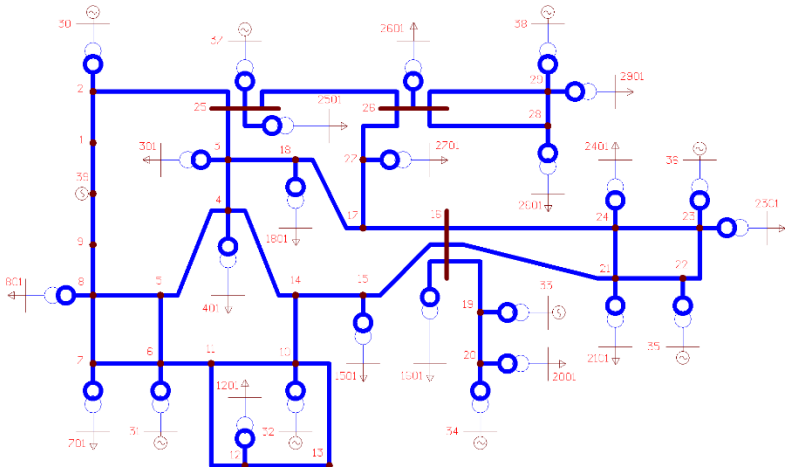

Figure 1. EPS schematic diagram.

This circuit contains 56 nodes, of which 17 are load-bearing (represented as a ZIP model), 9 are generating (represented as a PU model), and 29 are intermediate. The number of branches in the circuit is 64, of which 38 are OHPL, 17 are transformers connected to consumption nodes (LT), and 9 are transformers connected to generating sources (GT). The parameters of the same type of nodes and

branches are the same and are presented in Table 1 (U_{nom}, P_{nom}, Q_{nom} are the nominal values of voltage, active power, and reactive power, respectively) and Table 2 (R, X, G, B are active and inductive resistance, active and reactive conductivity, respectively; k_t is the transformation coefficient; Δk_t is the limits of change in the transformation coefficient).

Table 1. Node parameters.

Node	Parameters			
	U_{nom}, kV	P_{nom}, MW	Q_{nom}, Mvar	ZIP model
Loading	10	100	50	$K_{PZ}=0.47$; $K_{PI}=-0.3$; $K_{PP}=0.83$; $K_{QZ}=6.2$; $K_{QI}=-10.1$; $K_{QP}=4.9$
Generating	10.5	200	–	–
Intermediate	220	–	–	–

Table 2. Branch parameters.

Branch	Parameters					
	R, Ω	X, Ω	G, μS	B, μS	k_t	Δk_t
OHPL	7.5	42	–	270	–	–
LT	2	50.3	3.1	20.4	0.047826	±8x1.5 %
GT	0.7	26	4.6	21.3	0.043388	–

In the accepted formulation of the optimization problem, constraints in the form of inequalities are imposed on the currents flowing in the OHPL. The high ambient temperature leads to a decrease in the permissible OHPL current load, which is expressed in terms of a correction factor, the minimum value of which is 0.67, which corresponds to a temperature of +50 °C. Assuming these most severe conditions, we obtain that the maximum OHPL current limit is 536 A. The minimum and maximum limits for regulated parameters and voltages in EPS nodes are presented in Table 3.

Table 3. Limits of variable variation.

Variable	min	max
Active power, MW	50	200
Generator voltage, kV	10	11
Voltage in the intermediate nodes, kV	198	242
Voltage in the consumption nodes, kV	9	11

So, the effect of high ambient temperature is taken into account in the decision-making model by reducing the permissible OHPL current load. The effects of other extreme weather events that cause OHPL wires to break or supports to fall are taken into account in the model by disabling the corresponding OHPL. In this study, only two possible combinations are considered: disabling one OHPL (38 possible options) and disabling two OHPL (703 possible options). Disabling more OHPLS was not considered due to the increased computational and time costs incurred in sorting through all possible options (for example, when disabling three OHPL, there are 8436 possible options). Nevertheless, for the specific case of disabling several OHPL, the developed decision-making model allows us to determine the values of the regulated parameters corresponding to the most optimal mode of EPS operation. However, in the received mode, some of the electric energy consumers may be turned off.

Let's make an important point. In some of the considered variants, disabling OHPL leads to the separation of the EPS circuit into two independent subcircuits. In this case, the optimal mode is determined for the part of the circuit that contains node No 39, which is the basic balancing node.

Results for the case of disabling one OHPL are shown in Table 4. This table shows the number of shutdown options, in which consumers are fully supplied with electrical energy. In the case of optimal distribution of RES generation, the model solves the problem of determining the optimal location and power of generating sources in a given emergency situation. The uniform distribution of RES generation is taken into account by the presence of generation power consumption in the nodes, which ranges from 5 % to 20 % of the load capacity. The values shown in the columns with the distribution of RES generation take into account the number of options, in which the power supply to consumers is provided without RES.

Table 4. Calculation results when one OHPL is turned off.

Without RES	Optimal distribution of RES generation	Uniform distribution of RES generation			
		5 %	10 %	15 %	20 %
32 (84.2 %)	38 (100 %)	34 (89.5 %)	36 (94.7 %)	37 (97.4 %)	37 (97.4 %)

The data obtained show that the availability of RES-based generation contributes to a more complete supply of electric energy to consumers. With optimal distribution, full power supply to consumers is achieved in all emergency situations. However, such a solution is not universal, since the location and power of the generating source are determined for a specific emergency situation, with another emergency disturbance, the result will not be optimal. Therefore, in this formulation of the problem, the uniform distribution of RES generation is a more universal solution.

Similar results for the case of disabling two OHPL are presented in Table 5. These data also confirm the noted positive impact of RES generation on the power supply to consumers. However, in the case of disabling two OHPL, there is a decrease in the relative number of options, which indicates that there is no required minimum value of the objective function due to the concomitant aggravation of the EPS operating mode.

Table 5. Calculation results when two OHPL are disabled.

Without RES	Optimal distribution of RES generation	Uniform distribution of RES generation			
		5 %	10 %	15 %	20 %
450 (64 %)	691 (98.3 %)	517 (73.5 %)	585 (83.2 %)	625 (88.9 %)	641 (91.2 %)

With a uniform distribution of RES generation (10 %), three calculations were performed for the case of disconnection of one OHPL (3–4) and two OHPL (3–4 and 10–14). The average number of generations (iterations) required to obtain the minimum value of the objective function was 7 in the first case and 12 in the second. The convergence process for all cases is shown in Fig. 2 when one overhead line is disconnected and in Fig. 3 when two OHPL are disconnected. The results obtained demonstrate slower convergence to the solution in the case of disconnection of the two OHPL, which also indicates a more severe mode of EPS operation.

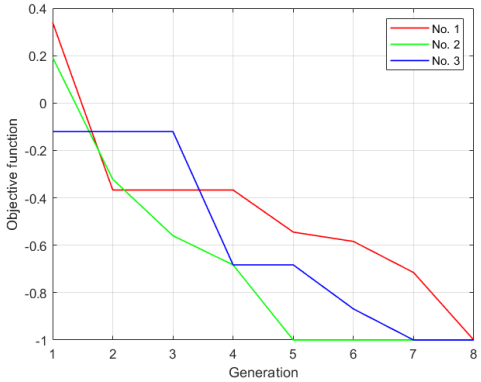

Figure 2. The process of convergence to the minimum of the objective function when one OHPL is turned off.

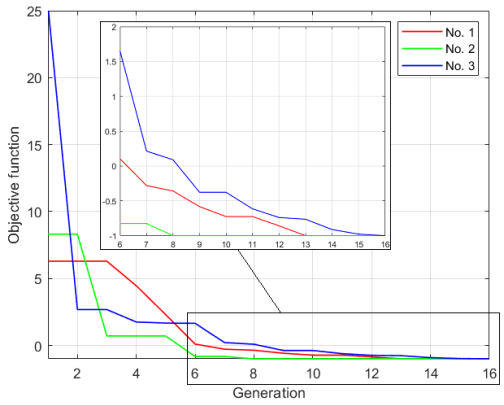

Figure 3. The process of convergence to the minimum of the objective function when two OHPL are disabled.

In the EPS scheme under consideration, the number of adjustable parameters is 35 (in the case of optimal RES generation distribution, the number of parameters is 52). Table 6 shows the values of some of these parameters for the above cases of disconnection of one OHPL (3–4) and two OHPL (3–4 and 10–14). The presented results confirm that the minimum of the objective function is generally achieved with different sets of values of the controlled parameters.

Table 6. Values of the regulated parameters.

Parameter	Disabling one OHPL (3–4)			Disabling two OHPL (3–4 и 10–14)		
	Calculation No 1	Calculation No 2	Calculation No 3	Calculation No 1	Calculation No 2	Calculation No 3
P_{G31}, MW	163.51	173.49	149.2	153.90	106.65	138.46
P_{G34}, MW	127.24	161.07	158.13	93.96	115.38	83.6
P_{G37}, MW	197.68	155.58	196.19	186.45	196.09	196.4
U_{G32}, kV	10.792	10.75	10.846	10.209	10.649	10.455
U_{G35}, kV	10.599	10.939	10.503	10.734	10.822	10.732
U_{G38}, kV	10.348	10.88	10.817	10.851	10.46	10.89
$k_{t(4-401)}$	0.053437	0.043281	0.050879	0.051704	0.049305	0.048554
$k_{t(20-2001)}$	0.05008	0.047826	0.046433	0.044489	0.045767	0.045767
$k_{t(26-2601)}$	0.046433	0.044489	0.045119	0.045767	0.051704	0.043877

Results shown in Table 4 and Table 5 were obtained by iterating through all possible options for disabling one OHPL and two OHPL. Consider the case of disabling three (3–4, 10–14, 28–29), four (3–4, 10–14, 28–29, 14–15), and five (3–4, 10–14, 28–29, 14–15, 16–24) OHPL in a scheme with uniform distribution of generating sources based on RES (10 %). We will perform three calculations for each case. The average number of generations required to achieve the minimum value of the objective function was 21, 25, and 31, respectively. The process of convergence to the solution, which is defined in each case for the calculation with the largest number of generations, is shown in Fig. 4. The results show that each addition of a disabled OHPL leads to a heavier EPS mode.

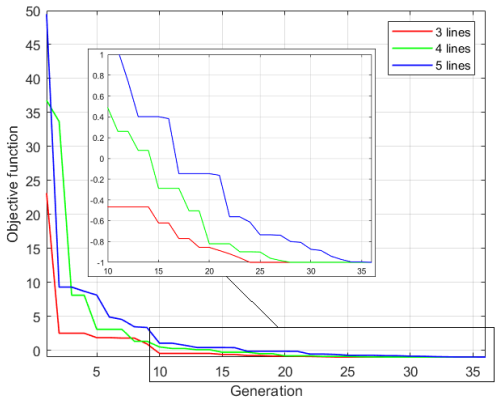

Figure 4. The process of convergence to the solution.

Thus, the calculations performed confirm that in conditions of exposure to extreme weather events, distributed generation based on RES makes it possible in some cases to fully provide consumers with electric energy. The cases of disconnection of one and two OHPL were considered in the most detail. It follows from the results obtained that even a small distributed generation (5 % of the consumption capacity) can save the power supply to consumers in case of 2 additional accidents in the first case and 67 accidents in the second case. Solutions with optimal distribution of sources based on RES have the greatest efficiency in fully providing electric energy, but each such solution is designed for a specific emergency situation. For this reason, this result is generally not acceptable.

The results of this study are consistent with the results obtained by other authors (for example, [7, 9, 10]). These studies note that the optimal implementation of distributed energy sources, including those based on RES, significantly increases the resilience of the system and reduces the amount of electric energy that is not supplied to consumers.

4. Conclusions

The performed research allows us to conclude the following:

- a decision-making model is proposed for the optimal functioning of EPS under the influence of extreme weather events, taking into account the availability of distributed energy sources based on RES;
- the algorithms implemented in the model make it possible to account for various regulated variables, constraints and functions without significant difficulties, which determines the flexibility of the model and the possibility of obtaining scalable solutions (both for large EPS schemes and for electric distribution network schemes);
- the application of the developed model to the modified IEEE-39 scheme made it possible to determine for a number of emergency situations the values of controlled variables, in which the full or maximum supply of electric energy to consumers is achieved;
- uniform (or proportional to the volume of load power) distribution of RES generation in the consumption nodes is preferable to optimal, since it allows to preserve the power supply to consumers in a larger number of emergency situations;
- an algorithm for solving the problem of optimal distribution of RES generation in consumption nodes in the event of a specific emergency can be used to develop an algorithm for solving a similar problem, but in the case of several emergencies.

References

1. Jufri, F.H., Widiputra, V., Jung, J. State-of-the-art review on power grid resilience to extreme weather events: Definitions, frameworks, quantitative assessment methodologies, and enhancement strategies. Applied Energy. 2019. 239. Pp. 1049–1065. DOI: 10.1016/j.apenergy.2019.02.017
2. Bao, M., Ding, Y., Sang, M., Daqing, Li., Shao, C., Yan, J. Modeling and evaluating nodal resilience of multi-energy systems under windstorms. Applied Energy. 2020. 270. Article no. 115136. DOI: 10.1016/j.apenergy.2020.115736
3. Salman, A.M., Li, Y., Stewart, M.G. Evaluating system reliability and targeted hardening strategies of power distribution systems subjected to hurricanes. Reliability Engineering & System Safety. 2015. 144. Pp. 319–333. DOI: 10.1016/j.ress.2015.07.028

4. Wang, C., Ju, P., Wu, F., Pan, X., Wang, Z. A systematic review on power system resilience from the perspective of generation, network, and load. Renewable and Sustainable Energy Reviews. 2022. 167. Article no. 112567. DOI: 10.1016/j.rser.2022.112567
5. Panteli, M., Mancarella, P. Influence of extreme weather and climate change on the resilience of power systems: Impacts and possible mitigation strategies. Electric Power Systems Research. 2015. 127. Pp. 259–270. DOI: 10.1016/j.epsr.2015.06.012
6. Tari, A.N., Sepasian, M.S., Kenari, M.T. Resilience assessment and improvement of distribution networks against extreme weather events. International Journal of Electrical Power & Energy Systems. 2021. 125. Article no. 106414. DOI: 10.1016/j.ijepes.2020.106414
7. Suresh, T.D., Thirumalai, M., Hemalatha, R., Bajaj, M., Blazek, V., Prokop, L. Resilient VPP cost optimization in DER-driven microgrids for large distribution systems considering uncertainty during extreme events. Energy Conversion and Management: X. 2025. 27. Article no. 101176. DOI: 10.1016/j.ecmx.2025.101176
8. Babu, C.H., Raju, H., Thangaraj, Y., Thanikanti, S.B., Nastasi, B. Optimizing power and energy loss reduction in distribution systems with RDGs, DSVCs and EVCS under different weather scenarios. Sustainable Energy Technologies and Assessments. 2025. 75. Article no. 104219. DOI: 10.1016/j.seta.2025.104219
9. Dehghan, M., Zadehbagheri, M., Kiani, M.J., Nejatian, S. Virtual power plants planning in the distribution network constrained to system resiliency under extreme weather events. Energy Reports. 2023. 9. Pp. 4243–4256. DOI: 10.1016/j.egyr.2023.03.080
10. Yuvaraj, T., Krishnamoorthy, R., Arun, S., Thanikanti, S.B., Nwulu, N. Optimizing virtual power plant allocation for enhanced resilience in smart microgrids under severe fault conditions using the hunting prey optimization algorithm. Energy Reports. 2024. 11. Pp. 6094–6108. DOI: 10.1016/j.egyr.2024.05.043
11. Piltan, G., Pirouzi, S., Azarhooshang, A., Jordehi, A.R., Paeizi, A., Ghadamyari, M. Storage-integrated virtual power plants for resiliency enhancement of smart distribution systems. Journal of Energy Storage. 2022. 55(B). Article no. 105563. DOI: 10.1016/j.est.2022.105563
12. Zeng, Y., Qin, C., Liu, J., Xu, X. Coordinating multiple resources for enhancing distribution system resilience against extreme weather events considering multi-stage coupling. International Journal of Electrical Power & Energy Systems. 2022. 138. Article no. 107901. DOI: 10.1016/j.ijepes.2021.107901
13. Mei, H., Wu, Q., Ren, H., Zhang, J., Li, Q. Optimization of electric vehicle charging station layout considering the improvement of distribution network resilience under extreme disasters. Energy. 2025. 323. Article no. 135831. DOI: 10.1016/j.energy.2025.135831
14. Yang, X., Xu, L. Optimal Distribution Grid Scheduling Strategy in the Context of Insufficient Power Supply During Extreme Weather Events. 2024 6th International Conference on Power and Energy Technology (ICPET). Beijing, 2024. Pp. 747–752. DOI: 10.1109/ICPET62369.2024.10940646
15. Widiputra, V., Jung, J. Optimal Grid Reconfiguration Algorithm for Improving System Resilience under Extreme Weather Events. 2020 4th International Conference on Green Energy and Applications (ICGEA). Singapore. 2020. Pp. 12–16. DOI: 10.1109/ICGEA49367.2020.239685
16. Velini, A., Cometa, R., Lorusso, F., La Scala, M., Bruno, S. Optimal Network Reconfiguration for Mitigating the Impact of Adverse Weather Events on Distribution Networks. 2024 IEEE International Humanitarian Technologies Conference (IHTC). Bari, 2024. Pp. 1–7. DOI: 10.1109/IHTC61819.2024.10855123
17. Trakas, D.N., Hatziargyriou, N.D. Strengthening Transmission System Resilience Against Extreme Weather Events by Undergrounding Selected Lines. IEEE Transactions on Power Systems. 2022. 37(4). Pp. 2808–2820. DOI: 10.1109/TPWRS.2021.3128020
18. Ghasemi, M., Kazemi, A., Bompard, E., Aminifar, F. A two-stage resilience improvement planning for power distribution systems against hurricanes. International Journal of Electrical Power & Energy Systems. 2021. 132. Article no. 107214. DOI: 10.1016/j.ijepes.2021.107214
19. Serrano-Fontova, A., Liao, Z., Li, H., Booth, C. A novel resilience assessment for active distribution networks including a DER voltage regulation scheme considering windstorms. International Journal of Electrical Power & Energy Systems. 2023. 153. Article no. 109310. DOI: 10.1016/j.ijepes.2023.109310
20. Ghosh, P., De, M. A stochastic investment decision making method for distribution system resilience enhancement considering automation, hardening and distributed energy resources. Reliability Engineering & System Safety. 2023. 237. Article no. 109395. DOI: 10.1016/j.ress.2023.109395
21. Shabani, A., Nafar, M., Niknam, T. Four-level framework for enhancing active distribution network resilience to wind storms. Electric Power Systems Research. 2025. 249. Article no. 112027. DOI: 10.1016/j.epsr.2025.112027
22. Ren, H., Jiang, Z., Wu, Q., Li, Q., Lv, H. Optimal planning of an economic and resilient district integrated energy system considering renewable energy uncertainty and demand response under natural disasters. Energy. 2023. 277. Article no. 127644. DOI: 10.1016/j.energy.2023.127644
23. Ma, S., Chen, B., Wang, Z. Resilience enhancement strategy for distribution systems under extreme weather events. IEEE Transactions on Smart Grid. 2018. 9(2). Pp. 1442–1451. DOI: 10.1109/TSG.2016.2591885
24. Ma, S., Su, L., Wang, Z., Qiu, F., Guo, G. Resilience Enhancement of Distribution Grids Against Extreme Weather Events. IEEE Transactions on Power Systems. 2018. 33(5). Pp. 4842–4853. DOI: 10.1109/TPWRS.2018.2822295
25. Moradi-Sepahvand, M., Amraee, T., Gougheri, S.S. Deep Learning Based Hurricane Resilient Coplanning of Transmission Lines, Battery Energy Storages, and Wind Farms. IEEE Transactions on Industrial Informatics. 2021. 18(3). Pp. 2120–2131. DOI: 10.1109/TII.2021.3074397
26. Das, A., Ni, Z., Zhong, X. Microgrid energy scheduling under uncertain extreme weather: Adaptation from parallelized reinforcement learning agents. International Journal of Electrical Power & Energy Systems. 2023. 152. Article no. 109210. DOI: 10.1016/j.ijepes.2023.109210
27. Zhou, Z., Wu, Z., Jin, T. Deep reinforcement learning framework for resilience enhancement of distribution systems under extreme weather events. International Journal of Electrical Power & Energy Systems. 2021. 128. Article no. 106676. DOI: 10.1016/j.ijepes.2020.106676
28. Tettey, A., Pham, H., Chen, H., Wu, D., Wooley, A. A decision support framework for electric demand planning in distribution systems during extreme minimum temperatures. Energy Reports. 2025. 14. Pp. 1137–1148. DOI: 10.1016/j.egyr.2025.06.020

29. Liu, Y., Wang, J., Liu, L. Physics-informed reinforcement learning for probabilistic wind power forecasting under extreme events. Applied Energy. 2024. 376(A). Article no. 124068. DOI: 10.1016/j.apenergy.2024.124068
30. Shi, Q., Liu, W., Zeng, B., Hui, H., Li, F. Enhancing distribution system resilience against extreme weather events: Concept review, algorithm summary, and future vision. International Journal of Electrical Power & Energy Systems. 2022. 138. Article no. 107860. DOI: 10.1016/j.ijepes.2021.107860

Contacts:

Aleksandr Feshin,
ORCID: https://orcid.org/0000-0002-4149-4348
E-mail: feshin_ao@spbstu.ru

Maxim Polyukhovich,
ORCID: https://orcid.org/0000-0003-2722-5552
E-mail: polyuhovich_ma@spbstu.ru

Yulia Logvinova,
ORCID: https://orcid.org/0000-0002-8392-1790
E-mail: logvinova_yuv@spbstu.ru

Vyacheslav Burlov,
ORCID: https://orcid.org/0000-0001-7603-9786
E-mail: burlov_vg@spbstu.ru

Viktor Barskov,
ORCID: https://orcid.org/0000-0001-6914-8212
E-mail: barskov_vv@spbstu.ru

Jose Arzola-Ruiz,
ORCID: https://orcid.org/0000-0002-4101-878X
E-mail: josearzolaruiz1945@gmail.com

Miguel Castro Fernandez,
ORCID: https://orcid.org/0000-0002-3983-469X
E-mail: mcastro@electrica.cujae.edu.cu

Received 04.12.2025. Approved after reviewing . Accepted .

Magazine of Civil Engineering

ISSN 2712-8172

journal homepage: http://engstroy.spbstu.ru/

Research article

UDC 624.13

DOI: 10.34910/MCE.141.2

Dynamic characteristics of machine foundation under harmonic loading on gypseous soil with various degrees of saturation

M.Y. Fattah[1] , ***A.S. Abood***[1], ***M.M. Sabri***[2,3] ✉ , ***A.Sh. Al-Adili***[1]

[1] *College of Civil Engineering, University of Technology, Baghdad, Iraq*

[2] *Peter the Great St. Petersburg Polytechnic University, St. Peterburg, Russian Federation*

[3] *Moscow Automobile and Road Construction State Technical University (MADI), Moscow, Russian Federation*

✉ *mohanad.m.sabri@gmail.com*

Keywords: amplitude, dynamic behavior, dynamic characteristics, gypseous soil, harmonic loading, saturation degree

Abstract. Most existing studies on collapsible soils report considerable scatter in their results, primarily due to variations in testing procedures and sampling methods. These studies have also often relied on static testing as the primary method of validation. However, as development continues, a gap remains in our understanding of how collapsible soil reacts to various dynamic stresses, including mechanical equipment, power stations, trains, roadways, and other dynamic loads. Conventional studies often fail to adequately represent real dynamic loading conditions. Accordingly, it is essential to investigate the response of gypseous soils to vibration and varying moisture content. This research aims to characterize the dynamic behavior of gypseous soil under different saturation states (unsaturated and saturated), subjected to harmonic loading at a relative density of 35 %, with additional consideration of foundation depth and eccentric mass. The experimental program aims to establish a database that enables reliable correlations between wave attenuation and soil damping in gypseous soils. Results showed that the dynamic characteristics of gypseous soil increased with frequency by approximately 50–52 % (settlement), 3–6 % (suction stress), 47–68 % (total stress), 42–46 % (acceleration), and 44–48 % (vertical displacement). With rising saturation up to 60 %, these properties decreased by 6–7 % (settlement and total stress), 2–5 % (acceleration), and 6–9 % (vertical displacement). Between 60 % and 100 % saturation, the values rose sharply, reaching 149–150 % (settlement), 139–173 % (total stress), 50–51 % (acceleration), and 52–54 % (vertical displacement). Foundation embedment from 0.0 B to 1.0 B reduced the peak dynamic responses by approximately 10 % to 15 %, whereas increasing the eccentric mass from 28 g to 44.8 g (a factor of about 1.6) amplified them by approximately 17 % to 68 %, with vertical stress and displacement showing the largest increases. Meanwhile, suction stress rose markedly (approximately 453–457 %) as saturation increased to 60 %, then fell by nearly 100 %, approaching zero, as saturation rose toward full saturation, consistent with the loss of matric suction.

Funding: This research was partially funded by the Ministry of Science and Higher Education of the Russian Federation (funding No FSFM-2024-0025).

Citation: Fattah, M.Y., Abood, A.S., Sabri, M.M., Al-Adili, A.Sh. Dynamic characteristics of machine foundation under harmonic loading on gypseous soil with various degrees of saturation. Magazine of Civil Engineering. 2026. 19(1). Article no. 14102. DOI: 10.34910/MCE.141.2

1. Introduction

Gypseous soils are widely distributed across arid and semi-arid regions, where they form a substantial portion of the surface and near-surface deposits; such soils are typically unsaturated or partially saturated, characterized by an air-water interface and a contractile skin resulting from the presence of pore water. According to [1], soil consists of air, water, and solids. However, recent research indicates that the air-water interface (or contractile skin) plays a crucial role that must be considered independently of other physical factors. The study [2] explains that when the air phase is continuous, the contractile skin interacts with soil particles, altering the mechanical behavior of unsaturated soil.

Several researchers have investigated the influence of various variables on stiffness and the material damping ratio [3–8]. The shear strain amplitude, mean effective confining stress, soil type, and plasticity index are all key factors in determining the shear modulus. Additionally, the number of loading cycles or the loading frequency plays a more critical role than the void ratio, over-consolidation ratio, grain characteristics, and degree of saturation. Other significant factors affecting the damping ratio include soil type, plasticity index, number of loading cycles, loading frequency, and shear strain amplitude [4].

The design and construction of machine foundations represent a critical component of industrial development. National investments in infrastructure and industrial facilities provide the basis for the expansion of other economic sectors, including commerce and tourism.

The foundations of machines subjected to vertical vibrations are commonly evaluated using peak acceleration as the primary control parameter for performance. Soil particles reach equilibrium at a characteristic peak acceleration that depends on the relative density of the granular soil. Further densification occurs only when this acceleration threshold is exceeded [9].

The authors [10] investigated the effects of cyclic loading on unsaturated soils using a triaxial system equipped with strain transducers for small-strain measurements and psychrometers for suction monitoring. A fixed water ratio was maintained during testing on kaolin specimens. The results indicated that suction decreased progressively with increasing number of loading cycles. Furthermore, the resilient modulus increased with rising water content up to an optimum level, beyond which it decreased sharply with further increases in water content.

The cyclic behavior of unsaturated soils was studied by the authors [11] using a triaxial test subjected to low loads and varying temperatures. Experiments have shown that under low loads, low temperatures, and high suction, the soil becomes consistently more rigid. The results of the cyclic triaxial test indicate that the soil's plasticity increases with the number of cycles, but all the unsaturated test samples reached a stable state after 100 cycles. The total plastic strain after 100 cycles was greater at higher temperatures and lower suction levels. Each result was influenced by either suction hardening or heat softening, respectively. The study also found that suction had a significant effect on the resilient modulus. The resilient modulus can increase by up to an order of magnitude when suction rises from zero to 250 kPa at a given temperature.

Physical, chemical, or combined types of weathering can break down rock components, but soil is among the most valuable natural resources produced by these processes. Soil formation in a specific location, or "zone," is heavily influenced by the region's geology, geography, and climate. Unsaturated soil is generally regarded as a three-phase system, comprising solid, liquid, and gaseous phases. Interactions among these parts, whether under static or dynamic stress, result in significant changes to the system's characteristics. Static loads remain constant over time and space, whereas dynamic loads change in direction, position, and/or amplitude. Many researchers are eager to explore the complexities of soil behavior under various dynamic loading conditions. The response of sedimentary soils to dynamic loading, such as strong earthquake motions, is significantly influenced by their dynamic properties, including stiffness degradation, modulus reduction, and damping [12]. Examples include shear wave velocity, changes in stiffness or decreasing modulus, material damping at strain levels, and components sensitive to liquefaction, all of which are extensively studied. The ability to predict or interpret dynamic behavior depends on understanding the soil's dynamic characteristics. Geotechnical earthquake engineering relies heavily on accurate estimates of dynamic soil parameters. Factors such as stress state, confinement, stress history, void ratio, water content, and other conditions influence dynamic soil properties [13].

The resilient modulus of subgrade soils has been widely investigated and is influenced by several factors, including the number of loading cycles, loading frequency, grain-size distribution, and stress history. The study [14] concluded that stress is the most critical parameter governing this behavior.

Two principal processes of soil deformation under dynamic loading are liquefaction and cyclic mobility. Both are associated with increases in pore water pressure, which reduces the effective stress and weakens soil resistance under repeated shear loading. In loose, non-cohesive, moisture-sensitive soils, particularly coarse silt and fine to medium sands, dynamic vibrations can induce liquefaction. Under such

conditions, soil grains densify, transferring intergranular stresses to the pore water. When the pore water pressure equals the total stress, the effective stress becomes zero, and the soil loses all its frictional shear strength. Liquefaction typically leads to rapid settlement and severe degradation of track or foundation geometry. Cyclic mobility, in contrast, can occur in both loose and dense soils, although liquefaction is predominantly associated with loose deposits [15].

The authors [16] experimentally demonstrated that embedment of a square footing in medium sand reduces settlement by approximately 15.2–17.3 % at a load amplitude of 0.5 t, and by 6.7–10.5 % at 1 t. In dense sand, settlement reduction reached 25.2–42.5 % at 0.5 t, 9.7–29.1 % at 1 t, and 12.6–23.2 % at 2 t.

Similarly, the authors [17] investigated contact pressure distribution beneath circular shallow foundations subjected to vertical and rocking vibration modes. Tests on dry sands of varying densities indicated that vertical settlement decreased with increasing embedment due to enhanced vertical stiffness. Under rocking vibration, stress distribution along the base increased toward the center before diminishing outward. Lateral edge strains rose from 100 % to 150 % in the rocking direction, while vertical rocking generally induced a central depression, resulting in maximum stresses beneath the footing.

Limited research has addressed the behavior of collapsible soils under vibration and repeated loading, particularly in the case of moisture-sensitive gypseous soils. To advance understanding, this study investigates the influence of repeated loading on sandy gypseous soils, with emphasis on how varying saturation levels affect key engineering properties. Factors considered include foundation type, machine characteristics, dynamic load frequency, number of load cycles, elastic modulus variation, foundation embedment, and displacement amplitude. Furthermore, the study aims to clarify the behavior of gypseous soil by analyzing the response of unsaturated samples subjected to vertical vibrations.

2. Methods

This section presents the experimental program, including soil characterization, model preparation, instrumentation, and testing procedures. The methods used for applying cyclic loads and monitoring the response of gypseous soil are described in detail to achieve the objectives of this research.

2.1. Soil Properties

The soil experiments in this paper were conducted on gypseous, collapsible soil. The soil underwent a standard set of tests to determine its physical properties. Fig. 1 displays the soil grain size distribution, and Table 1 presents some of the physical features of gypseous soil that were examined.

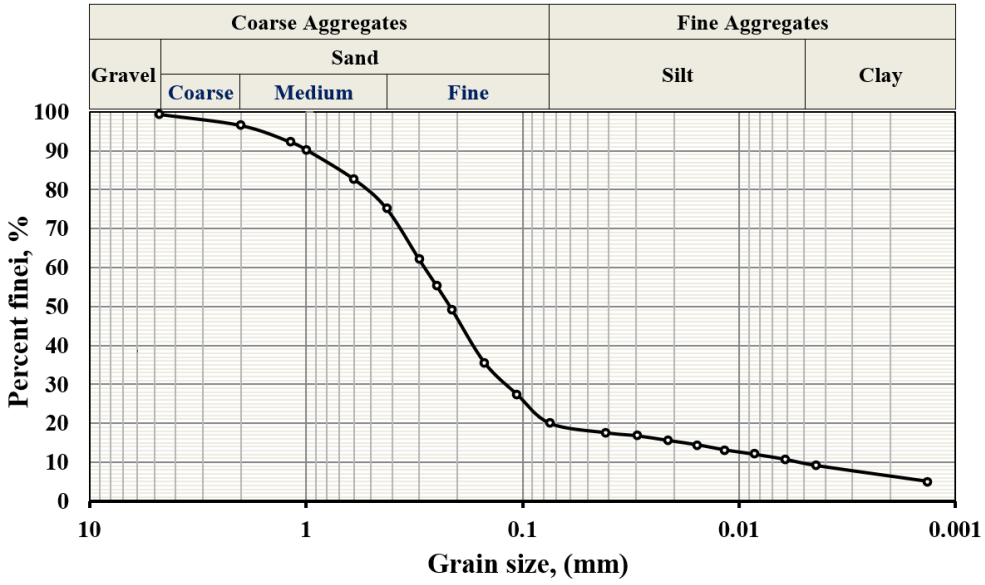

Figure 1. Grain size in the gypseous soil.

Table 1. The characteristics of the gypseous soil.

Property		Value	Reference
Specific gravity	G_s	2.43	ASTM D854[1]
Distribution of particle size, %	Fines	20	ASTM D422[2]
	Sand	79	
	Gravel	1	
Atterberg limits, %	L.L	20	ASTM D854[1]
	P.L	16	ASTM D4318[3]
	P.I	4	ASTM D4318[3]
Classification of soil	U.S.C.S	SM	ASTM D2487[4]
Min. of dry density	$\rho_{d\text{-}min}$, g/cm^3	1.20	ASTM D4254[5]
	e_{max}	1.03	
Max. of dry density	$\rho_{d\text{-}max}$, g/cm^3	1.71	ASTM D4253[6]
	e_{min}	0.42	

Additionally, the B.S. 1377[7] specification was followed to conduct a standard set of experiments necessary to determine the soil's chemical properties. The various chemical characteristics of soil are shown in Table 2 [18].

Table 2. A summary of gypseous soil's chemical characteristics.

Property	Rate of value
Gypsum content ($CaSO_4$), %	45.0
Carbonate content ($CaCo_3$), %	22.5
Total sulphate content (SO_3), %	21.07
Organic matters (O.M), %	0.72
Total soluble salts (T.S.S), %	40.1
pH value (pH)	7.23

2.2. Model tests

To investigate the behavior of gypseous soil at different saturation levels under harmonic loading and to replicate the dynamic properties of the physical model for the machine's foundation, a small-scale model was created at a 1:100 scale. Each component was carefully calibrated, and built-in measuring sensors were included. At a relative density of 35 %, 54 models were tested. Fig. 2 shows the detailed testing schedule.

[1] *ASTM D854. Standard Test Methods for Specific Gravity of Soil Solids by Water Pycnometer. ASTM International. West Conshohocken, PA, USA.*

[2] *ASTM D422. Standard Test Method for Particle-Size Analysis of Soils. ASTM International. West Conshohocken, PA, USA.*

[3] *ASTM D4318. Standard Test Methods for Liquid Limit, Plastic Limit, and Plasticity Index of Soils. ASTM International. West Conshohocken, PA, USA.*

[4] *ASTM D2487. Standard Practice for Classification of Soils for Engineering Purposes (Unified Soil Classification System). ASTM International. West Conshohocken, PA, USA.*

[5] *ASTM D4254. Standard Test Methods for Minimum Index Density and Unit Weight of Soils and Calculation of Relative Density. ASTM International. West Conshohocken, PA, USA.*

[6] *ASTM D4253. Standard Test Methods for Maximum Index Density and Unit Weight of Soils Using a Vibratory Table. ASTM International. West Conshohocken, PA, USA.*

[7] *BS 1377. Methods of Test for Soils for Civil Engineering Purposes. British Standards Institution. London, UK.*

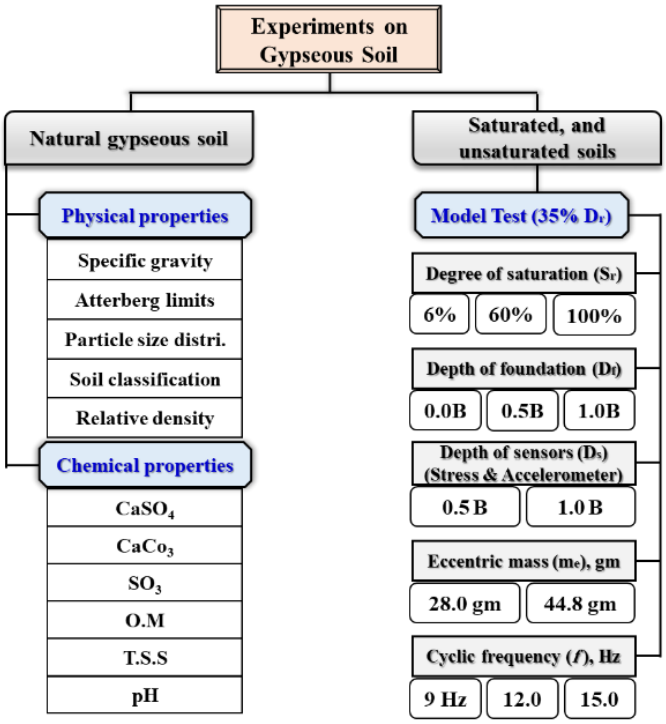

Figure 2. Testing program.

2.3. The Model and Instruments

The prototype container box has a steel plate thickness of 6 mm, with external dimensions of 500 mm by 500 mm by 570 mm. Two layers of absorbent material (each 10 mm thick) were attached to the inside surfaces of the iron box to reduce the reflection of vibration waves at the box boundaries. Each absorption layer is made from different materials (rubber and polystyrene). The steel container box used in the tests is shown in Fig. 3.

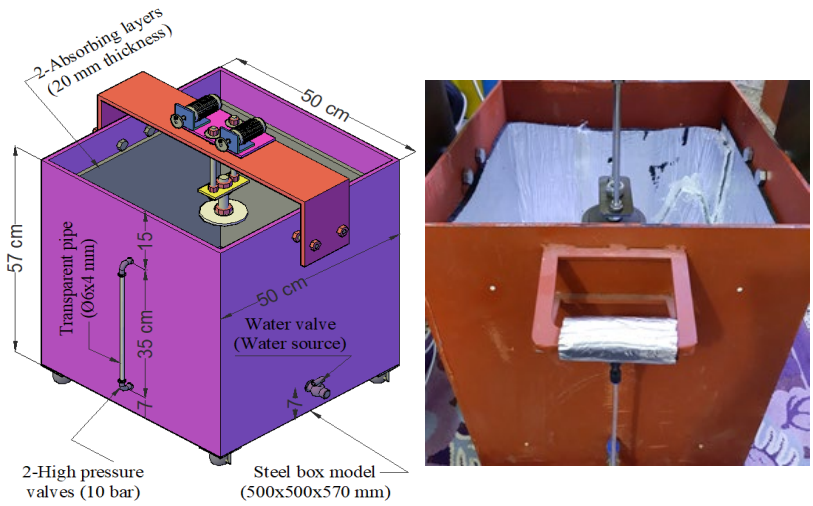

Figure 3. The steel container box.

For this purpose, a compact oscillator was built for lab testing. Also known as a 2-mass oscillator, this device is used to generate harmonic vibrations. The speed regulator panel enables the user to adjust the voltage supplied to the motor, which in turn alters the motor's speed and the oscillator's vibration frequency, ranging from 5.0 Hz to 40.0 Hz, depending on the required cyclic frequency for testing. The machine that produces the harmonic vibrations is shown in Fig. 4.

Soil mechanics relies heavily on stress sensors, which measure total soil pressure, typically with a capacity of 100 kPa. Soil properties, including strength, compressibility, and stability, can be evaluated with their help [19]. The shape of the stress sensor is illustrated in Fig. 5.

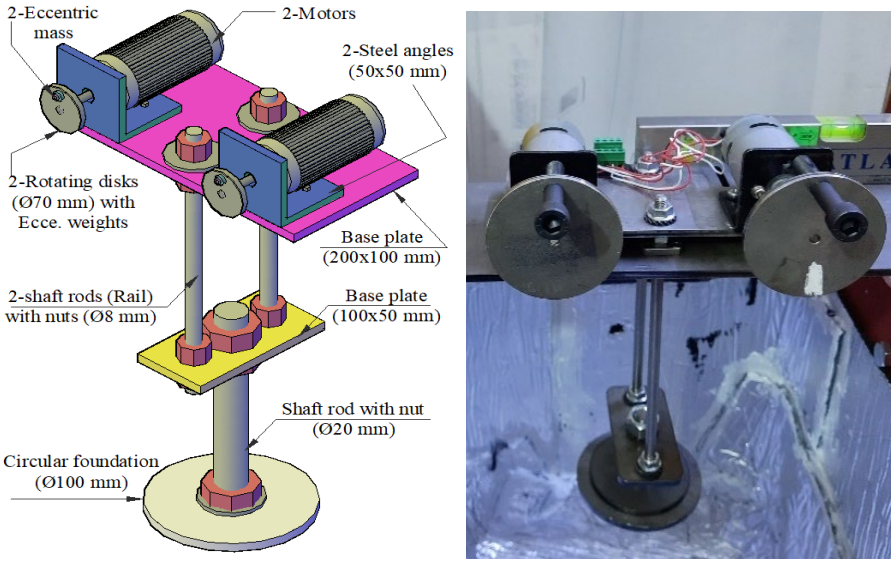

Figure 4. Harmonic vibration generator (mechanical oscillator).

The accelerometer sensor records acceleration along three axes (X, Y, and Z) with adjustable ranges and resolutions, capturing both dynamic accelerations induced by motion or impact, as well as static acceleration due to gravity. The sensor has a measurement capacity of up to 16 g. Data collected by the accelerometer and its recorder were processed using SeismoSignal software to compute displacement, velocity, and acceleration time histories for each axis and at sensor locations within or around the soil model. The accelerometer is illustrated in Fig. 6.

Figure 5. Stress sensors.

Figure 6. Accelerometer sensor.

Measuring pore water pressure is crucial for assessing soil behavior. In this study, a suction pressure sensor with a range of −100 kPa to +100 kPa was used to monitor the pressure difference (i.e., Ua-Uw) between pore air and pore water. Negative values indicate suction (tensile state), while positive values show compression.

The Linear Variable Differential Transformer (LVDT) is an electromechanical transducer that converts linear mechanical displacement into a proportional electrical signal. LVDTs are widely used as

displacement meters due to their high precision, which enables them to measure movements as small as a few micrometers.

Soil moisture, pH, and light intensity were measured using portable soil meters. Two different devices were employed to assess moisture conditions in both unsaturated and saturated soil specimens. The models of the meters and their specifications are presented in Fig. 7.

a. Model of (SKU-6281) **b. Model of (BAF-2.0)**

Figure 7. The soil moisture meters.

2.4. Preparation of the Model for the Test

The subsequent assessment method may be demonstrated*:*

1. To ensure uniform density, the soil sample was placed in successive layers. The net surface area of the model box was approximately 480 × 480 mm, with each layer compacted to a thickness of 50 mm.
2. The gypseous soil was first weighed to determine its target density (loose or medium). It was then placed in the box and compacted manually using a steel or wooden tamper until a uniform 50 mm layer was achieved (Fig. 8a).
3. Figs. 8b and 8c demonstrate the ideal locations for stress and accelerometer sensors inside the model; thus, it is important to follow the instructions in paragraph (2) above until the desired model height (about 500 mm) is obtained.
4. A bubble level was used to make sure the surface was even after the earth was compacted and placed in the steel box.
5. As shown in Fig. 8e, the foundation model, including the harmonic vibration system, was positioned at the plan center (X-Y center) of the box.
6. A single LVDT-equipped magnetic holder was fastened to the sides of the container. The zero reading was obtained by touching the LVDT to the wings at the footing's specified center.
7. Fig. 8e depicts how the models were saturated with water to the desired level: a 50-liter water tank was placed on a wooden table at a height of 500 mm, and a plastic tube with a diameter of 6 mm was connected from the tank to the steel box via the valve at the box's base. After filling the model to capacity with water, the air was forced out of the soil by leaving it uncovered for one day under a double nylon cover, resulting in a fully saturated sample of granular gypseous soil.
8. A piece of plastic pipe (as a cover) with an inner diameter of 102 mm was placed on the soil's surface and around the foundation in order to prevent collapse while preparing a sample with a foundation depth of 0.5 B and 1.0 B. The soil was then sprinkled with a little water using a small water sprinkler until the gypseous soil granules adhered to a small degree and protected it from collapsing. As shown in Fig. 8f, the ring was cut transversely to allow for easy insertion and removal of the pipe section from the foundation system. Additionally, the granular soil sample had already absorbed the necessary amount of water before the test commenced.
9. A harmonic vibration system was used to apply dynamic loads. Fig. 8g displays tension, pressure, accelerometer, and LVDT sensor data over time.

As shown in Fig. 8h, the cyclic frequencies are maintained until failure occurs or the target strain ratio is reached.

The case numbers, model configurations, and experimental variables are summarized in Table 3. The main parameters considered were:

- Saturation degree: three levels were tested (6 %, 60 %, and 100 %);
- Depth of foundation: foundations were embedded at 0.5 B and 1.0 B below the soil surface to assess the effect of embedment on dynamic response;
- Depth of sensors: stress and accelerometer sensors were installed at 0.5 B and 1.0 B to evaluate vibration penetration with depth;
- Eccentric mass: two eccentric masses (28 g and 44.8 g) were applied using the harmonic vibration machine, corresponding to operating frequencies of 9 Hz, 12 Hz, and 15 Hz.

a. Compaction of soil at 5 cm layer

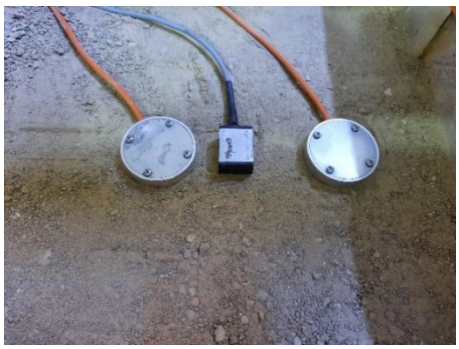

b. Placing sensors inside a model

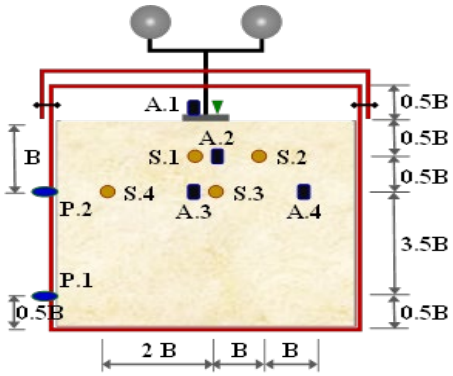

c. The distribution of sensors

d. Placing of foundation at a center

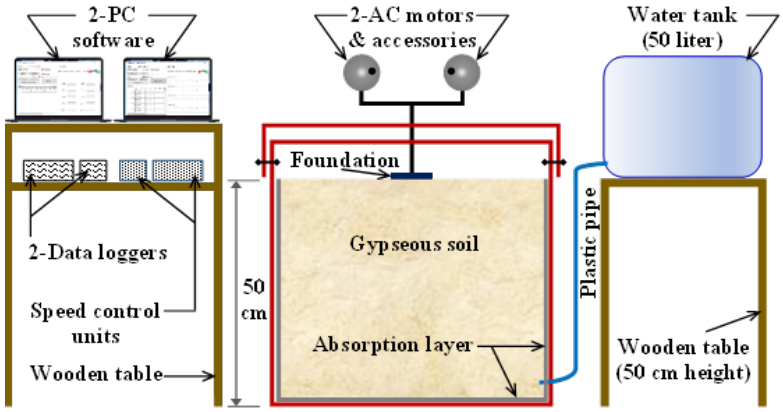

e. The harmonic vibration and soil in the model box with equipment

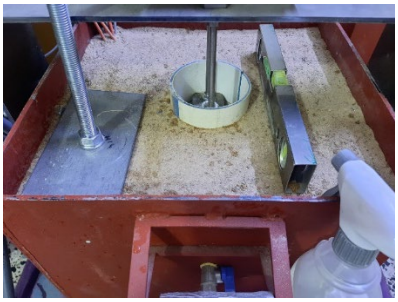


f. Preparing a model at depth foundation (D_f = 0.5 B or 1.0 B)


g. Beginning of the test **h. The model at failure state**

Figure 8. A summary of model preparatory procedures up until their failure.

Table 3. Case studies and models with explanatory variables.

Model details and variable factors			At D_f (0.0B)		At D_f (0.5B)		At D_f (1.0B)	
S_r (%)	m_e (gm)	f_n (Hz)	D_f (mm)	Case No.	D_f (mm)	Case No.	D_f (mm)	Case No.
		9		1		19		37
	28.0	12		2		20		38
Dry (Natural)		15		3		21		39
6%		9		4		22		40
	44.8	12		5		23		41
		15		6		24		42
		9		7		25		43
	28.0	12	0.0 B	8	0.5 B	26	1.0 B	44
Unsaturated		15		9		27		45
60%		9	(0.0)	10	(50.0)	28	(100)	46
	44.8	12	mm	11	mm	29	mm	47
		15		12		30		48
		9		13		31		49
	28.0	12		14		32		50
Saturated		15		15		33		51
100%		9		16		34		52
	44.8	12		17		35		53
		15		18		36		54

Three frequencies 9 Hz, 12 Hz, and 15 Hz were used in this study to calculate D_z, B_z, A_z, k_z, ω_n, c_z, f_n, f_m, m, and G for each frequency, as shown in Equations (1) to (12) [20].

$$D_z = \frac{c_z}{c_{cz}} = \frac{0.425}{\sqrt{B_z}}; \quad (1)$$

$$B_z = \left[\left(\frac{1-\mu}{4}\right)\times\left(\frac{m}{\rho r_o^3}\right)\right] = \left[\left(\frac{1-\mu}{4}\right)\times\left(\frac{W}{\gamma r_o^3}\right)\right]; \quad (2)$$

$$m = \frac{W}{g}; \quad (3)$$

$$c_z = \frac{(3.4r_o)}{(1-\mu)}\sqrt{G\rho}; \quad (4)$$

$$c_{cz} = 2\omega_n m = 2\sqrt{k_z m}; \quad (5)$$

$$G = \frac{k_z(1-\mu)}{4r_o}; \quad (6)$$

$$k_z = \left(\frac{4Gr_o}{1-\mu}\right) = \left[m(2\pi f_n)^2\right] = m\omega^2 = \frac{P}{u}; \quad (7)$$

$$\omega = \omega_n = 2\pi f_n = \sqrt{k_{z/m}} = \sqrt{g/u}; \quad (8)$$

$$f_n = \frac{1}{2\pi}\sqrt{\frac{k_z}{m}}; \quad (9)$$

$$f_m = \frac{f_n}{\sqrt{(1-2D_z^2)}}; \quad (10)$$

$$A_z = \left(\frac{2m_e e_o}{m}\right)\times\left(\frac{B_z}{0.85\sqrt{B_z - 0.18}}\right); \quad (11)$$

$$Q(t) = m\ddot{u} + c_z\dot{u} + k_z u, \quad (12)$$

where, D_z = Damping ratio; B_z = Modified mass ratio; c_z = Coefficient of damping; c_{cz} = Coefficient of critical damping in (N-sec/m); m, W = Total machinery and foundation masses in (kg) and (kN), respectively; ρ, γ = Soil density in (kg/m^3) and (kN/m^3), respectively; g = Ground acceleration (g = 9.81 m/sec^2); μ = Poisson's ratio; r_o = Radius of the circular foundation (radius of the loaded area) in (m); G = Dynamic shear modulus of the soil in (kPa); k_z = Static Spring constant (N/m); ω_n = Rotating masses' natural circular frequency in (rad/sec); f_n = Frequency of natural circular in (Hz); f_m = Resonant frequency in (Hz); A_z = Amplitude of the vibration at frequency resonance in (mm); mRe = The mass of eccentricity in (kg); $eROR$ = The distance of eccentricity in (mm); P = The maximum of vertical load (N); $Q(t)$ = Total force in (N); u = Displacement in (mm); $\dot{u}$ = Velocity in (m/sec); and $\ddot{u}$ = Acceleration in (m/sec^2).

3. Results and Discussion

Fig. 9 presents representative time histories of settlement, acceleration, velocity, displacement, total stresses, and suction pressure obtained from the model tests. For clarity, one case model was selected for each saturation condition (natural, partially saturated, and fully saturated) to illustrate the general response, since the overall shapes of the dynamic curves were similar, differing mainly in average magnitudes. Figs. 10–21 further illustrate the relationships between dynamic soil properties and operating frequency (f_n) or degree of saturation (S_r), considering additional variables such as foundation depth (D_f) and eccentric mass (m_e).

In general, Figs. 10, 12, 14, 16, 18, and 20 illustrate the variation of gypseous soil dynamic properties with operating frequency at different foundation depths (0.0 B, 0.5 B, and 1.0 B) and eccentric masses (28 g and 44.8 g). In contrast, Figs. 11, 13, 15, 17, 19, and 21 illustrate the impact of saturation degree on the same dynamic properties under identical foundation depths and eccentric masses.

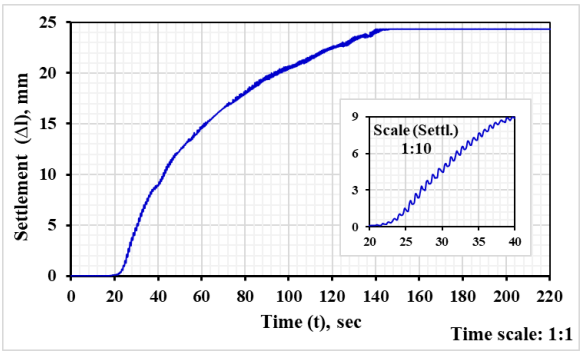

a. Settlement–Time curve

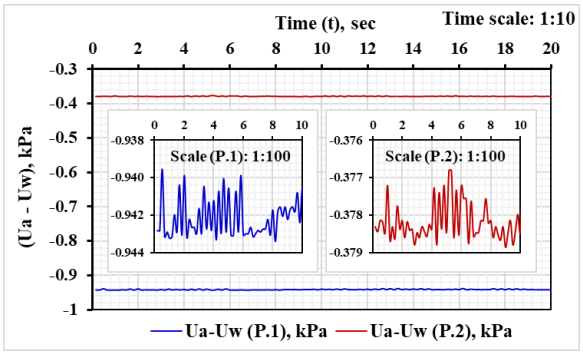

b. Suction pressure–Time curves

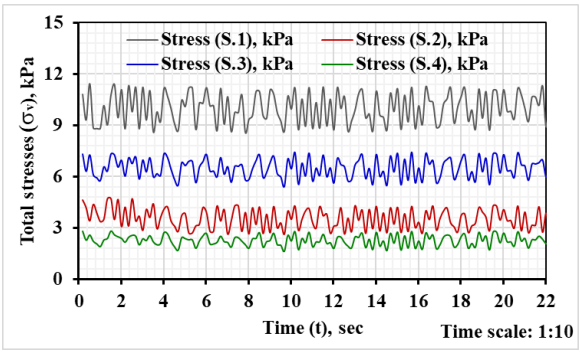

c. Total stress–Time curves at points number 1 to 4

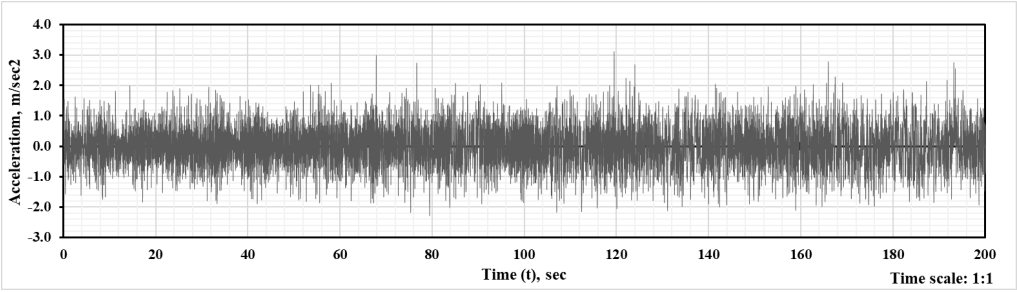

d1. Acceleration–Time curve at point number 1

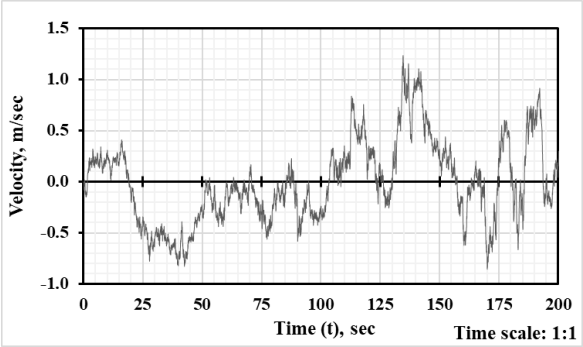

d2. Velocity–Time curve at point 1

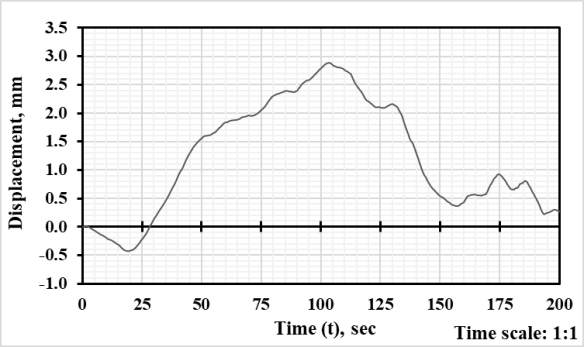

d3. Displacement–Time curve at point 1

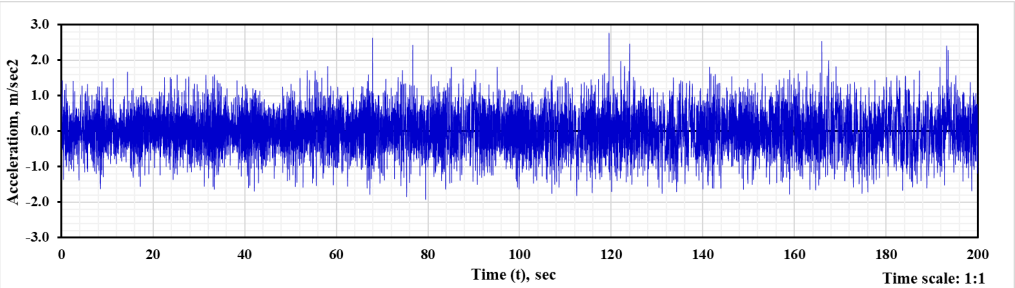

e1. Acceleration–Time curve at point number 2

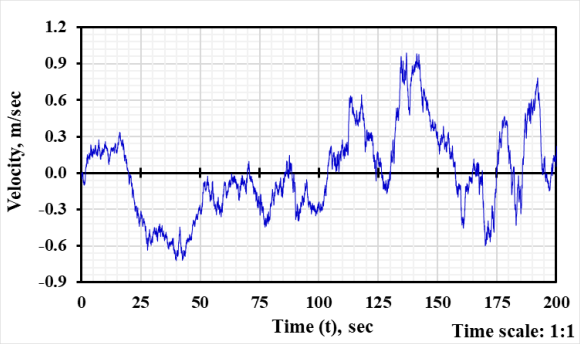

e2. Velocity–Time curve at point 2

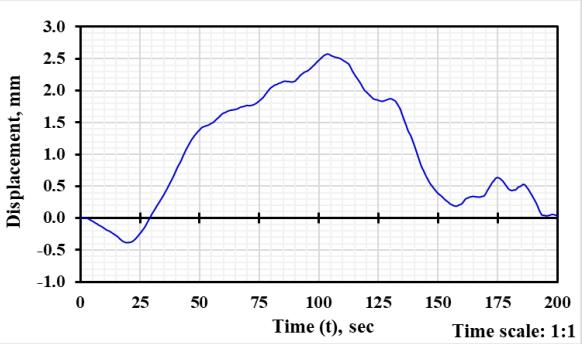

e3. Displacement–Time curve at point 2

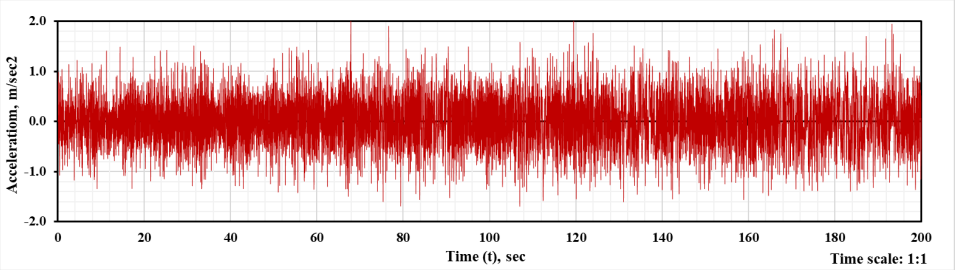

f1. Acceleration–Time curve at point number 3

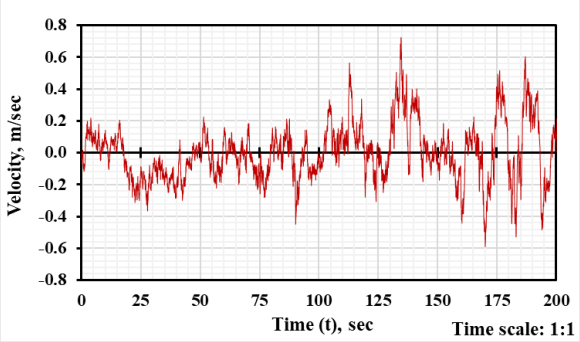

f2. Velocity–Time curve at point 3

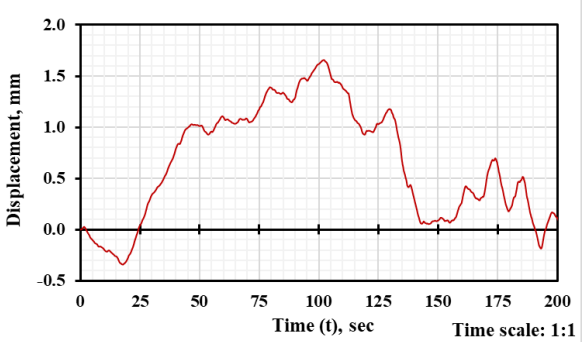

f3. Displacement–Time curve at point 3

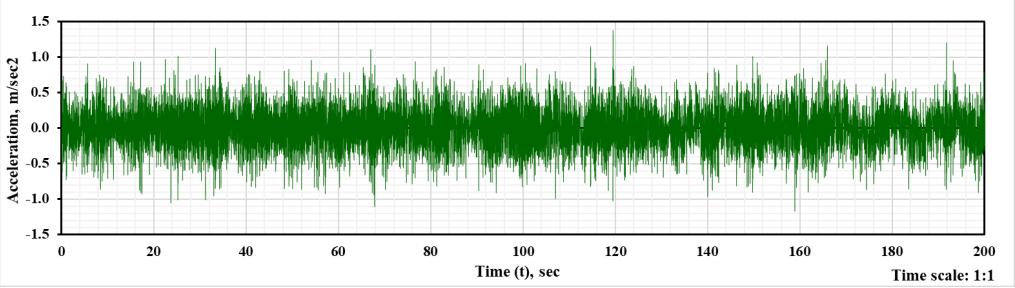

g1. Acceleration–Time curve at point number 4

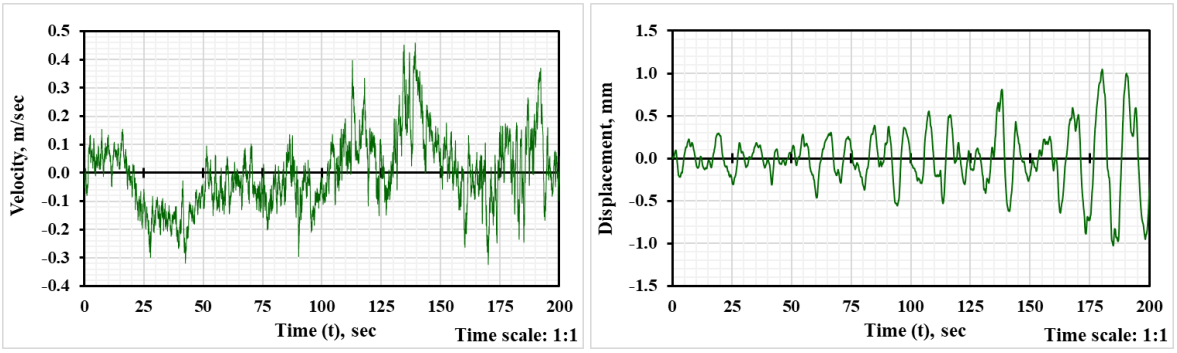

g2. Velocity–Time curve at point 4 g3. Displacement–Time curve at point 4

Figure 9. Typical dynamic characteristics at 100 percent saturation.

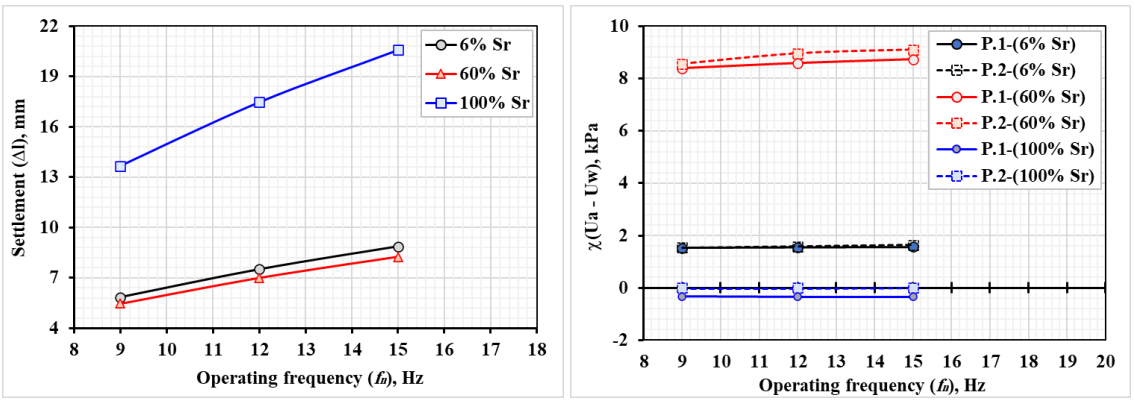

a. Settlement–Frequency curves b. Suction stress–Frequency curves

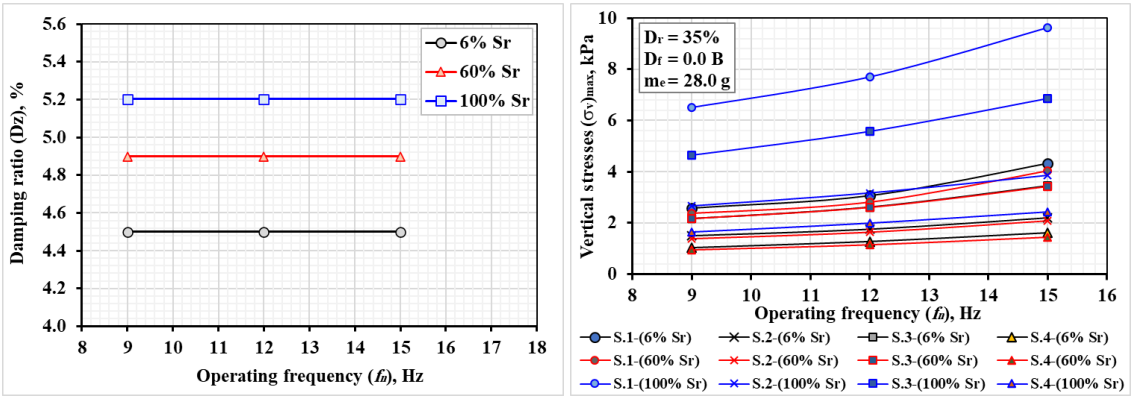

c. Damping ratio–Frequency curves d. Vertical stresses–Frequency curves

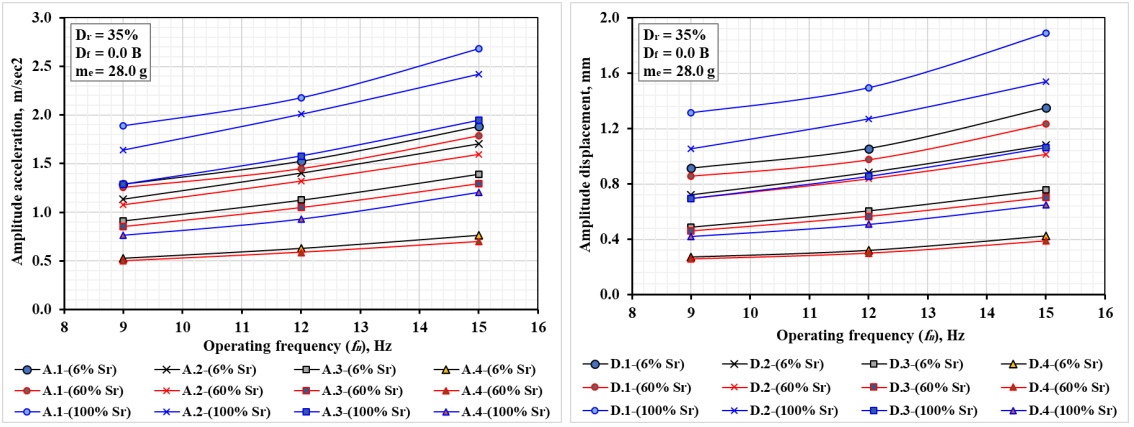

e. Acceleration–Frequency curves f. Displacement–Frequency curves

Figure 10. The behavior of gypseous soil's dynamic properties at different operating frequencies for case study numbers 1, 2, 3, 7, 8, 9, 13, 14, and 15, with m_e = 28.0 g, D_f = 0.0 B, and D_r = 35%.

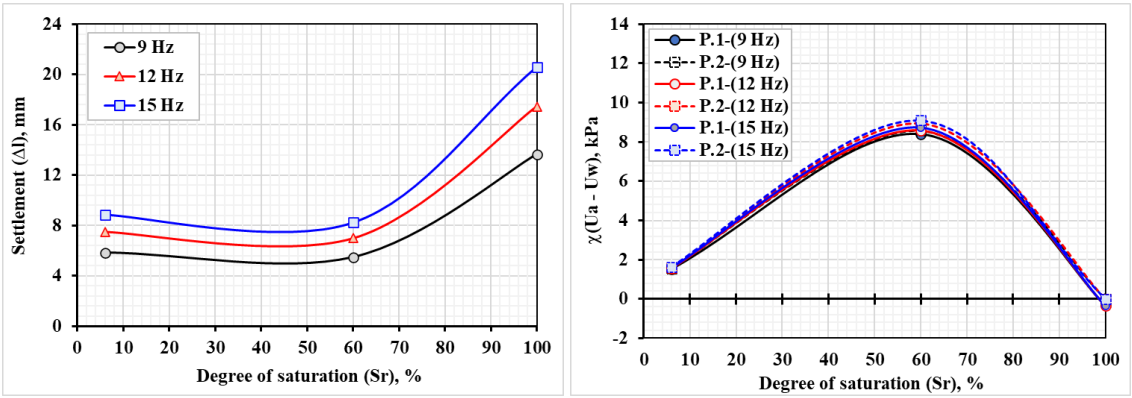

a. Settlement–Saturation degree curves

b. Suction stress–Sr curves

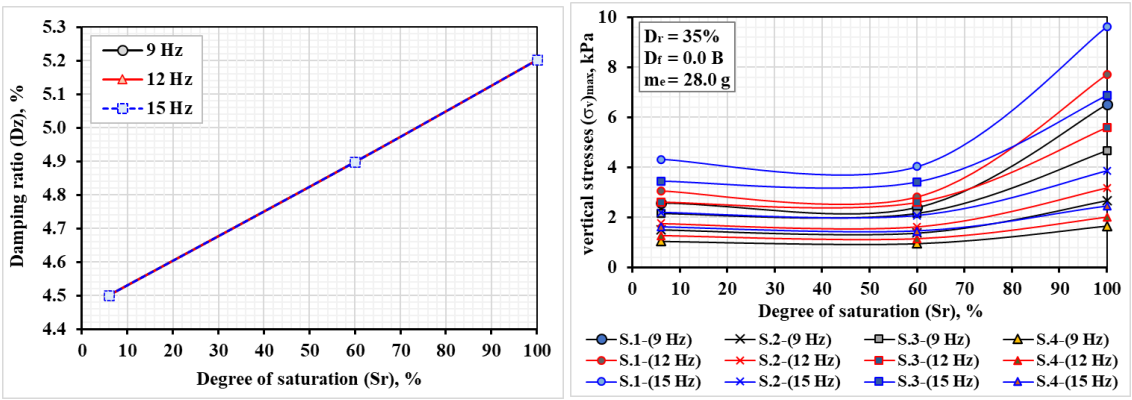

c. Damping ratio–Sr curves

d. Vertical stresses–Sr curves

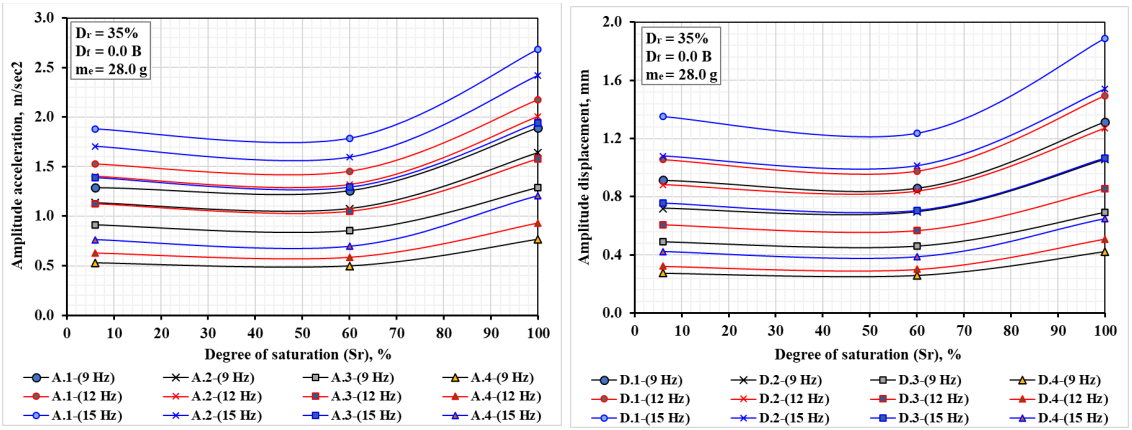

e. Acceleration–Sr curves

f. Displacement–Sr curves

Figure 11. The behavior of gypseous soil's dynamic properties at different saturation levels with m_e = 28.0 g, D_f = 0.0 B, and D_r = 35% for case study numbers 1, 2, 3, 7, 8, 9, 13, 14, and 15.

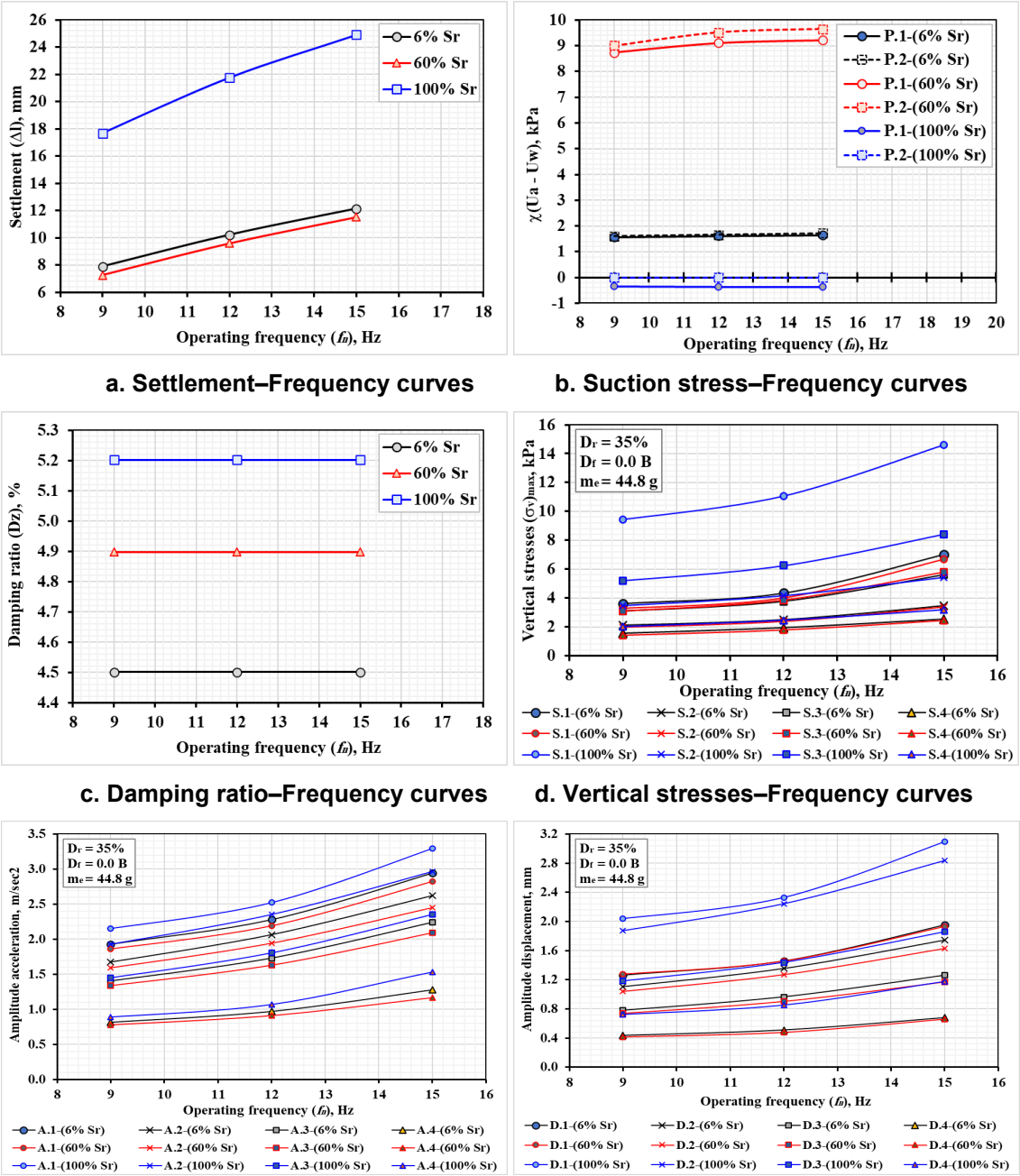

a. Settlement–Frequency curves **b. Suction stress–Frequency curves**

c. Damping ratio–Frequency curves **d. Vertical stresses–Frequency curves**

e. Acceleration–Frequency curves **f. Displacement–Frequency curves**

Figure 12. The behavior of gypseous soil's dynamic properties with varying operating frequencies at m_e = 44.8 g, D_f = 0.0 B, and D_r = 35% for case study numbers 4, 5, 6, 10, 11, 12, 16, 17, and 18.

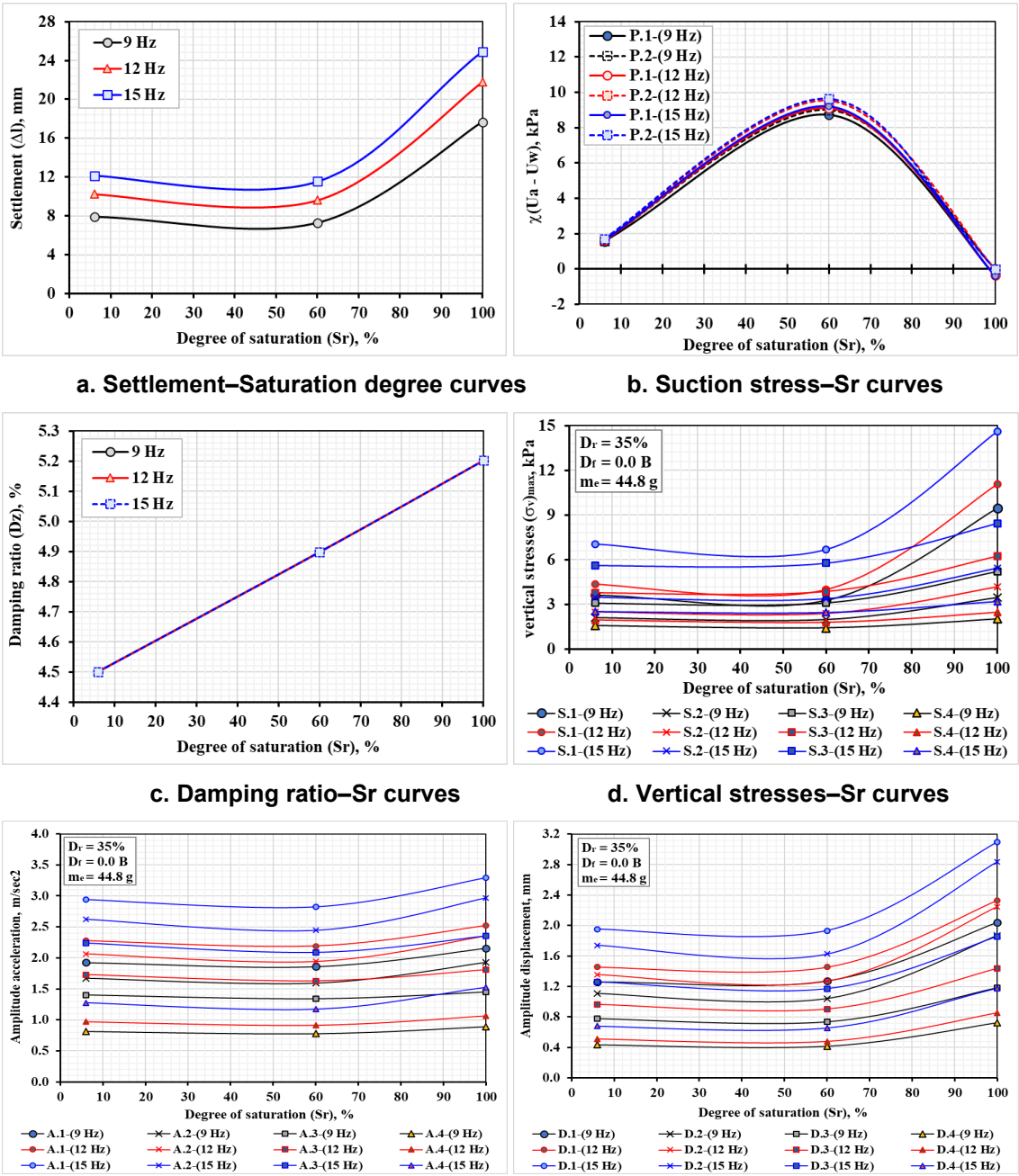

a. Settlement–Saturation degree curves

b. Suction stress–Sr curves

c. Damping ratio–Sr curves

d. Vertical stresses–Sr curves

e. Acceleration–Sr curves

f. Displacement–Sr curves

Figure 13. The behavior of gypseous soil's dynamic properties with varying degrees of saturation for case study numbers 4, 5, 6, 10, 11, 12, 16, 17, and 18 at m_e = 44.8 g, D_f = 0.0 B, and D_r = 35%.

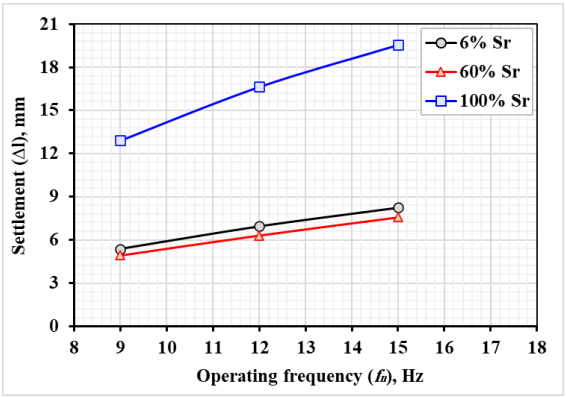

a. Settlement–Frequency curves

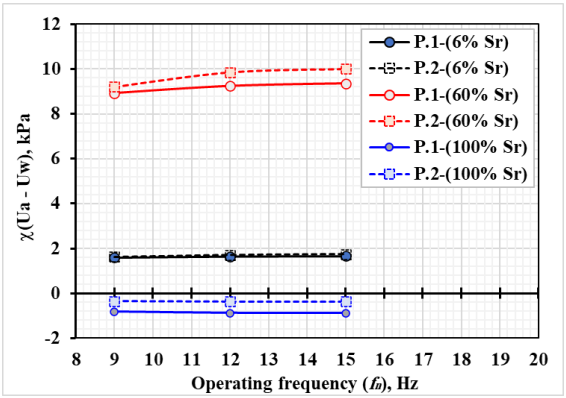

b. Suction stress–Frequency curves

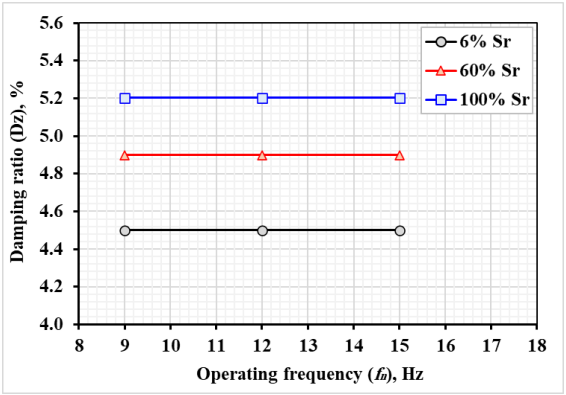

c. Damping ratio–Frequency curves

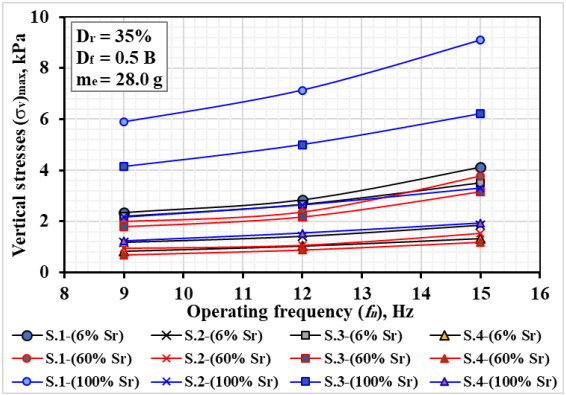

d. Vertical stresses–Frequency curves

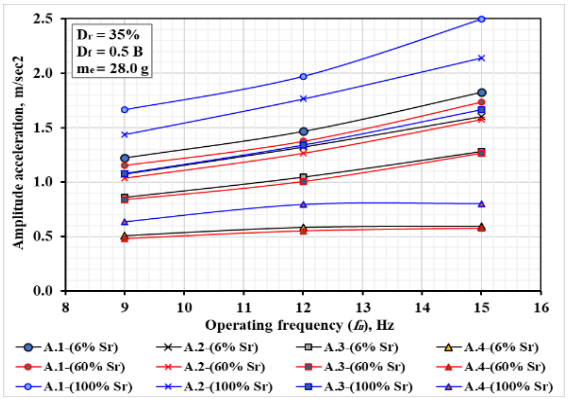

e. Acceleration–Frequency curves

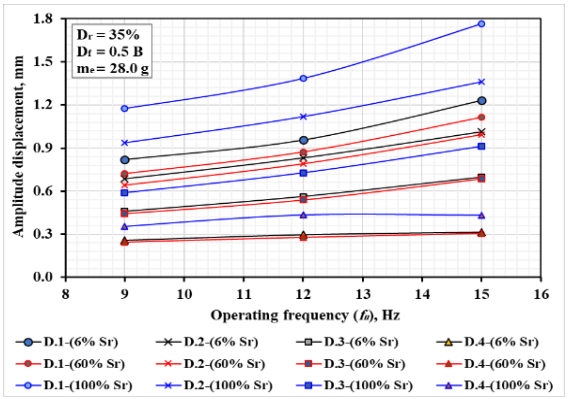

f. Displacement–Frequency curves

Figure 14. The behavior of gypseous soil's dynamic properties at various operating frequencies with m_e = 28.0 g, D_f = 0.5 B, and D_r = 35% for case studies numbered 19, 20, 21, 25, 26, 27, 31, 32, and 33.

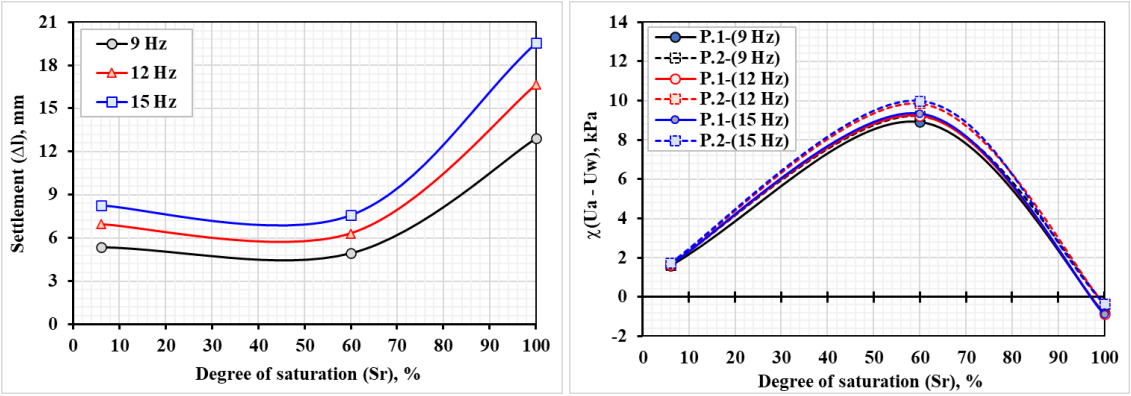

a. Settlement–Saturation degree curves

b. Suction stress–Sr curves

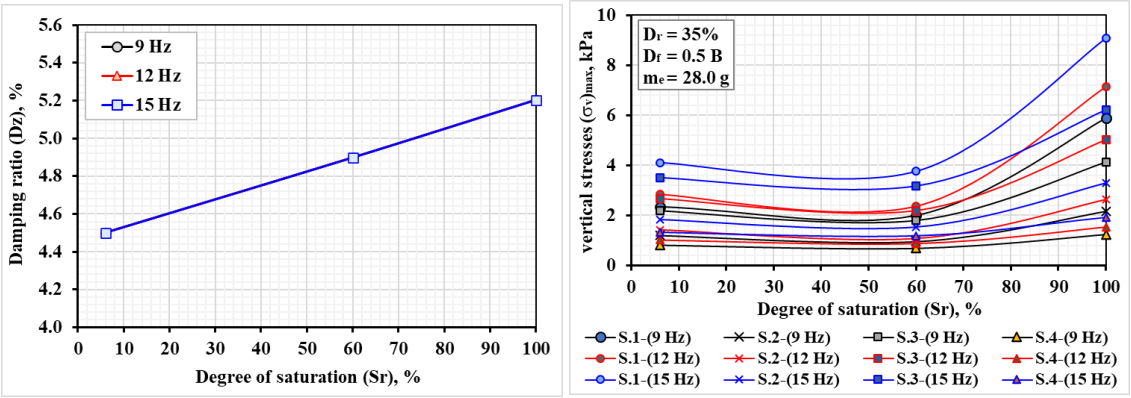

c. Damping ratio–Sr curves

d. Vertical stresses–Sr curves

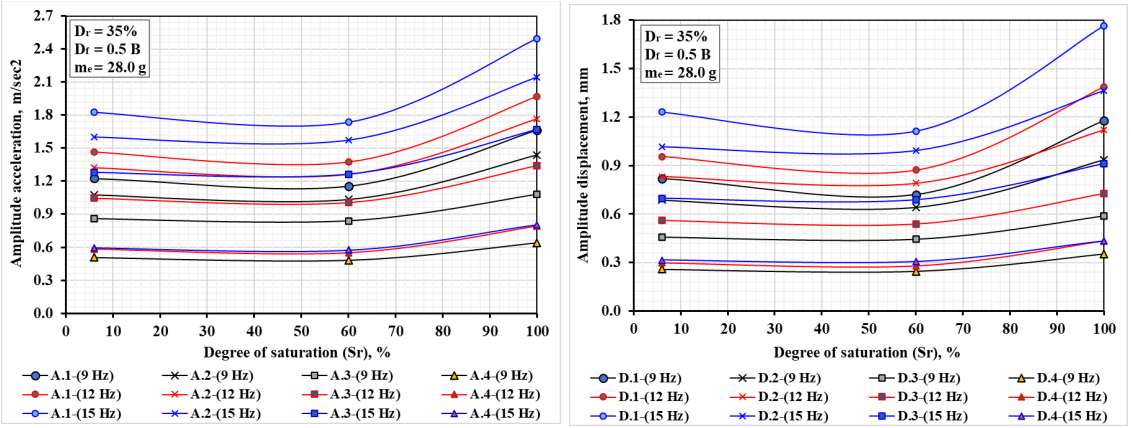

e. Acceleration–Sr curves

f. Displacement–Sr curves

Figure 15. The behavior of gypseous soil's dynamic properties with varying degrees of saturation at m_e = 28.0 g, D_f = 0.5 B, and D_r = 35% for case study numbers 19, 20, 21, 25, 26, 27, 31, 32, and 33.

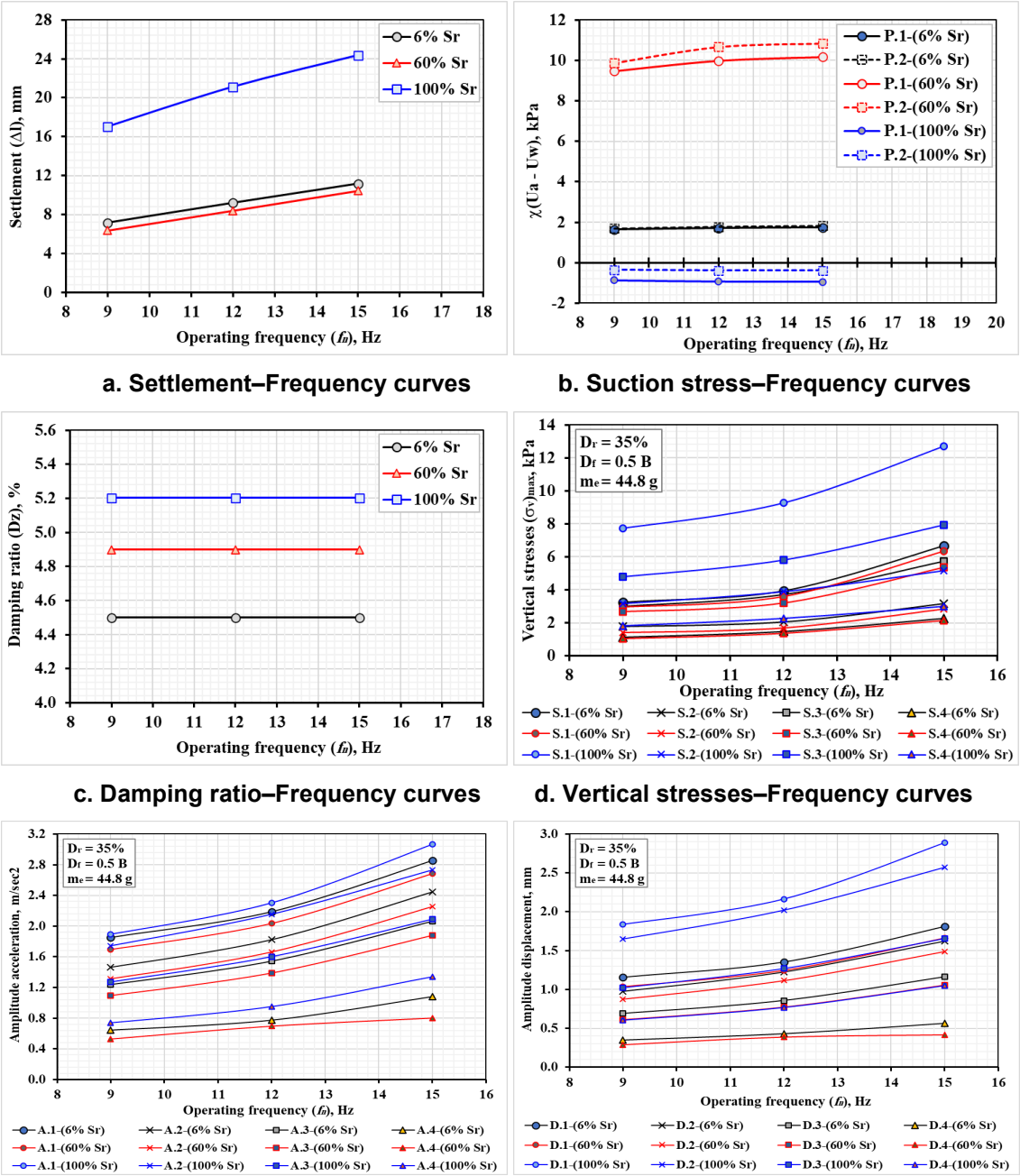

a. Settlement–Frequency curves **b. Suction stress–Frequency curves**

c. Damping ratio–Frequency curves **d. Vertical stresses–Frequency curves**

e. Acceleration–Frequency curves **f. Displacement–Frequency curves**

Figure 16. The behavior of gypseous soil's dynamic properties under varying operating frequencies at m_e = 44.8 g, D_f = 0.5 B, and D_r = 35% for case study numbers 22, 23, 24, 28, 29, 30, 34, 35, and 36.

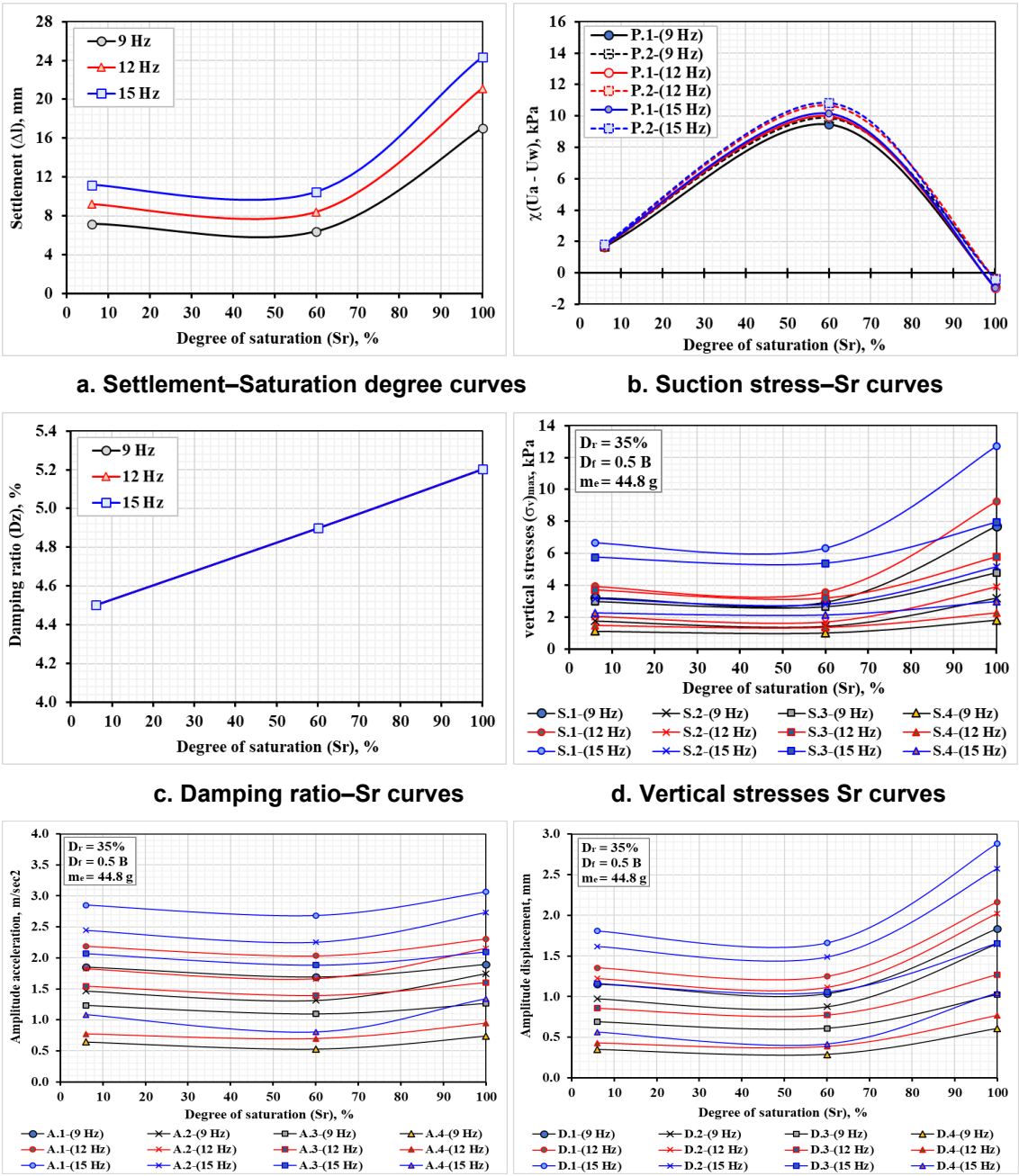

a. Settlement–Saturation degree curves **b. Suction stress–Sr curves**

c. Damping ratio–Sr curves **d. Vertical stresses Sr curves**

e. Acceleration–Sr curves **f. Displacement–Sr curves**

Figure 17. The behavior of gypseous soil's dynamic properties with varying degrees of saturation at m_e = 44.8 g, D_f = 0.5 B, and D_r = 35% for case study numbers 22, 23, 24, 28, 29, 30, 34, 35, and 36.

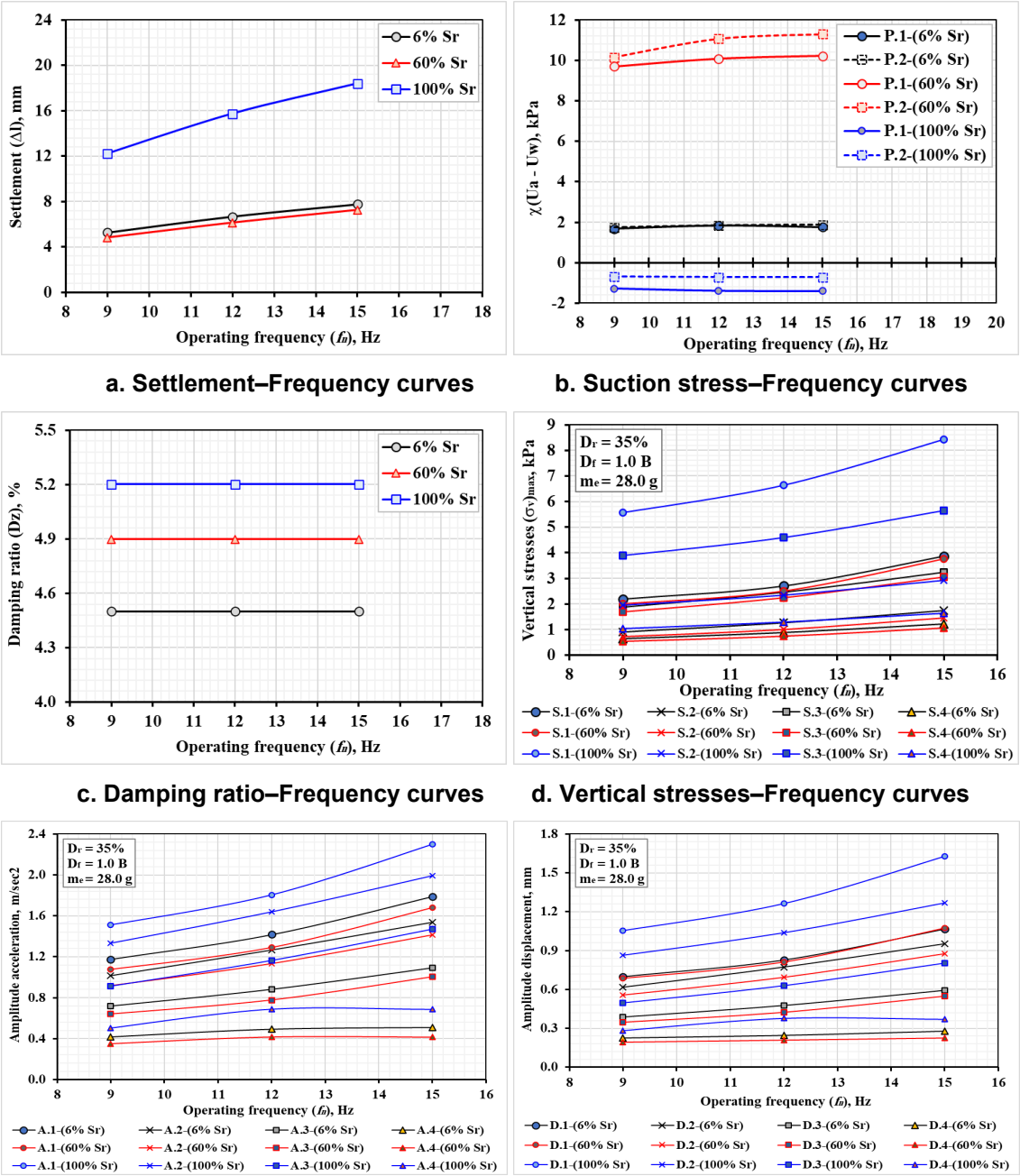

a. Settlement–Frequency curves **b. Suction stress–Frequency curves**

c. Damping ratio–Frequency curves **d. Vertical stresses–Frequency curves**

e. Acceleration–Frequency curves **f. Displacement–Frequency curves**

Figure 18. The dynamic properties of gypseous soil behavior with varying operating frequencies at m_e = 28.0 g, D_f = 1.0 B, and D_r = 35% for case study numbers 37, 38, 39, 43, 44, 45, 49, 50, and 51.

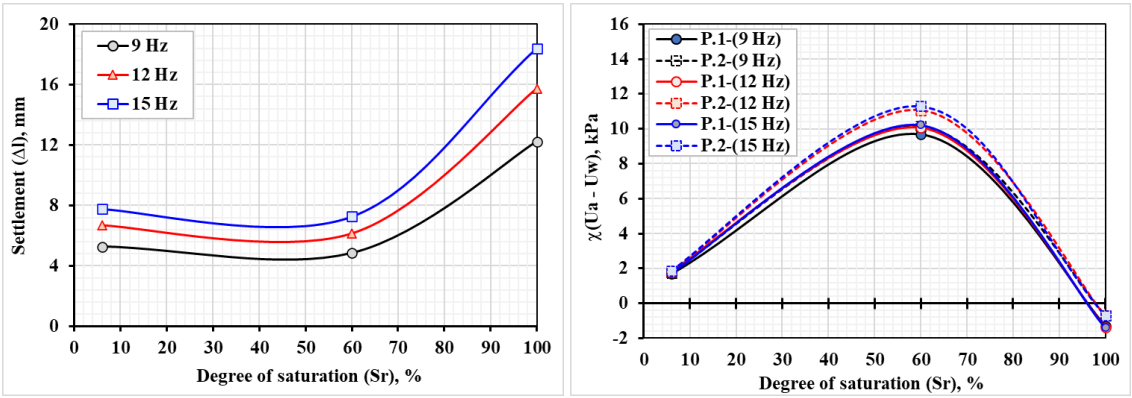

a. Settlement–Saturation degree curves

b. Suction stress–Sr curves

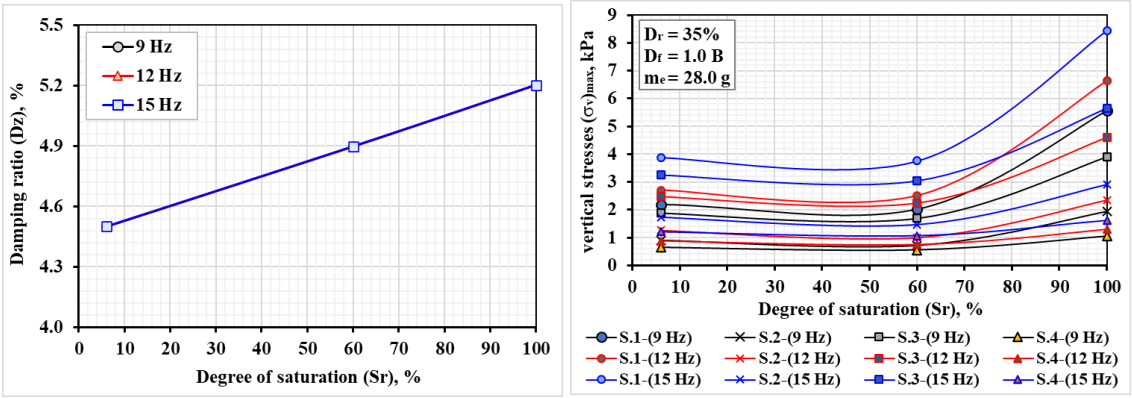

c. Damping ratio–Sr curves

d. Vertical stresses–Sr curves

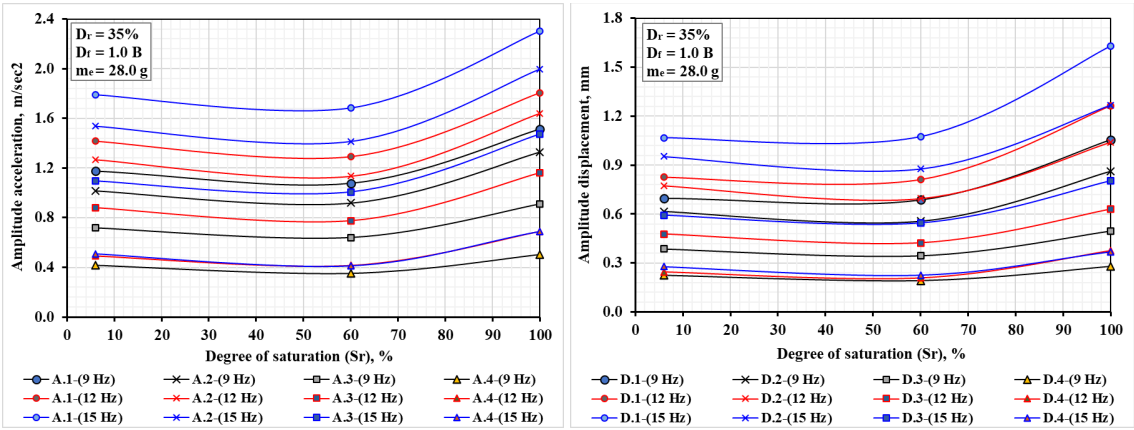

e. Acceleration–Sr curves

f. Displacement–Sr curves

Figure 19. The behavior of gypseous soil's dynamic properties with varying degrees of saturation at m_e = 28.0 g, D_f = 1.0 B, and D_r = 35% for case study numbers 37, 38, 39, 43, 44, 45, 49, 50, and 51.

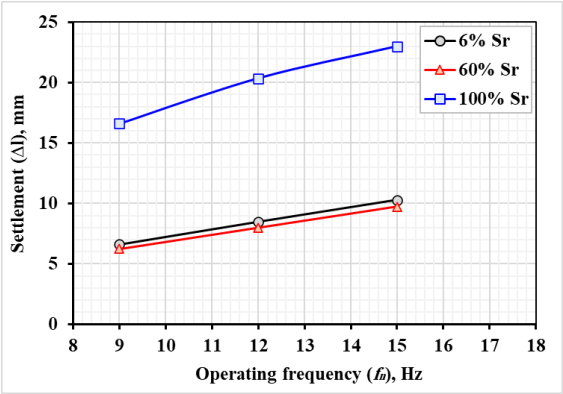

a. Settlement–Frequency curves

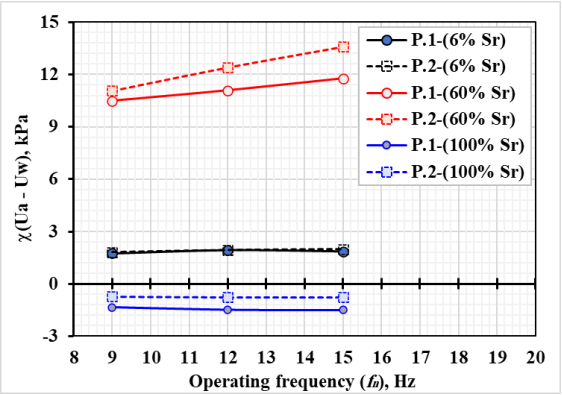

b. Suction stress–Frequency curves

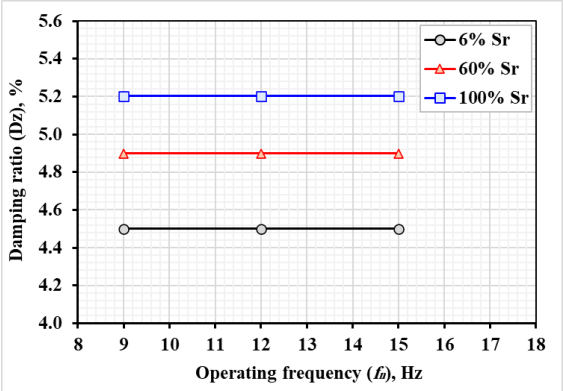

c. Damping ratio–Frequency curves

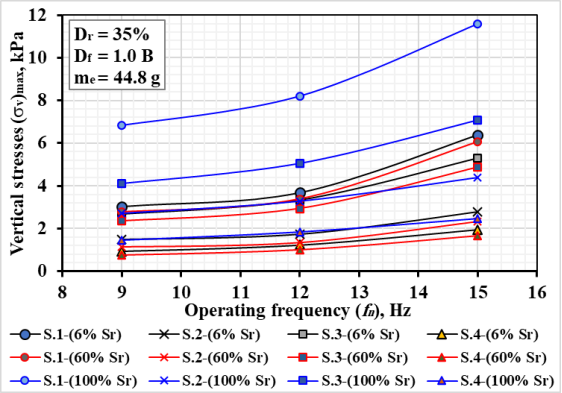

d. Vertical stresses–Frequency curves

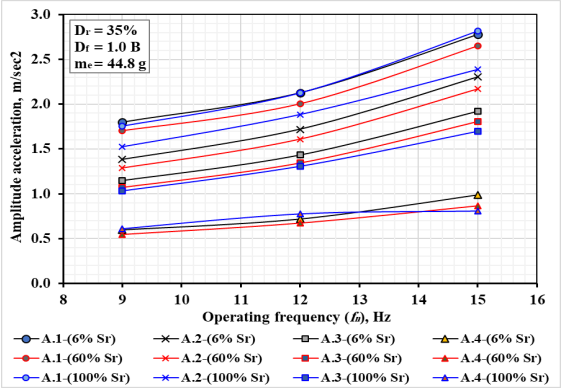

e. Acceleration–Frequency curves

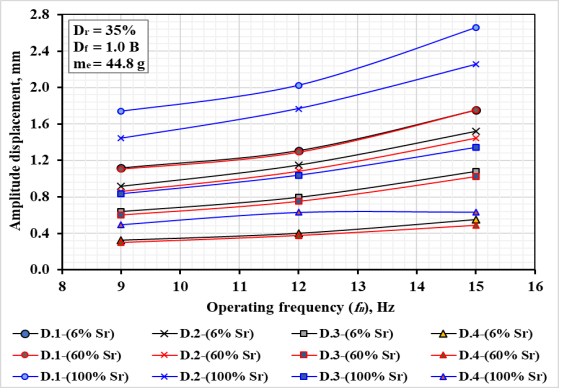

f. Displacement–Frequency curves

Figure 20. The behavior of gypseous soil under dynamic properties with varying operating frequencies at m_e = 44.8 g, D_f = 1.0 B, and D_r = 35% for case study numbers 40, 41, 42, 46, 47, 48, 52, 53, and 54.

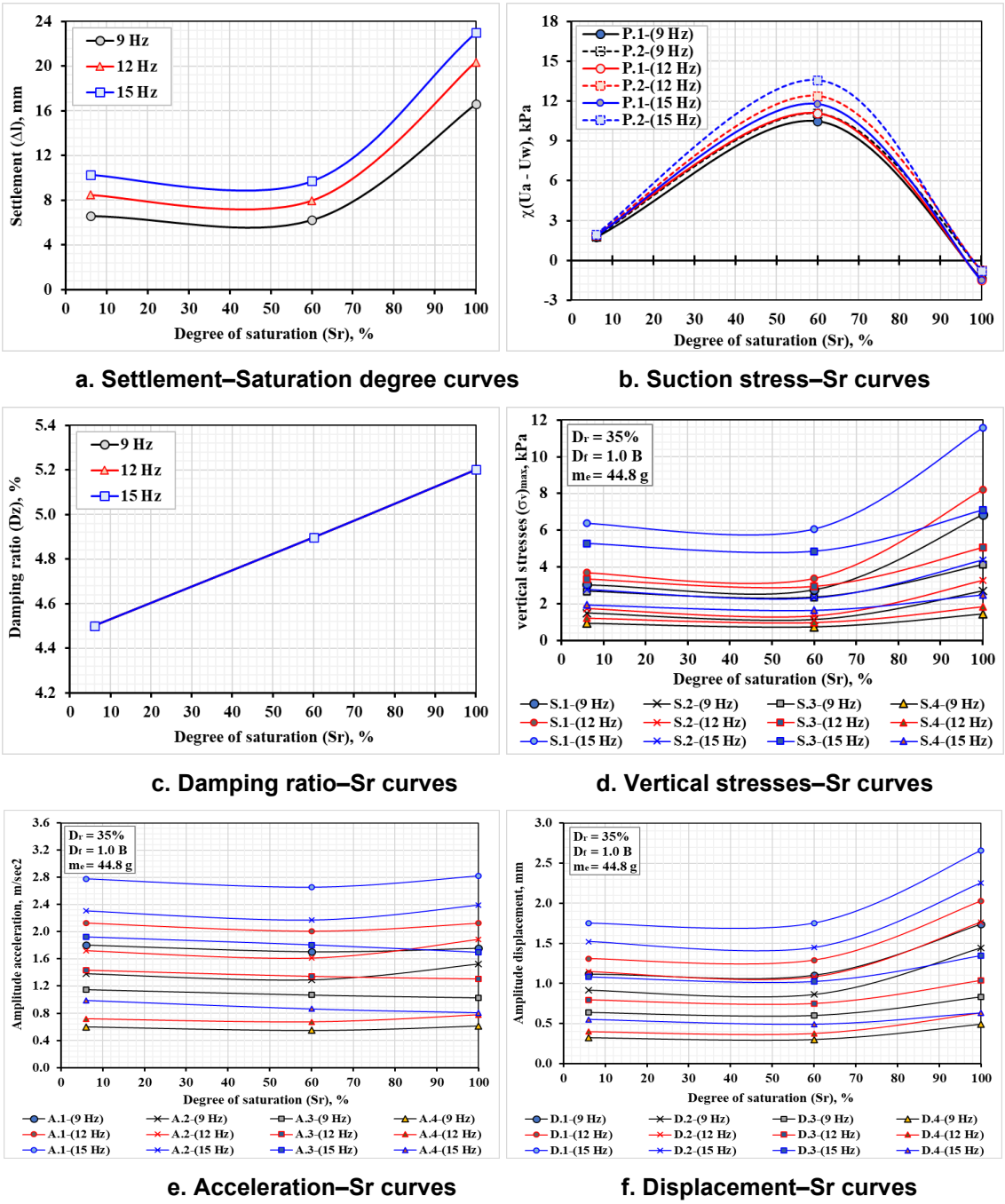

a. Settlement–Saturation degree curves **b. Suction stress–Sr curves**

c. Damping ratio–Sr curves **d. Vertical stresses–Sr curves**

e. Acceleration–Sr curves **f. Displacement–Sr curves**

Figure 21. The behavior of gypseous soil's dynamic properties with varying degrees of saturation for case studies 40, 41, 42, 46, 47, 48, 52, 53, and 54, with m_e = 44.8 g, D_f = 1.0 B, and D_r = 35%.

As shown in Fig. 1, sand is the predominant fraction of the tested soil, with 79 % sand and 1 % gravel, while 20 % passed the No. 200 sieve. Based on the classification results, the gypseous soil from Tikrit is identified as "SM" (silty sand) according to the Unified Soil Classification System (USCS).

The results showed that the tested soil contained 45.0 % gypsum ($CaSO_4$), which is consistent with the findings reported by the authors [21] and [22]. The carbonate content ($CaCO_3$) was relatively high, which typically imparts greater shear strength to soils in their natural or slightly unsaturated state due to the limited presence of clay minerals. The total sulfate content (SO_3) was also elevated, indicating potential interaction with reinforced concrete foundations under wet conditions. The measured pH value of 7.23 reflects a neutral chemical environment. The organic matter content was very low (0.72 %), which explains the pale color and lack of odor in the soil. Additionally, the high level of total soluble salts (TSS) suggests influence from a shallow groundwater table during winter or following irrigation.

The authors [23] conducted preliminary research on the chemical properties of water and their influence on soil behavior. The study demonstrated that water chemistry has a significant impact on the rate and extent of gypseous soil disintegration. Distilled water was found to be more aggressive than saline

water, accelerating the dissolution of gypsum. During the early stages of hydration, gypsum is primarily produced through modifications in the formation of calcium silicate hydrate, making it a key binding agent that contributes to soil stability. In gypseous soils, sulfate ions released from gypsum interact with the alumina phase. When gypsum remains dry, the mechanical response of gypseous soils is similar to that of non-gypsum soils under loading. However, sudden exposure to large volumes of pure water destroys the chemical bonds between gypsum and soil particles, leading to rapid collapse and loss of strength.

Accurate evaluation of ground response in soil–structure interaction, particularly under cyclic and dynamic loading, requires reliable models for shear modulus and damping ratio across a wide range of strains, as soil energy dissipation must be adequately represented. Building on earlier formulations for the initial shear modulus of unsaturated soils, the authors [7] proposed models that incorporate average skeleton stress, bonding variable, void ratio, and degree of saturation to predict shear modulus, damping ratio, and shear strain behavior.

Experimental results of the present study indicate that, under constant soil saturation, foundation depth, and eccentric mass, the dynamic properties of gypseous soil (settlement, acceleration, velocity, displacement, total stress, and suction pressure) increase progressively with operating frequency (Figs. 10, 12, 14, 16, 18, and 20). This trend is attributed to higher cyclic and dynamic stresses imposed beneath the machine foundation at elevated frequencies. However, due to wave damping within the soil, the magnitude of these responses diminishes with increasing distance from the foundation center in both vertical and horizontal directions.

At constant operating frequency and identical testing conditions (saturation, foundation depth, and eccentric mass), Figs. 11, 13, 15, 17, 19, and 21 demonstrate that the dynamic properties of gypseous soil – settlement, acceleration, velocity, displacement, total stress, and suction pressure – are strongly influenced by the degree of saturation. The soil exhibits maximum stiffness and shear strength at an intermediate saturation of 60%, where matric suction peaks, while strength decreases sharply at full saturation (100 % Sr). The damping ratio, in contrast, increased steadily with saturation, from about 4.5 % at 6 % Sr to 4.9 % at 60 % Sr and 5.2 % at 100 % Sr. Compared to the natural condition (6 % Sr), dynamic responses at 60 % Sr are reduced; however, beyond this level, the dissolution of gypsum in water causes bond degradation, leading to increased collapse potential and a higher dynamic response at full saturation.

The dissolution process of gypsum under wetting, particularly under static and cyclic stresses, plays a critical role in soil instability. This process depends on gypsum content, hydraulic gradient, void ratio, and other factors [24].

Quantitatively, the dynamic characteristics of gypseous soil increased with frequency by approximately 50–52 % (settlement), 3–6 % (suction stress), 47–68 % (total stress), 42–46 % (acceleration), and 44–48 % (vertical displacement). With rising saturation up to 60 %, these properties decreased by 6–7 % (settlement and total stress), 2–5 % (acceleration), and 6–9 % (vertical displacement). Between 60 % and 100 % saturation, however, the values rose sharply, reaching increases of 149–150 % (settlement), 139–173 % (total stress), 50–51 % (acceleration), and 52–54 % (vertical displacement). Suction stress showed the opposite trend: it rose dramatically by 453–457 % as saturation increased from 0 % to 60 % then decreased by nearly 100 % (approaching zero) as saturation increased from 60 % to 100 %, reflecting the near-complete loss of matric suction at full saturation.

4. Conclusions

Based on the experimental results and analyses presented in this study, the following conclusions can be drawn:

1. For constant soil saturation, foundation depth, and eccentric mass, the dynamic properties of gypseous soil (acceleration, velocity, displacement, suction pressure, total stress, and settlement) increased progressively with operating frequency.
2. At constant frequency and boundary conditions, the dynamic responses of gypseous soil increased with rising saturation and reached their maximum at full saturation (100 % Sr), where gypsum dissolution degraded interparticle bonding and increased collapse potential.
3. At 60 % saturation, the dynamic properties decreased relative to the natural condition (6 % Sr) by about 7 % (settlement and total stress), 5 % (acceleration), and 9 % (vertical displacement), reflecting maximum stiffness and matric suction at intermediate saturation.
4. Increasing foundation embedment from 0.0 B to 1.0 B reduced the peak dynamic responses of the gypseous soil by approximately 10 % to 15 % (settlement, vertical stress, acceleration, and displacement) at full saturation, owing to the confinement and added vertical stiffness provided by the surrounding soil (Figs. 10, 14, 18).

5. Increasing the eccentric mass from 28 g to 44.8 g (a factor of about 1.6) amplified all dynamic responses at full saturation: settlement and acceleration rose by roughly 17 % to 22 %, vertical stress by about 50 %, and displacement amplitude by about 68 %, consistent with the rotating-mass force scaling as $me \cdot e \cdot \omega^2$ (Figs. 10 and 12).
6. Quantitatively, with increasing frequency, dynamic responses increased by approximately 50–52 % (settlement), 3–6 % (suction stress), 47–68 % (total stress), 42–46 % (acceleration), and 44–48 % (vertical displacement).

References

1. Fredlund, D.G., Rahardjo, H. Soil Mechanics for Unsaturated Soils. John Wiley & Sons. New York, 1993. DOI: 10.1002/9780470172759
2. Ng, C.W., Menzies, B. Advanced Unsaturated Soil Mechanics and Engineering. Taylor and Francis. New York, 2007. DOI: 10.1201/9781482266122
3. Zhou, Y.G., Chen, Y.M. Influence of Seismic Cyclic Loading History on Small Strain Shear Modulus of Saturated Sands. Soil Dynamics and Earthquake Engineering. 2005. 25(5). Pp. 341–353. DOI: 10.1016/j.soildyn.2005.03.001
4. Zhang, J., Andrus, R.D., Juang, C.H. Normalized Shear Modulus and Material Damping Ratio Relationships. Journal of Geotechnical and Geoenvironmental Engineering. 2005. 131(4). Pp. 453–464. DOI: 10.1061/(ASCE)1090-0241(2005)131:4(453)
5. Okur, D.V., Ansal, A. Stiffness Degradation of Natural Fine-Grained Soils during Cyclic Loading. Soil Dynamics and Earthquake Engineering 2007. 27(9). Pp. 843–854. DOI: 10.1016/j.soildyn.2007.01.005
6. Xenaki, V.C., Athanasopoulos, G.A. Dynamic Properties and Liquefaction Resistance of Two Soil Materials in an Earth Fill Dam-Laboratory Test Results. Soil Dynamics and Earthquake Engineering 2008. 28(8). Pp. 605–620. DOI: 10.1016/j.soildyn.2007.10.001
7. Biglari, M., Ashayeri, I. An Empirical Model for Shear Modulus and Damping Ratio of Unsaturated Soils. Proceedings of the Unsaturated Soils: Theory and Practice 2011. Kasetsart University. Thailand, 2011. Pp. 591–595.
8. Abdulrasool, A.S., Fattah, M.Y., Salim, N.M. Displacements and Stresses Induced by Vibrations of Machine Foundation on Clay Soil of Different Degrees of Saturation. Case Studies in Construction Materials. 2022. 17. Article no. e01327. DOI: 10.1016/j.cscm.2022.e01327
9. Das, B.M., Luo, Z. Principles of Soil Dynamics. 3rd ed. Cengage Learning. USA, 2017. 608 p.
10. Sivakumar, V., Kodikara, J., Ohagan, R., Hughes, D., Cairns, P., Mckinley, J.D. Effects of Confining Pressure and Water Content on Performance of Unsaturated Compacted Clay under Repeated Loading. Geotechnique. 2013. 63(8). Pp. 628–640. DOI: 10.1680/geot.10.P.103
11. Chao, Z. Experimental Study and Constitutive Modeling of Cyclic Behavior at Small Strains of Unsaturated Silt at Various Temperatures. Ph.D. Thesis. University of Science and Technology. Hong Kong, 2014.
12. Yuan, B., Huang, X., Li, R., Luo, Q., Shiau, J., Wang, Y., Yuan, J., Sabri, S.M., Huang, S., Liao, C. Dynamic Behavior and Deformation of Calcareous Sand under Cyclic Loading. Soil Dynamics and Earthquake Engineering 2025. 199. Article no. 109730. DOI: 10.1016/j.soildyn.2025.109730
13. Kumar, S.S., Krishna, A.M., Dey, A. Parameters Influencing Dynamic Soil Properties: A Review Treatise. International Journal of Innovative Research in Science, Engineering and Technology. 2014. 3(4). Pp. 47–60.
14. Lekarp, F., Isacsson, U., Dawson, A. State of the Art. I: Resilient Response of Unbound Aggregates. Journal of Transportation Engineering, ASCE 2000. 126(1). Pp. 66–75. DOI: 10.1061/(ASCE)0733-947X(2000)126:1(66)
15. Li, D., Sussmann, T.R., Hyslip, J., Chrismer, S.M. Railway Geotechnics. Taylor and Francis Ltd. Boca Raton, 2016. 448 p.
16. Fattah, M.Y., Salim, N.M., Haleel, R.J. Liquefaction Potential of Sandy Soil from Small Laboratory Machine Foundation Model. International Review of Civil Engineering 2018. 9. Pp. 11–19.
17. Fattah, M.Y., Salim, N.M., Alwan, K.K. Contact Pressure Distribution under Circular Shallow Foundation Subjected to Vertical and Rocking Vibration Modes. Journal of Building Engineering 2019. 26. Article no. 100908. DOI: 10.1016/j.jobe.2019.100908
18. Abood, A.S., Fattah, M.Y., Al-Adili, A.S. Studying Characteristics and Strength of the Unsaturated Gypseous Soil with Various Saturation Degrees. Engineering and Technology Journal 2023. 41 (11). Pp. 1309–1324. DOI: 10.30684/etj.2023.140119.1453
19. Abood, A.S., Fattah, M.Y., Al-Adili, A.S. Assessment of Shear Strength Characteristics of the Unsaturated Gypseous Soil at Various Saturation Degrees. Cogent Engineering. 2023. 10(2). Article no. 2283303. DOI: 10.1080/23311916.2023.2283303
20. Das, B.M., Ramana, G. V Principles of Soil Dynamics. 2nd ed. Cengage Learning. Stamford, 2011. 575 p.
21. Al-Gharbawi, A.S.A., Fattah, M.Y., Mahmood, M.R. Effect of Carbonation on the Collapse Potential of Magnesium Oxide Treated Gypseous Soil. International Journal of Engineering. 2022. 35(4). Pp. 706–714. DOI: 10.5829/IJE.2022.35.04A.10
22. Zidan, A.J., Hussein, M.A. Behavior of Square Footing Subjected to Gypseous Soil under Eccentricity-Inclined Load. Journal of Tikrit of the Engineering Sciences. 2013. 20. Pp. 1–15.
23. Salih, N.B. Field Models on Gypseous Soils Reinforced with Stone Columns Stabilized with Asphalt and Lime. Thesis for M.Sc. Baghdad. University of Technology, 2003.
24. Al-Mufty, A.A. Effect of Gypsum Dissolution on the Mechanical Behavior of Gypseous Soils. Ph.D. Thesis. University of Baghdad, 1997.

Information about the authors:

***Mohammed Fattah**, PhD*
ORCID: https://orcid.org/0000-0002-4356-651X
E-mail: 40011@uotechnology.edu.iq

Ahmed Abood,
E-mail: bce.20.32@grad.uotec

Mohanad Sabri, *PhD*
ORCID: https://orcid.org/0000-0003-3154-8207
E-mail: mohanad.m.sabri@gmail.com

Aqeel Al-Adili, *PhD*
E-mail: 40077@uotechnology.edu.iq

Received 23.09.2025. Approved after reviewing 02.01.2026. Accepted 03.02.2026.

Magazine of Civil Engineering

ISSN 2712-8172

journal homepage: http://engstroy.spbstu.ru/

Research article

UDC 69

DOI: 10.34910/MCE.141.3

Improvements of mechanical and physical features of cement mortar by nano Al_2O_3 and $CaCO_3$ as additives

S.A. Al-Mashhadi[1], ***M.S. Radhi***[1], ***I.H. Obead***[1], ***Z. Al-Khafaji***[1,2] ✉, ***Z.A. Mohammed***[3], ***S.F. Jabr***[3]

[1] *University of Babylon, Hillah, Iraq*

[2] *National University of Malaysia, Bangi, Malaysia*

[3] *Babil Tower for Studies and Scientific Researches, Hillah, Iraq*

✉ *p123005@siswa.ukm.edu.my*

Keywords: cement mortar, Al_2O_3 nanoparticles, $CaCO_3$ nanoparticles, compressive strength, density, ultrasonic pulse velocity

Abstract. The current research aimed to investigate the impact of Al_2O_3 and $CaCO_3$ nanoparticles on the properties of cement mortar. The research methodology primarily focused on preparing mortars using Al_2O_3 nanoparticles with a mean diameter of ~50 nm and $CaCO_3$ nanoparticles with a particle size of 100 nm. These were utilized at three different substitution levels of 1, 3, and 5 % by weight of cement as binary blending materials. The mechanical and physical properties of the cement mortar (compressive strength, density) were tested after 7 and 28 days, while ultrasonic pulse velocity was tested after 28 days of water curing. The experimental results illustrated that utilizing Al_2O_3 nanoparticles improved the mortar's compressive strength at an early age (7 days of curing) more than at 28 days, with 3 % substitution being the optimal proportion. Similarly, the use of $CaCO_3$ nanoparticles as a binary blending mixture at substitution levels of 1, 3, and 5 % by cement weight improved the compressive strength at an early age (7 days of curing) more than at 28 days. The optimal proportion was again 3 %, with 87 and 40 % improvement for 7 and 28 days of curing, respectively. When comparing Al_2O_3 and $CaCO_3$ nanoparticles, the latter yielded better results than Al_2O_3 nanoparticles for both early and later ages. The combined effect of substituting 1 and 3 % of Al_2O_3 and $CaCO_3$ nanoparticles in cement mortar increased compressive strength by 28 and 74 % at 7 days of curing and by 30 and 42 % at 28 days of curing, respectively.

Funding: The research was supported by the Al-Mustaqbal University grant No. MUC-E-0122.

Citation: Al-Mashhadi, S.A., Radhi, M.S., Obead, I.H., Al-Khafaji, Z., Mohammed, Z.A., Jabr, S.F. Improvements of mechanical and physical features of cement mortar by nano Al_2O_3 and $CaCO_3$ as additives. Magazine of Civil Engineering. 2026. 19(1). Article no. 14103. DOI: 10.34910/MCE.141.3

1. Introduction

Ordinary Portland cement (OPC) is a type of cement that is commonly used in concrete and mortar. It is produced by heating limestone and clay at high temperatures and grinding the resulting material into a fine powder [1–3]. OPC is the most common type of cement utilized in various applications, including foundations, driveways, sidewalks, and walls. It is also used in the construction of structures, including bridges and dams. OPC is highly durable and has a long lifespan. It is also inexpensive and has high compressive strength (CS), meaning it can withstand substantial pressure. OPC concrete is made by mixing OPC with water and aggregate (sand, gravel, or crushed stone). This mixture is then poured into forms and

allowed to harden. OPC concrete is strong, durable, and has a long lifespan, making it a popular choice for construction projects [4].

OPC is an essential component of concrete, but its manufacturing process produces significant amounts of CO_2. The primary sources of CO_2 emissions are the burning of fossil fuels (coal and natural gas) used to heat the rotary kiln and the calcination process itself [5–7]. Other sources of emissions include the combustion of fuels to operate grinding, as well as the transportation of materials throughout the cement manufacturing process [8–12]. However, there are several alternatives to OPC such as fly ash, slag cement, silica fume, and nanomaterials that have recently been incorporated into the cement matrix, which involved various types such as SiO_2, TiO_2, Al_2O_3, carbon nanofibers, Fe_2O_3, and $CaCO_3$ nanoparticles. It has been found that the nanomaterials utilized in cement and concrete improve their mechanical, physical, and other properties [13].

The addition of nanoparticles such as Al_2O_3 and $CaCO_3$ to cement mortar has been studied to understand their effects on mechanical and physical features. Research has shown that including 1 and 3 % Al_2O_3 nanoparticles in cement mortar improves its mechanical properties, including compressive, tensile, and flexural strength [17]. Similarly, adding SiO_2 and $CaCO_3$ nanoparticles to cement mortars increases their flexural and CS, with optimal replacement levels of 2 and 4 %, respectively [18].

Several researchers investigated the influence of adding Al_2O_3 to concrete to improve workability and CS. In [14, 15], the influence of Al_2O_3 nanoparticles with an average diameter of 15 nm on the CS and workability of blended concrete was investigated. The nanoparticles were incorporated into the system at four distinct weight percentages: 0.5, 0.1, 1.5, and 2.0 %. The findings indicate that incorporating Al_2O_3 nanoparticles at an optimal substitution level of 2 % yields concrete with enhanced strength features. Nevertheless, the optimal structural integrity of the concrete was achieved when a cement replacement of 1.0 wt% was employed. The increase in Al_2O_3 nanoparticle amount resulted in a reduction in the workability of fresh concrete. Based on the findings, it can be inferred that incorporating Al_2O_3 nanoparticles as a partial substitute for cement enhances CS of concrete, albeit at the expense of reduced workability.

On the other hand, the use of $CaCO_3$ nanoparticles as an additive material to improve concrete properties has become widespread in recent times. In [16], the impact of $CaCO_3$ nanoparticles on cement paste was investigated. Nanoparticles were added at three various substitution levels (1, 2, and 3 %) of cement weight, with a mean particle size of 15–50 nm. The water-to-cement ratio was 0.45. CS testing was conducted at 7 and 28 curing days. Samples were cubic bars with dimensions of 20×20×80 mm. The result illustrated that CS at both ages increased with the content of $CaCO_3$ until it reached an optimal content of 2 % and then it decreased. When the content of $CaCO_3$ was 2 %, the CS was 111.2 and 108.6 % of blank sample at the age of 7 and 28 days, respectively. The enhancement of flexural and CS of hardened cement paste was due to the consuming and refinement of $Ca(OH)_2$ grain, which occurred during the hydration of cement especially at early ages.

Numerous studies have focused on improving the mechanical properties of cement mortar by utilizing nanoparticles, including Al_2O_3 and $CaCO_3$ nanoparticles. Most researchers have observed that substituting cement with Al_2O_3 nanoparticles at levels of 4–5 % by cement weight reduces the CS of cement mortar. At the same time, some authors observed that a 5 % substitution of Al_2O_3 nanoparticles increases CS, while others have reported no significant effect. Regarding $CaCO_3$ nanoparticles, most researchers have noted that substitution levels of 3, 4, and 7 % by cement weight increase CS at 7 and 28 curing days, whereas some have observed a decrease in CS at both ages. Based on previous research, inconsistent findings have been reported when using different proportions of Al_2O_3 and $CaCO_3$ nanoparticles. Therefore, this research aims to study the impact of adding nanomaterials, including Al_2O_3 and $CaCO_3$ nanoparticles, to cement mortar and to determine the optimal percentage of nanoparticle addition to improve the physical and mechanical properties of cement mortar.

2. Material and Methods

2.1. Materials

OPC was used; the physical and chemical properties are illustrated in Table 1. This work used locally available natural sand as fine aggregate with a fineness modulus of 2.17. The grading of this aggregate was zone 3 as limits of Iraqi specification, No. 45/1984.

Table 1. The physical and chemical properties of cement.

Chemical composition	Amounts (by weight), %	Limits of Iraqi Requirement No. 5/2019 (42.5 R)
Cao	60.60	–
SiO_2	19.80	–
Al_2O_3	4.80	–
Fe_2O_3	3.00	–
MgO	3.50	≤ 5.0 %
SO_3	2.22	≤ 2.8 % if C3A > 3.5 %
Loss on Ignition	3.10	≤ 4.0 %
Insoluble residue	0.70	≤ 1.5 %
OPC main compounds (Bogue's Eq.)		
C_3S		59.63
C_2S		11.78
C_3A		7.64
C_4AF		9.12
Test name	Findings	Limits of Iraqi Requirement No. 5/2019 (42.5 R)
Fineness (Blaine method), m^2/kg	320	≥ 280
Setting time (Vicat's method),		
Initial setting time (min)	90	≥ 45
Final setting time (h)	5	≤ 10
CS (MPa),		
Early strength (2 days)	24	≥ 20
Standard strength (28 curing days)	43	≥ 42.5

Al_2O_3 nanoparticles with a mean particle size of ~50 nm were used. The physical and chemical properties of Al_2O_3 nanoparticles are given in Table 2.

Table 2. Physical and chemical properties of Al_2O_3 nanoparticles.

Purity, %	Mean particle size, nm	Typical impurities	Ca	K	Cu	Mg	Fe	Mn	Zn	Si
99.9+ (trace metal basis)	50	–	< 100	< 100	< 10	< 50	< 100	< 50	< 50	< 100

$CaCO_3$ nanoparticles with a mean particle size of less than 100 nm were used. The properties of $CaCO_3$ nanoparticles are illustrated in Table 3.

Table 3. The physical and chemical properties of $CaCO_3$ nanoparticles.

Appearance	Density	Size	Specific area	MgO	Moisture amount	Loss on ignition	Residue on Sieve	$CaCO_3$ amount
White powder	2.5	> 100	≥ 20	≤ 0.8	≤ 0.9	44 ± 1	≤ 0.02	≥ 96
Alumina + Iron oxide		**PH**	**Insoluble matter with acid**		**Activation rate**		**DOP absorbed does**	
≤ 0.3		8.5–9.7	≤ 0.3		≥ 95		35–55	

Finally, tap water was used throughout this work for mixing and curing.

2.2. Mixing Procedure and Samples Preparing

In this study, nine types of mixes were produced to investigate the impact of Al_2O_3 and $CaCO_3$ nanoparticles on the CS of cement mortar. These mixes were designated as A, B_1, B_2, B_3, C_1, C_2, C_3, B_1+C_1, and B_2+C_2. Type A mixture was produced of fine natural aggregate, cement, and water. Types B_1, B_2, B_3, C_1, C_2, and C_3 were produced with various content of Al_2O_3 and $CaCO_3$ nanoparticles. These mixes were prepared with cement substitution levels of 1, 3, and 5 % by weight. The B_1+C_1 and B_2+C_2 mixtures were produced with Al_2O_3 and $CaCO_3$ nanoparticles at cement substitution levels of 1 and 3 % by weight.

In the initial step of mixing the nanomaterials, the binder-to-sand ratio was 1:2 and the water-to-cement ratio was 0.46. The materials were mixed in a dry condition for 1 min and another 2 min after adding the water. Cubes with dimensions of 50×50×50 mm were cast for CS testing and compacted in two layers on a vibrating table, with each layer vibrated for 15 sec. The mold was covered for 24 hours. Then, the samples were demolded and cured in water for the 24 hours. The CS tests were conducted at 7 and 28 curing days. The mixtures with Al_2O_3 and $CaCO_3$ nanoparticles are presented in Fig. 1 and Table 4.

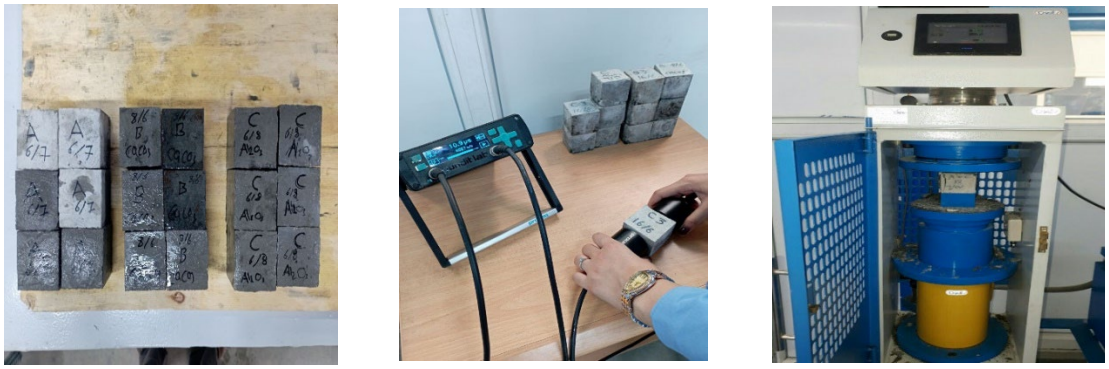

a) **b)** **c)**

Figure 1. a) various mortar cubes, b) test of ultrasonic pulse velocity (UPV), c) CS test machine.

Table 4. Mixtures of Al_2O_3 and $CaCO_3$ nanoparticles.

Sample	Cement, gm	Sand, g	Water, g	Nano-Al_2O_3, g, %	Nano-$CaCO_3$, g, %	W/C
A (control)	650	1300	300	–	–	0.46
B_1	643	1300	300	7, 1 %		0.46
B_2	630	1300	300	20, 3 %		0.46
B_3	620	1300	300	30, 5 %		0.46
C_1	643	1300	300		7, 1 %	0.46
C_2	630	1300	300		20, 3 %	0.46
C_3	620	1300	300		30, 5 %	0.46
B_1+C_1	643	1300	300	3.5, 1 %	3.5, 1 %	0.46
B_2+C_2	630	1300	300	10, 3 %	10, 3 %	0.46

3. Result and Discussion

3.1. Mechanical and Physical Properties

Fig. 2 demonstrates the CS findings of the selected mixtures before and after replacing OPC with different proportions of Al_2O_3 and $CaCO_3$ nanoparticles. The use of nanomaterials (Al_2O_3, $CaCO_3$, and Al_2O_3+$CaCO_3$) at substitution levels of 1 and 3 % increases the CS at early ages, whereas the substitution level of 5 % leads to significant decrease in CS due to the formation of ettringite [23]. The 3 % substitution level is considered the optimal replacement ratio at early ages.

The use of nanomaterials (Al_2O_3, $CaCO_3$, and Al_2O_3+$CaCO_3$) at substitution levels of 1 and 3 % increases the CS at later ages, whereas the substitution level of 5 % leads to significant decrease in CS due to the conversion of ettringite to cement gel (C–H, C–S–H). The 3 % substitution level is considered the optimal replacement ratio at later ages.

When the content of Al_2O_3 nanoparticles is increased to 3 %, the mechanical properties are severely reduced. The researchers attribute this to a reduction in the distance between nanoparticles and the limited space for $Ca(OH)_2$ crystals to grow to an appropriate size, along with nanoparticle agglomeration, which together cause a reduction in CS. The results demonstrate that 1 % of $CaCO_3$ nanoparticles yields the highest CS at all ages. Due to their high surface energy during the hydration process, these nanoparticles grow and clusters, acting as nuclei that accelerate and enhance the hydration process.

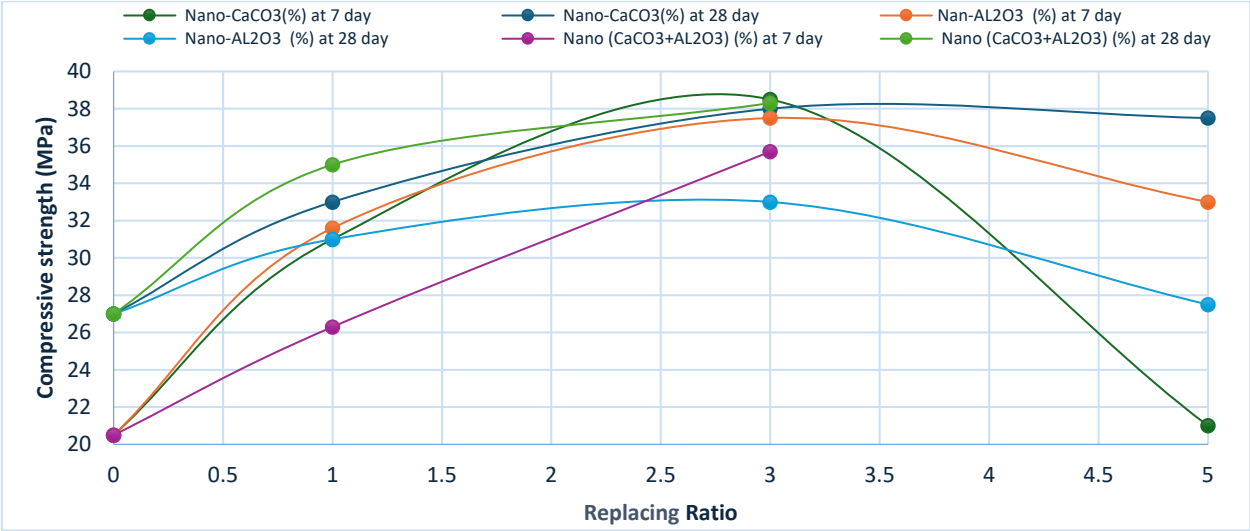

Figure 2. Impact of adding $CaCO_3$, Al_2O_3, and $CaCO_3$+Al_2O_3 nanoparticles to OPC on CS at 7 and 28 curing days.

Fig. 3 demonstrates the density findings of the selected mixtures before and after replacing OPC with different proportions of Al_2O_3 and $CaCO_3$ nanoparticles. The use of 1 % of Al_2O_3 nanoparticles increases the density at 7 and 28 days, whereas the use of 3 % of Al_2O_3 nanoparticles significantly decreases the density at early ages. The use of 1 % of $CaCO_3$ nanoparticles decreases the density at 7 and 28 days, whereas the use of 3 % of $CaCO_3$ nanoparticles slightly increases the density at the early ages and significantly increases it at later ages. The combination of 1 and 3 % of Al_2O_3+$CaCO_3$ nanoparticles reduces density at both 7 and 28 curing days, with better results observed at later ages compared to earlier ones.

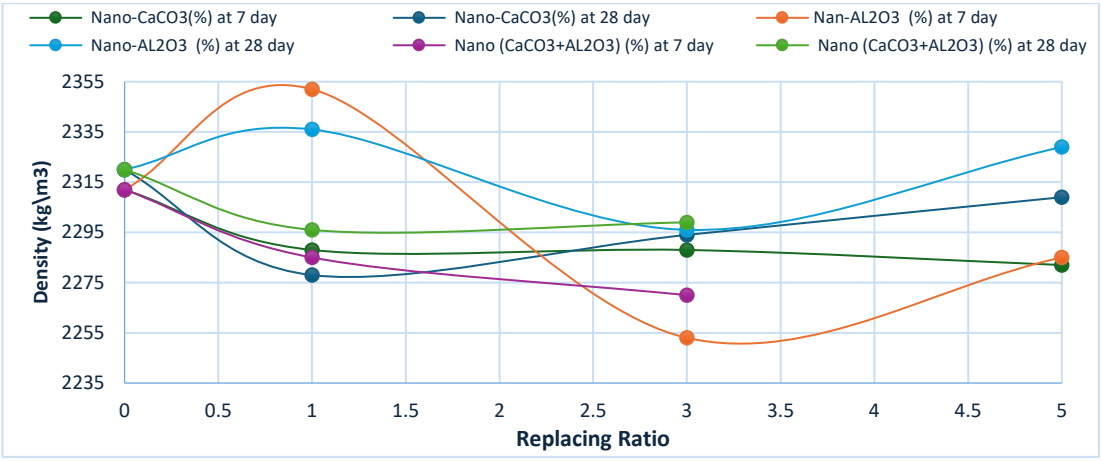

Figure 3. Impact of adding $CaCO_3$, Al_2O_3, and $CaCO_3$+Al_2O_3 nanoparticles to OPC on density at 7 and 28 curing days.

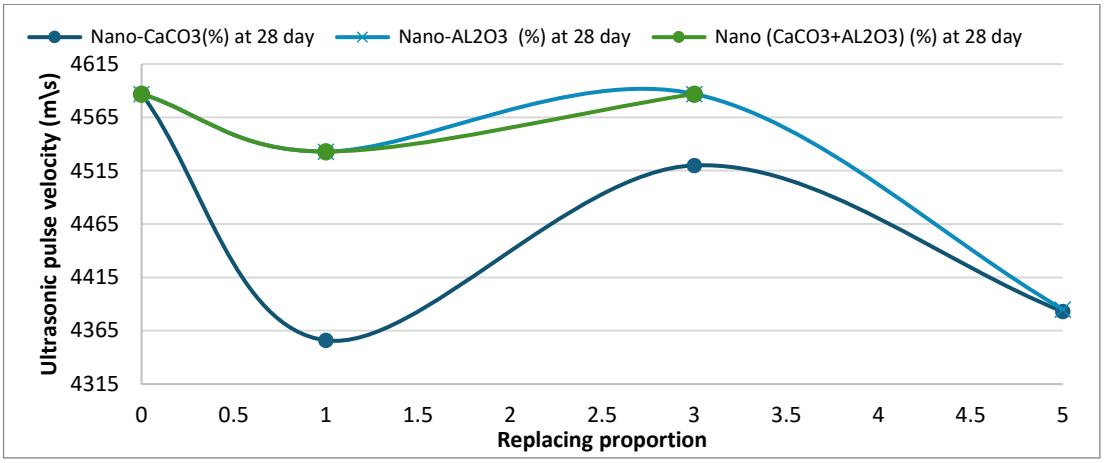

Figure 4. Impact of adding $CaCO_3$, Al_2O_3, and $CaCO_3$+Al_2O_3 nanoparticles to OPC on UPV at 7 and 28 curing days.

It was found that the CS of cement mortar with Al_2O_3 nanoparticles (1, 3, and 5 %) increased by 54, 82, and 61 % at 7 curing days and 14, 22, and 1 % at 28 curing days, respectively. It was observed that the use of 5 % of Al_2O_3 nanoparticles reduced the CS to a level close to that of the control sample A. It might be due to an excess of Al_2O_3 nanoparticles beyond what is necessary to react with the free lime during the hydration process, resulting in excess silica leaching out and weakening the concrete, as it only replaces a portion of the cementitious material. Additionally, weak areas might result from defects created during nanoparticle dispersion. The best CS among all cement mortar mixtures was observed with substitution levels of 1 and 3 % of Al_2O_3 nanoparticles, attributed to the high activity of Al_2O_3. The presence of nanoparticles in the cementitious system leads to the consumption of portlandite $Ca(OH)_2$ through a pozzolanic reaction, filling capillaries, reducing porosity, and increasing strength.

Furthermore, no clear effects were observed when replacing with 1, 3, and 5 % of Al_2O_3 and $CaCO_3$ nanoparticles on the density and UPV of cement mortar at 7 and 28 curing days, respectively. This is probably attributed to the small size of cubes with dimensions of 50×50×50 mm.

For $CaCO_3$ nanoparticles replacing cement at 1, 3, and 5 % by weight, the findings illustrated that the CS increased by 51, 87, and 2.4 % at 7 curing days and by 22, 40, and 38 % at 28 curing days, respectively. It was noted that the increase in CS was observed at 1 and 3 % substitution levels, because the $CaCO_3$ nanoparticles are chemically stable, fill the pores, and increase surface activity.

The substitution of 1 and 3 % of combined nanoparticles in cement mortar increased CS by 28 and 74 % at 7 curing days and by 30 and 42 % at 28 curing days, respectively. This is due to the high activity of the Al_2O_3 nanoparticles, whose presence in the cementitious system leads to the consumption of portlandite $Ca(OH)_2$ through a pozzolanic reaction that fills capillaries, reduces porosity, and increases strength, while the $CaCO_3$ nanoparticles fill the pores and increase surface activity.

4. Conclusion

The mechanical properties of cement mortar affected by the substitution of Al_2O_3 and $CaCO_3$ nanoparticles were investigated in the current research. Based on the replacement of Al_2O_3 and $CaCO_3$ nanoparticles in cement mortar, the following was observed:

1. The CS of cement mortar with 1 and 3 % Al_2O_3 nanoparticles substitution by cement weight increased by 54 and 82 % at 7 curing days, and by 14 and 22 % at 28 curing days, respectively.
2. The use of 5 % Al_2O_3 nanoparticles reduced the CS at 28 curing days to a value close to that of the control sample A. The best CS among all cement mortar mixtures was observed with 1 and 3 % substitution of Al_2O_3 nanoparticles.
3. The substitution of 1 and 3 % of combined nanoparticles in cement mortar increased the CS by 28 and 74 % at 7 curing days, and by 30 and 42 % at 28 curing days, respectively.
4. Al_2O_3 nanoparticles increased CS at 7 days but reduced it at 28 curing days. With 3 % substitution of $CaCO_3$ nanoparticles, the CS at 7 and 28 curing days was higher than that of the control sample A, whereas with 5 % substitution of $CaCO_3$ nanoparticles, the CS decreased at 7 curing days and increased at 28 curing days.
5. No significant influence was observed when Al_2O_3 and $CaCO_3$ nanoparticles were substituted at 1, 3, and 5 % by cement weight on the density and UPV of cement mortar at 7 and 28 curing days.

Reference

1. Ali, Y.A., Falah, M.W., Ali, A.H., Al-Mulali, M.Z., AL-Khafaji, Z.S., Hashim, T.M., Al Sa'adi, A.H.M., Al-Hashimi, O. Studying the effect of shear stud distribution on the behavior of steel–reactive powder concrete composite beams using ABAQUS software. *Journal of the Mechanical Behavior of Materials*. 2022. 31(1). Pp. 416–425. DOI: 10.1515/jmbm-2022-0046
2. Hamad, M.A., Nasr, M., Shubbar, A., Al-Khafaji, Z., Al Masoodi, Z., Al-Hashimi, O., Kot, P., Alkhaddar, R., Hashim, K. Production of Ultra-High-Performance Concrete with Low Energy Consumption and Carbon Footprint Using Supplementary Cementitious Materials Instead of Silica Fume: A review. *Energies*. 2021. 14(24). Article no. 8291. DOI: 10.3390/en14248291
3. Ali, A.M., Falah, M.W., Hafedh, A.A., Al-Khafaji, Z.S., Radhi, S. Evaluation the influence of steel-fiber on the concrete characteristics. *Periodicals of Engineering and Natural Sciences*. 2022. 10(5). Pp. 368–379. DOI: 10.21533/pen.v10i3.3111
4. Zhang, G., Ali, Z.H., Aldlemy, M.S., Mussa, M.H., Salih, S.Q., Hameed, M.M., Al-Khafaji, Z.S., Yaseen, Z.M. Reinforced concrete deep beam shear strength capacity modelling using an integrative bio-inspired algorithm with an artificial intelligence model. *Engineering with Computers*. 2022. 38. Pp. 15–28. DOI: 10.1007/s00366-020-01137-1
5. Hussain, A.J., Al-Khafaji, Z.S. Reduction of Environmental Pollution and Improving the (Mechanical, Physical and Chemical Characteristics) of Contaminated Clay Soil by Using of Recycled Oil. *Journal of Advanced Research in Dynamical and Control Systems*. 2020. 12(04). Pp. 1276–1286. DOI: 10.5373/JARDCS/V12SP4/20201604
6. Al-Khafaji, Z.S., Al-Naely, H.K., Al-Najar, A.E. A Review Applying Industrial Waste Materials in Stabilisation of Soft Soil. *Electronic Journal of Structural Engineering*. 2018. 18(2). Pp. 16–23. DOI: 10.56748/ejse.182602
7. Al-Masoodi, Z., Dulaimi, A., Jafer, H., Al-Khafaji, Z., Atherton, W., Hussien, S.A. Soft Soil Treated with Waste Fluid Catalytic Cracking as a Sustainable Stabilizer Material. *Iraqi Geological Journal*. 2022. 55(1C). Pp. 39–50. DOI: 10.46717/igj.55.1C.4Ms-2022-03-23
8. Al-Khafaji, Z.S., Majdi, A., Shubbar, A.A., Nasr, M.S., Al-Mamoori, S.F., Alkhulaifi, A., Al-Mufti, R.L., Al-Rifaie, A., Alkhayyat, A., Hashim, K. Impact of high volume GGBS replacement and steel bar length on flexural behaviour of reinforced concrete beams. *IOP Conference Series: Materials Science and Engineering*. 2021. 1090. Article no. 12015. DOI: 10.1088/1757-899X/1090/1/012015
9. Hussain, A.J., Al-Khafaji, Z.S. The Fields of Applying the Recycled and Used Oils by the Internal Combustion Engines for Purposes of Protecting the Environment against Pollutions. *Journal of Advanced Research in Dynamical and Control Systems*. 2020. 12(01). Pp. 698–706. DOI: 10.5373/JARDCS/V12SP1/20201119
10. Shubbar, A.A., Jafer, H., Abdulredha, M., Al-Khafaji, Z.S., Nasr, M.S., Al Masoodi, Z., Sadique, M. Properties of cement mortar incorporated high volume fraction of GGBFS and CKD from 1 day to 550 days. *Journal of Building Engineering*. 2020. 30. Article no. 101327. DOI: 10.1016/j.jobe.2020.101327
11. Falah, M.W., Hafedh, A.A., Hussein, S.A., Al-Khafaji, Z.S., Shubbar, A.A., Nasr, M.S. The Combined Effect of CKD and Silica Fume on the Mechanical and Durability Performance of Cement Mortar. *Key Engineering Materials*. 2021. 895. Pp. 59–67. DOI: 10.4028/www.scientific.net/KEM.895.59
12. Majdi, H.S., Shubbar, A.A., Nasr, M.S., Al-Khafaji, Z.S., Jafer, H., Abdulredha, M., Masoodi, Z.A., Sadique, M., Hashim, K. Experimental data on compressive strength and ultrasonic pulse velocity properties of sustainable mortar made with high content of GGBFS and CKD combinations. *Data in Brief*. 2020. 31. Article no. 105961. DOI: 10.1016/j.dib.2020.105961
13. Mukhopadhyay, A.K. Next-Generation Nano-based Concrete Construction Products: A Review. *Nanotechnology in Civil Infrastructure*. Springer. Berlin, Heidelberg. 2011. Pp. 207–223. DOI: 10.1007/978-3-642-16657-0_7
14. Nazari, A., Riahi, S., Riahi, S., Shamekhi, S.F., Khademno, A. Influence of Al_2O_3 nanoparticles on the compressive strength and workability of blended concrete. *Journal of American Science*. 2010. 6(5). Pp. 6–9.
15. Arefi, M.R., Javeri, M., Mollaahmadi, E. To study the effect of adding Al_2O_3 nanoparticles on the mechanical properties and microstructure of cement mortar. *Life Science Journal*. 2011. 8(4). Pp. 613–617.
16. Liu, X., Chen, L., Liu, A., Wang, X. Effect of Nano-$CaCO_3$ on Properties of Cement Paste. *Energy Procedia*. 2012. 16(B). Pp. 991–996. DOI: 10.1016/j.egypro.2012.01.158
17. Barbhuiya, S., Mukherjee, S., Nikraz, H. Effects of nano-Al_2O_3 on early-age microstructural properties of cement paste. *Construction and Building Materials*. 2014. 52. Pp. 189–193. DOI: 10.1016/j.conbuildmat.2013.11.010
18. Al Ghabban, A., Al Zubaidi, A.B., Jafar, M., Fakhri, Z. Effect of Nano SiO_2 and Nano $CaCO_3$ on The Mechanical Properties, Durability and Flowability of Concrete. *IOP Conference Series: Materials Science and Engineering*. 2018. 454. Article no. 012016. DOI: 10.1088/1757-899X/454/1/012016
19. Cosentino, I., Liendo, F., Arduino, M., Restuccia, L., Bensaid, S., Deorsola, F., Ferro, G.A. Nano $CaCO_3$ particles in cement mortars towards developing a circular economy in the cement industry. *Procedia Structural Integrity*. 2020. 26. Pp. 155–165. DOI: 10.1016/j.prostr.2020.06.019
20. Jawad, Z.F., Salman, A.J., Ghayyib, R.J., Hawas, M.N. Investigation the effect of different nano materials on the compressive strength of cement mortar. *AIP Conference Proceedings*. 2020. 2213(1). Article no. 020190. DOI: 10.1063/5.0000164
21. Iskra-Kozak, W., Konkol, J. The Impact of Nano-Al_2O_3 on the Physical and Strength Properties as Well as on the Morphology of Cement Composite Crack Surfaces in the Early and Later Maturation Age. *Materials*. 2021. 14(16). Article no. 4441. DOI: 10.3390/ma14164441
22. Muhsin, Z.F., Fawzi, N.M. Effect of Nano Calcium Carbonate on Some Properties of Reactive Powder Concrete. *IOP Conference Series: Earth and Environmental Science*. 2021. 856. Article no. 012026. DOI: 10.1088/1755-1315/856/1/012026
23. Al-Khafaji, Z.S., Al Masoodi, Z., Jafer, H., Dulaimi, A., Atherton, W. The effect of using fluid catalytic cracking catalyst residue (FC3R) "as a cement replacement in soft soil stabilisation." *International Journal of Civil Engineering and Technology (IJCIET)*. 2018. 9(4). Pp. 522–533.

Information about the authors:

Samir Al-Mashhadi,
ORCID: https://orcid.org/0000-0002-3352-9010
E-mail: eng.samer.abdul@uobabylon.edu.iq

Mohammed Sattar Radhi,
E-mail: mat.mohammed.sattar@uobabylon.edu.iq

Imad Habeeb Obead,
E-mail: eng.imad.habeeb@uobabylon.edu.iq

Zainab Al-Khafaji, *PhD*
ORCID: https://orcid.org/0000-0002-5450-7312
E-mail: p123005@siswa.ukm.edu.my

Zainab Adel Mohammed,
E-mail: Zoozadil97@gmail.com

Sarah Fadel Jabr,
E-mail: sara.fadeljaber97@gmail.com

Received: 21.01.2023. Approved: 22.09.2023. Accepted: 18.11.2023.

Magazine of Civil Engineering

ISSN 2712-8172

journal homepage: http://engstroy.spbstu.ru/

Research article

UDC 691.535

DOI: 10.34910/MCE.141.4

Cement paste stratification at critical cementing point

V.S. Kovalchuk[1] ✉ , ***E.Y. Tsigelnyuk***[2], ***E.V. Korolev***[1]

[1] *St. Petersburg State University of Architecture and Civil Engineering, St. Petersburg, Russian Federation*
[2] *LLC "GEOKEM", St. Petersburg, Russian Federation*
✉ *kovalchuk.vsk@gmail.com*

Keywords: casing cementing, structure formation, sedimentation, cement density, cement bleeding, cement segregation, solids settling, fluid loss

Abstract. The relevance of this research is driven by the necessity to investigate and predict the technological parameters of grouting mixtures in conditions that closely resemble real-world scenarios. The subject of this study is a grouting compound used in well construction, which serves to ensure the adhesion between the casing and the formation, strengthen the borehole walls, and prevent the leakage of underground fluids. The objective is to develop a methodology for investigating the cement mixture formation based on both theoretical and empirical data, with the aim of most accurately representing the actual behavior of the grouting solution within the annulus of a wellbore. The authors have proposed a model for two types of cement mortar structures. A method for examining the sedimentation stability of cement mortars using a specially designed experimental setup and monitoring protocol is presented. The analysis of samples collected at the proposed site allows us to study changes in the density of cement slurry over time, while simulating the behavior of cement in the annulus during the first hour of pumping. The findings indicate a tendency towards thickening and hardening of the cement mixture, as well as highlight potential issues that may arise when the cement composition does not meet the requirements set by downhole conditions. The statistical analysis of measured data demonstrates good reproducibility with low error, allowing us to simulate deposition of cement under various conditions. The results and the proposed recommendations for improving cement stability will be of value to technical experts and researchers, enabling them to achieve the objectives of environmentally friendly, time-efficient, and economically viable well construction.

Citation: Kovalchuk, V.S., Tsigelnyuk, E.Y., Korolev, E.V. Cement paste stratification at critical cementing point. Magazine of Civil Engineering. 2026. 19(1). Article no. 14104. DOI: 10.34910/MCE.141.4

1. Introduction

During the construction of wells, cement-based formulations are primarily used, which must comply with the requirements outlined in relevant regulatory documents such as Russian State Standards GOST 1581-2019 and GOST 34532-2019, as well as API Specification 10A:2019 and API RP 10B-2-2024. These standards specify the type and range of properties for both cement paste and the resulting artificial stone. The main purpose of grouting mixtures is to fill the annular space between the casing and the borehole.

The problem of the lack of a homogeneous cement stone structure creates the need for a more detailed study of the issue of quality violations during well construction [1, 2]. The active stratification of the grouting composition by the depth of cementation negatively affects the quality of rock insulation and the tightness of the borehole, and also forms a highly porous cement stone, significantly reducing the operational lifespan of the well [3]. The appearance of water in the upper zones of the cementing sites is one of the observed consequences of uneven filling of annular space with cement paste during drilling. The

aim of this study is to develop a technique for determining water separation in cement slurry, free from the shortcomings of the standard method, as well as identifying correlations with key factors influencing water separation in grouting mixtures.

It is known that the denser the packing of Portland cement particles, the higher the ability of cement paste to hold a certain volume of water. The cohesion of the structure is crucial when designing a cement mix with specified rheological properties. If the normal density of the cement paste is significantly exceeded, the particles do not come into direct contact with each other, as they are sufficiently removed and separated by layers of water. This type of system is sedimentationally unstable, leading to water separation. This process can also be described as the stratification of the cement dispersion system. Stratification occurs throughout the entire height, forming a material density gradient. Naturally, the density in the upper layers will be lower than in the deeper layers. This density gradient, after hardening, will naturally lead to differences in porosity and strength in the cement stone.

Water separation is a structural heterogeneity of the cement paste, and, as a result, a negative factor leading to the formation of a cement stone with gradients in its density and properties, particularly during the construction of deep boreholes, where there is a difference in the height of the cementing intervals. To eliminate this inhomogeneity, various methods have been proposed, including the introduction of filler additives such as chalk, quartz, clay, fly ash, asbestos, and others, which reduce water segregation (plasticizing and hydrophilic surfactants), as well as the use of aqueous solutions containing chloride and sodium carbonate [4–6].

The water-cement (W/C) ratio of a cement paste of normal density is dependent not only on the mineral composition of the clinker and the content and properties of mineral additives but also on the conditions, under which the structure forms. For normal Portland cement, this parameter is approximately 0.25 under hardening conditions. It is known that when filling borehole spaces with a grouting mixture, the initial W/C ratio specified may differ significantly from the actual concentration of the cement gel, depending on the depth of the mass distribution. By analogy with Boltzmann's barometric formula [7], we can consider a problem regarding the effect of forces on a cement particle evenly surrounded by water in a state of equilibrium. In this case, the downward gravitational force will be balanced by the resistance forces of the medium and Archimedes. This model accurately describes the issue of uneven filling of the annulus of the well with cement slurry, followed by strata formation and possible absorption or migration of the cement mix into nearby heterogeneous formations. As a consequence, the resulting anisotropic cement rock will not meet the standards for high-quality isolation of the borehole from corrosive subsurface fluids (liquids and gases), which could lead to industrial incidents.

The analysis of standard requirements reveals that to assess the stability of grouting mixes (cement slurry or mortar) against sedimentation, the characteristic "water separation" is used, defined as the volume of water that separates. In this instance, a measuring cylinder with a capacity of 250 cm^3 is employed, which significantly differs from the depth of the well being cemented. This disadvantage could be overcome by simulating the sedimentation process of cement-water systems. Nevertheless, addressing this issue involves overcoming challenges related to the interaction of settling particles and the formation of agglomerates, whose structure and properties vary significantly over time. Consequently, experimental statistical models have gained popularity, the production of which entails conducting experimental studies using equipment that avoids the shortcomings of known methods [8–10].

The rheological properties of cement slurry are influenced by various factors, including the concentration, average size, and volume distribution of cement particles. These factors also include the shape, structure, surface properties, and physical properties of the liquid and solid components [11, 12].

Additionally, water segregation in cement slurries is influenced by physical and chemical processes such as the sedimentation, aggregation, and hydration of cement particles. This process leads to the formation of a dispersed phase, which can be observed in the chemical equation for the hydration of tricalcium silicate C_3S, a major component of cement [13]:

$$2\left(3\mathrm{CaO}\cdot\mathrm{SiO_2}\right)+6\mathrm{H_2O}\rightarrow 3\mathrm{CaO}\cdot\mathrm{SiO_2}\cdot 3\mathrm{H_2O}+3\mathrm{Ca}\left(\mathrm{OH}\right)_2. \quad (1)$$

It follows from this equation that the ratio of the volumes of the solid phases of the hydration products V_g and the starting material V_{ng} is $V_g/V_{ng}=1.65$. Some of these processes are considered in the standards for determining the water separation rate of a cement mix using a measuring cylinder [14]. A cement paste is placed in a cylinder and allowed to set for a specific period of time. After this, the stratification of the mixture is visually examined, and the extent of stratification is calculated based on the volume of water displaced in the upper portion of the cylinder [15–17]. However, this method of water separation measurement does not consider many geological, technical, and other significant factors, including the influence of external environmental conditions (geological characteristics of rocks in contact

with cement), physical and mechanical parameters (pressure, temperature), and technological aspects of well construction (geometrical parameters of the well, construction method, type of flushing fluid, etc.).

The study [18] showed the technological limitations of the current standards for water separation analysis using a measuring glass cylinder in revealing the true picture of cement particle sedimentation in the annulus. The work also identified and described cracks and voids (migration pathways) that may be filled during cement injection.

W/C ratios are among the key cement parameters that affect the mixture characteristics and mechanical properties of grouting materials. Micro-cement compositions with W/C ratios ranging from 0.8:1 to 2:1 were examined in [19]. It was found that density, workability, rate of cement-stone formation, and bending and compressive strengths of cement stones gradually decreased with increasing W/C ratio. Conversely, the spreadability and fluidity of micro-cement mixes gradually increased.

A method for investigating the water separation properties of cement mixtures using low-field nuclear magnetic resonance (NMR) has been proposed in the study [20]. The findings indicate that the NMR technique in a weak magnetic field can be successfully employed not only to measure the extent of water separation, investigate the microstructure of cement materials but also to provide information on the concentrations of substances present in the separated water. Furthermore, it has been determined that the migration of a substantial amount of water from the porous structure of a maturing cement slurry gives rise to significant alterations and deterioration in the microstructure of the resulting cement stone.

To address the issue of static segregation, it is common practice to select formulations with the lowest possible W/C or water-binder ratio, as well as to utilize microsilica to reduce water segregation while maintaining the structural properties of the cement matrix in studies of high-performance mobile concrete mixes [21]. At the same time, it has been established that superplasticizers, which increase the flowability (workability) of the cement paste, adversely affect the mechanical characteristics of mortar mixtures and reduce the durability of molded cement products [22]. In order to explore the correlation between cement properties and the propensity of cement mixtures to water segregation, the authors of [23] discovered that with a lower specific surface area and higher alkali content, there is a greater tendency towards intensive water segregation.

The authors of [24] investigated the deposition of cement mixtures by visual observation, which revealed two stages of delamination: an initial phase of rapid water separation followed by a stage with a decreasing sedimentation rate, where the upper layer gradually became transparent.

In predicting the sedimentation of cement mixtures, the laws of suspension dynamics may be applied. Specifically, article [25] addresses the issue of particle sedimentation in a stationary fluid. The authors conclude that the concentration of solids in the flow and the density increase linearly with depth, while the pressure increase follows a weakly quadratic trend.

One of the most significant criteria for assessing the quality of concrete is the density of the concrete mixture. The researchers in [26] developed a method for determining the density of settling concrete suspensions by sampling from specific heights at different times. This study demonstrated that the characteristics of the concrete mixtures, including their uniformity and flowability, vary significantly depending on the height and time of sampling. Further research into the relationship between concrete mixture properties and their tendency to separate revealed that mixtures with a smaller specific surface area have a higher tendency for water displacement. It has also been shown that due to obvious separation, the water-to-cement ratio and phase content in the settled suspension layer do not match the initial concrete composition parameters.

The main limitation of previous studies is the significant gap between laboratory testing of grouting materials during the initial phase of cement-stone structure formation and the measurement of the state of the cement annulus after hardening in the borehole.

The classical approach to the sedimentation process involves determining the sedimentation rate of a particulate, which is influenced by the forces of Stokes and Archimedes, as well as the gravitational force of the Earth. However, the actual rate of deposition of grouting mixtures may differ from the calculated value, due to both assumptions made in determining the geometric properties of the particles, and the influence of adjacent particles [27]. The Lyashenko method has been used to study the constrained deposition rate of particles with different geometric shapes. However, this method has the disadvantage of relying solely on experimental measurements, which are used as the primary method for determining the properties of sedimentation. As mentioned above, and in other studies [28–30], completely experimental dependencies are used to calculate the parameters of suspended deposition.

The quality of grouting material cannot be determined solely based on average laboratory test results. In practice, there are always variations from the obtained results. Changes in mixing and injecting the mixture, composition of clinker, activity and normal density of cement, dosage of improving additives,

and other technological and geological factors affecting the formation and hardening of the structure have an impact on the quality of well construction. To improve the quality of cementing operations, it is necessary to modernize existing laboratory methods for simulating borehole conditions.

In accordance with the objectives set by the authors, this paper presents the findings of a study on the sedimentation of cement particles and stratification of cement slurry prior to cement setting when it is injected into a borehole. A method has been devised to analyze the heterogeneity of cement matrix formation based on a density analysis of grouting mixture at various depths after a specific period of time. To implement the method for measuring cement slurry density, an experimental setup is proposed, and the process of sample preparation and experimentation is described in detail. The results obtained indicate consistent trends in the behavior of the cement mixture in simulated conditions of cement structure formation in a wellbore.

2. Materials and Methods

For the experiments, casing Portland cement I-50 brand similar to Portland cement I-G-CC-1 brand was used, which meets the requirements of GOST 1581-2019. The properties of the cement mixtures were investigated using methods specified in GOST 33213-2014, GOST 34532-2019, and GOST 30744-2001. Storage, preparation, labelling and sample preparation were conducted in accordance with GOST 30515-2013. The standard specifications and actual characteristics of the cement are presented in Table 1 below.

Table 1. Characteristics of the cement mixture with a W/C ratio of 0.5.

Physical and mechanical characteristics	GOST requirements	Actual performance
Bending strength, MPa at the age of 2 days, not less than MPa	2.7	3.1
Spreading capacity of cement paste, not less than mm	200	220
Bleeding capacity, no more than ml	8.7	2.5
Thickening time to consistency of 30 Bc, not less than min	90	320

To meet the requirements for pumpability and workability of standard grouting cement, it is common to use W/C = 0.44…0.5. However, for lightweight and heavyweight cements, this ratio can vary between 0.3 and 1.3. In this study, we will consider compositions with W/C = 0.5…1.0.

When discussing the structural and rheological properties of cement paste, the concept of water retention capacity is introduced [31–33]. This is the amount of water that is retained within the cement paste after it has been formed. The W/C ratio of a cement paste of normal density indicates at what water content the paste will form, without any separation of its components (phases). As the W/C increases, a more heterogeneous structure begins to form, with increased structural heterogeneity. To assess this heterogeneity, we utilize a modified version of the phase separation coefficient proposed by A.N. Bobryshev et al. [34, 35]. For cement pastes, this coefficient takes the following form:

$$\psi_{f,m} = \frac{2 \cdot v_{w,0} - v_w}{v_{w,0}}, \quad \text{for } v_w \geq v_{w,0}, \tag{2}$$

where $v_{w,0}$ – volume fraction of water for sedimentation-resistant cement paste; v_w – volume fraction of water of the studied composition.

For $v_w < v_{w,0}$, formula (2) must be converted to the form:

$$\psi_{f,m} = \frac{v_w}{v_{w,0}}. \tag{3}$$

It is evident that structural heterogeneity is the origin of water separation (phase segregation), and at $v_w = 2v_{w,0}$ structural heterogeneity reaches its maximum (Fig. 1).

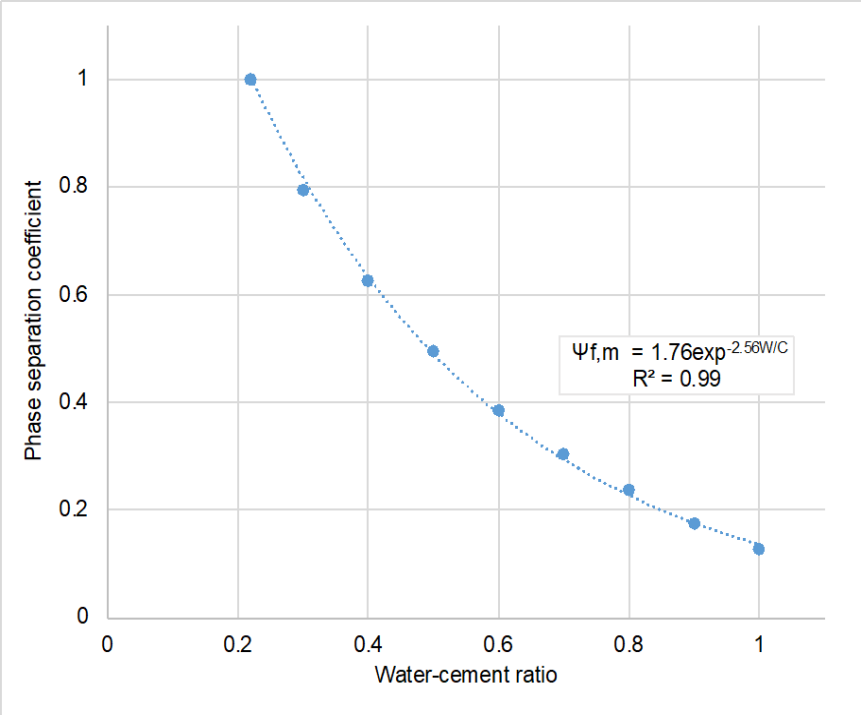

Figure 1. The dependence of the coefficient of uniformity on the W/C ratio.

As the proportion of water in a cement mixture increases, the distance between the cement particles also increases:

$$h_w = \frac{v_w}{(1-v_w)\cdot S_u \cdot \rho_c}, \tag{4}$$

where S_u and ρ_c – unit surface and cement density.

Furthermore, the rate of increase in the thickness of the water layer increases proportionately $1/(1-v_w)^2$. Obviously, the natural process aims to minimize the potential energy of all particles in a dispersed system affected by the Earth's gravitational field. The model, which allows assessing the influence of the main factors at the initial stage, is based on the classical effect of forces on a particle as well as the limitations of: 1) the absence of the influence of other particles, and 2) the absence of compaction of the particle sediment. A particle with a diameter d_f in the initial state is surrounded by a layer of water of thickness $h_{w,0}$, and after sedimentation (steady state) – by a layer with thickness h_w. Let the height of the column where the suspension is located be H_0, and the area of the base S_0. In its initial state, this column will be divided into thin layers $d_f + 2h_{w,0}$. To reach a stable state for the particle in the first layer, that is the layer located immediately adjacent to the lower boundary, or bottom, requires that an equal distance $\Delta l = 2(h_{w,0} - h_w)$ be traversed. The particle in the second layer must traverse the distance to the interface with the first layer Δl, as well as the distance the first particle has already traversed – Δl. Thus, the total distance that particles in the second layer need to travel before reaching a stable position is equal to $2\Delta l$. Similar reasoning applies to particles in any other layer, and their distance will be equal to $i \cdot \Delta l$ (where i is the layer index). These distances are related to sedimentation rates [36–38]:

$$\frac{i\cdot\Delta l}{t_i} = \frac{1}{18}\cdot\frac{g\cdot d_f^2(\rho_f - \rho_m)}{\mu}, \tag{5}$$

where μ and ρ_m – viscosity and density of the medium, in which occurs the sedimentation of particles with density ρ_f; g – gravitational acceleration.

In this scenario, all particles, regardless of their position, will move an equal distance over time t_i. The motion of particles in the upper regions under the influence of gravity corresponds to the creation of a layer of liquid on the surface of the system. When determining the requirements for the thickness of the liquid layer, it is feasible to assess the geometric properties of the container used in a study on the distribution of fractions of the material in various states (Fig. 2).

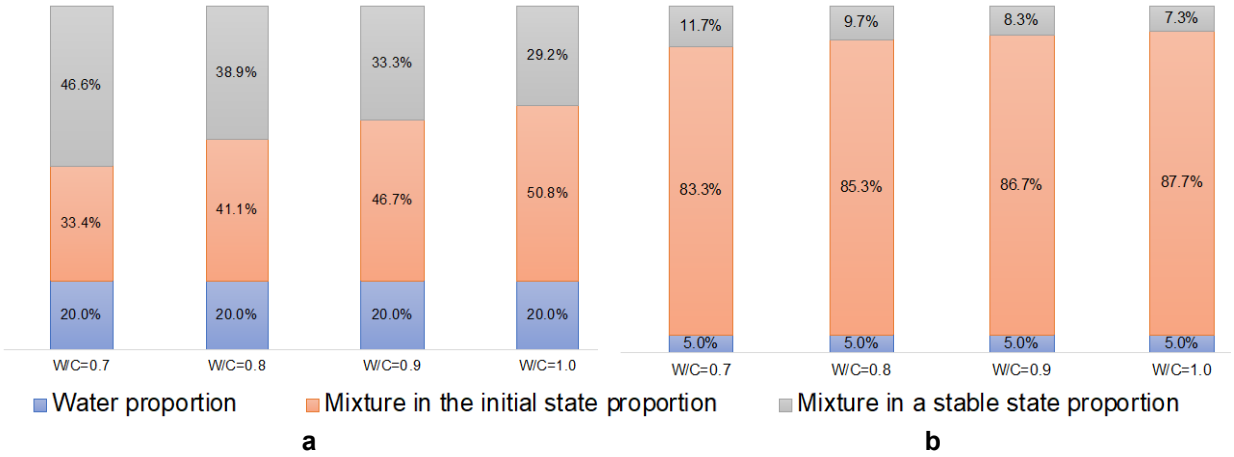

Figure 2. The effect of column height on the distribution of types of mixture states at the relative height: a) H_0:S_0 = 1:1; b) H_0:S_0 = 4:1.

The data presented in Fig. 2 illustrate that at low column heights, stratification of the mixture occurs more rapidly, specifically the formation of a stable layer of particle mixture and a layer of liquid. The time required to reach stratification is found to be proportional to the height ratio between the two containers under comparison (at $S_0 = \text{const}$). Another implication of the model is the possibility of describing the structure of the mixture as a system composed of different compositional types. Based on the presented model, it is sufficient for there to be two such structural types.

Obviously, the model under consideration is a rather crude approximation. In actual mixtures, there would not be distinct boundaries between structures. Nevertheless, it allows us to fully assess both the origin of structural heterogeneity and the impact of various factors, including the depth of well cementing.

Using the presented model, we will determine mixture density as a feature characterizing cement paste's structural characteristic at various depths. Let us imagine that the cement mixture consists of a three-phase system "cement – water – air":

$$\varphi_c + \varphi_w + \varphi_{air} = 1, \tag{6}$$

where φ_c – cement volume fraction; φ_w – water volume fraction; φ_{air} – air volume fraction.

Considering a hypothetical scenario where a cement particle is spherical in shape. At the initial point in time, the contribution from its hydration process can be disregarded, and the physical and chemical interaction results in the formation of a water adsorption layer on the surface of the cement particles. This adsorption layer differs significantly from the properties of freely flowing water (Fig. 3a). Regarding the model discussed previously, as well as the various phases that constitute the cement slurry, we can identify two main types of structures: 1. "cement – adsorbed water – free water;" 2. "cement – adsorbed water – free water – air" (Fig. 3b).

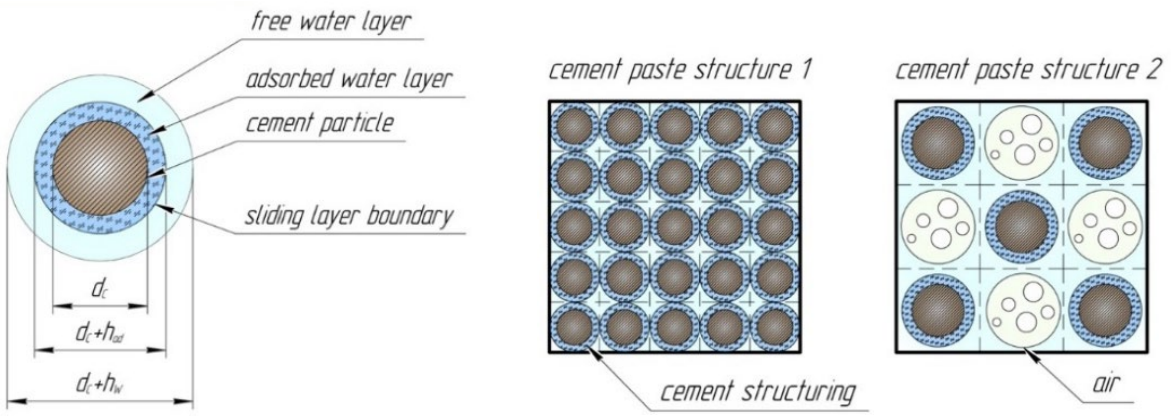

a **b**

Figure 3. Cement structuring by two types of particle arrangement: a) model of a cement particle surrounded by water; b) types of cement paste structures, where d_c – diameter of the cement particle; h_{ad} – thickness of the adsorbed water layer; h_w – thickness of the free water layer.

The geometric characteristics of each structural type are determined by a set of parameters, which are shown in Table 2.

Table 2. Parameters for the types of structures.

Type	Number of phases	Phases	Phase Parameters			
			Cement	$Water_{ad}$	$Water_w$	Air
I	3	Cement, adsorbed water, free water	φ_c	φ_{ad}	φ_w	φ_{air}
II	4	Cement, adsorbed water, free water, air	d_c	h_{ad}	h_w	d_{air}
			ρ_c	ρ_{ad}	ρ_w	ρ_{air}
			S_u			

The values of the parameters presented are derived from literature sources [39–41]. Under the given conditions $h_w >> h_{ad}$ and $\rho_{ad} > \rho_w$, we derive the following system of equations to calculate density according to type 1:

$$\begin{cases} \rho_1 = \varphi_c\rho_c + \varphi_{ad}\rho_{ad} + \varphi_w\rho_w \\ \varphi_c + \varphi_{ad} + \varphi_w = 1 \end{cases}. \quad (7)$$

For type II is valid $\varphi_c = \varphi_c - \varphi_{air}$, therefore, we obtain a system of equations:

$$\begin{cases} \rho_{II} = \varphi_c\rho_c + \varphi_{ad}\rho_{ad} + \varphi_w\rho_w \\ \varphi_c + \varphi_{ad} + \varphi_w + \varphi_{air} = 1 \end{cases}. \quad (8)$$

The density of the cement paste, taking into account ρ_1 and ρ_{II} will be equal to:

$$\rho_{cp} = \omega_1\rho_1 + \omega_{II}\rho_{II}, \quad (9)$$

where ω_1 and ω_{II} – volume fractions of the corresponding types of structures: $\omega_1 + \omega_{II} = 1$.

The determination of ω_1 and ω_{II} is only possible through solving the inverse problem. This involves using calculated ρ_1, ρ_{II} and experimentally determined values ρ_{cp}. Furthermore, the cement slurry for determination can be chosen at any depth within the pipe column.

In order to experimentally determine the variation in the density of the cement paste, a specialized experimental setup has been designed. The schematic diagram of this setup is shown in Fig. 4.

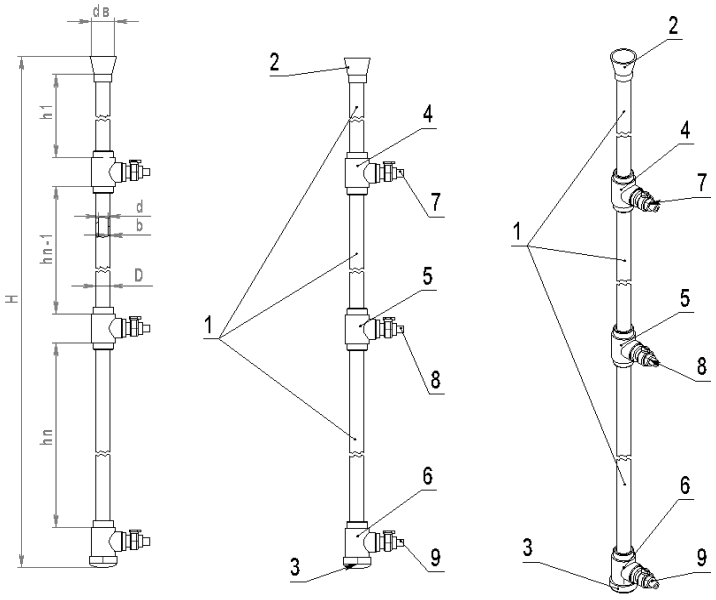

Figure 4. General view of the experimental installation for measuring the density of the cement mixture: a – side view; b – spatial view, where 1 – pipeline; 2 – funnel; 3 – removable plug; 4, 5 and 6 – tees; 7, 8 and 9 – taps.

The device is a vertically positioned housing consisting of a pipeline (1) with a diameter of d and a length of l, having a circular cross-section with a diameter that does not change in the axial direction of the pipeline. The body can be a metal or plastic pipe, industrial ceramics, plexiglass, or other material that simulates downhole conditions. A funnel (2) is fixed in the upper part of the housing for feeding the analyzed grouting mixture, and a removable plug (3) closes the bottom of the pipeline. At distances H_1, H_{n-1} and H_n from the pipe mouth, there are tees A_1 (4), A_{n-1} (5), and A_n (6), with taps X_1 (7), X_{n-1} (8), and X_n (9) connected to them. Depending on the simulated conditions, it is recommended to use at least three measuring taps. In addition, the height of the pipe column depends on the specific set conditions.

The proposed method for measuring the density of a grouting mixture is as follows. The upper edge of the stand is taken as the zero reference point, and subsequent measurements are counted down along the depth of filling the pipe column with cement paste. Cement mixture is prepared according to GOST 34532-2019. The prepared mixture is poured into a funnel to enter the pipeline, until it is completely filled with the test cement paste to the plug, after which it is tightly closed for sealing. The cement paste settles in the installation during the studied measurement time T_1, T_2 … T_n – from 15 to 60 minutes. By alternately opening the ball valves connected through tees to the pipeline, samples are taken for further measurement of the density of the cement mixture by the weighing method. Using mathematical methods of experiment planning, two variable independent factors were selected: W/C ratio and sampling depth, on the basis of which a series of experiments were conducted. The experimental density is taken to be the arithmetic mean of the results of three measurements, the discrepancy between which should not exceed 200 kg/m^3. Proper filling and opening of taps in a certain sequence helps to avoid the occurrence of air bags and water in the laboratory installation in order to obtain correct data. After the measurements, the pipe space is cleaned of the remaining cement paste by rinsing with water.

3. Results

After preparing cement slurry with various water-to-cement ratios, the initial specific gravity was measured under standard conditions. The results of the measurements of the specific gravities of grout mixtures at W/C = 0.5…1.0, and their associated errors, are presented in Table 3.

Table 3. Initial density of cement mixtures.

W/C ratio	0.5	0.6	0.7	0.8	0.9	1.0
Average initial density, kg/m^3	1790	1710	1610	1550	1500	1420
Measurement error, %	8	8	7	6	6	5

After preparing the cement slurry and filling the mold, samples were collected in a volume of 100 mL from each height level, and their density was measured using an electronic balance and the weighting method. Based on the results from three measurements, an average value for density at each height and time point (from the start of setting) was calculated. The findings of the study are presented in Table 4.

If the setting time is less than 15 minutes, the cement paste with a high water-to-cement ratio does not form a densified structure, which can lead to inaccurate density readings. Therefore, any measurements taken with a hydration time of less than 15 minutes have been excluded from the table.

When conducting laboratory tests on the cement mixture with W/C = 0.5, measurements were taken at the installation 15 and 20 minutes after the beginning of the active growth of the setting and the lack of laminar leakage from the tap. With an increase in the W/C to 0.6, the mobility of the cement system increased, allowing for sampling after 30 and 40 minutes from the start of mixing.

Table 4. Experimental density of cement slurries, kg/m^3.

W/C	Thickening time, min	Sampling depth, m		
		H_1 = 0.5	H_2 = 1.5	H_3 = 2.5
0.5	T_1 = 15	1730	1820	1900
	T_2 = 20	1700	1800	1870
0.6	T_1 = 15	1610	1750	1800
	T_2 = 20	1600	1740	1780
	T_3 = 30	1600	1730	1770
	T_4 = 40	1590	1720	1770
0.7	T_1 = 15	1550	1660	1740
	T_2 = 20	1550	1660	1730
	T_3 = 30	1540	1650	1720
	T_4 = 40	1530	1640	1720
	T_5 = 60	1520	1640	1710
0.8	T_1 = 15	1500	1600	1690
	T_2 = 20	1490	1590	1650
	T_3 = 30	1480	1610	1680
	T_4 = 40	1470	1590	1650
	T_5 = 60	1460	1580	1640
0.9	T_1 = 15	1460	1570	1620
	T_2 = 20	1460	1570	1610
	T_3 = 30	1450	1560	1610
	T_4 = 40	1450	1550	1600
	T_5 = 60	1440	1550	1590
1.0	T_1 = 15	1360	1460	1540
	T_2 = 20	1350	1450	1530
	T_3 = 30	1340	1450	1520
	T_4 = 40	1330	1440	1520
	T_5 = 60	1320	1430	1500

Experimental data have shown that when using cement slurry with a water-to-cement ratio up to 0.6, it is important to carefully monitor the initial consistency, density, and setting time of the mixture in order to prevent premature thickening in the pipeline, which would prevent the extraction of samples of the material in liquid form. Later, the density results obtained for W/C ratios of 0.5 and 0.6 were not considered due to insufficient time measurements for further analysis.

It has been decided to divide the process of cement sedimentation and structure formation into three stages. In the first stage, the binder is sealed and pumped into the column, during which the most active phase of stratification occurs. The second stage, lasting from 15 minutes to 60 minutes, or the beginning

of the setting of the cement mixture, reflects the main phase of structure formation. During the third stage, the cement slurry thickens until it has completely cured. The first stage is the most difficult to accurately measure due to high error and the short time period. Therefore, the most suitable stage for study is the structure formation of cement prior to its setting. Fig. 5 illustrates the kinetic curves of density versus time for W/C = 0.8.

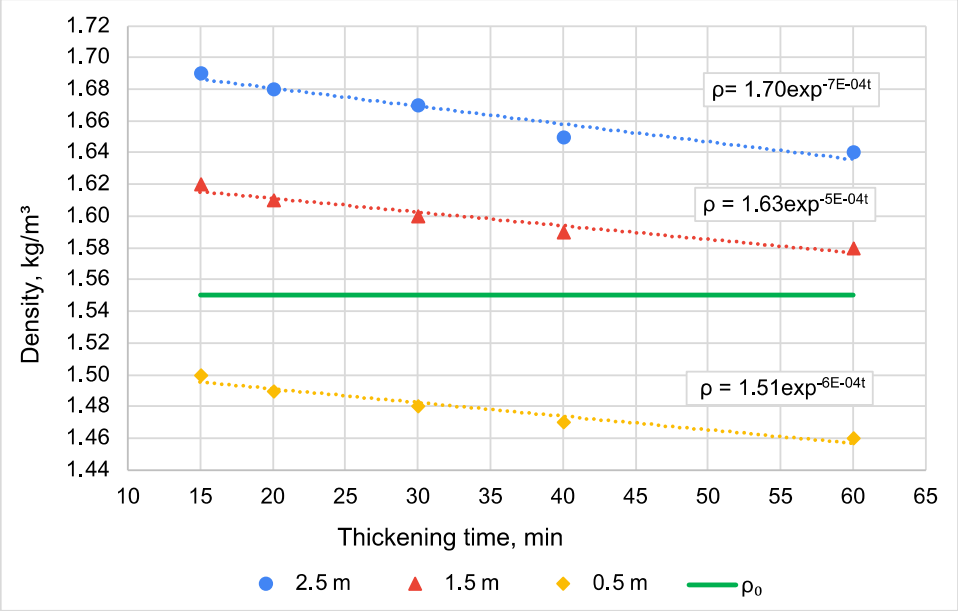

Figure 5. Kinetic curves of density as a function of time, W/C = 0.8.

It has been observed that over time, there is a decrease in density at a certain height in the column, with a maximum reduction of 2.9 %. This can be attributed to the formation of hydration products from the cement paste, as water molecules surround the cement particles and fill the empty space. Due to the small error in density measurements at each time point between T_1 and T_5, we did not consider the effect of time on sedimentation stability for the grouting mixture for up to 60 minutes after mixing. Instead, we averaged the density values of the mixture at each height for further calculations.

The results obtained allowed us to identify several trends. As the W/C ratio increases, there is a general decrease in density due to an increase in the liquid phase of the suspension. Additionally, the lower the sample, the higher the density of the cement paste, indicating a deposition of the solid phase at greater depths and, consequently, a lower sedimentation stability of the mixture within the volume of the pipe.

The W/C ratio also significantly influences sedimentation. As one dives deeper into the cement mixture, the density increases. This pattern is typical for suspensions, as within 40 minutes of starting the mixing process, the heaviest fractions of cement are deposited at the base of a narrow cylinder.

To determine the relationship between the density of the cement mixture, the W/C ratio and depth, considering the effect of sedimentation, the actual W/C ratio was calculated at each measuring level, which was determined as a result of the sedimentation process:

$$\frac{m_w}{m_c} = \frac{\rho_w\left(\rho_c - \rho_{cp}\right)}{\rho_c\left(\rho_{cp} - \rho_w\right)}, \tag{10}$$

where m_w – mass of water, kg; m_c – mass of cement, kg; ρ_w, ρ_c – density of water and true density of cement, respectively, kg/m^3; ρ_{cp} – density of cement paste, kg/m^3 [38, 42].

For a mathematical analysis of the obtained density values and an understanding of the possibility of forecasting, based on experimental data, a graph was constructed-the surface of the dependence of W/C at the H_n level and the density of cement paste on the depth of measurements at the initial W/C = 0.7…1.0 (Fig. 6).

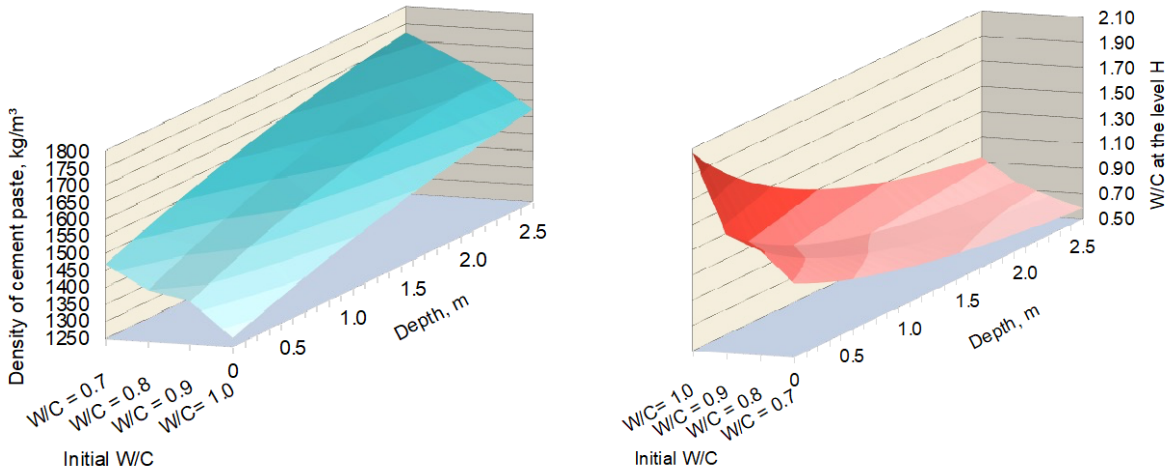

a **b**

Figure 6. The dependence of the physical parameters of the cement pastes on the sampling depth: a – dependence of density; b – dependence of the W/C ratio at the level of H_n.

Fig. 7 shows the dependencies of density and W/C at H_n at the initial W/C = 0.8, representing projections of the surface graph onto corresponding planes of the Cartesian coordinate system.

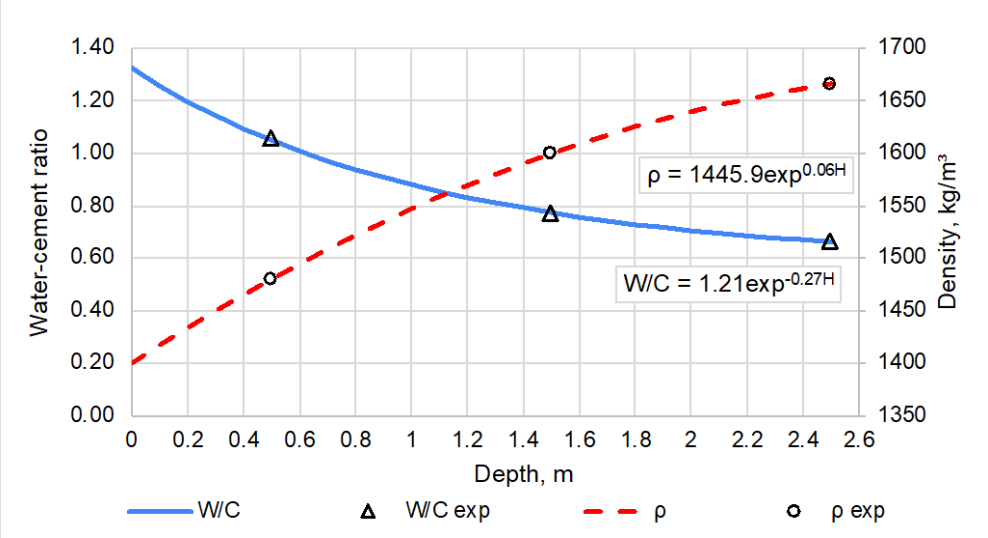

Figure 7. Dependence of density and W/C steady at the H level.

Taking into account the surface density data obtained at H = 0 m, it should be noted that as a result of sedimentation of the cement composition, the density at the bottom of the column is 14–19 % higher than that at the surface. Thus, it is possible to present a general view of the equation obtained for the dependence of cement paste density on the total depth of the column:

$$\rho_n = 2.22 \cdot \exp^{-0.42\left(\frac{W}{C}\right)_n}, \quad (11)$$

where ρ_n – density of cement paste at the level H_n; $\left(\frac{W}{C}\right)_n$ – actual W/C ratio calculated at the level H_n.

In order to study the stability of high-density suspensions and to test cement mixtures with W/C ratios of 0.5 and 0.6, plasticizing and/or retardant additives are recommended to be used when forming a mixture in order to solve the technical problem of well cementing under specified conditions. The results of laboratory measurements with W/C = 0.7…1.0 provide a significant level of reliability in simulating the rheology of the cement paste and offer a more accurate representation of the mixture's behavior at various readings of hydrostatic pressure and gravitational loads.

4. Discussion

Solving the inverse problem, values of a combination of indicators for two types of structures were determined from the sampling depth with initial W/C = 0.7…1.0 (Fig. 8).

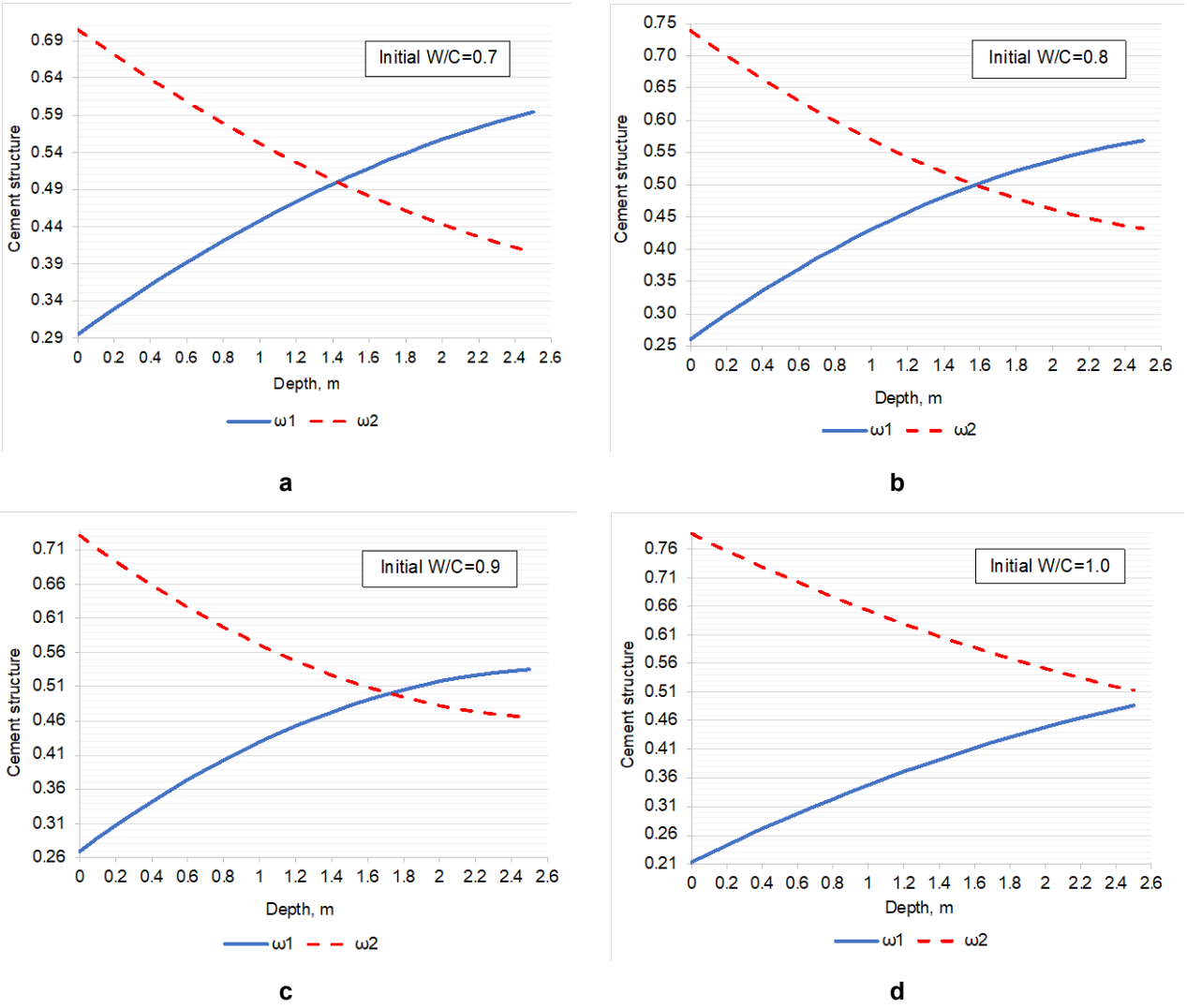

Figure 8. Dynamics of cement precipitation by two types of structures: a – W/C = 0.7; b – W/C = 0.8; c – W/C = 0.9; d – W/C = 1.0.

Based on the calculations, it has been established that as the measurement depth increases, a phenomenon of inversion occurs, where one structural phase is replaced by a second. With increasing measurement depth, the proportion of a homogeneous structure of type I increases, while the proportion of air phase of structure type II decreases. This can be attributed to the effect of air displacement during constrained deposition of the cement slurry. It has also been determined that an increase in the water content of the cement paste leads to a structural inversion as the depth increases.

The dependencies $\omega_i = f(H)$ follow the general form:

$$\omega_i = a_{0,i} \cdot \exp\left(b_{0,i} \cdot H\right), \tag{12}$$

where $a_{0,i}$ and $b_{0,i}$ – the coefficients, the values of which are given in Table 5.

Table 5. Dependency coefficients $\omega_i = f(H)$.

No.	W/C ratio	Structure type			
		Type I structure		Type II structure	
		$a_{0,I}$	$b_{0,I}$	$a_{0,II}$	$b_{0,II}$
1	0.7	0.33	0.27	0.70	-0.23
2	0.8	0.30	0.29	0.72	-0.22
3	0.9	0.31	0.26	0.70	-0.19
4	1.0	0.24	0.32	0.78	-0.17

When approximating the presented data with an exponential curve, a general trend of the observed relationship between the initial W/C, the structures equilibrium point ω_{inv}, and the depth at which phase inversion occurs H_{inv} can be inferred:

$$H_{inv} = 6 \cdot 10^{-5} \cdot e^{20.53 \cdot \omega_{inv}}; \quad (13)$$

$$H_{inv} = 0.54 \cdot e^{1.44 \cdot \frac{W}{C}}. \quad (14)$$

In the case of the presented experiment, the calculated point of structural equilibrium for the grouting compound with an initial W/C = 0.7 is located at ~1.53 m, and for W/C = 0.9 at ~1.84 m.

It is important to take into account the effect of sedimentation during injection of cement into a well, as it is directly related to how the composition of grouting mixtures is selected. In early stages of hydration, cement composition in upper horizons more actively penetrates adjacent rocks, causing the formation of voids, channels, and cavities until grouting mixture becomes fully manifested. In comparison with well-known standard methods for measuring fluid loss [15–17], the proposed method for measuring density of grouting mix allows simulating behavior of cement paste depending upon depth of column, solving problem of mixture penetration into rocks complicated by mining and geologic features. The results of this study confirm that the spreadability and fluidity of cement mixtures gradually increase with increasing W/C ratio, according to [19], however, the density values have an exponential character of change with depth, unlike a linear function [25]. Furthermore, the findings regarding the presence of different stages in the stratification of cement paste [24] were confirmed. According to obtained research, there is an initial phase with a high segregation rate and a subsequent one with a smoother sedimentation process throughout the depth of the column. This provides a more comprehensive understanding of the stratification process of cement paste under actual well conditions.

Due to the obtained mathematical dependencies and low errors in experimental measurements, it is possible to predict the behavior of grouting mixtures during the time period before cement sets. This study will allow us to develop an understanding of the cement hydration process in wells and avoid the negative consequences of high sedimentation of grout mixtures at the most critical time – the first hour after cement is injected into a wellbore.

5. Conclusion

Since the geometric parameters of the distribution of the grouting mixture in the annular space of the borehole are very specific, the resistance of the cement paste to deposition in the annular volume plays a significant role.

The proposed cement slurry density measurement system consists of a vertical column with sampling ports located at various sections of the pipe. Improvements to the current method of measuring cement density are required in order to predict the behavior of the material in unstable rock formations. Based on experimental data, patterns in the behavior of the cement slurry in the annulus of the wellbore were identified as a function of increasing depth. The results from these measurements indicate a direct relationship between the density of the cement sludge and its depth distribution over a given volume or, in other words, its sedimentation stability. As the water content of the mixture increases, the overall density of the final cement mixture decreases, as does the tendency for solid sedimentation to occur with air pockets. Strong density differences in the initial stages indicate a high level of water separation processes and gravitational stratification of the grouting material during the first 15 minutes following the sealing of cement clinker. As the measuring time increases to 60 minutes, the density distribution along the column becomes stable. The suggested approach for determining structure formation using two types provides a

visual representation of the behavior of fully hydrated cement particles and air voids during the constrained placement of the cement mixture.

This research forms the foundation for further experiments aimed at studying the structure formation of grouting mixes with various compositions and improving their physical and mechanical properties throughout the wellbore depth to predict the technical parameters of cement rock under actual conditions.

References

1. Hu, X., Liu, S., Wen, C., Wang, Y., Wang, Y., Zhang, Y., Yang, M. Failure Mechanism of Zonal Isolation for Cement Sheath Induced by Density Reduction Operations after Liner Casing Cementing. ACS Omega. 2025. 10(18). Pp. 18657–18667. DOI: 10.1021/acsomega.5c00006
2. Wu, X., Li, Z., Hou, M. Z., Liu, J., Huang, S., Su, D., Li, J., Cao, C., Wu, L., Song, W. Analytical Perspectives on Cement Sheath Integrity: A Comprehensive Review of Theoretical Research. ACS Omega. 2024. 9(16). Pp. 17741–17759. DOI: 10.1021/acsomega.4c00475
3. Alkhamis, M., Imqam, A. A Simple Classification of Wellbore Integrity Problems Related to Fluids Migration. Arabian Journal for Science and Engineering. 2021. 46. Pp. 6131–6141. DOI: 10.1007/s13369-021-05359-3
4. Stryczek, S., Kremieniewski, M. Multi-Component Cements for Sealing Casing Columns in Boreholes. Buildings. 2023. 13(7). Article no. 1633. DOI: 10.3390/buildings13071633
5. Khazaei, M., Dehvedar, M. A Novel Fluid Loss Control Agent for Reducing Transition Time and Optimizing Fluid Loss and Rheological Properties in Fresh Cement Slurry. Heliyon. 2025. 11(4). Article no. e42699. DOI: 10.1016/j.heliyon.2025.e42699
6. El Bitouri, Y., Azema, N. Potential Correlation Between Yield Stress and Bleeding. ACI Materials Journal. 2021. 349. Pp. 479–494. DOI: 10.14359/51732766
7. Yu, Y., He, Y., Tang, R., Liang, D., Yuan, H-Z. Lattice Boltzmann simulation of power-law fluid flow past fixed and counter-rotating tandem cylinders. Physics of Fluids. 2025. 37. Article no. 033102. DOI: 10.1063/5.0257073
8. Chernyshov, S., Galkin, V., Ulyanova, Z., Macdonald, D. Development of mathematical models to control the technological properties of cement slurries. Journal of Mining Institute. 2020. 242. Pp. 179–190. DOI: 10.31897/pmi.2020.2.179
9. Kolawole, J., Combrinck, R., Boshoff, W. Understanding the role of rheology in the plastic settlement and shrinkage cracking of early age concrete. RILEM Technical Letters. 2022. 7. Pp. 112–126. DOI: 10.21809/rilemtechlett.2022.139
10. Wang, X., Li, S., Zhou, A., Liu, R., Liu, Y., Zhang, C. An analytical model of apparent viscosity in bleeding process. Construction and Building Materials. 2021. 303. Article no. 124471. DOI: 10.1016/j.conbuildmat.2021.124471
11. Brykov, A. The Aspects of Bleeding Instability of Portland Cement. Recent Progress in Science and Technology. 2023. 9. Pp. 1–7. DOI: 10.9734/bpi/rpst/v9/5802A
12. Peng, Y., Pedersen, B., Ng, S., De Weerdt, K., Jacobsen, S. Filler and Water Reducer Effects on Sedimentation, Bleeding and Zeta-Potential of Cement Paste. Nordic Concrete Research. 2018. 58(1). Pp. 107–125. DOI: 10.2478/ncr-2018-0007
13. Chen, Z., Liu, Y., Sui, H., Souza, F., Sagoe-Crentsil, K., Neild, A., Duan, W. Investigating tricalcium silicate dissolution kinetics in cementitious materials through single-particle analysis. Journal of the American Ceramic Society. 2025. 108(7). Article no. e20491. DOI: 10.1111/jace.20491
14. Perrot, A., Lecompte, T., Khelifi, H., Brumaud, C., Hot, J., Roussel, N. Yield stress and bleeding of fresh cement pastes. Cement and Concrete Research. 2012. 42(7). Pp. 937–944. DOI: 10.1016/j.cemconres.2012.03.015
15. Chajec, A., Sadowski, Ł. Bleeding of Cement Pastes Modified with the Addition of Granite Powder. International RILEM Conference on Early-Age and Long-Term Cracking in RC Structures. RILEM Bookseries. 2021. 31. Pp. 307–318. DOI: 10.1007/978-3-030-72921-9_25
16. El Bitouri, Y., Azéma, N. Contribution of turbidimetry on the characterization of cement pastes bleeding. Advances in Cement Research. 2023. 35(4). Pp. 180–190. DOI: 10.1680/jadcr.22.00040
17. Massoussi, N., Keita, E., Roussel, N. The heterogeneous nature of bleeding in cement pastes. Cement and Concrete Research. 2017. 95. Pp. 108–116. DOI: 10.1016/j.cemconres.2017.02.012
18. Draganović, A., Stille, H. Bleeding and Bleeding Measurement of Cement-Based Grout. Proceedings of the Fourth International Conference on Grouting and Deep Mixing. New Orleans, LA, 2012. Pp. 1681–1690. DOI: 10.1061/9780784412350.0143
19. Wang, N., Gao, Y., Pang, H., Zhu, L., Xia, L., Xia, B. Study on Physical and Mechanical Properties of Micro-Cement Grouting Materials with Different Water-Cement Ratio. Journal of Physics: Conference Series. 2022. 2381. Article no. 012099. DOI: 10.1088/1742-6596/2381/1/012099
20. Yanliang, J., Sun, Z., Yang, J., Pel, L., Raja, A., Ge, H. NMR study on bleeding properties of the fresh cement pastes mixed with polycarboxylate (PCE) superplasticizers. Construction and Building Materials. 2020. 240. Article no. 117938. DOI: 10.1016/j.conbuildmat.2019.117938
21. Gökçe, H.S., Andiç-Çakır, Ö. Bleeding characteristics of high consistency heavyweight concrete mixtures. Construction and Building Materials. 2019. 194. Pp. 153–160. DOI: 10.1016/j.conbuildmat.2018.11.029
22. Abadassi, M., El Bitouri, Y., Azéma, N., Garcia-Diaz, E. Effect of Excessive Bleeding on the Properties of Cement Mortar. Construction Materials. 2023. 3(2). Pp. 164–179. DOI: 10.3390/constrmater3020011
23. Jancarikova, D., Hela, R., Netsvet, D., Perina, T. Variability in cement properties – influence on bleeding of cement paste. IOP Conference Series: Materials Science and Engineering. 2018. 385. Article no. 012021. DOI: 10.1088/1757-899X/385/1/012021
24. Peng, Y., Lauten, R.A., Reknes, K., Jacobsen, S. Bleeding and sedimentation of cement paste measured by hydrostatic pressure and Turbiscan. Cement and Concrete Composites. 2017. 76. Pp. 25–38. DOI: 10.1016/j.cemconcomp.2016.11.013
25. Obgadze, T.A. On mathematical modeling of suspension dynamics. IV Mezhdunarodnyy Kosyginskiy Forum “Problemy inzhenernykh nauk: formirovaniye tekhnologicheskogo suvereniteta.” Sbornik nauchnykh trudov Mezhdunarodnogo nauchno-tekhnicheskogo simpoziuma “Sovremennyye inzhenernyye problemy klyuchevykh otrasley ekonomiki strany” (20–22 fevralya 2024 g.) [The 4th International Kosygin Forum “Problems of Engineering Sciences: Formation of Technological Sovereignty.” Proceedings of the International Scientific and Technical Symposium “Modern Engineering Problems of Key Sectors of the National Economy” (February 20–22, 2024)]. Moscow: The Kosygin State University of Russia, 2024. Pp. 102–105.

26. Von Bronk, T., Haist, M., Lohaus, L. The Influence of Bleeding of Cement Suspensions on Their Rheological Properties. Materials. 2020. 13(7). Article no. 1609. DOI: 10.3390/ma13071609
27. Selyaev, V.P., Nizina, T.A., Lankina, Yu.A., Zimin, A.N., Nizin, D.R. The program complex for modelling of unfettered by sedimentation of the particles of the filler in the process of curing polymer systems. Construction materials, equipment, technologies of the 21st century Roofing and insulation materials. 2012. 8(163). Pp. 34–37.
28. Bauman, A.V. Sgushchenie i vodooborot. Kompleksnye resheniya i “nou-khau.” [Condensation and water circulation. Comprehensive solutions and “KNOW-HOW.”] [Online]. System requirements: AdobeAcrobatReader. URL: https://gmexp.ru/netcat_files/multifile/2382/Sguschenie_i_vodooborot.pdf (date of application: 03.05.2025).
29. Rahimbaev, Sh.M., Shatov, A.A., Dryamina, M.A., Kamaliev, I.Z. Influence of soda waste products to fluidity properties and settling stability of cement systems. Bashkir Chemical Journal. 2006. 13(3). Pp. 114–117.
30. Mamedtagizade, M.A. Statistical analysis of the influence of the cement slurry composition and properties on the sedimentation stability. Equipment and technologies for the oil and gas industry. 2017. 4. Pp. 25–28.
31. Shahova, L.D., Kotliarov, R.A. Requirements for normal consistency, water demand and water separation of cements for transport construction. Stroitel’nye Materialy [Construction Materials]. 2018. 5. Pp. 57–60.
32. Kastornykh, L.I., Rautkin, A.V., Raev, A.S. Effect of water-retaining admixtures on some properties of self-compacting concretes. Part 1. Rheological characteristics of cement compositions. Stroitel’nye Materialy [Construction Materials]. 2017. 7. Pp. 34–38.
33. Brykov, A.S. Sauses of instability of water separation of cement paste. Cement and Its Application. 2021. 6. Pp. 72–74.
34. Bobryshev, A.N., Lakhno, A.V., Voronov, P.V. New approaches for evaluating rheological models in composites. IOP Conference Series: Materials Science and Engineering. 2015. 86. Article no. 012001. DOI: 10.1088/1757-899X/86/1/012001
35. Bobryshev, A.N., Galimov, E.R., Kozomazov, N.V. Analiticheskaya otsenka kriticheskogo soderzhaniya elementov v zadachakh teorii protekaniya [Analytical assessment of the critical content of elements in flow theory problems]. Bulletin of Kazan Technological University. 2013. 16(20). Pp. 30–34.
36. Bobryshev, A.N., Zubarev, P.A., Kuvshinov, P.I., Lakhno, A.V. Analysis of filler distribution in the structure of composites. Online bulletin of VolgGASU. Polythematic Series. 2012. 1(20). Pp. 1–28.
37. Yuan, Y., Wang, X., Chen, X., Xiao, P., Koenders, E., Dai, Y. Mathematical models of apparent viscosity as a function of water–cement/binder ratio and superplasticizer in cement pastes. Scientific Reports. 2023. 13. Article no. 22301. DOI: 10.1038/s41598-023-48748-4
38. Kravchenko, V.V. Modeling of the parameters of the poral state of the cement stone within the concept of “internal moisture.” Vestnik of the Polotsk State University. Part F. Constructions. Applied Sciences. 2017. 8. Pp. 28–41.
39. Khohryakov, O.V., Bahtin, M.A. About the role of changes in state of water in hardening cement of low water requirement. Izvestiya KGASU. 2011. 3(17). Pp. 166–170.
40. Xuebing, W., Shengbo, G. Influence of different curing conditions on water absorption of cement-based materials under dry and wet cycles. Materials Research Express. 2022. 9. Article no. 095203. DOI: 10.1088/2053-1591/ac8cd1
41. Li, H., Shi, M., Zhang, J., Peng, L. An experimental study on the influence of low - cement content on improved filling characteristics of geotextile bags filled with fine tailings slurry. Frontiers in Materials. Section Structural Materials. 2025. 12. Article no. 1529905. DOI: 10.3389/fmats.2025.1529905
42. Nikolaev, N., Kozhevnikov, E. Enhancing the cementing quality of the well with horizontal profile. Perm Journal of Petroleum and Mining Engineering. 2014. 11. Pp. 29–37. DOI: 10.15593/2224-9923/2014.11.3

Information about the authors:

***Vlada Kovalchuk**,*
ORCID: https://orcid.org/0000-0001-5985-8050
E-mail: kovalchuk.vsk@gmail.com

***Elena Tsigelnyuk**, PhD in Technical Sciences*
E-mail: etsygelnyuk@inbox.ru

***Evgeny Korolev**, Doctor in Technical Sciences*
ORCID: https://orcid.org/0000-0003-3600-812X
E-mail: korolev@nocnt.ru

Received 06.06.2025. Approved after reviewing 05.02.2026. Accepted 06.02.2026.

Magazine of Civil Engineering

ISSN 2712-8172

journal homepage: http://engstroy.spbstu.ru/

Research article

UDC 624.042

DOI: 10.34910/MCE.141.5

Videogrammetric method for measuring of concrete beam deformations under dynamic vertical loading

S.A.S. Sabir ✉, ***J.A.A. Al-Baghdadi, R.M. Hamdoon***

Surveying Engineering, Technical Engineering College, Baghdad, Iraq

✉ *sanaohasan4@gmail.com*

Keywords: videogrammetry, 3D coordinates, vertical loading, concrete beam, deformation, PhotoModeler software

Abstract. Many studies have examined their use in civil and close-range applications, including building structural monitoring due to advances in videogrammetric systems. However, the videogrammetric system's ability to reliably identify concrete beam dynamic deformations under vertical loads has not been fully studied. This study aims to examine the efficacy of the videogrammetric system in detecting the dynamic deformation of various concrete beams through the utilization of the videogrammetry technique. The researchers utilized PhotoModeler software to generate a three-dimensional stereo model of concrete beams. This was done both before and after applying a vertical load. The primary objective of this research is to determine the deflection values exhibited by these beams. The videogrammetric system employs a pair of stationary video cameras to record the dynamic deformations of loaded beams. This study involves the selection and calibration of two identical model video cameras, specifically the Canon IXUS. In the practical trials, three distinct types of concrete beam sections of identical length are employed. The beams possess cross-sectional dimensions of 10×13×300 cm and have been chosen with varying compositions. In the laboratory setting, the apparatus is utilized to apply a consistent load to each of the three beams. The video results are subsequently examined based on the civil design calculations. The study provides evidence that the utilization of videogrammetric system approaches enables accurate and efficient measurement of deformation in various types of concrete beams, achieving precision at the millimeter level. Based on the aforementioned findings, it is evident that this particular technique holds the potential for effective implementation and utilization in the context of conducting destructive inspections on critical civil structural components

Citation: Sabir, S.A.S., Al-Baghdadi, J.A.A., Hamdoon, R.M. Videogrammetric method for measuring of concrete beam deformations under dynamic vertical loading. Magazine of Civil Engineering. 2026. 19(1). Article. No. 14105. DOI: 10.34910/MCE.141.5

1. Introduction

Extensive investigations have been conducted in recent years about the deformation of structural elements in civil engineering. Nevertheless, the measurement of structural deformation in the bulk of these studies was conducted using conventional equipment, such as a dial gauge. Several of these equipment items are characterized by high costs, whereas the remaining one lacks precision and is not specifically engineered for measuring or displaying dynamic deformation [1]. An excellent method for assessing the performance of a structure is to measure its displacement when subjected to operational loads. Nevertheless, measuring structural deformation with high precision is still challenging, especially in complicated structures [2]. The fatigue life of the structure can be reduced by fluctuating cyclic loading. Cracks are frequently observed as a result of fatigue failure in reinforced concrete structures [3]. Various imaging techniques, including laser scanners and digital photogrammetry, have demonstrated their

effectiveness and accuracy in capturing deformations in both large and small areas subjected to static loading circumstances. Close-range photogrammetry (CRP) is widely recognised as a cost-effective, secure, and precise measuring method across various industries [4]. Videogrammetry is the technique used to acquire three-dimensional data of objects. It utilizes cameras to capture and analyse spatial data [5]. Videogrammetry, which involves determining the coordinates of object points using several video streams captured by camcorders, is an auspicious area of research that holds the capacity to surmount the constraints of current methodologies. A videogrammetric approach is automated and may produce high-quality results without the need for human intervention [6]. Recently, some studies have utilized a video camera and employed videogrammetry, a specialized branch of photogrammetry, to quantify the displacement of the oscillating bridge structure. Lidar has numerous advantages and a diverse range of applications in comparison to photogrammetry, particularly in accurately capturing the movements of objects in motion. The presence of objects makes it a desirable option as a 3D measurement tool [7, 8]. Multiple studies have suggested the potential of utilizing cameras and photogrammetric techniques to accurately quantify the movement of objects that can change shape in three dimensions [9–11]. For instance, the utilization of a high-resolution camcorder in digital photogrammetry on a shipyard enables the measurement of object points. This is done by using retro-reflective targets to provide accurate dimension checking and control [10]. To achieve precise calibration, a robust network geometry was established by capturing 8 images from 5 camera stations, some of which involved panning or rotating the camera axis [12]. Demonstrated that CRP may be employed in both static and dynamic modes. Furthermore, it emphasized the advantages of rapid measurements, comprehensive coverage, and non-contact, which were not possible with alternative methods. The researchers employed two Pulnix (TM-1020-15) digital cameras. Video cameras are used throughout the practical examinations. The cameras were fitted with a built-in ring lamp to provide uniform illumination for retroreflective targets. Moreover, numerous prior research has employed videogrammetric methods in industrial settings. A videogrammetric system with a large field of view, consisting of four cameras, was utilized to perform feature detection and matching, reconstruction of 3D coordinates and displacements, as well as computation of motion parameters. The experiments provided evidence that the suggested method achieved a high level of accuracy, with measurements of dynamic length accurate to within a margin of 0.5 mm [11].

The experiments tests showed that the four-camera video measurement system can accurately predict the position within a range of vision measuring 5000×5000 mm. Consequently, numerous researchers have successfully employed digital photogrammetric approaches to monitor deformations in structures and civil construction [13, 14]. In general, the digital photogrammetric method involves employing digital stereo images captured by a digital camera to monitor deflections in structures and civil elements. Digital photogrammetry offers numerous advantages compared to traditional tools when it comes to measuring deflection. Photogrammetry is a non-contact method that eliminates the need for manually reading dials and generates three-dimensional data. It takes measurements and generates visual recordings of the tests. It is particularly well-suited for conducting destructive testing since only a few inexpensive targets are lost or damaged, in contrast to the expensive Linear Variable Differential Transformers (LVDTs) or dial gauges [13]. For instance [15], photogrammetric techniques were used to evaluate various civil engineering materials. Two cameras with mirrors were used to analyse structures from a rear perspective. Additionally, photogrammetry was employed for on-site monitoring during load tests. Two distinct cameras were employed to capture images, and the results were compared toLVDTs displacement measures [16]. This study investigates the outcomes of utilizing photogrammetry to assess the distortions of bar and plate components in the steel structures of hoisting machines. It analyses the primary difficulties that arise during the processing of these components and suggests remedies to attain the necessary accuracy. The study suggested by [17] presents a novel videogrammetry technique to accurately measure the displacement of a vibration pre-stressed concrete bridge. The technique is applied in both daylight and day-night circumstances utilizing reflective targets. The investigation was carried out in two stages using four High-Definition (HD) video cameras. Additionally, [1] developed a unique transducer to measure the deformation of a high-speed shaking table. This was achieved by utilizing videogrammetric measurements with a high-speed CMOS camera. This study aimed to assess the precision of the shaking table's three-dimensional coordinates using the high-speed videogrammetric measurement method outlined. Based on the literature study, it is evident that digital photogrammetric and videogrammetric approaches are suitable for measuring and observing the changes in shape or structure in civil constructions. Previous studies have not examined the capability of utilizing the videogrammetric systems to identify deflections and the deformations in various types of steel beams subjected to the same load. Therefore, this study seeks to investigate the videogrammetric system's ability to detect deflections and deformations in different sections of steel beams under a dynamic uniform vertical load.

1.1. Mathematical Algorithm

The mathematical algorithm employed in videogrammetry encompasses the utilization of photogrammetric procedures, such as bundle correction, which relies on collinearity Equations (1) and (2).

Bundle adjustment is a prevalent optimization technique that finds extensive application in the field of image processing.

Scene reconstruction is a fundamental aspect of computer vision and computer graphics [18]. The methodology involves the utilization of recorded picture coordinates as well as the consideration of external and internal factors. The intrinsic camera parameters, along with the object space coordinates of the seen points, are essential components in computer vision and image processing. The latter entities exert control over the resultant nonlinear system. The equations of collinearity serve as the fundamental basis for the proposed mathematical model and integrate the observed picture coordinates with the outside and internal camera parameters. The characteristics, as well as the object space coordinates, of the observed points were determined:

$$\left(x-x_0\right)=-f+\frac{r_{11}\left(X-XL\right)+r_{21}\left(Y-YL\right)+r_{31}\left(Z-ZL\right)}{r_{13}\left(X-XL\right)+r_{23}\left(Y-YL\right)+r_{33}\left(Z-ZL\right)}; \tag{1}$$

$$\left(y-y_0\right)=-f+\frac{r_{12}\left(X-XL\right)+r_{22}\left(Y-YL\right)+r_{32}\left(Z-ZL\right)}{r_{13}\left(X-XL\right)+r_{23}\left(Y-YL\right)+r_{33}\left(Z-ZL\right)}, \tag{2}$$

where $\left(x,y\right)$, $\left(x_0,y_0\right)$: are image coordinates of an object and a principal point respectively; $\left(r_n\right)$: rotation matrix according to angles $\left(\omega,\varphi,\kappa\right)$; $\left(f\right)$: focal length of a camera; $\left(X,Y,Z\right)$, $\left(XL,YL,ZL\right)$: are ground coordinates of the object and principal point respectively.

1.2. Structural Concrete Beam Design

Three identical concrete beams were prepared and monitored for testing under emotional load. The length of the beams is 3200 mm and has a rectangular cross-section of 130×100 mm (Fig. 1a). Each type of concrete consists of a different ratio of mixtures, as the first specimen contains a mixture (1:2:4), which means one part of resistant cement two parts of fine sand and four parts of coarse gravel. The second specimen is the mixing ratio (1:3:6) one part of resistant cement, half a part of fine sand, and three parts of crushed gravel (crushed kashi). The third specimen is the mixing ratio (1:1:2), which is one part of resistant cement, one part of fine sand, and two parts of coarse gravel. The concrete used in the beams contains compressive design strength at 28 days and has a fair face. Note that the reason behind testing three concrete beams made from three different ratios of mixture is to make sure that the developed videogrammetric system can capture dynamic deformations of various types of concrete beams. Each girder is reinforced with two lower bars with a diameter of 12 mm and two top bars with a diameter of 12 (Fig. 1). Models have been tested on a testing machine.

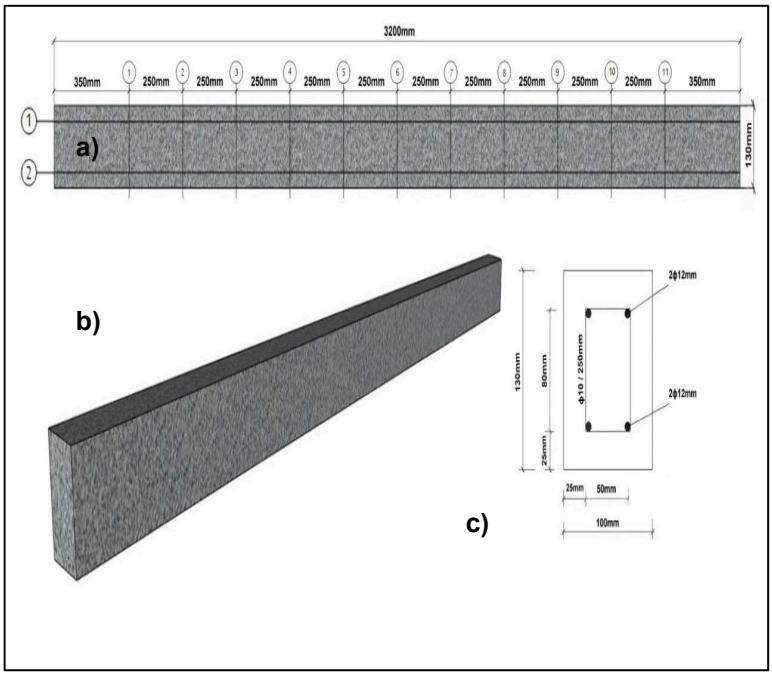

Figure 1. The tested concrete beam: a) longitudinal view; b) perspective view; c) cross-section.

2. Methods

Two non-metric Canon IXUS 185 cameras were used in the study. Additionally, engineering testing equipment manufacture was studied. The equipment is a 10-ton hydraulic jack. Three different concrete formulations have been used to make 10×13×300 cm concrete beams. Custom-made Light Emitting Diode (LED) gadget for video-frame synchronisation was used. The Topcon Total Station (GM 50 series) is used in surveying and construction. Our research relies on this equipment's exact three-dimensional ground coordinate and distance readings. The target was encoded in 10 pixels. Project management software creates targets. Print and attach captured objects. During processing, the project management software may recognise and detect targets in object photos. These targets' proportions depend on the camera's distance from captured items. This study attaches targets to industrial videogrammetric systems. These targets are likewise mounted on the systems' front of concrete beams' surfaces. Internet-accessible Virtual Dub software is free. This tool software breaks a movie into image sequences for many uses. Extract photos from the video. Software like PhotoModeler Scanner (PMS) creates precise 3D models from photos. This programme was integrated by Canadian business Eos Systems Inc. PMS has many uses. Many photogrammetric and videogrammetric applications include quantifying 3D points and creating 3D models. Using images or videos to analyse surfaces as shown in Fig. 2.

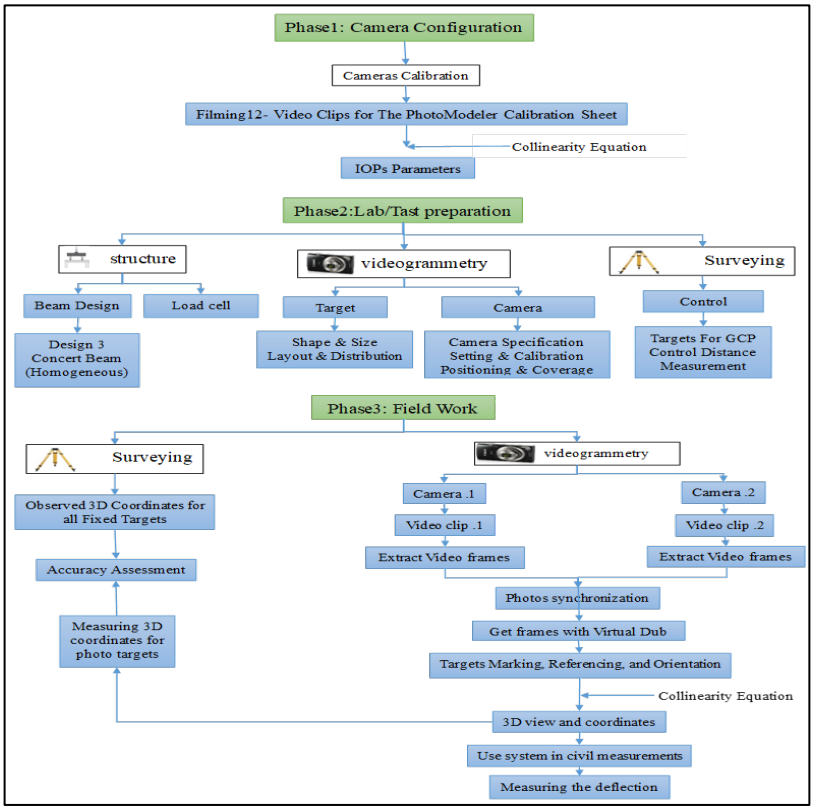

Figure 2. The chart showing the Research Methodology processing.

2.1. Video Camera Calibration

Through camera calibration, the focal length (f), main point coordinates (x_c, y_c) and radial and decentering lens distortions are determined to determine the camera's internal orientation parameters (IOPs). As [13] stated, camera characteristics largely affect relative photogrammetric measurements. The (IOPs) are calculated by linearizing collinearity equations for unknown parameters such as camera lens centre coordinates (XL, YL, ZL), orientation $(\omega, \varphi, \kappa)$, and lens distortion (K_1, K_2, K_3). K_1 provides intermediate precision. Wide-angle cameras and accurate photogrammetric applications require K_2 and K_3. Also, least-squares methods are used to determine the decentering parameters (P_1, P_2) and their affinity and shear properties (C_1, C_2). Iterative computation estimates small constant corrections like the sensor chip's principle distance (f) and principal point (x_0, y_0). The collinearity models determine the target's 3D coordinates after obtaining parameter values. The calibration sheet has four coded targets and 96 grid dots (Fig. 2a). Each camera captured 12 videos. Each camera was photographed on Fig. 3a's

calibration sheet. For calibration, each photo was taken from a different location and angle (Fig. 3b). The calibrating process for sheets frequently requires three movies from each corner. Capture video frames with Virtual Dub. The PMS programme then generates a report with the selected cameras' calibrated inner orientation parameters and camera calibration residuals Root Mean Square Error (RMSE). Information is in Table 1. Camera 1 had 0.102 pixels residuals and camera 2 0.112 pixels. Every calibration residual was below half a pixel. The lens distortion PMS calibration process has been employed to enhance the accuracy of picture coordinates. The study's camera parameters are Type (1) and type (2) cameras including the Canon IXUS 185.

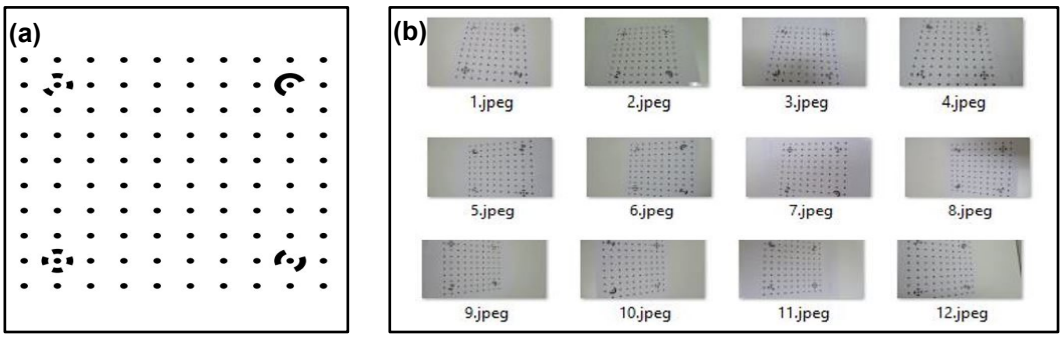

Figure 3. (a) Single-sheet for camera calibration PhotoModeler User Manual, 2020; (b) Twelve photos by every chosen camera were captured on the calibration sheet, PhotoModeler User Manual, 2020.

Table 1. Camera calibration parameters of the two selected cameras.

Items	Camera Canon IXUS 185	
	Left camera	Right Camera
Focal length	7.51563 mm	7.493389 mm
(X0, Y0)	4.596474 mm × 2.596654 mm	4.503162 mm ×2.585972 mm
K1	4.735e-04	5.540e-04
K2	–2.907e-06	–6.138e-06
K3	0.000e+00	0.000e+00
P1	–3.9843e-04	–1.971e-04
P2	3.984e-04	1.372e-04
No. of photos	12	12
Overall RMSE	o.106	0.111
Maximum RMSE	0.322	0.266

2.2. Load Cell Calibration

A load cell is a measuring instrument utilized for the direct or indirect measurement of loads. There are different types of load cells available, namely hydraulic load cells, pneumatic load cells, and strain gauge load cells [19, 20]. Only pneumatic load cells were utilized in this paper. The steel beams were attached to an electrical indication device to measure the imposed load. The calibration was performed between the load cell and the indication. By utilizing varying weights of 5 kg, 10 kg, and 15 kg, as depicted in Fig. 4.

Figure 4. Load Cell Calibration steps.

2.3. Capturing and Processing Videos

After calibration, cameras are set at the right distance from objects. To generate perfect stereo films, the base-to-height ratio was about 1. As shown in Fig. 6, "base" is the horizontal distance between the two cameras' exposure stations, while "height" is the vertical distance between the cameras, the ground, and the subject taken by the camera. As mentioned, stereo recordings use two cameras along the same line to film objects simultaneously. The video parts were then analysed and manipulated on a computer. Uploading videos to Virtual Dub turned them into frames. The two contemporaneous stereo images from the left and right cameras were visually selected for processing. The PMS determines the tridimensional (x, y, and z) coordinates of test apparatus points. Fig. 6 shows the camera's position relative to the test apparatus's targets.

Figure 6. Study area and the equipment for this investigation.

2.4. Accuracy Assessment

This article employed an accuracy assessment to validate the outcomes of video measuring methodologies. The evaluation was conducted by examining the coordinates and extracting the horizontal distances between the points; where these points were fixed on the steel frame (yellow frame), as shown in Fig. 6. The technique involves recording the coordinates of 24 targets, with 12 points serving as a control and 12 points as a chick point. A total station (GM50) with an accuracy of 1 mm was utilized to find the precise 3D ground coordinates of the 24 target points. PMS software was used also to determine the 3D ground coordinates of the 12 checkpoints using the selected stereo images from the video frames. The accuracy assessment process was done by comparing the coordinates of the 12 checkpoints that were measured using the total station with the coordinates of the same points computed using PMS. Subsequently, the variance for each point was computed, followed by the calculation of the cumulative residual of all the points.

2.5. Determining the Target Points' Three-D Coordinates for Deflection Detection

To detect deflection, the team will put 11 10-pixel targets on reinforced concrete beams. To synchronise the camera, an LED light was attached to the steel frame (Fig. 10) before videotaping. TOPCON Total Station (GM50) accuracy (1 mm) The target points' 3D ground coordinates were measured before and after loading. Video measurement determined the target points' 3D positions. Thus, the two cameras recorded six videos of the thing. The video camera's detection is tested. Load-induced deflection of three similar reinforced concrete beams with varied mixture percentages The photos' stereo recordings were uploaded from both cameras before and after the application was installed to the PC for processing. Virtual Dub converted stereo. Videos for every situation in stereo frames. Optical synchronisation of stereo frames from left and right cameras allows PMS software to calculate target point 3D coordinates. Installed encrypted targets (fixed objects) were control points. 12 checkpoints (CPs) were established to provide data tracking and calculating coordinates for targets on steel frames and concrete beams under stresses.. Ensure the 3D coordinates are precise and free of artefacts.

Figure 8. Shows the distribution targets on the test device.

3. Results and Discussion

3.1. Accuracy Assessment Result

Important (error-free) 3D coordinates of target sites as measured using a total station were considered in section 6. The device used PMS to determine the 3D spatial placement of target points attached to the steel frame using stereo video images. The 3D spatial location of target points (PMS) findings were measured by the total station, as shown in Table 2.

Table 2. 3D GCP coordinates of fixed-on-a-steel-frame targets, measured, computed, and residuals.

No.	Observed (m) (Total Station)			Computed coordinates (with photo modeller) (m)			Differences between coordinates (m)		
	x	y	z	x	y	z	vx	vy	vz
1	104.6454	101.9679	30.9364	104.6414	101.9628	30.936	0.004	0.005	0.004
2	104.4009	102.2072	30.9474	104.4059	102.2134	30.9486	–0.005	–0.006	–0.001
3	104.1327	102.4848	30.9436	104.1355	102.4876	30.9416	–0.002	–0.002	0.002
4	103.8176	102.8082	30.9429	103.8189	102.8052	30.9427	–0.001	0.003	0.002
5	103.6078	103.0228	30.9389	103.6028	103.0178	30.9387	0.005	–0.005	–0.004
6	102.9734	103.6647	30.9374	102.9722	103.6632	30.9376	0.001	0.001	–0.002
7	102.7611	103.8751	30.9279	102.7639	103.8765	30.9268	–0.002	–0.001	0.001
8	102.4655	104.1763	30.9354	102.4645	104.175	30.9366	0.001	0.001	–0.001
9	102.2094	104.4314	30.9481	102.2078	104.4298	30.9473	0.002	0.002	–0.002
10	101.9559	104.689	30.9273	101.9492	104.6855	30.9275	–0.006	0.003	–0.002
11	101.7376	104.9028	31.0787	101.7361	104.9031	31.0747	0.001	–0.003	0.004
12	103.3112	103.3678	32.0807	103.3117	103.3648	32.0787	–0.005	0.003	0.003
RMSE							0.00313	0.00321	0.00258

$$RMSE = \sqrt{\frac{\sum v2}{n}}.$$

3.2. Concrete Beam Deflection Results According to Applying Load

Three experiments were performed for each type of reinforced concrete beam of 3.2 m length utilizing a video imaging technology system to record two clips. 11 points for each type of concrete beam were determined using the four loading case weights. Tables following exhibit the length law in Equation (3) used to compute the lengths between every two coordinates of the same object point of no-load situation. According to load, these distances are concrete beam deviation values. At beam number one, the deviation value was high, notably in the bearing zone, as illustrated in Tables 3 and 4 and in Fig. 8. The concrete beam's natural high deflection, especially in the loading area, makes the video measurement system reliable for precise applications. Fig. 9 shows that the gradient in the deflection value of the second and third beams, which have significant resistance, decreases with concrete beam stiffness, verifying these readings. According to Table 5, the video imaging technology system's accuracy lies in sensing deflection values detected for small values (millimetres) and not in loading areas. Figs. 10–12 depict Tables 6 to 12.

$$L = \sqrt{(x_1 - x_2)^2 + (y_1 - y_2)^2 + (z_1 - z_2)^2}. \quad (3)$$

Table 3. The three-dimensional coordinates of the targets that were installed on the first concrete beam were measured before and after loading 300 kg.

Point	Before loading (Zero Load)			After loading (300 Kg)			Deflection (m)
	X_0 (m)	Y_0 (m)	Z_0 (m)	X_A (m)	Y_A (m)	Z_A (m)	
1	104.3971	102.3046	31.52695	104.3951	102.2966	31.51895	0.008
2	104.19	102.5238	31.52496	104.185	102.5168	31.51596	0.009
3	103.9855	102.7428	31.52421	103.9765	102.7358	31.51321	0.011
4	103.7807	102.9602	31.52325	103.7717	102.9522	31.51125	0.012
5	103.5734	103.1759	31.52564	103.5634	103.1669	31.51264	0.013
6	103.3636	103.3947	31.5255	103.3506	103.3867	31.5105	0.015
7	103.1502	103.6098	31.52291	103.1402	103.6008	31.50991	0.013
8	102.9399	103.82	31.52311	102.9309	103.812	31.51111	0.012
9	102.7266	104.0337	31.52465	102.7186	104.0277	31.51465	0.01
10	102.5201	104.2485	31.52768	102.5151	104.2415	31.51868	0.009
11	102.3093	104.4604	31.51998	102.3073	104.4524	31.51198	0.008

Table 4. The three-dimensional coordinates of the targets that were installed on the first concrete beam were measured before and after loading 600 kg.

Point	Before loading (Zero Load)			After loading (600 Kg)			Deflection (m)
	X_0 (m)	Y_0 (m)	Z_0 (m)	X_A (m)	Y_A (m)	Z_A (m)	
1	104.3971	102.3046	31.52695	104.3831	102.2956	31.50995	0.017
2	104.19	102.5238	31.52496	104.173	102.5148	31.50596	0.019
3	103.9855	102.7428	31.52421	103.9655	102.7358	31.50321	0.021
4	103.7807	102.9602	31.52325	103.7587	102.9532	31.50025	0.023
5	103.5734	103.1759	31.52564	103.5504	103.1689	31.50164	0.024
6	103.3636	103.3947	31.5255	103.3396	103.3867	31.5005	0.025
7	103.1502	103.6098	31.52291	103.1282	103.6018	31.49991	0.023
8	102.9399	103.82	31.52311	102.9189	103.813	31.50111	0.022
9	102.7266	104.0337	31.52465	102.7066	104.0297	31.50465	0.02
10	102.5201	104.2485	31.52768	102.5031	104.2395	31.50868	0.019
11	102.3093	104.4604	31.51998	102.2953	104.4514	31.50298	0.017

Table 5. The three-dimensional coordinates of the targets that were installed on the first concrete beam were measured before and after loading 900 kg.

Point	Before loading (Zero Load)			After loading (900 Kg)			Deflection (m)
	X_0 (m)	Y_0 (m)	Z_0 (m)	X_A (m)	Y_A (m)	Z_A (m)	
1	104.3971	102.3046	31.52695	104.3761	102.2876	31.49995	0.027
2	104.19	102.5238	31.52496	104.174	102.5008	31.49696	0.028
3	103.9855	102.7428	31.52421	103.9635	102.7218	31.49421	0.03
4	103.7807	102.9602	31.52325	103.7567	102.9392	31.49125	0.032
5	103.5734	103.1759	31.52564	103.5454	103.1559	31.49164	0.034
6	103.3636	103.3947	31.5255	103.3346	103.3727	31.4895	0.036
7	103.1502	103.6098	31.52291	103.1292	103.5838	31.48991	0.033
8	102.9399	103.82	31.52311	102.9169	103.799	31.49211	0.031
9	102.7266	104.0337	31.52465	102.7036	104.0127	31.49365	0.031
10	102.5201	104.2485	31.52768	102.5001	104.2275	31.49868	0.029
11	102.3093	104.4604	31.51998	102.2883	104.4434	31.49298	0.027

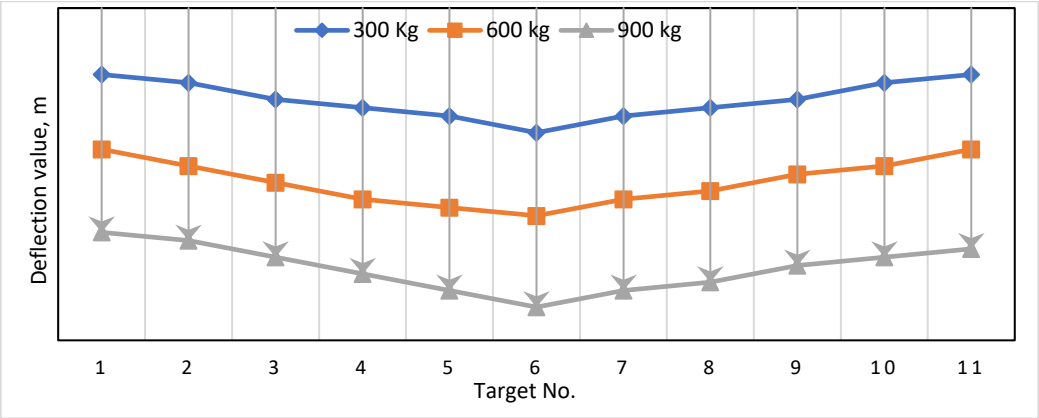

Figure 9. Beam1 deflection under 300, 600, and 900 kg vertical load.

Table 6. The three-dimensional coordinates of the targets that were installed on the second concrete beam were measured before and after loading 300 kg.

Point	Before loading (Zero Load)			After loading (300 kg)			Deflection (m)
	X_0 (m)	Y_0 (m)	Z_0 (m)	X_A (m)	Y_A (m)	Z_A (m)	
1	104.3973	102.3037	31.527	104.3953	102.2977	31.521	0.006
2	104.191	102.5241	31.5238	104.189	102.5161	31.5158	0.008
3	103.9853	102.7429	31.5232	103.9802	102.7359	31.5142	0.009
4	103.7827	102.9622	31.5228	103.7747	102.9562	31.5128	0.01
5	103.5721	103.1734	31.5263	103.5630	103.1664	31.5153	0.011
6	103.363	103.3924	31.5237	103.3520	103.3834	31.5107	0.013
7	103.153	103.6116	31.5212	103.1440	103.6036	31.5092	0.012
8	102.942	103.8199	31.5233	102.9339	103.8139	31.5133	0.01
9	102.7308	104.0351	31.5244	102.7257	104.0281	31.5154	0.009
10	102.5204	104.2475	31.5285	102.5183	104.2395	31.5205	0.008
11	102.3125	104.4628	31.5210	102.3104	104.4558	31.5140	0.007

Table 7. The three-dimensional coordinates of the targets that were installed on the second concrete beam were measured before and after loading 600 kg.

Point	Before loading (Zero Load)			After loading (600 kg)			Deflection (m)
	X_0 (m)	Y_0 (m)	Z_0 (m)	X_A (m)	Y_A (m)	Z_A (m)	
1	104.3973	102.3037	31.527	104.3833	102.2947	31.51	0.017
2	104.191	102.5241	31.5238	104.175	102.5151	31.5058	0.018
3	103.9853	102.7429	31.5232	103.968278	102.6529	31.5042	0.019
4	103.7827	102.9622	31.5228	103.762706	102.9582	31.5028	0.02
5	103.5721	103.1734	31.5263	103.552083	103.1664	31.5053	0.021
6	103.363	103.3924	31.5237	103.342019	103.3844	31.5017	0.022
7	103.153	103.6116	31.5212	103.133028	103.6046	31.5002	0.021
8	102.942	103.8199	31.5233	102.924993	103.8109	31.50433	0.019
9	102.7308	104.0351	31.5244	102.716768	104.026	31.5074	0.017
10	102.5204	104.2475	31.5285	102.507374	104.2375	31.5125	0.016
11	102.3125	104.4628	31.5210	102.299452	104.4548	31.5060	0.015

Table 8. The three-dimensional coordinates of the targets that were installed on the second concrete beam were measured before and after loading 900 kg.

Point	Before loading (Zero Load)			After loading (900 kg)			Deflection (m)
	X_0 (m)	Y_0 (m)	Z_0 (m)	X_A (m)	Y_A (m)	Z_A (m)	
1	104.3973	102.3037	31.527	104.3773	102.2967	31.506	0.021
2	104.191	102.5241	31.5238	104.17	102.5161	31.5018	0.022
3	103.9853	102.7429	31.5232	103.9632	102.7349	31.5002	0.023
4	103.7827	102.9622	31.5228	103.7587	102.9542	31.4978	0.025
5	103.5721	103.1734	31.5263	103.5510	103.1564	31.4993	0.027
6	103.363	103.3924	31.5237	103.3550	103.3654	31.4957	0.028
7	103.153	103.6116	31.5212	103.1320	103.5946	31.4942	0.027
8	102.942	103.8199	31.5233	102.9389	103.7939	31.4973	0.026
9	102.7308	104.0351	31.5244	102.7067	104.027	31.4994	0.025
10	102.5204	104.2475	31.5285	102.4973	104.2395	31.5045	0.024
11	102.3125	104.4628	31.5210	102.2914	104.454	31.4990	0.022

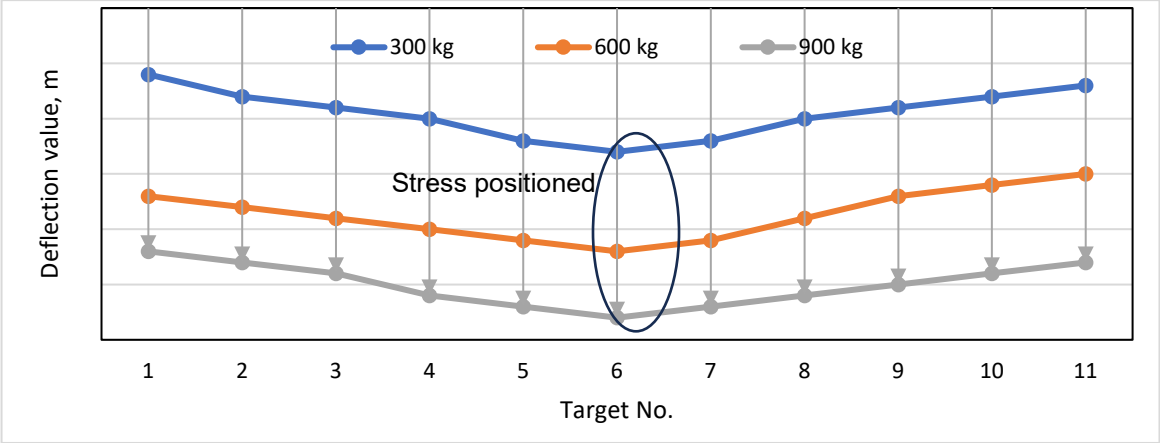

Figure 10. Beam2 deflection under 300 kg ,600 kg, and 900 kg vertical load.

Table 9. The three-dimensional coordinates of the targets that were installed on the third concrete beams were measured before and after loading 300 kg.

Point	Before loading (Zero Load)			After loading (300 kg)			Deflection (m)
	X_0 (m)	Y_0 (m)	Z_0 (m)	X_A (m)	Y_A (m)	Z_A (m)	
1	104.4011	102.324	31.533	104.3991	102.32	31.529	0.004
2	104.2012	102.557	31.527	104.1992	102.551	31.521	0.006
3	103.99	102.779	31.522	103.988	102.771	31.514	0.008
4	103.7927	102.994	31.522	103.7877	102.987	31.513	0.009
5	103.588	103.209	31.527	103.579	103.202	31.516	0.011
6	103.463	103.413	31.5247	103.454	103.405	31.5127	0.012
7	103.155	103.62	31.5213	103.146	103.613	31.5103	0.011
8	102.942	103.833	31.5273	102.934	103.827	31.5173	0.01
9	102.7408	104.052	31.53	102.7358	104.045	31.521	0.009
10	102.5402	104.267	31.531	102.5382	104.259	31.523	0.008
11	102.321	104.478	31.522	102.319	104.471	31.515	0.007

Table 10. The three-dimensional coordinates of the targets that were installed on the third concrete beam were measured before and after loading 600 kg.

Point	Before loading (Zero Load)			After loading (600 kg)			Deflection (m)
	X_0 (m)	Y_0 (m)	Z_0 (m)	X_A (m)	Y_A(m)	Z_A (m)	
1	104.4011	102.324	31.533	104.3921	102.316	31.521	0.012
2	104.2012	102.557	31.527	104.1902	102.548	31.514	0.013
3	103.99	102.779	31.522	103.977	102.771	31.507	0.015
4	103.7927	102.994	31.522	103.7787	102.985	31.505	0.017
5	103.588	103.209	31.527	103.572	103.2	31.509	0.018
6	103.463	103.413	31.5247	103.443	103.409	31.5047	0.020
7	103.155	103.62	31.5213	103.138	103.611	31.5023	0.019
8	102.942	103.833	31.5273	102.926	103.824	31.5093	0.018
9	102.7408	104.052	31.53	102.7278	104.042	31.514	0.016
10	102.5402	104.267	31.531	102.5272	104.259	31.516	0.015
11	102.321	104.478	31.522	102.31	104.469	31.509	0.013

Table 11. The three-dimensional coordinates of the targets that were installed on the third concrete beam were measured before and after loading 900 kg.

Point	Before loading (Zero Load)			After loading (900 kg)			Deflection (m)
	X_0 (m)	Y_0 (m)	Z_0 (m)	X_A (m)	Y_A (m)	Z_A (m)	
1	104.4011	102.324	31.533	104.3811	102.32	31.513	0.020
2	104.2012	102.557	31.527	104.1802	102.549	31.505	0.022
3	103.99	102.779	31.522	103.968	102.771	31.499	0.023
4	103.7927	102.994	31.522	103.7687	102.986	31.497	0.025
5	103.588	103.209	31.527	103.585	103.183	31.501	0.026
6	103.463	103.413	31.5247	103.455	103.386	31.4967	0.028
7	103.155	103.62	31.5213	103.152	103.594	31.4953	0.026
8	102.942	103.833	31.5273	102.939	103.807	31.5013	0.026
9	102.7408	104.052	31.53	102.7168	104.044	31.505	0.025
10	102.5402	104.267	31.531	102.5182	104.259	31.508	0.023
11	102.321	104.478	31.522	102.301	104.471	31.501	0.021

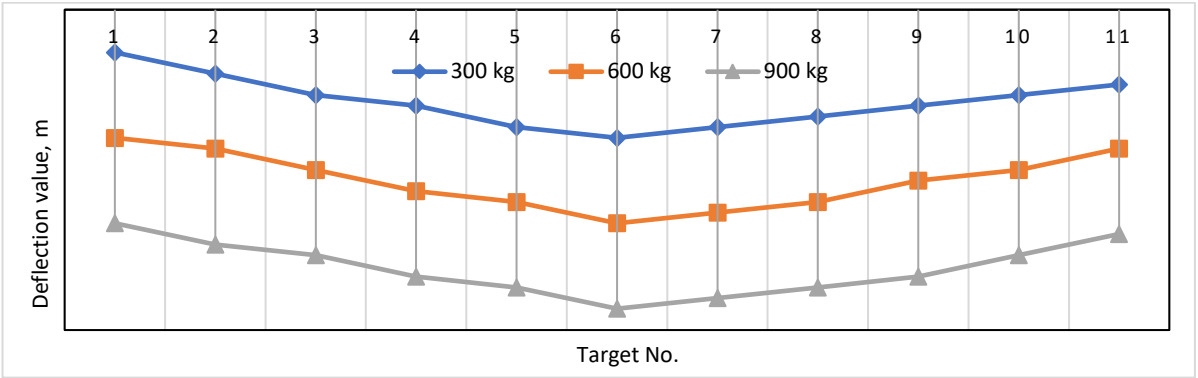

Figure 11. Beam3 deflection under 300 kg, 600 kg, and 900 kg vertical load.

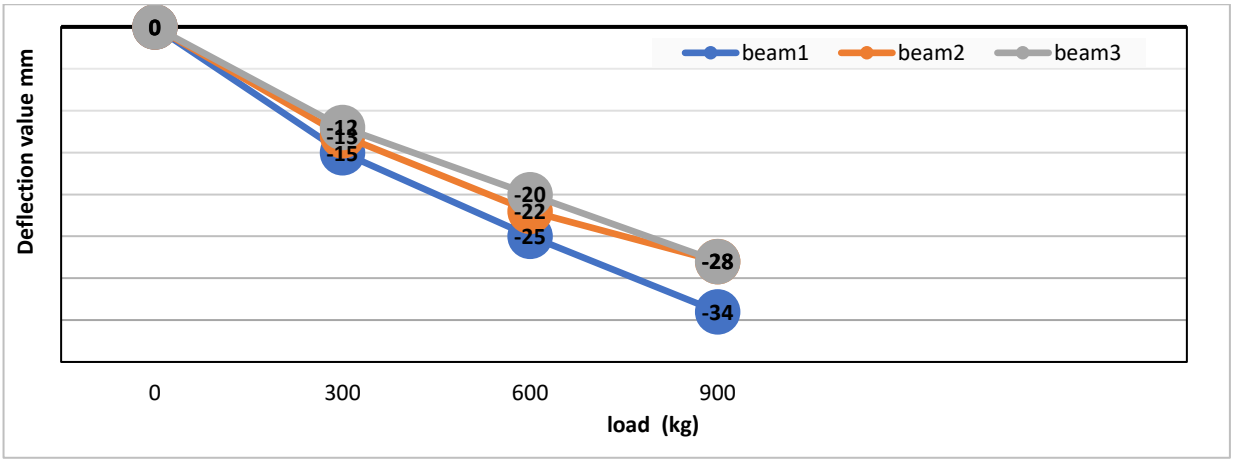

Figure 12. Deflection values in the load area.

4. Conclusions

This study analyses if video measuring and digital cameras can detect concrete beam deformations under pressure. Concrete threshold monitoring and recording are part of the project. The differential load affects concrete beam deflection precision. This study used three 3.20-m-long, 130-by-100-mm-cross-section concrete beams, where three experiments were conducted for three types of concrete beams with the same cross-sectional and longitudinal dimensions. Two low-resolution digital cameras (Canon IXUS 185) were used in these experiments. The research discussed the validation of the results in several steps while observing the dynamic behavior of the concrete beams under vertical loading. The RMS values from the camera calibration process were up to 0.111 pixels. To assess the suitability of video measurement techniques for capturing differences in measurements. Each camera photographed the identical concrete beam three times. It was empty before 300 kg were added. After being laden with 600 kg and 900 kg, there was no burden again. Target site three-dimensional coordinates were obtained using PMS. The RMSE values in the 3D measurements of targets fixed on the steel frame were 0.00313 m, 0.00321 m, and 0.00258 m in the X, Y, and Z coordinates respectively. Thus, the videogrammetric method was used to calculate the 3D coordinates of concrete beam locations before and during load. Deflection values are accurately determined using this method. The obtained deflection values were highly accurate, down to the millimeter level. The study shows the parameter-load correlation. In addition to resistance and cross-sectional properties, video measurement equipment calculates concrete beam deflection. 1) The study compared the photogrammetric triangulation methodology, used for 3D measurement applications, with the accurate conventional method known as Total Station. The results showed that the photo modeler is a reliable tool. Computer programme. 2) The proposed methodology proved that good accuracy can be obtained, by comparing the coordinates observed by the total station with those measured by the videogrammetric system technique. 3) The results provided evidence for the applicability of the Dynamic Videogames methods to assess the concrete beam's structural behaviors and cracks measurement and for the satisfactory level of accuracy of the attained results. This method works well for extensive inspections of critical civil structural elements.

The research discussed the validation of the results in several steps while observing the dynamic behavior of the concrete beams under vertical loading.

References

1. Tong, X, Luan, K, Liu, X, Liu, S, Chen, P, Jin, Y, Lu, W, Huang, B. Tri-Camera High-Speed Videogrammetry for Three-Dimensional Measurement of Laminated Rubber Bearings Based on the Large-Scale Shaking Table. Remote Sensing. 2018. 10(12). Article no. 1902. DOI: 10.3390/rs10121902
2. Galloway, T., Cole, M., & Lewis, C. (2017). Interactions of microplastic debris throughout the marine ecosystem. Journal of Cleaner Production, 169, 41-48. DOI: 10.1016/j.jclepro.2017.05.011.
3. Olsson, K., Pettersson, J. Fatigue Assessment Methods for Reinforced Concrete Bridges in Eurocode: Comparative study of design methods for railway bridges. Master of Science Thesis in the Master's Programme Structural Engineering and Building Performance Design. Chalmers University of Technology. Göteborg, 2010. 167 p.
4. Alaloul, W.S., Qureshi, A.H., Musarat, M.A., Saad, S. Evolution of close-range detection and data acquisition technologies towards automation in construction progress monitoring. Journal of Building Engineering. 2021. 43(3). Article no. 102877. DOI: 10.1016/j.jobe.2021.102877
5. Radi, F.M., Al-Baghdadi, J.A.A. The possibility of using a digital camera and videogrammetric techniques for monitoring of objects moving at different speeds. International Journal of Civil Engineering and Technology. 2018. 9(8). Pp. 318–331.
6. Fathi, H., Brilakis, I. Automated sparse 3D point cloud generation of infrastructure using its distinctive visual features. Advanced Engineering Informatics. 2011. 25(4). Pp. 760–770. DOI: 10.1016/j.aei.2011.06.001

7. Ortiz-Coder, P., Sánchez-Ríos, A. An Integrated Solution for 3D Heritage Modeling Based on Videogrammetry and V-SLAM Technology. Remote Sensing. 2020. 12(9). Article no. 1529. DOI: 10.3390/rs12091529
8. Gruen, A. Fundamentals of videogrammetry – A review. Human Movement Science. 1997. 16(2–3). Pp. 155–187. DOI: 10.1016/S0167-9457(96)00048-6
9. Shi, H., Chen, P., Zhang, D., Yang, J., Xu, Z., Tong, X. High-speed videogrammetric measurement of the displacement of suspendome structure node. Proceedings of The Fifth International Conference on Geoscience and Remote Sensing Mapping (ICGRSM 2023). 2024. 12980. DOI: 10.1117/12.3020958.
10. Maas, H.G., Kersten, T.P. Experiences with a high resolution still video camera in digital photogrammetric applications on a shipyard. Intercongress Symposium. Vol. 30. Part V. Melbourne, 1994. Pp. 250–255.
11. Hu, H., Liang, J., Xiao, Z.Z., Tang, Z.Z., Asundi, A.K., Wang, Y.X. A four-camera videogrammetric system for 3-D motion measurement of deformable object. Optics and Lasers in Engineering. 2012. 50(5). Pp. 800–811. DOI: 10.1016/j.optlaseng.2011.12.011
12. Black, J.T., Pappa, R.S. Photogrammetry and Videogrammetry Methods for Solar Sails and Other Gossamer Structures. Collection of Technical Papers – AIAA/ASME/ASCE/AHS/ASC Structures, Structural Dynamics and Materials Conference 2003. 3. 1–11. DOI: 10.2514/6.2004-1662
13. Whiteman, T., Lichti, D.D., Chandler I. Measurement of deflections in concrete beams by close-range digital photogrammetry. Symposium on Geospatial Theory, Proceedings and Applications. Ottawa, 2002. 9 p.
14. Dai, F., Lu, M. Assessing the Accuracy of Applying Photogrammetry to Take Geometric Measurements on Building Products. Journal of Construction Engineering and Management. 2010. 136(2). Pp. 242–250. DOI: 10.1061/(ASCE)CO.1943-7862.0000114
15. Ji, Y., Chang, C.C. Identification of structural dynamic behavior for continuous system based on videogrammetric technique. Smart Structures and Materials 2006: Smart Structures and Integrated Systems. SPIE, 2006. Pp. 447–458.
16. Ganshkevich, Yu.A., Shikhov, N.S., Stoyantsov, N.M. Estimation of deformations of steel constructions of cranes based on photogrammetry. Journal of Physics: Conference Series. 2021. 1926(1). Article no. 012061. DOI: 10.1088/1742-6596/1926/1/012061
17. Chong, A.K., Al-Baghdadi, J.A.A., Alshadli, D. High definition video cameras for measuring movement of vibrating bridge structure. Int Conf Vib Vibro-acoustics. 2014. 1–10.
18. Chen, X., Davis, J., Slusallek, P. Wide area camera calibration using virtual calibration objects. Proceedings IEEE Conference on Computer Vision and Pattern Recognition. CVPR 2000 (Cat. No.PR00662). Vol. 2. Hilton Head, SC, 2000. Pp. 520–527. DOI: 10.1109/CVPR.2000.854901
19. Qandil, A., Zaid, A.I.O. Considerations in the design and manufacturing of a load cell for measuring dynamic compressive loads. 2015 Power Generation System and Renewable Energy Technologies (PGSRET). Islamabad, 2015. Pp 1–6. DOI: 10.1109/PGSRET.2015.7312209
20. Hastawan, A.F., Haryono, S., Utomo, A.B., Hangga, A., Setiyawan, A., Septiana, R., Hafidz, C.M., Triantino, S.B. Comparison of testing load cell sensor data sampling method based on the variation of time delay. IOP Conference Series: Earth and Environmental Science. 2021. 700(1). Article no. 012018. DOI: 10.1088/1755-1315/700/1/012018

Information about the authors:

Sanarya Sabir,
E-mail: sanaohasan4@gmail.com

Jasim Al-Baghdadi,
E-mail: jasim76@gmail.com

Rana Hamdoon,
E-mail: ranamounjeo@mtu.edu.iq

Received 07.06.2024. Approved after reviewing 02.02.2026. Accepted 03.02.2026.

Magazine of Civil Engineering

ISSN 2712-8172

journal homepage: http://engstroy.spbstu.ru/

Research article

UDC 624

DOI: 10.34910/MCE.141.6

Properties of concrete incorporating treated prickly pear fibers

I. Tarkhani[1], ***Z. Kammoun***[2,3] ✉ , ***A. Trabelsi***[1 2], ***H. Smaoui***[4]

[1] *LGC for National Engineering School of Tunis (ENIT), University of Tunis El Manar, Tunis, Tunisia*

[2] *Military Academy of Fondouk Jedid, Nabeul, Tunisia*

[3] *GESTE for National School of Engineers of Sfax, University of Sfax, Sfax, Tunisia*

[4] *Faculty of Engineering. King Abdulaziz University, Jeddah, Kingdom of Saudi Arabia*

✉ *kammounzied@yahoo.fr*

Keywords: concrete, prickly pear, fiber, treatment, long-term, strength, mechanical properties, thermal properties

Abstract. The integration of natural fibers into building materials is key to enhancing sustainability within the construction industry. However, vegetable fibers are known to undergo mechanical degradation over time when embedded in the alkaline environment of cementitious matrices. This study investigates the incorporation of prickly pear fibers into concrete, evaluating the efficacy of three surface treatments (epoxy, lime, and bitumen) over a curing period extending from 3 to 180 days. Results indicate that while untreated fibers reduce compressive strength, the applied treatments significantly mitigate this loss. Notably, epoxy-treated fiber concrete exhibited only an 11 % decrease in compressive strength at 28 days compared to ordinary concrete, eventually achieving a strength 53 % higher than that of untreated fiber concrete by 180 days. At the optimal dosage of 15 kg/m^3, epoxy treatment enhanced 28-day flexural strength by 333 %, while lime treatment yielded a 229 % increase. Furthermore, whereas untreated fibers exhibited mechanical degradation after 28 days, treated fibers demonstrated sustained strength gains up to 180 days. Additionally, a fiber dosage of 40 kg/m^3 substantially improved thermal performance, reducing conductivity by 40–45 % and increasing specific heat capacity by 22–24 %. These findings highlight the potential of treated prickly pear fibers as a viable, sustainable reinforcement for high-performance construction applications.

Citation: Tarkhani, I., Kammoun, Z., Trabelsi, A., Smaoui, H. Properties of concrete incorporating treated prickly pear fibers. Magazine of Civil Engineering. 2026. 19(1). DOI: 10.34910/MCE.141.6

1. Introduction

Plant fibers are increasingly incorporated into cementitious materials owing to their renewability, biodegradability, low embodied energy, and near carbon-neutral life cycle [1]. Beyond these environmental benefits, their low density and cost-competitiveness relative to synthetic fibers make them attractive for lightweight, sustainable construction [2, 3]. Numerous plant-based reinforcements – including straw, date palm, Stipa tenacissima (Alfa), bamboo, sisal, coconut shell, and Ampelodesmos mauritanicus (Diss) – have been evaluated in concrete and mortar composites [4–12]. A consistent finding across the literature is a reduction in composite density, primarily due to the lower intrinsic density of lignocellulosic materials compared to mineral aggregates. In parallel, several studies report enhanced thermophysical performance, specifically reductions in thermal conductivity, diffusivity, and effusivity, alongside increased specific heat capacity. These effects are attributed both to the low intrinsic thermal conductivity of plant fibers and the additional porosity introduced within the matrix [1].

Mechanical performance is highly dependent on fiber morphology, dosage, dispersion, and the quality of the fiber–matrix interface. Although compressive strength often declines with increasing fiber content – largely due to higher porosity and interfacial weaknesses – improvements in flexural strength, splitting tensile strength, and post-cracking toughness are frequently observed. Alfa fiber-reinforced concrete, for example, exhibited reduced compressive strength at high dosages, yet flexural and tensile strengths peaked at 15 kg/m^3, accompanied by improved ballistic resistance [13]. Similarly, incorporating 50 mm maguey fibers pretreated with calcium oxide (0.9 % by cement weight) increased compressive, flexural, and tensile strengths by 13.4, 17.4, and 1.5 %, respectively, while boosting the modulus of elasticity by 53.8 % [14]. In ultra-high-performance concrete, sisal fibers (6–18 mm, 1–3 % by volume) had negligible effects on compressive strength but successfully transitioned the failure mode from brittle to ductile; at a 2 % volume fraction, flexural strength and toughness increased by 16.7 and 540 %, respectively [15]. Comparable trends were observed with palm leaf sheath fibers, whereas banana fibers led to performance losses attributed to inadequate interfacial bonding [16].

Among various lignocellulosic reinforcements, prickly pear fibers exhibit significant structural and thermal potential. In lightweight concrete, their incorporation reduced density by approximately 25 % and thermal conductivity by 42 %, while increasing flexural strength by 170 %; compressive strength remained above 22 MPa, thereby meeting structural-grade requirements [17]. In high-strength concrete, density reductions of up to 30 % and thermal conductivity decreases of 50 % were reported, with compressive strengths ranging from 41 to 59 MPa and flexural strength gains reaching 35 % at 28 days [18]. Furthermore, improved impact resistance and toughness highlight their suitability for both conventional and high-performance systems.

Despite these advantages, long-term durability remains a critical challenge. Plant fibers consist primarily of cellulose, hemicellulose, and lignin, all of which are susceptible to degradation in the highly alkaline cementitious environment (pH > 12). Alkaline hydrolysis of hemicellulose and lignin, partial depolymerization of cellulose chains, and the diffusion of pore solution toward the fiber surface progressively weaken the lignocellulosic structure. Moreover, the precipitation of hydration products within the lumen and cell walls promotes stiffening and embrittlement, while cyclic swelling and shrinkage of the hydrophilic fibers under fluctuating moisture conditions induce interfacial microcracking [19, 20]. Collectively, these mechanisms compromise long-term strength and toughness.

To mitigate degradation and enhance fiber–matrix compatibility, several pretreatment strategies have been explored. Lime treatment of palm nut shells increased 28-day compressive strength by 10 %, whereas polyvinyl alcohol (PVA) primarily reduced water absorption without providing mechanical benefits [21]. Boiling and linseed oil coating of Diss fibers improved tensile behavior and delayed crack initiation [22]. A 60-minute $Ca(OH)_2$ treatment of date palm fibers enhanced flexural strength by removing inhibitory extractives and promoting interfacial bonding [23]. Mineral and organic coatings have also been investigated to control dimensional instability: oil impregnation reduced drying shrinkage in wood-based composites by 43.6 %, while lime coatings improved compatibility more effectively than cement [24]. Paraffin wax coatings acted as hydrophobic barriers to optimize moisture exchange, whereas prolonged pre-wetting (48 h) reduced performance due to diminished suction capacity [25]. In straw-reinforced sand concrete, hot water treatment provided the most balanced improvement (a 30 % increase in flexural strength), while gasoil minimized shrinkage and waste oil adversely affected dimensional stability despite strength gains [26].

While various treatments have been evaluated for different plant fibers, research on prickly pear fibers remains limited, with existing studies primarily focused on hot-water treatments and assessments restricted to 28 days of age. The present study aims to fill this gap by evaluating the impact of three coating-based treatments – resin, lime solution, and bitumen – on the mechanical (compressive and flexural), physical (density), and thermal (conductivity) behavior of prickly pear fiber-reinforced concrete. The analysis extends to 180 days to evaluate the evolution of properties beyond standard curing ages. Treated and untreated composites are compared to identify the most effective method for enhancing interfacial stability and mitigating alkaline-induced degradation.

2. Materials and Methods

The development of sustainable construction materials often involves either the optimization of the binder [27] or the reinforcement of the matrix with agricultural residues [28]. In the present study, the focus is placed on the incorporation of cactus fiber sheets as a natural reinforcement within a standardized concrete matrix. All materials and experimental procedures followed the international standards prevailing in the region of study to ensure technical consistency. The binder used is a Portland cement manufactured according to EN 197-1 specifications. The mechanical characterization of the concrete was performed

according to the EN 12390 series, specifically EN 12390-1 for specimen geometry (16×32 cm cylinders) and EN 12390-6 for splitting tensile strength. The following subsections describe the aggregate and binder properties, the fiber treatments, the concrete mix design, and the experimental techniques applied.

2.1. Aggregate and Binder Properties

The binder is a CEM I 42.5 Portland cement, with a density of 3.15 g/cm^3, a compactness of 0.574, and a Blaine specific surface area of 346.6 m^2/kg. The fine aggregate is a 0/2 mm sand extracted from the Borj Hfaiedh quarry. Its measured sand equivalent (SE = 81, NF P18-597) confirms a high level of cleanliness. The coarse aggregate is a 4/12 mm gravel obtained from the Jbel Ressas quarry. The sand exhibits an apparent density of 1650 kg/m^3 and an absolute density of 2510 kg/m^3, while the gravel presents an apparent density of 1560 kg/m^3 and an absolute density of 2521 kg/m^3. The particle size distributions of the aggregates (Fig. 1) were determined by dry sieving, a methodology consistent with the characterization of alternative and conventional granular materials [29, 30]. According to EN 12620, the sand is classified by its fineness modulus, which was calculated as 1.85, identifying it as a fine sand. The coarse aggregate is classified as a 4/12 mm class gravel, with a maximum particle size $(D_{\max})$ of 12.5 mm, as confirmed by the grading analysis. These classifications are essential for ensuring an optimal granular skeleton and for monitoring the water demand of the cementitious matrix.

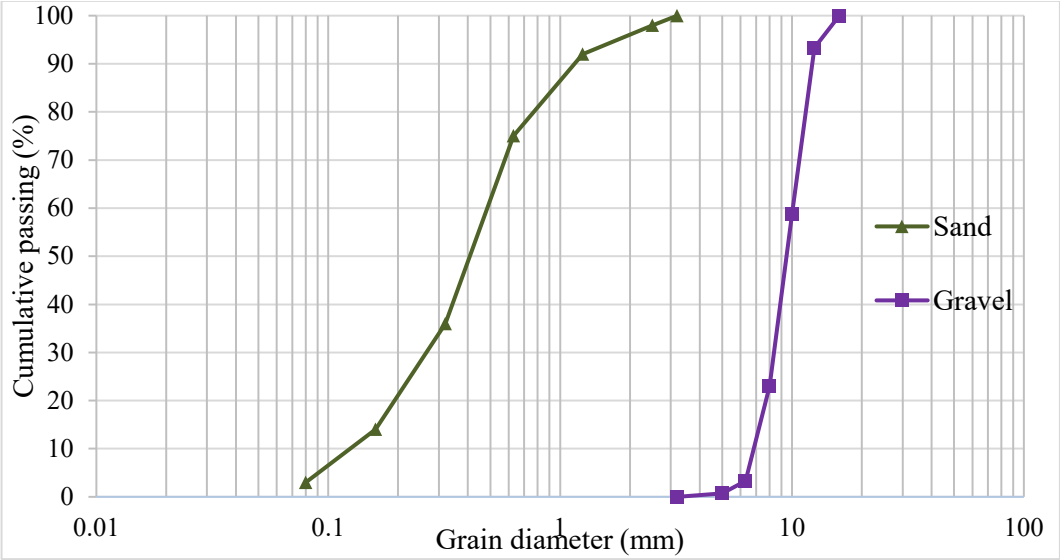

Figure 1. Particle size distribution curves for sand and gravel.

2.2. Fibers

Opuntia ficus-indica, commonly known as the prickly pear cactus, is prevalent in Africa, the Americas, and the Mediterranean basin [31]. This species is characterized by its stems, referred to as “cladodes” or “nopalitos,” which fulfill the function of leaves [32]. Upon the decay of an *Opuntia* trunk or cladode, the outer layer gradually decomposes, exposing an underlying structure composed of multiple fibrous layers arranged in a honeycomb-like pattern, as illustrated in Fig. 2.

Figure 2. Dead prickly pear cladode.

The fibers used in this study were sourced from naturally dead cladodes and trunks and manually cut into 5 × 5 cm pieces. According to Mannai et al. [33], *Opuntia ficus-indica* fibers exhibit a chemical composition of approximately 53.6 % cellulose, 4.8 % lignin, and 10.9 % hemicellulose. While the relatively high cellulose content is favorable for mechanical performance, the presence of lignin and hemicellulose – components known to be chemically unstable in highly alkaline environments such as Portland cement – raises concerns regarding potential degradation over time when the fibers are embedded in cementitious matrices. This consideration motivates the use of protective surface treatments aimed at improving their durability within concrete. In addition to their chemical characteristics, the mechanical behavior of *Opuntia* fibers displays significant variability in the literature, as highlighted in [34]. This dispersion is mainly attributed to differences in extraction methods, environmental factors, and particularly the maturity of the cladodes. Reported tensile elastic modulus values range from 0.15 to 2.93 GPa, while tensile strengths vary between 1 and 27 MPa, with the highest values generally obtained from older cladodes where the lignocellulosic network is more developed.

The treatments applied in this study involved coating the fibers with lime, epoxy, or bitumen, as illustrated in Fig. 3. Consequently, the study examined five distinct types of concrete: ordinary concrete (OC) serving as the control; concrete reinforced with untreated prickly pear fibers (UTFC); and concretes reinforced with lime-treated (LFC), epoxy-treated (EFC), and bitumen-treated (BFC) prickly pear fibers. The lime treatment involved immersing the fibers in a lime solution for 30 seconds, followed by drying for 24 hours. This process aims to improve the bond between the fibers and the cementitious matrix. The bitumen treatment entailed immersing the fibers in bitumen heated to 160 °C, followed by drying at ambient temperature to allow the bitumen to solidify. The epoxy treatment involved coating the fibers with an epoxy resin, which acts as a binding agent that encapsulates the fibers. The objective of the bitumen and epoxy treatments is mainly to enhance the moisture protection of the fibers and, consequently, to improve their resistance to the alkaline environment.

a b c d

Figure 3. Untreated (a), epoxy (b), bitumen (c), and lime (d) treated fibers.

The densities of the concrete samples incorporating prickly pear fibers varied depending on the treatment applied. The untreated fibers had a density of 571 kg/m^3. While fiber density increased slightly with treatment, the maximum increase remained below 5 %. Consequently, the density variation of the fibers was neglected in the concrete mix design.

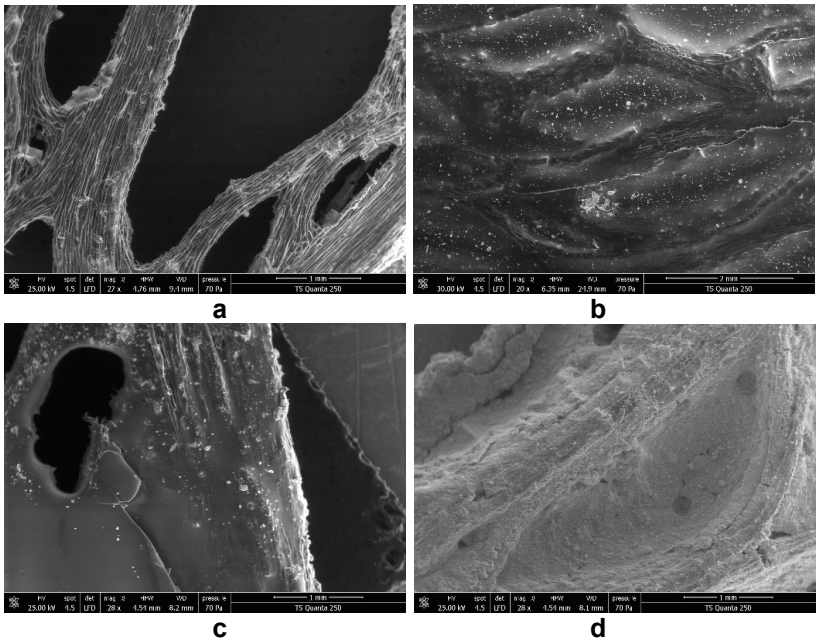

a b c d

Figure 4. SEM of untreated (a), epoxy (b), bitumen (c), and lime (d) treated fibers.

Fig. 4 presents Scanning Electron Microscopy (SEM) images of both treated and untreated prickly pear fibers. The SEM image of the untreated fiber reveals a fibrous structure with loosely attached impurities and plant residues. In the case of the lime-treated fiber, a thin layer of lime is visible, coating the fibers and filling the gaps between them, resulting in a granular surface texture. The bitumen-treated fiber appears coated with a smooth, continuous layer of bitumen that obscures the natural surface features. The SEM image of the epoxy-treated fiber shows a uniform, smooth epoxy resin coating that encapsulates the fibers, effectively covering the natural surface texture and filling the inter-fiber spaces, with fewer visible microfibrils.

2.3. Elaboration of the Concrete

The baseline formulation (C0) was designed using the Dreux–Gorisse method to achieve a specific target consistency and strength class. The mix proportions, which resulted in a constant water-to-cement (W/C) ratio of 0.4375, are detailed in Table 1. The fibers were incorporated as a volumetric replacement for the aggregates, maintaining a constant sand-to-gravel volume ratio. Any variation in fiber density resulting from the different treatments was considered negligible and was therefore not accounted for during the mix design process. Consequently, five different fiber dosages were evaluated: 5, 10, 15, 20, and 40 kg/m^3 (Table 1).

Table 1. Composition of concrete (kg/m^3).

Designation	C0	C5	C10	C15	C20	C40
Gravel	1175	1161	1146	1132	1118	1060
Sand	646	638	630	622	613	581
Cement	400	400	400	400	400	400
Water	175	175	175	175	175	175
Fibers	0	5	10	15	20	40

The untreated and lime-treated fibers were pre-saturated with water before mixing to prevent them from absorbing water from the fresh concrete. This step was unnecessary for the epoxy- and bitumen-treated fibers, as their treatment effectively prevents water absorption. Following the mixing process, which ensured a random distribution of the fibers, three specimens of each concrete composition were prepared for each test. The specimens were demolded 24 hours after casting.

2.4. Experimental Techniques

The workability of fresh concrete was assessed using the slump test, in accordance with the aforementioned EN 12350-2. Compressive and flexural tests were performed on cubic (15 × 15 × 15 cm) and prismatic (7 × 7 × 28 cm) specimens, respectively, using a universal testing machine (Fig. 5). As previously specified, splitting tensile strength was determined on the 16 × 32 cm cylindrical specimens. These tests were performed at curing ages of 3, 7, 28, 90, and 180 days to assess the strength evolution of the concrete over time.

a **b** **c**

Figure 5. Experimental setup for compression (a), flexural (b), and splitting tensile (c).

Thermal conductivity, diffusivity, and specific heat were measured using a Fox 314 calorimeter, following the ASTM C518 and ISO 8301 standards.

3. Results and Discussion

3.1. Workability and Densities

Fig. 6 presents the effect of fiber type and treatment on the workability of the concrete. The reference OC exhibits a slump of 11.0 cm. At a low dosage of 5 kg/m^3, untreated fibers slightly reduce the slump to 10.8 cm, while bitumen-, lime-, and epoxy-treated fibers result in values of 11.1, 11.2, and 10.9 cm, respectively. These variations indicate that fiber treatments modify the fresh behavior of the mix, likely due to differences in fiber morphology and the quality of the fiber–matrix interface induced by each treatment.

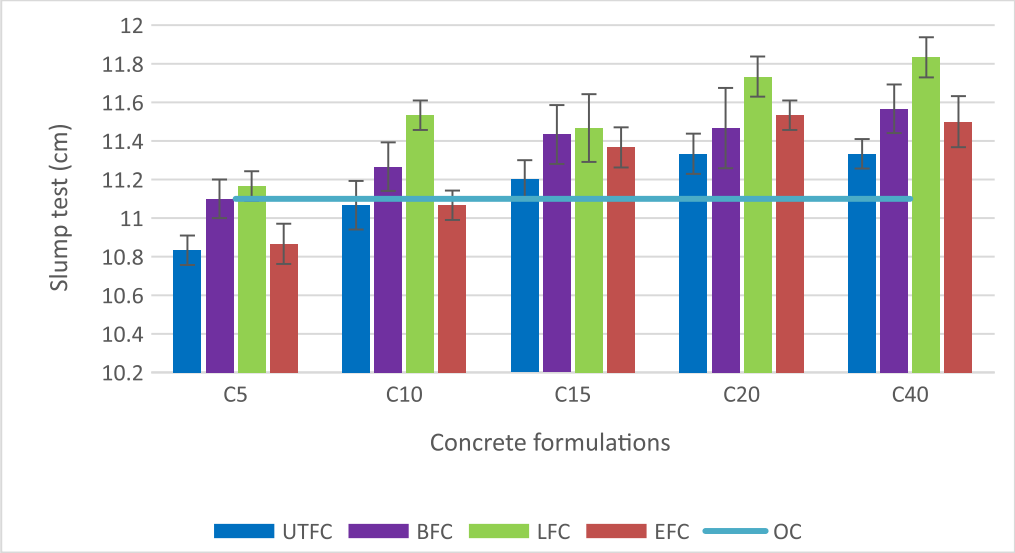

Figure 6. Workability of concrete.

As the fiber content increases, an overall improvement in workability is observed. At 40 kg/m^3, slump values reach 11.3 cm for UTFC, 11.6 cm for BFC, 11.8 cm for LFC, and 11.5 cm for EFC, confirming that the lime treatment provides the greatest enhancement, followed by bitumen and epoxy, while untreated fibers remain the least effective. Despite these changes, all mixtures maintain an S3 consistency class, indicating that the addition of treated or untreated fibers does not compromise the required workability level.

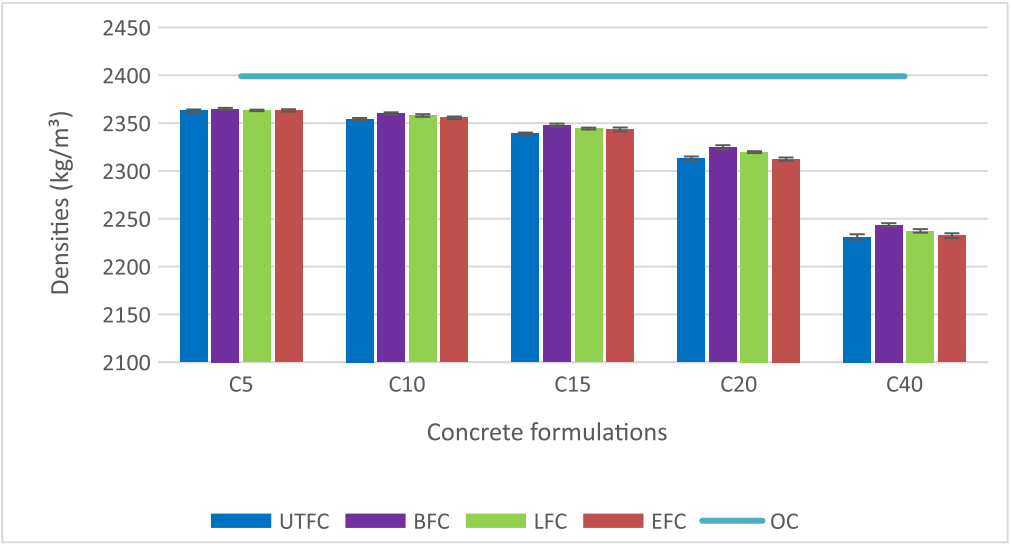

Figure 7. Density of concrete.

Fig. 7 shows that the incorporation of plant fibers leads to a measurable decrease in concrete density. The reference concrete exhibits a density of 2399 kg/m^3. At a low dosage of 5 kg/m^3, the density decreases slightly, reaching 2363–2365 kg/m^3 depending on the fiber treatment, which corresponds to a reduction of about 1.5 %. Increasing the fiber dosage amplifies this effect: at 40 kg/m^3, densities range from 2231 to 2244 kg/m^3, representing a reduction of approximately 7 % compared to the reference mix. This decrease

is primarily attributed to the partial replacement of dense mineral aggregates with fibers of significantly lower density.

3.2. Compressive Strength

Fig. 8 presents the evolution of compressive strength at 3, 7, 28, 90, and 180 days for the different concrete formulations. The reference concrete exhibits strengths of 36.3 MPa at 28 days, increasing to 37.5 MPa at 90 days and 38.5 MPa at 180 days, reflecting the expected hydration of the cement matrix over time.

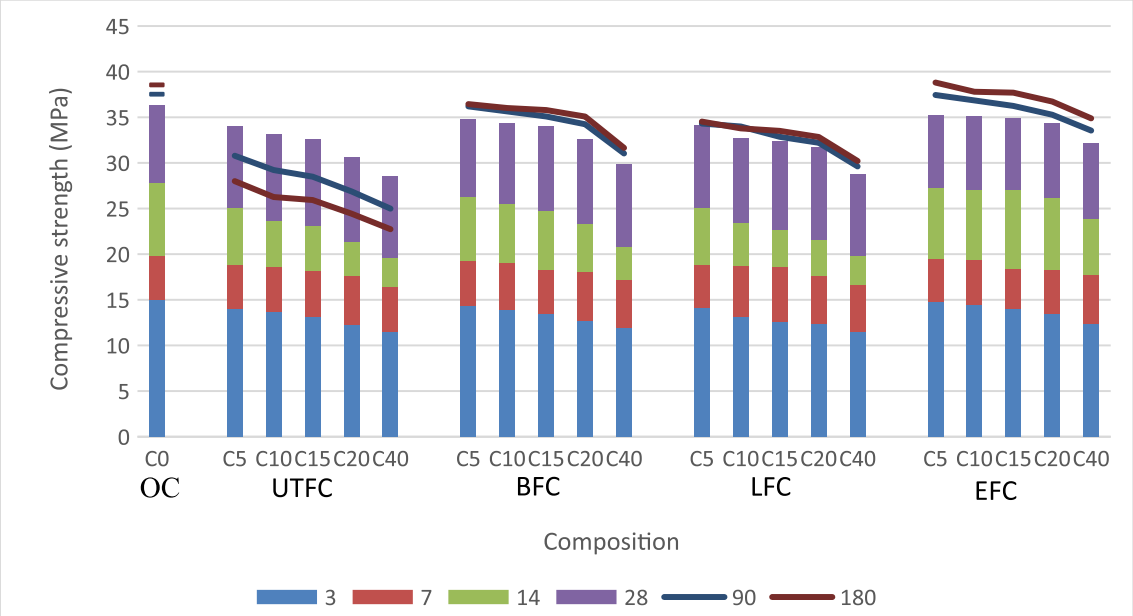

Figure 8. Compressive strength at different ages (S_{dmax} = 0.8 MPa).

For all fiber dosages and treatments, the incorporation of plant fibers leads to a reduction in compressive strength compared to the reference mix. At low dosages, this reduction remains limited, but it becomes more pronounced at higher fiber contents. At a dosage of 40 kg/m^3, UTFC exhibits a 28-day strength of 28.5 MPa, corresponding to a reduction of approximately 21.5 % relative to OC. The effect of fiber treatment is clearly observable: LFC reaches 28.8 MPa (a ≈ 20 % reduction), BFC reaches 29.8 MPa (a ≈ 17 % reduction), while EFC achieves the highest value, 32.2 MPa, representing only an 11 % strength loss at 28 days. These results confirm that surface conditioning of the fibers mitigates the mechanical performance loss caused by fiber addition.

Strength evolution over time further highlights the contrasting behavior between untreated and treated fibers. For UTFC at 40 kg/m^3, strength continues to decrease beyond 28 days, reaching 25.0 MPa at 90 days and 22.7 MPa at 180 days, corresponding to reductions of 33 and 41 % relative to OC. This progressive deterioration suggests fiber degradation within the alkaline cementitious environment. In contrast, concretes incorporating treated fibers exhibit strength gains between 28 and 180 days, similar to the trend observed in OC. At 90 and 180 days, reductions relative to the reference mix range from 21 % for LFC to 17–18 % for BFC and only 9.5–10.5 % for EFC. The long-term improvement observed for treated mixes confirms that fiber treatments enhance durability and stabilize fiber–matrix interactions, preventing the degradation observed in untreated fibers.

The microstructural observations obtained through optical microscopy (Fig. 9) reinforce the mechanical results by illustrating the distinct behaviors of treated and untreated fibers within the cementitious matrix. In specimens containing untreated fibers, several degradation features are apparent. Figs. 9d to 9f show interfacial gaps and fiber–matrix detachment, indicating insufficient adhesion and early debonding. Adjacent voids and the altered morphology of the fibers provide evidence of moisture-driven swelling and subsequent shrinkage, mechanisms known to promote fiber–matrix debonding, as documented in several studies [35–38]. In Fig. 9g, the fiber appears partially cracked and separated from the surrounding matrix, while Fig. 9h shows a longitudinal subdivision of the fiber into individual microfilaments located within a void. Notably, matrix cracking is not observed in these regions, confirming that degradation primarily affects the fibers and their interface rather than the cement paste itself. These mechanisms explain the progressive loss of mechanical performance observed between 28 and 180 days.

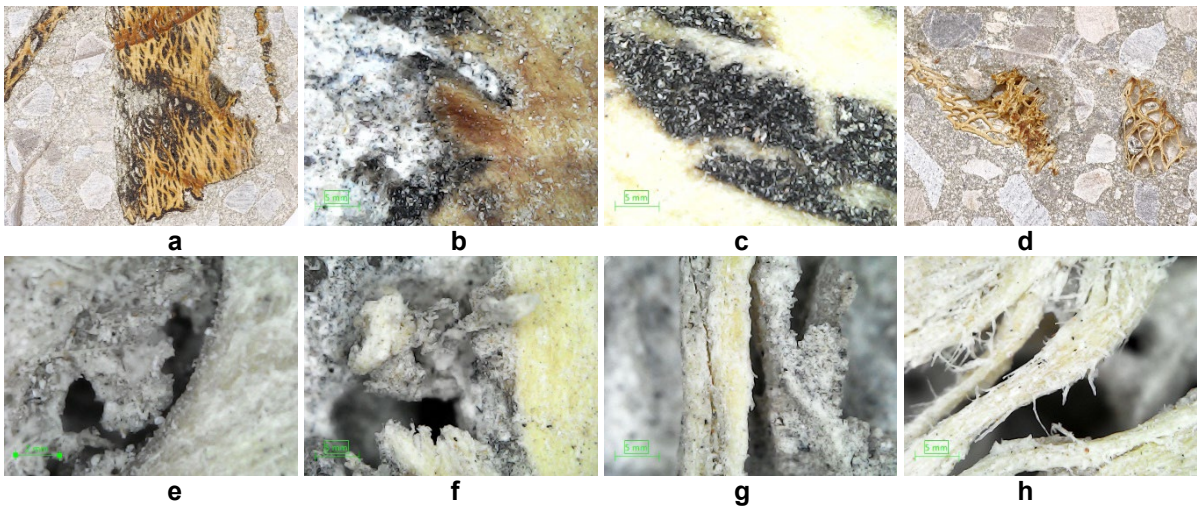

Figure 9. An image of concrete with fibers treated by bitumen (a), microscopic images fibers treated by bitumen in concrete (b, c), an image of concrete with untreated fibers (d), microscopic images of untreated fibers in concrete (e–h).

In contrast, treated fibers exhibit markedly improved interfacial behavior. Figs. 9a to 9c show continuous, well-bonded interfaces without visible detachment or voids. The protective coating limits water ingress and reduces direct exposure to the alkaline pore solution, thereby preventing swelling-induced stresses and preserving interfacial integrity. These stabilized fiber–matrix interactions directly correlate with the improved and sustained compressive strength development observed beyond 28 days in concretes incorporating treated fibers.

3.3. Flexural Strength

The flexural strength results at 3, 7, 28, 90, and 180 days for all mixtures and fiber treatments are presented in Fig. 10. The reference concrete (C0) exhibits a flexural strength of 2.8 MPa at 28 days, increasing slightly to 2.85 MPa at 90 days and 2.92 MPa at 180 days. The introduction of plant fibers significantly improves flexural performance, with the magnitude of enhancement depending on fiber dosage and treatment.

At the lowest dosage (C5), the 28-day flexural strength increases to 7.9–9.7 MPa depending on the treatment, which corresponds to improvements of approximately 180 to 245 % relative to C0. In this case, lime treatment yields the lowest strength values – slightly higher than those of untreated fibers – whereas bitumen and epoxy treatments achieve considerably greater gains. The C15 mixtures exhibit the highest flexural strengths across all curing ages, with 28-day values ranging from 9.2 MPa for lime-treated fibers to 12.1 MPa for epoxy-treated fibers, representing increases of approximately 229 to 333 % relative to the C0. This dosage consistently maximizes the efficiency of fiber incorporation, irrespective of the treatment applied.

At the highest dosage (C40), flexural strengths at 28 days remain markedly higher than those of the C0, with values of 7.6 MPa for untreated fibers, 7.7 MPa for lime treatment, 8.2 MPa for bitumen treatment, and 10.7 MPa for epoxy treatment. Although these absolute values are slightly lower than those at C15, the same hierarchy among treatments is observed, with epoxy remaining the most effective and lime providing the lowest improvement.

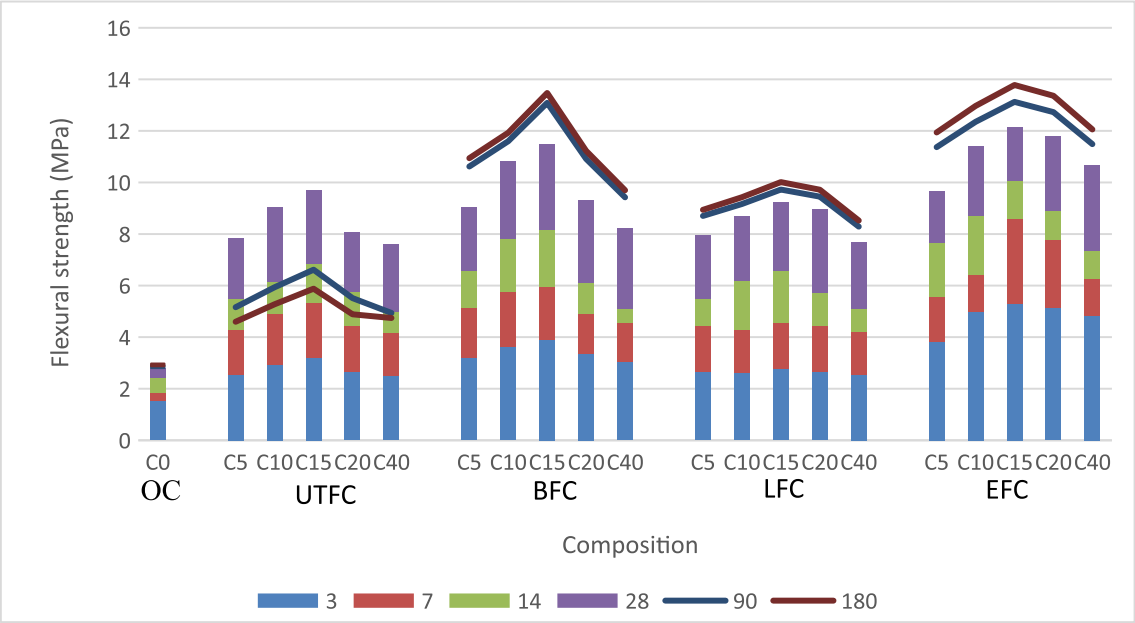

Figure 10. Flexural strength results (S_{dmax} = 0.45 MPa).

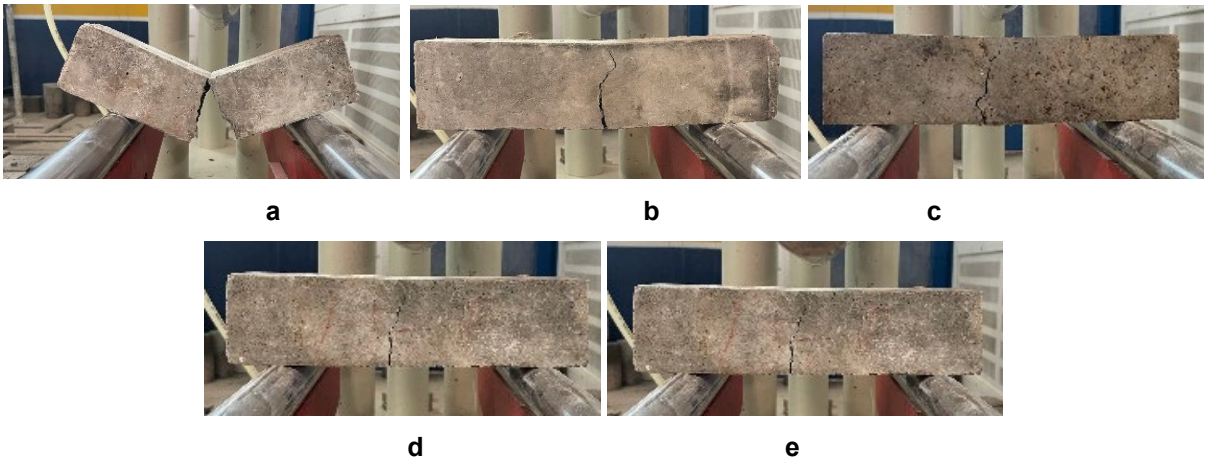

Figure 11. Flexural test: a – OC, b – UTFC, c – BFC, d – LFC, e – EFC.

Post-failure observations presented in Fig. 11 further support these results. The C0 exhibits brittle fracture and complete separation once the maximum load is reached, which is characteristic of unreinforced cementitious materials. In contrast, fiber-reinforced specimens retain partial integrity after failure due to fibers bridging the cracked surfaces and maintaining residual load transfer. This bridging mechanism, widely reported in the literature for cementitious composites incorporating natural fibers [5, 17], explains the substantial increase in flexural strength observed despite the reduction in compressive strength.

Fig. 12 shows SEM images of crack zones in specimens incorporating bitumen-treated fibers. The images reveal fibers fully coated with bitumen and embedded within a continuous and cohesive interface, with no visible separation between the coating and the surrounding cement matrix. These results are consistent with the optical microscopy observations (Fig. 9) and confirm that the protective coating stabilizes the fiber–matrix interface, enhances stress transfer after matrix cracking, and contributes to the sustained flexural performance for up to 180 days.

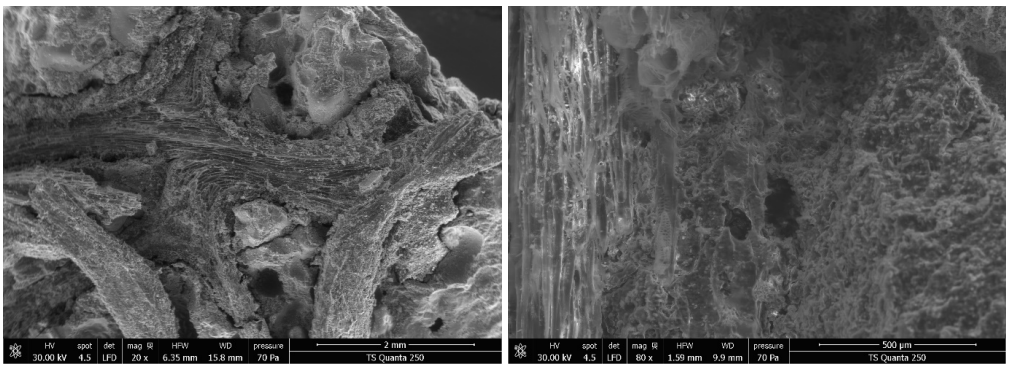

a b

Figure 12. SEM of concrete with fibers treated by bitumen: a – concrete and fibers, b – concrete and fiber interface.

The evolution of the flexural strength relative to the compressive strength provides further insight into the mechanical behavior of the fiber-reinforced concrete. According to Ahmed et al. [39], the relationship between the flexural tensile strength f_R and the compressive strength f_c is frequently expressed in the literature as a power equation in the form $f_R = af_c^n$. Several standards provide formulas for this relationship in the form $f_R = af_c^{0.5}$. For instance, AS 3600 and CSA-A23.3 specify $f_R = 0.6f_c^{0.5}$, while the ACI 363-92 standard proposes a different equation: $f_R = 0.94f_c^{0.5}$ [40]. Fig. 13 presents the flexural tensile strength as a function of the compressive strength for the current study.

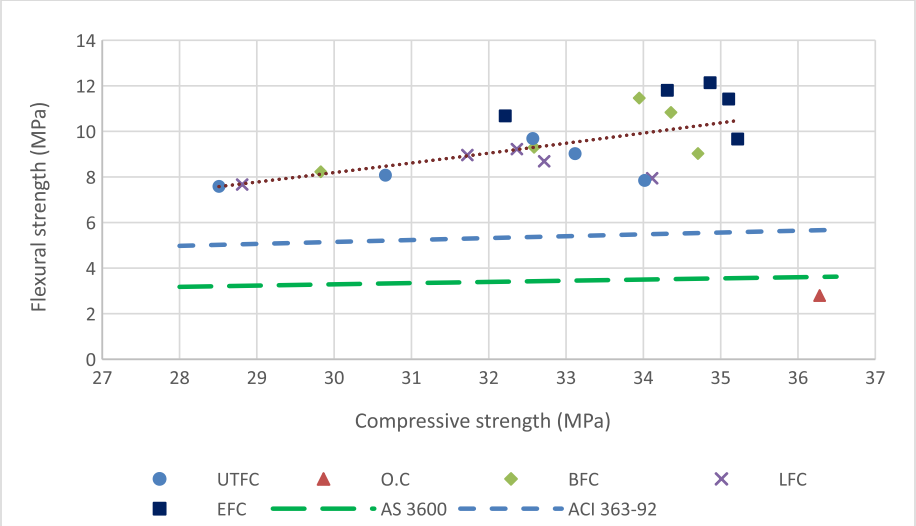

Figure 13. Flexural and compressive strength relationship.

The experimental results exhibit a clear increasing trend of flexural strength relative to compressive strength. A power-law regression performed on the experimental dataset of the fibrous concrete specimens (treated and untreated) yielded the following relationship:

$$f_R = 0.045f_c^{1.533}. \quad (1)$$

The exponent obtained from this regression (1.533) is significantly higher than the value implicitly assumed in current design standards (0.5), indicating that the flexural strength of fibrous concrete increases at a faster rate than predicted by code-based formulations. This behavior reflects the dominant role of the reinforcement and matrix modification mechanisms under flexural loading.

Fig. 13 further shows that the fibrous concrete specimens subjected to epoxy and bitumen treatments are located in the upper-right region of the diagram, corresponding to the highest flexural and compressive strength values. This indicates that these two treatments are the most effective in enhancing overall mechanical performance, particularly in flexure. This superior behavior can be attributed to the improved crack-bridging efficiency of the fibers, combined with enhanced fiber–matrix interaction and reduced

microcrack propagation due to the presence of epoxy or bitumen. By contrast, the non-fibrous concrete is represented by a single data point located in the lower region of the figure, lying very close to the AS 3600 prediction curve. This observation confirms that, in the absence of fiber reinforcement, the standard code-based relationship remains applicable within the investigated strength range.

Overall, the deviation of the fibrous and treated concretes from the normative predictions highlights the limitations of existing flexural–compressive strength relationships when applied to modified concretes. The proposed empirical relationship should therefore be interpreted as representative of fibrous concrete behavior within the investigated domain, with epoxy and bitumen treatments playing a key role in achieving superior flexural performance.

3.4. Splitting Tensile Strength

Fig. 14 shows the evolution of the splitting tensile strength. The values at 28, 90, and 180 days – points at which mechanical properties stabilize – allow for a direct comparison. The C0 records 2.18, 2.22, and 2.27 MPa at these ages. Incorporating fibers significantly enhances tensile performance, with the maximum improvement obtained at a dosage of 15 kg/m^3. At 28 days, C15 exhibits tensile strengths of 7.84 MPa with untreated fibers, 7.47 MPa with lime-treated fibers, 9.28 MPa with bitumen-treated fibers, and 9.82 MPa with epoxy-treated fibers. These values correspond to increases of approximately 260, 243, 326, and 350 % relative to the C0. At later ages, untreated fibers show a decline in tensile strength (5.45 MPa at 90 days and 4.68 MPa at 180 days), whereas lime-, bitumen-, and epoxy-treated fibers maintain or improve their performance, reaching up to 11.17 MPa at 180 days with epoxy treatment. Increasing the fiber dosage to 40 kg/m^3 reduces tensile strength relative to C15 but still yields values higher than those of the C0. At 28 days, C40 reaches 6.14 MPa for untreated fibers, 6.21 MPa for lime-treated fibers, 6.69 MPa for bitumen-treated fibers, and 8.64 MPa for epoxy-treated fibers. This confirms that excessive fiber content induces fiber clustering and matrix discontinuities, limiting mechanical efficiency [41].

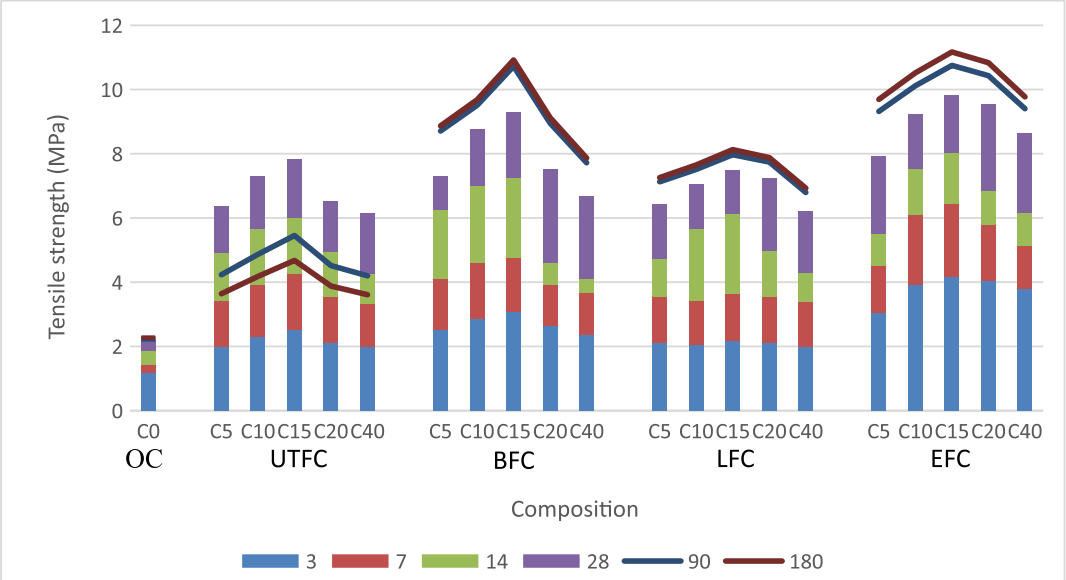

Figure 14. Splitting tensile test results.

The failure patterns support the mechanical observations. The C0 splits abruptly into two detached halves, whereas the fiber-reinforced specimens remain connected after testing, with the cracks bridged by fibers. Manual separation reveals fracture surfaces containing randomly distributed prickly pear fibers (Fig. 15), most of which underwent fracture rather than pullout. This indicates strong fiber–matrix adhesion, particularly in the treated-fiber mixtures.

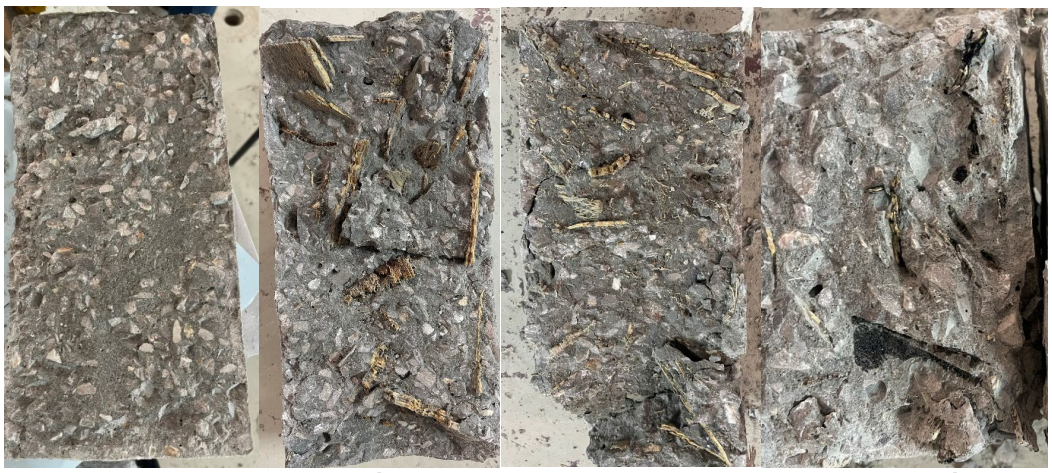

a b c d

Figure 15. Splitting tensile test results: a – OC, b – EFC, c – LFC, d – BFC.

3.5. Thermal Characteristics

This section examines the influence of prickly pear fibers and their surface treatments on the thermal behavior of concrete. Three fundamental properties are considered: thermal conductivity, specific heat capacity, and thermal diffusivity. These parameters are intrinsically linked to the microstructure of cementitious composites and are affected by the addition of low-conductivity plant fibers.

3.5.1. Thermal conductivity

Thermal conductivity governs the heat transfer capacity of cementitious composites and is strongly influenced by microstructural variables such as moisture content, aggregate volume fraction, pore connectivity, and the nature of the embedded inclusions. Fig. 16 reports the evolution of thermal conductivity as a function of fiber dosage and surface treatment. A monotonic reduction is observed with increasing fiber content, with values decreasing from 1.91 W/(m·K) for the reference mixture to a range of 1.04–1.14 W/(m·K) at 40 kg/m^3, depending on the treatment; this corresponds to a decrease of approximately 40–45 %. Given that common mineral aggregates exhibit conductivities between 1.16 and 8.6 W/(m·K) [42], such reductions are consistent with the replacement of higher-conductivity constituents with materials of lower intrinsic conductivity.

The decrease in effective conductivity can be explained by considering the microstructural role of the fibers. Materials with low intrinsic conductivity or highly porous internal structures act as insulating inclusions that alter the topology of conduction pathways. With an intrinsic conductivity of approximately 0.057 W/(m·K) and a naturally porous morphology, prickly pear fibers reduce the continuity of solid heat transfer routes within the matrix and, therefore, behave as thermally insulating inclusions.

To assess these experimental results, they were compared with classical homogenization models formulated for isotropic two-phase composites. The cementitious matrix is considered the continuous phase with conductivity λ_m, while the prickly pear fibers constitute the dispersed phase with conductivity λ_f, and respective volume fractions V_m and V_f satisfying $V_m + V_f = 1.$ Under these assumptions, the extremal estimates of effective conductivity are provided by the Voigt and Reuss bounds [43]:

$$\lambda_V = V_m \lambda_m + V_f \lambda_f; \tag{2}$$

$$\lambda_R = \left(\frac{V_m}{\lambda_m} + \frac{V_f}{\lambda_f} \right)^{-1}. \tag{3}$$

Eqs. (2) and (3) represent the maximal conductivity corresponding to a parallel-phase configuration and the minimal conductivity associated with a series configuration, respectively. Although these idealized morphologies are not strictly representative of the present composite, they provide an essential admissible interval for assessing the effective thermal behavior. A more physically constrained prediction is given by the Hashin–Shtrikman bounds, which are derived from variational principles and are applicable to isotropic composites with arbitrarily shaped inclusions [44]:

$$\lambda_{HS+} = \lambda_m + \frac{V_f}{\frac{1}{\lambda_f - \lambda_m} + \frac{V_m}{3\lambda_m}}; \tag{4}$$

$$\lambda_{HS-} = \lambda_f + \frac{V_m}{\frac{1}{\lambda_m - \lambda_f} + \frac{V_f}{3\lambda_f}}. \tag{5}$$

These bounds (Eqs. (4) and (5)) define the narrowest theoretically admissible interval for the effective conductivity of an isotropic two-phase material. The measured values remain well below the Voigt limit while staying above the Reuss bound; however, in several cases, they lie below the Hashin–Shtrikman lower limit. This departure indicates that the actual microstructure – featuring elongated pores, anisotropic fiber arrangements, and potentially a third interfacial phase – creates a higher thermal tortuosity than assumed in classical isotropic models.

The slightly higher conductivities measured for the treated fibers are consistent with improved interfacial bonding. Enhanced adhesion reduces the volume of interfacial air voids – the conductivity of which is extremely low – increasing the continuity of solid heat transfer paths and, consequently, raising the effective thermal conductivity.

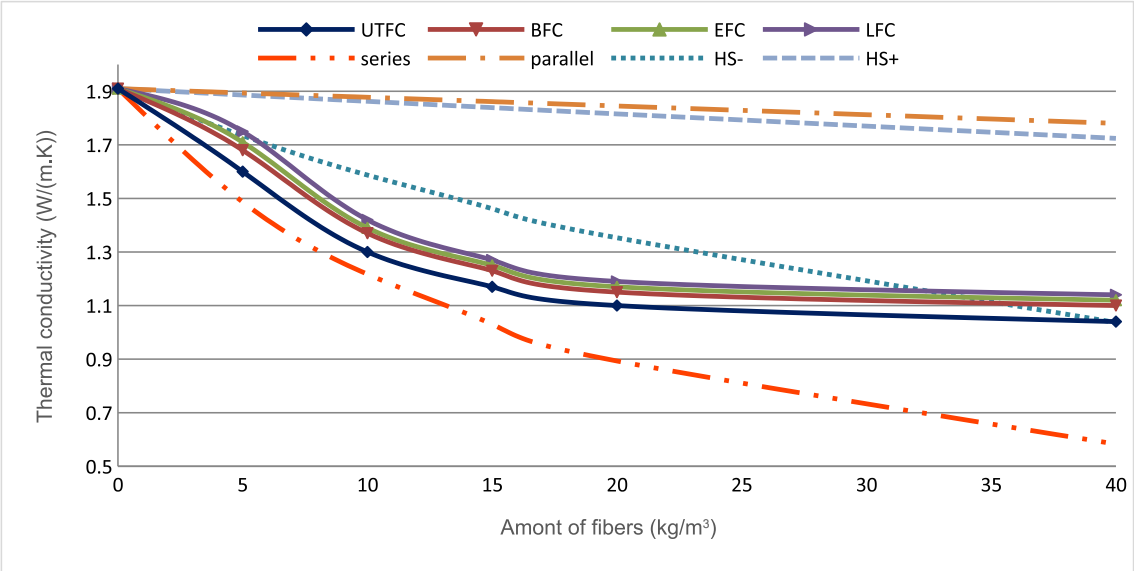

Figure 16. Thermal conductivity of concrete incorporating treated fibers (S_{dmax} = 0.015 W/(m.K)).

3.5.2. Specific heat

Specific heat capacity (c_p) represents the amount of heat required to increase the temperature of a unit mass by one degree [40]. In cementitious materials, this property depends on the thermal behavior of the constituent solid phases. Prickly pear fibers contain high fractions of cellulose, hemicellulose, and lignin, which exhibit greater heat capacities than mineral aggregates. Their cellular microstructure, rich in voids and capable of retaining bound water, also contributes to increasing the heat storage capacity of the composite.

Fig. 17 shows that the incorporation of fibers leads to a systematic increase in the specific heat capacity for all treatment types. When considering only the reinforced mixtures (5–40 kg/m^3), the evolution of c_p with fiber dosage is quasi-linear. This behavior is consistent with a progressive increase in the volumetric fraction of organic phases, whose intrinsic heat capacity is significantly higher than that of the mineral matrix. At 40 kg/m^3, the specific heat capacity rises by approximately 22–24 % compared to the C0.

Differences between treatment types follow a consistent hierarchy across all dosages. EFC systematically exhibits the highest c_p values, with an increase of approximately 1–3 % relative to UTFC. This enhancement is primarily linked to the stabilization of the fiber surface by the epoxy coating, which

prevents fiber degradation and preserves a durable and continuous contact with the cement matrix. LFC shows slightly lower values, typically within 0.5–2 % lower than those of EFC, reflecting the partial mineralization induced by the lime treatment and the improved compatibility of the fibers with the surrounding matrix. UTFC presents the lowest c_p values among the reinforced mixtures. This is attributed to the absence of surface modification, which results in weaker fiber–matrix adhesion and a less efficient contribution of the fibers to the overall thermal storage capacity. Collectively, the results indicate that both fiber dosage and surface treatment contribute to variations in the specific heat capacity of the composite, with the dominant effect being associated with the fiber fraction.

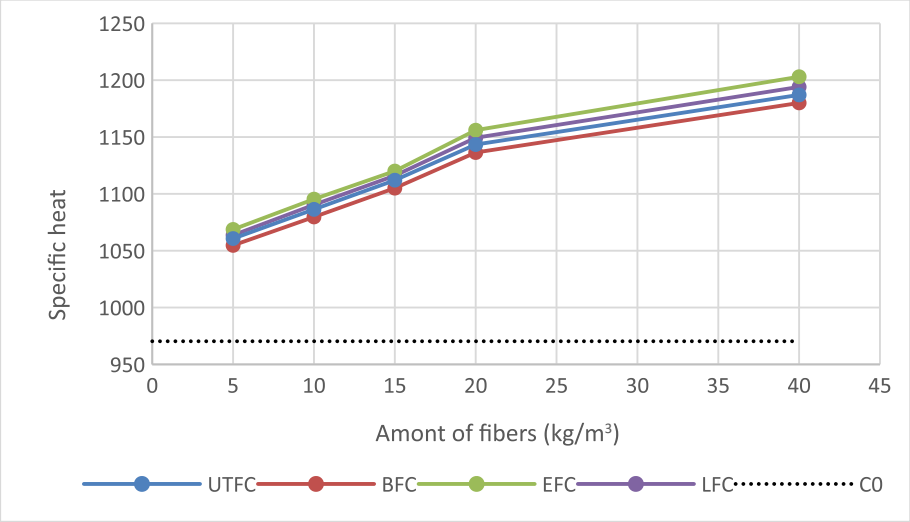

Figure 17. Specific heat of concrete incorporating treated fibers (S_{dmax} = 4.5 J/(kg.K)).

3.5.3. Thermal diffusivity

Thermal diffusivity α quantifies the rate at which heat propagates through a material and is defined as:

$$a = \frac{\lambda}{\rho c_p}\left(\mathrm{m}^2/\mathrm{s}\right), \tag{6}$$

where λ represents the thermal conductivity (W/(m.K)), ρ is the density (kg/m³), and c_p is the specific heat capacity (J/(kg·K)).

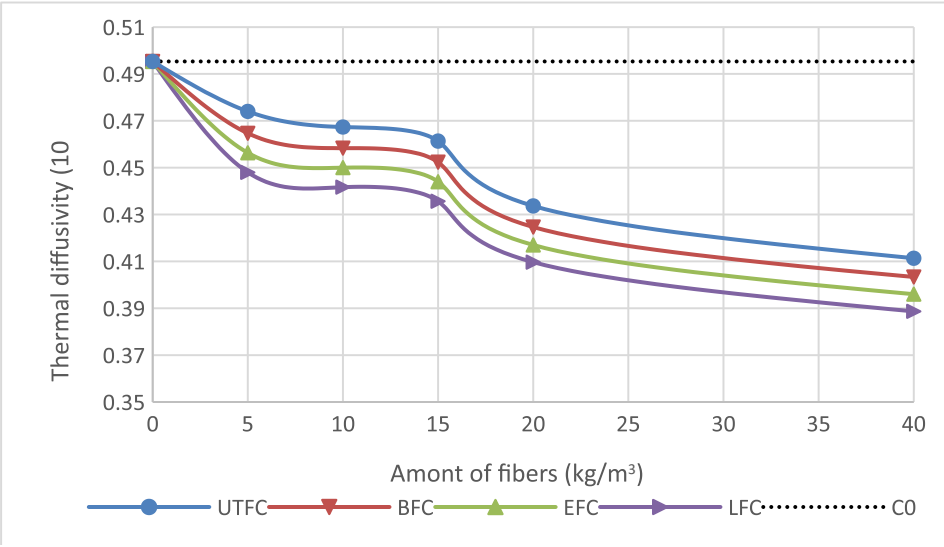

Figure 18. Thermal diffusivity of concrete incorporating treated fibers (S_{dmax} = 4×10^{-9} m^2/s).

Fig. 18 shows that thermal diffusivity decreases consistently with increasing fiber content, regardless of the treatment applied. The C0 presents a diffusivity of 0.50 mm²/s. At 40 kg/m³, the values decrease to

0.41 mm²/s for UTFC, 0.40 mm²/s for BFC, 0.40 mm²/s for EFC, and 0.39 mm²/s for LFC, representing reductions of approximately 18–22 %.

This reduction stems primarily from microstructural modifications induced by the fibers and their treatments. The dominant factor is the marked decrease in thermal conductivity λ: the fibers and their internal air cavities lower the effective conductivity of the composite by about 40–45 % at 40 kg/m³, directly reducing the numerator of α. A secondary effect arises from changes in the volumetric heat capacity ρc_p: fiber incorporation increases c_p by roughly 22–24 % while slightly reducing the bulk density (≈7 %), which increases the denominator of α and contributes further to the decrease in diffusivity. Although the reduction in density alone would tend to raise α, the combined effect of reduced conductivity and increased heat capacity overrides this tendency, producing the observed decline.

Differences among treatments remain limited but systematic. Epoxy- and bitumen-treated fibers lead to the lowest diffusivities at equivalent dosages, followed by lime-treated fibers, which slightly outperform untreated ones at higher fiber contents. These distinctions reflect the influence of surface treatments on fiber integrity and interfacial contact: epoxy and bitumen create more stable coatings that limit interfacial voids and maintain the insulating character of the fibers, whereas lime treatment induces partial mineralization that modifies thermal behavior to a lesser extent. The overall decrease in diffusivity shows that the presence of prickly pear fibers enhances the material's thermal inertia by simultaneously restricting heat transfer and increasing its heat storage capacity.

4. Conclusion

This study investigated the long-term mechanical and thermal performance of concrete reinforced with prickly pear fibers, comparing untreated fibers with three coatings: epoxy, bitumen, and lime. The following findings highlight the main contributions of this research:

1. Surface conditioning of the fibers significantly mitigates the loss of compressive strength; notably, the epoxy treatment limits the 28-day reduction to only 11 %, compared to a 21.5 % loss for untreated fibers at a dosage of 40 kg/m³.
2. Long-term durability is critically enhanced by these treatments. While untreated fibers degrade in the alkaline cementitious environment (reaching a 41 % strength loss at 180 days), treated fibers maintain stable performance, with strength reductions relative to the reference mix limited to 10.5–21 % at the same age.
3. An optimal dosage of 15 kg/m³ maximizes mechanical efficiency, yielding peak increases in flexural and splitting tensile strengths at 28 days of up to 333 and 350 %, respectively (obtained with epoxy-treated fibers).
4. High fiber content (40 kg/m³) leads to a relative decline in mechanical performance compared to the 15 kg/m³ dosage due to fiber clustering and matrix discontinuities; however, values remain significantly higher than those of the plain reference concrete (0 kg/m³) in both flexural and tensile strength.
5. Thermal properties are substantially improved with increasing fiber content. A dosage of 40 kg/m³ achieves a 40–45 % reduction in thermal conductivity and a 22–24 % increase in specific heat capacity. This enhancement is driven by the higher volumetric fraction of organic phases, with epoxy-treated concrete showing the highest thermal storage capacity due to stabilized fiber-matrix adhesion.

In summary, pretreating prickly pear fibers – particularly with epoxy – overcomes the durability limitations typically associated with natural fibers, offering a high-performance, sustainable alternative with reliable long-term properties.

References

1. Rachedi, M., Kriker, A. Thermal Properties of Plaster Reinforced with Date Palm Fibers. Civil and Environmental Engineering. 2020. 16(2). Pp. 259–266. DOI: 10.2478/cee-2020-0025
2. Özkılıç, Y.O., Beskopylny, A.N., Stel'makh, S.A., Shcherban, E.M., Mailyan, L.R., Meskhi, B., Madenci, E. Lightweight expanded-clay fiber concrete with improved characteristics reinforced with short natural fibers. Case Studies in Construction Materials. 2023. 19. Article no. e02367. DOI: 10.1016/j.cscm.2023.e02367
3. Marvila, M.T., Rocha, H.A., de Azevedo, A.R.G., Colorado, H.A., Zapata, J.F., Vieira, C.M.F. Use of natural vegetable fibers in cementitious composites: concepts and applications. Innovative Infrastructure Solutions. 2021. 6. Article no. 180. DOI: 10.1007/s41062-021-00551-8

4. Arcila Londoño, S.L., Garcia Chumacero, J.M., Villegas Granados, L.M., Damiani Lazo, C.A., Arriola Carrasco, G.G., Villena Zapata, L.I., Idrogo Perez, C.A. Valorization of treated bamboo fiber in the mechanical strength and durability of concrete. Innovative Infrastructure Solutions. 2025. 10(6). Article no. 219. DOI: 10.1007/s41062-025-02022-w
5. Kammoun, Z., Trabelsi, A. A high-strength lightweight concrete made using straw. Magazine of Concrete Research. 2020. 72(9). Pp. 460–470. DOI: 10.1680/jmacr.19.00225
6. Lahouioui, M., Ben Arfi, R., Fois, M., Ibos, L., Ghorbal, A. Investigation of Fiber Surface Treatment Effect on Thermal, Mechanical and Acoustical Properties of Date Palm Fiber-Reinforced Cementitious Composites. Waste and Biomass Valorization. 2020. 11. Pp. 4441–4455. DOI: 10.1007/s12649-019-00745-3
7. Sonebi, M., Abdalqader, A., Amziane, S., Dvorkin, L., Ghorbel, E., Kenai, S., Khatib, J., Lushnikova, N., Perrot, A. Trends and opportunities of using local sustainable building materials in the Middle East and North Africa region. RILEM Technical Letters. 2022. 7. Pp. 127–138. DOI: 10.21809/rilemtechlett.2022.169
8. Charai, M., Mezrhab, A., Moga, L., Karkri, M. Hygrothermal, mechanical and durability assessment of vegetable concrete mixes made with Alfa fibers for structural and thermal insulating applications. Construction and Building Materials. 2022. 335. Article no. 127518. DOI: 10.1016/j.conbuildmat.2022.127518
9. Abdelouahed, A., Kechkar, C., Hebhoub, H., Merzoud, M., Enhancing the Performance and Durability of Eco-Friendly Mortar with Diss Fibers (Ampelodesmos *mauritanicus*). Revue des Composites et des Matériaux Avancés – Journal of Composite and Advanced Materials. 2023. 33(4). Pp. 219–226. DOI: 10.18280/rcma.330402
10. Ramasubramani, R., Gunasekaran, K. Study on plastic shrinkage of coconut shell concrete slab made with M-sand. Innovative Infrastructure Solutions. 2022. 7(1). Article no. 12. DOI: 10.1007/s41062-021-00614-w
11. Muñoz Pérez, S.P., Alarcón Peltroche, M., Eugenio Pachas, E.T., Villena Zapata, L.I., Bernal Izquierdo, A.P., Rodriguez Lafitte, E.D., García Chumacero, J.M. Effect of Peruvian sisal fiber on the mechanical and microstructural strength of concrete. Innovative Infrastructure Solutions. 2025. 10. Article no. 257. DOI: 10.1007/s41062-025-02061-3
12. Hasan, N.M.S., Sobuz, M.H.R., Shaurdho, N.M.N., Basit, M.A., Paul, S.C., Meraz, M.M., Miah, M.J. Investigation of Lightweight and Green Concrete Characteristics Using Coconut Shell Aggregate as a Replacement for Conventional Aggregates. International Journal of Civil Engineering. 2024. 22(1). Pp. 37–53. DOI: 10.1007/s40999-023-00881-x
13. Tahenti, B., Trabelsi, A., Kammoun, Z. Enhancing concrete's ballistic impact resistance using Alfa fiber. International Journal of Protective Structures. 2024. 16(2). Pp. 529–547. DOI: 10.1177/20414196241271452
14. Paisig Saucedo, B.Y., Muñoz Pérez, S.P., García Chumacero, J.M., Sánchez Diaz, E., Villena Zapata, L.I., Diaz Ortiz, E.A., Rodriguez Laffite, E.D., Zuloeta, O.C., Ramos Brast, C.E. Experimental and microstructural study of concrete reinforced with maguey fiber: Peruvian case. Innovative Infrastructure Solutions. 2024. 9(12). Article no. 451. DOI: 10.1007/s41062-024-01761-6
15. Ren, G., Yao, B., Huang, H., Gao, X. Influence of sisal fibers on the mechanical performance of ultra-high performance concretes. Construction and Building Materials. 2021. 286. Article no. 122958. DOI: 10.1016/j.conbuildmat.2021.122958
16. Saad, M., Agwa, I.S., Abdelsalam, B., Amin, M. Improving the brittle behavior of high strength concrete using banana and palm leaf sheath fibers. Mechanics of Advanced Materials and Structures. 2022. 29(4). Pp. 564–573. DOI: 10.1080/15376494.2020.1780352
17. Kammoun, Z., Trabelsi, A. Development of lightweight concrete using prickly pear fibres. Construction and Building Materials. 2019. 210. Pp. 269–277. DOI: 10.1016/j.conbuildmat.2019.03.167
18. Trabelsi, A., Kammoun, Z. Mechanical properties and impact resistance of a high-strength lightweight concrete incorporating prickly pear fibres. Construction and Building Materials. 2020. 262. Article no. 119972. DOI: 10.1016/j.conbuildmat.2020.119972
19. Vo, L.T., Navard, P. Treatments of plant biomass for cementitious building materials – A review. Construction and Building Materials. 2016. 121. Pp. 161–176. DOI: 10.1016/j.conbuildmat.2016.05.125
20. Santos, S.F.D., Tonoli, G.H.D., Mejia, J.E.B., Fiorelli, J., Savastano Jr, H. Non-conventional cement-based composites reinforced with vegetable fibers: A review of strategies to improve durability. Materiales de Construcción. 2015. 65(317). Article no. e041. DOI: 10.3989/mc.2015.05514
21. Traoré, Y., Messan, A., Tsobnang, F., Gérard, J. Propriétés mécaniques d'un béton de granulats légers à base de coques de noix de palme traitées. 33èmes rencontres universitaires de Génie Civil. Université de Pau et des pays de l'Adour, 2015. Pp. 27–29.
22. Sellami, A., Merzoud, M., Amziane, S. Improvement of mechanical properties of green concrete by treatment of the vegetals fibers. Construction and Building Materials. 2013. 47. Pp. 1117–1124. DOI: 10.1016/j.conbuildmat.2013.05.073
23. Hussain, T.H., Alwan, A.S., Manea, A.K., Naje, A.S., Al-Zubaidi, H.A.M. Mechanical and Microstructural Properties of Lime-Treated Palmdate Fiber Cement Composites for Sustainable Development. Journal of Green Engineering. 2021. 11(2). Pp. 1767–1777. DOI: 10.13140/RG.2.2.35215.30881
24. Bederina, M., Gotteicha, M., Belhadj, B., Dheily, R. M., Khenfer, M.M., Queneudec, M. Drying shrinkage studies of wood sand concrete – Effect of different wood treatments. Construction and Building Materials. 2012. 36. Pp. 1066–1075. DOI: 10.1016/j.conbuildmat.2012.06.010
25. Nozahic, V., Amziane, S. Influence of sunflower aggregates surface treatments on physical properties and adhesion with a mineral binder. Composites Part A: Applied Science and Manufacturing. 2012. 43(11). Pp. 1837–1849. DOI: 10.1016/j.compositesa.2012.07.011
26. Bederina, M., Belhadj, B., Ammari, M.S., Gouilleux, A., Makhloufi, Z., Montrelay, N., Quéneudéc, M. Improvement of the properties of a sand concrete containing barley straws – Treatment of the barley straws. Construction and Building Materials. 2016. 115. Pp. 464–477. DOI: 10.1016/j.conbuildmat.2016.04.065
27. Arfien Khan, M.A., Saha, M.S., Sultana, S., Mustafi, S. Possible Use of Coal Fly Ash for Portland Cement Clinker Synthesis. Iranian Journal of Science and Technology, Transactions of Civil Engineering. 2026. 50. Pp. 1531–1539. DOI: 10.1007/s40996-025-01887-2
28. Burga Bustamante, G., Muñoz Pérez, S.P., García Chumacero, J.M., Sánchez Diaz, E., Ruiz Pico, A.A., Rodriguez Laffite, E.D., Damiani Lazo, C.A., Ramos Brast, C.E. Evaluation of the mechanical behavior of concrete with the addition of dry corn fiber. Innovative Infrastructure Solutions. 2025. 10(1). Article no. 29. DOI: 10.1007/s41062-024-01839-1
29. Shen, N.J., Hasan, M. Transforming waste into stability: improving the soft clay soil with polyethylene terephthalate (PET) column as a sustainable solution. Journal of Engineering and Applied Science. 2025. 72(1). Article no. 52. DOI: 10.1186/s44147-025-00620-0

30. Shen, N.J., Hasan, M. Installation of polyethylene terephthalate (PET) columns to promote the soil-bearing capacity of soft kaolin clay. Journal of King Saud University – Engineering Sciences. 2025. 37(4). Article no. 14. DOI: 10.1007/s44444-025-00011-z
31. Sabtain, B., Farooq, R., Shafique, B., Ranjha, M., Mahmood, S., Mueen-Ud-Din, G., Irfan, S., Shehzadi, K., Rubab, Q., Asad, L., Ishfaq, M. A Narrative Review on the Phytochemistry, Nutritional Profile and Properties of Prickly Pear Fruit. Open Access Journal of Biogeneric Science and Research. 2021. 7(2). DOI: 10.46718/JBGSR.2021.07.000164
32. Alam-Eldein, S.M., Ennab, H.A., Omar, A.E.D.K., Omar, A.A. Harvest and Postharvest Technology of *Opuntia* spp. Opuntia spp.: Chemistry, Bioactivity and Industrial Applications. Springer. Cham, 2021. Pp. 219–255. DOI: 10.1007/978-3-030-78444-7_10
33. Mannai, F., Ammar, M., Yanez, J.G., Elaloui, E., Moussaoui, Y. Cellulose fiber from Tunisian Barbary Fig "*Opuntia ficus-indica*" for papermaking. Cellulose. 2016. 23(3). Pp. 2061–2072. DOI: 10.1007/s10570-016-0899-9
34. Castellano, J., Marrero, M.D., Ortega, Z. *Opuntia* Fiber and Its Potential to Obtain Sustainable Materials in the Composites Field: A Review. Journal of Natural Fibers. 2022. 19(15). Pp. 10053–10067. DOI: 10.1080/15440478.2021.1993479
35. Singh, A.A. Effect of Water Absorption on Interface and Tensile Properties of Jute Fiber Reinforced Modified Polyethylene Composites Developed by *Palsule* Process. Applied Polymer Composites. 2013. 1(2). Pp. 113–124.
36. Alomayri, T., Assaedi, H., Shaikh, F.U.A., Low, I.M. Effect of water absorption on the mechanical properties of cotton fabric-reinforced geopolymer composites. Journal of Asian Ceramic Societies. 2014. 2(3). Pp. 223–230. DOI: 10.1016/j.jascer.2014.05.005
37. Mohammed, M., Jawad, A.J.A.M., Mohammed, A.M., Oleiwi, J.K., Adam, T., Osman, A.F., Dahham, O.S., Betar, B.O., Gopinath, S.C.B., Jaafar, M. Challenges and advancement in water absorption of natural fiber-reinforced polymer composites. Polymer Testing. 2023. 124. Article no. 108083. DOI: 10.1016/j.polymertesting.2023.108083
38. Haigh, R., Sandanayake, M., Bouras, Y., Vrcelj, Z. A review of the mechanical and durability performance of kraft-fibre reinforced mortar and concrete. Construction and Building Materials. 2021. 297. Article no. 123759. DOI: 10.1016/j.conbuildmat.2021.123759
39. Ahmed, M., Hadi, K.M.E., Hasan, M.A., Mallick, J., Ahmed, A. Evaluating the co-relationship between concrete flexural tensile strength and compressive strength. International Journal of Structural Engineering. 2014. 5(2). Pp. 115–131. DOI: 10.1504/IJSTRUCTE.2014.060902
40. Sankar, B., Ramadoss, P. Experimental and Statistical Investigations on Alccofine Based Ternary Blended High-performance Concrete. International Journal of Engineering. 2022. 35(8). Pp. 1629–1640. DOI: 10.5829/ije.2022.35.08b.19
41. Li, Z., Li, J., Lu, W., Zhang, Y. Research Progress and Application Prospects of Plant Fibers in Geopolymer Concrete: A Review. Materials. 2025. 18(10). Article no. 2342. DOI: 10.3390/ma18102342
42. Daza-Badilla, L., Gómez, R., Díaz-Noriega, R., Avudaiappan, S., Skrzypkowski, K., Saavedra-Flores, E. I., Korzeniowski, W. Thermal Conductivity in Concrete Samples with Natural and Synthetic Fibers. Materials. 2024. 17(4). Article no. 817. DOI: 10.3390/ma17040817
43. Bessenouci, M.Z., Triki, N.B., Khelladi, S., Draoui, B., Abene, A. The Apparent Thermal Conductivity of Pozzolana Concrete. Physics Procedia. 2011. 21. Pp. 59–66. DOI: 10.1016/j.phpro.2011.10.010
44. Mydin, M.A.O. Assessment of Thermal Conductivity, Thermal Diffusivity and Specific Heat Capacity of Lightweight Aggregate Foamed Concrete. Jurnal Teknologi. 2016. 78(5). Pp. 477–482. DOI: 10.11113/jt.v78.8374

Information about the authors:

***Imeen Tarkhani**, PhD*
E-mail: imeentarkhani16@gmail.com

***Zied Kammoun**,*
ORCID: https://orcid.org/0000-0002-3000-661X
E-mail: kammounzied@yahoo.fr

***Abderraouf Trabelsi**,*
E-mail: abederraouftrabelsi@gmail.com

***Hichem Smaoui**,*
E-mail: hismaoui@yahoo.fr

Received 10.08.2025. Approved after reviewing 14.01.2026. Accepted 14.01.2026.

Magazine of Civil Engineering

ISSN 2712-8172

journal homepage: http://engstroy.spbstu.ru/

Research article

UDC 624

DOI: 10.34910/MCE.141.7

Finite element analysis of the effect reinforced concrete beams under pure torsion strengthened by SIFCON jacketing with different fiber types

M.J. Mohammed [1]✉ , ***A.A. Al-Azzawi***[2]

[1]*Department of Civil Engineering, College of Engineering, Al-Nahrain University, Baghdad, Iraq*
[2]*Department of Forensic Engineering, Higher Institute of Forensic Sciences, Al-Nahrain University, Jadriya, Baghdad, Iraq*

✉ *st.Mohammed.g.m.f@nahrainuniv.edu.iq*

Keywords: pure torsion, slurry infiltrated fiber concrete, SIFCON, strengthening layer, hybrid fibers, finite element.

Abstract. In recent years, emphasis has been made on studying the effect and behavior of beams under pure torsion, which required the emergence of different types of strengthening. Because of concrete's poor tensile strength, fiber can be added with high or low percentages. This paper aimed to study the torsional behavior of reinforced concrete beams and the jacketing technique. Reinforced beams were strengthened using a layer of Slurry Infiltrated Fiber Concrete (SIFCON) and with different types of fiber. SIFCON is a special type of fiber concrete that contains a high percentage of fiber. It is an effective substance used for repair and strengthening. The finite element (FE) method through ABAQUS software is carried out to test seven samples previously tested experimentally. Reasonable agreement was acquired between the ultimate torque and angle of twist of FE numerical models and found experimentally, in which the value of the mean and coefficient of variations were 0.998 and 0.247 %, respectively for the ultimate torque, whilst for the angle of twist, the value of the mean and coefficient of variation were 0.945 and 3.823 %, respectively. The effect of increasing longitudinal reinforcement ratio is found to be higher for torsional unreinforced beams and marginal for other beams for the selected range of reinforcement ratio or diameter (8 to 12 mm bar diameter). The effect of thickness of the SIFCON layer on the behavior is found to be higher for steel fiber SIFCON and lower for hybrid fiber SIFCON jacketing. The effect of hybrid fiber on behavior is studied.

Citation: Mohammed, M.J., Al-Azzawi, A.A. Finite element analysis of the effect reinforced concrete beams under pure torsion strengthened by SIFCON jacketing with different fiber types. Magazine of Civil Engineering. 2026. 19(1). Article no. 14107. DOI: 10.34910/MCE.141.7

1. Introduction

Reinforced concrete (RC) beams are one of the fundamentals that transfer building loads, so it is necessary to study their properties and behavior. Buildings made of concrete are prone to torsion [1]. When exposed to extreme torsion, concrete beams can lose strength, the concrete cover can break off, crack, and less efficient steel reinforcing or collapses the structure. So, it is necessary to find a way to strengthen beams. Effective strengthening may be performed on concrete beams for them to increase their structural performance. Two methods can be subjected to strengthening RC beams [1] internal by using fiber to cast beams or cast layer within (2) externally by using a precast layer or by casting a strengthening layer on beams. This method's efficiency enhances the torsional capacity, Slurry Infiltrated Fiber Concrete (SIFCON) is included in fiber at a volume-relative level of 4–20 % [2, 3].

Ali [4] studied finite element (FE) analysis for beams under pure torsion; she studied RC beams strengthened with near-surface mounted (NSM) reinforcement bars by using ABAQUS. Results from the numerical analysis were in good agreement with those from the experimental investigation. The failure and final torque patterns and processes showed this convergence. The ultimate torque increased by approximately 18.06 % for beams with torsional reinforcement. At the same time, it increased by about 9.62 % for beams without torsional reinforcement strengthening with four faces of double NSM U stirrups. When strengthening configurations with four faces of NSM closed stirrups and three faces of NSM stirrups (U-shape) at a spacing of 130 mm, respectively. Beams with torsional reinforcement were identified as the most effective system for strengthening RC beams of torsion resistance.

Le and Coa [5] investigated the torsional effect of circular steel tubes filled with concrete (CFST) under pure torsion numerically. CFST numerical models were created in ABAQUS which describe the mechanism of torsional stress transmission from steel plates to CFST. The parametric study's findings showed that while concrete avoided buckling and enhanced the efficiency of the steel tubes, its compressive strength only slightly increased the torsional moment capacity of the CFST. The yield torsional moment of the CFST rose by around 50 % when the yield strength of steel increased from 235 to 420 MPa.

Majed et al. [6] used of composite materials to reinforce structural components has gained a lot of interest. Under pure torsion, the response of rectangular RC reinforced with fiber-reinforced polymer (FRP) laminates was examined numerically and verified. Parametric research was conducted, taking into account variables including the amount of FRP plies, the compressive strength of the concrete, and the orientation of FRP strips. The findings demonstrated that by raising the number of FRP plies and the compressive strength of the concrete, the torsional capacity could be improved. Furthermore, no discernible difference in the torsional strength of RC beams reinforced with a 45 or 90 ° FRP laminate was found.

The failure mode of RC structural members retrofitted by FRP can be changed, while torsion plays a vital role in loading. Ganganagoudar et al. [7] presented an analytical and FE study to propose a modified softened membrane model for torsion (SMMT-FRP). Their results proved an increase in structural behavior such as post-cracking stiffness, ultimate strength, and localized damage of RC retrofitted members, also showed agreement with Jain et al. [8]. This paper will use strengthened by using SIFCON.

To determine the efficiency of the strengthening layer of SIFCON with different fiber types of RC beams under pure torsion, this research used the ABAQUS program, as it is a very important program in an analytical study of this method. The study concentrated on the effects of normal concrete (NC) compressive strength, reinforcement diameter bar, thickness of the SIFCON layer, different percepts of steel fiber (SF) and glass fiber (GB) within the hybrid fiber (HF), length of the strengthening SIFFCON layer.

2. Methods

2.1. Modeling

2.1.1. Parts

A simply supported beam with a span of 2000 mm a section height of 250 mm and a width of 100 mm, cover of a beam of 20 mm shown in Fig. 1 [9]. In ABAQUS, the concrete adopted C3D8R element as shown in Figs. 2 to 5 (NC beams).

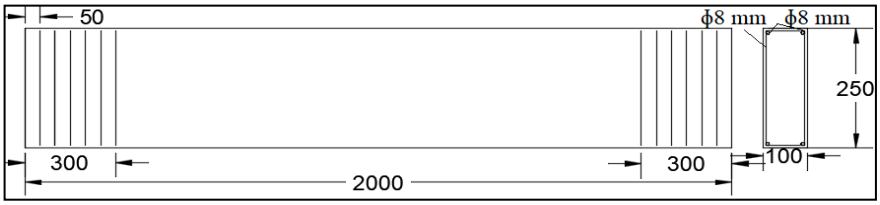

a)

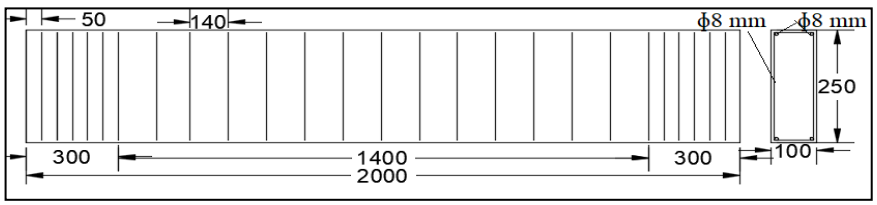

b)

Figure 1. Reinforcement details of beams: a) BN, BSSSFa, BSSSFb, BSSHFa, BSSHFb, BSSGF; and b) BW.

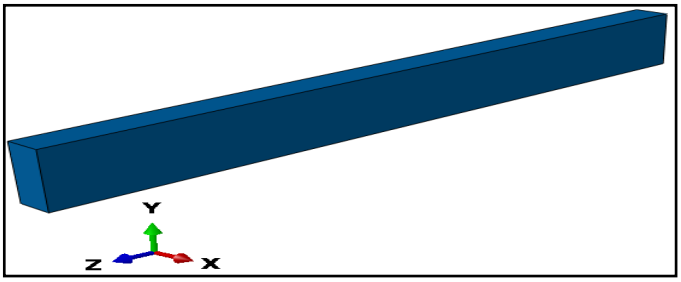

Figure 2. Normal concrete beam.

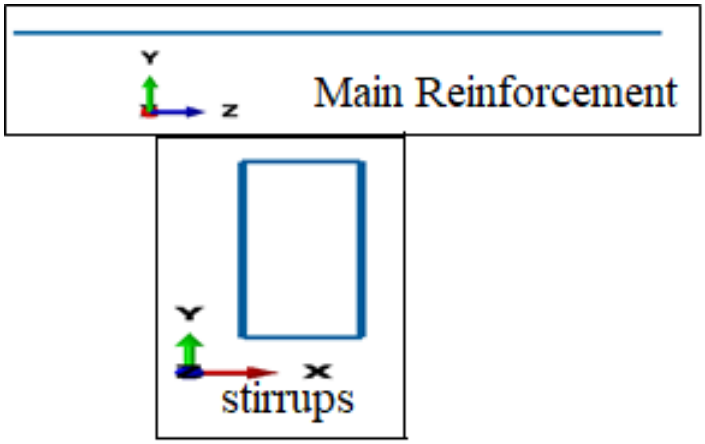

Figure 3. Main and stirrups reinforcement.

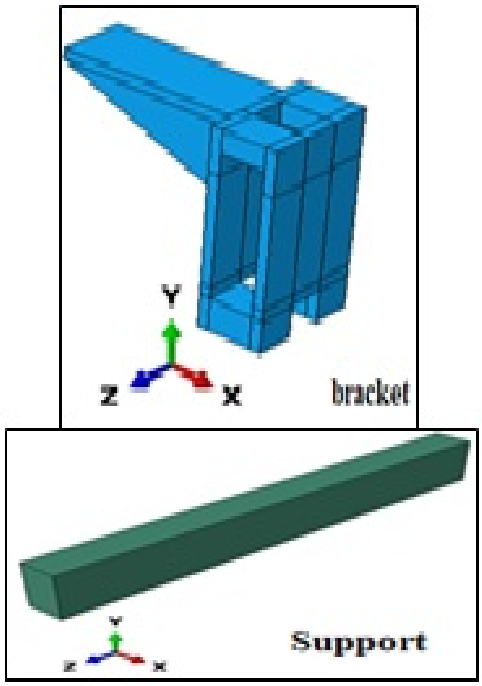

Figure 4. Bracket and support.

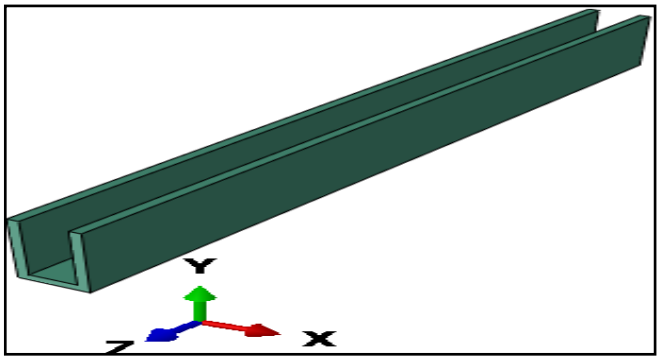

Figure 5. SIFCON layer.

2.2. Materials

2.2.1. Concrete

In a model of simple linear elasticity for isotropic concrete materials, the material constants are Young's modulus of elasticity (E_c) = 25000 MPa and Poisson's ratio (v) = 0.15. Lee and Fenves improved the concrete damaged plasticity (CDP) model [10]. The CDP model is employed in the ABAQUS manual, used in Table 1 [11].

Table 1. The parameters of the concrete damaged plasticity models.

Plasticity	Default
Dilation angle (Ψ)	30-45
Eccentricity (€)	0.1
fb0/fc0	1.16
K	0.667
Viscosity parameter (μ)	0.001

2.2.2. Steel reinforcement

In ABAQUS, the behavior of the steel reinforcement is expressed as a bilinear elastic-plastic curve. Bond slip is not considered in the embedded region modeling approach, according to [12]. Agree with ASTM A1064 and A615 G 60 [13, 14], the elastic modulus (E_c) =200000 MPa and Poisson's ratio (v) =0.15. Steel reinforcement properties given in Table 2.

Table 2. Steel reinforcement properties.

D (mm)	F_y (MPa)	F_u (MPa)	Elongation (%)
8	425.3	680.1	18.1
ASTM A1064	515	585	9
10	524	687	13
12	530	681	12
ASTM A615	420	620	9

2.2.3. Defining SIFCON material behavior

SIFCON material is a composite of concrete and fiber, it may give more compressive strength compared with NC, some properties can be directly and others indirectly. The difference factor between SIFCON and NC is not only compressive strength but also an increase in tensile strength. There is a number of studies that investigated the differences between fiber concrete and NC in FEs. It is suggested that tension stiffening represents this difference [15].The used models in literature are Scanlon-Murray model, Lin and Scordelis model, Vebo and Ghali model, and Gilbert and Warner model [16]. Fiber concrete has stress-strain properties that are pretty comparable to NC. They exhibit initially elastic behavior, which is followed by yielding and strain to harden. Additionally, the model uses these curves in a lack of stress-strain data. The stress-strain relationship for NC is modeled by an Excel sheet. The SIFCON mechanical behavior of compression and tension will be comparable. The tension stiffening model is shown in Fig. 6. In the same way as above, the SIFCON materials are defined by known tension stiffening from the Lin and Scordelis model [16]. Table 3 shows the properties of NC and SIFCON given from the test that occurred in Al-Nahrain University Laboratories.

Table 3. Normal concrete and SIFCON properties.

Mix	f′c	fcu	fr	fct	E
Normal	28.35	35.64	4.044	3.901	25000
5 % SF	57.56	70.23	7.525	6.910	37200
(4 % SF + 1 % GF)	48.13	58.69	4.616	4.500	35250
(3 % SF + 2 % GF)	44.97	54.85	3.781	3.725	34500
(2.5 % SF + 2.5 % GF)	37.40	46.32	3.451	3.423	32450
(2 % SF + 3 % GF)	33.50	40.81	3.210	2.943	31725

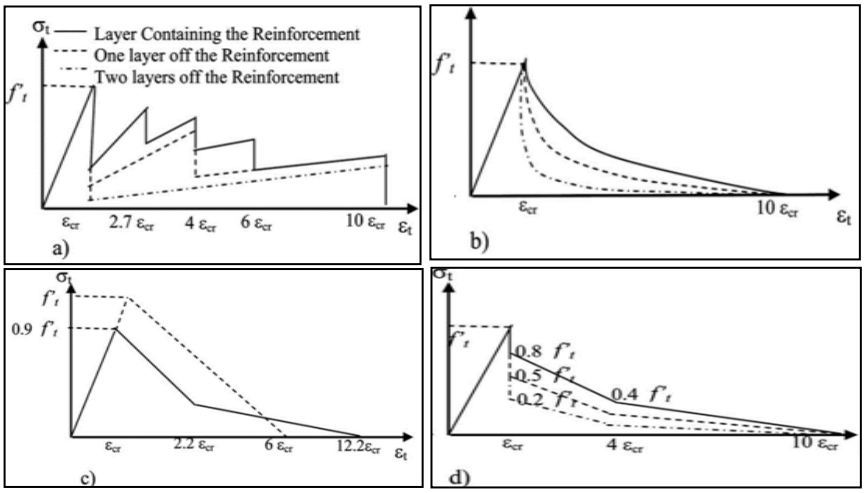

Figure 6. Various models of tension stiffening: a) Scanlon-Murray model; b) Lin and Scordelis model; c) Vebo and Ghali model; and d) Gilbert and Warner model [16].

2.3. Sections

Each material in ABAQUS needs the definition of a section. A section describes the characteristics or region of a part [17]. The section involving a concrete part, SIFCON, loader, bracket, and support is defined as a "solid homogeneous" section. A truss section was assigned for the steel reinforcement part, defined by the cross-sectional area. In addition, the second objective of the section assignment is to associate the desired material with the element [18].

2.4. Assembling of Components

Using an assembly module, each item developed in the simulation model was gathered in a coordinate system and made independent of the other elements of the model, Figs. 7 to 9.

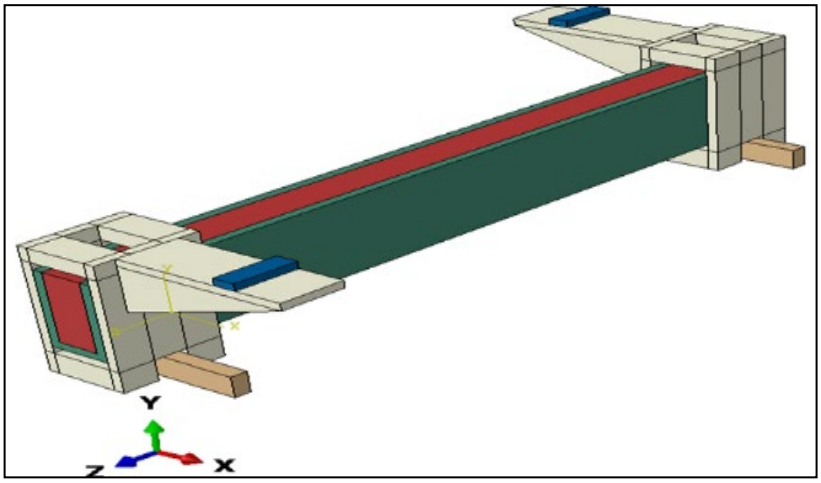

Figure 7. Assembly of the beam parts.

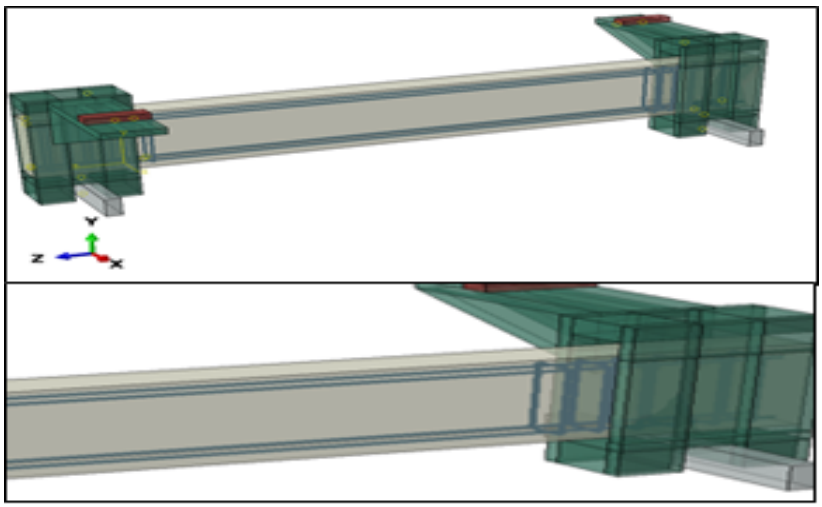

Figure 8. Assembling of the beam (BN).

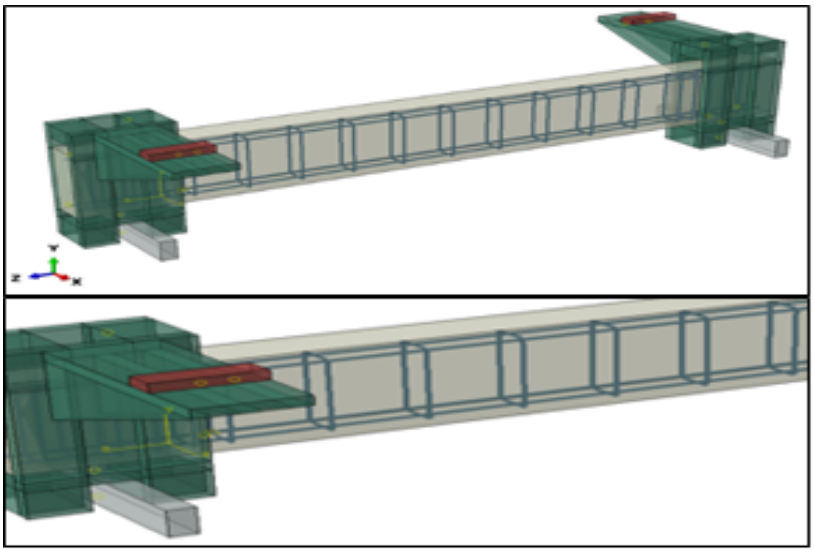

Figure 9. Assembling of the beam (BW).

2.5. Constraints and Interaction

A steel-to-concrete connection is required for RC construction. This contact permits longitudinal forces from the reinforcement to be transmitted to the surrounding concrete and vice versa. ABAQUS provides several constitutive models for representing surface interactions [19].

For bonding the loader with bracket, support with bracket, and concrete beam with bracket by using (General Contact) surface to surface contact (Standard) with step-1 and from General Contact. Based on the characteristics of the interaction kind of contact, choose two categories 1-normal behavior (Hard Contact), 2-tangential behavior with the penalty, and the coefficient of friction are equal (0.35) [18]. Furthermore, an embedded region constraint is used to represent the interaction between the steel reinforcement and the concrete section, and welded parts of the bracket by tie constrains interaction. A full bond with no relation slip between the SIFCON layer and RC beam by using (General Contact) surface-to-surface contact (Standard) with step-1 and from General Contact. In addition, for the loading arm, the alternative "rigid body" constraint type is employed. To change the arm's deformability into its non-deformability.

2.6. Meshing

Meshing is a common occurrence in every model that must be simulated using the FE approach. ABAQUS has several components and forms, each designed for a certain simulation application [20]. The numerical model's mesh size is shown in Fig. 10. A mesh sensitivity analysis to obtain the optimum mesh size considering beam behavior and element sizes 25, 35, 50 mm was performed as shown in Fig. 11.

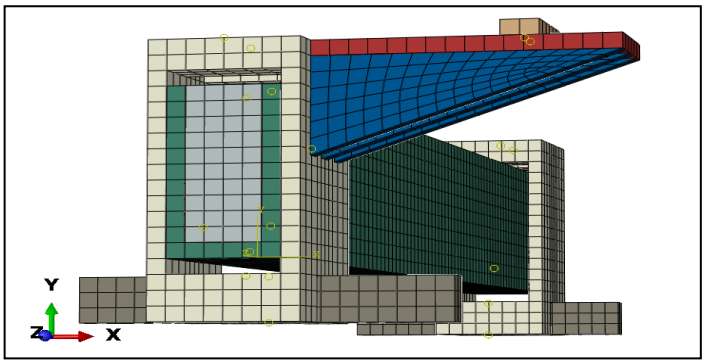

Figure 10. Mesh sensitivity study.

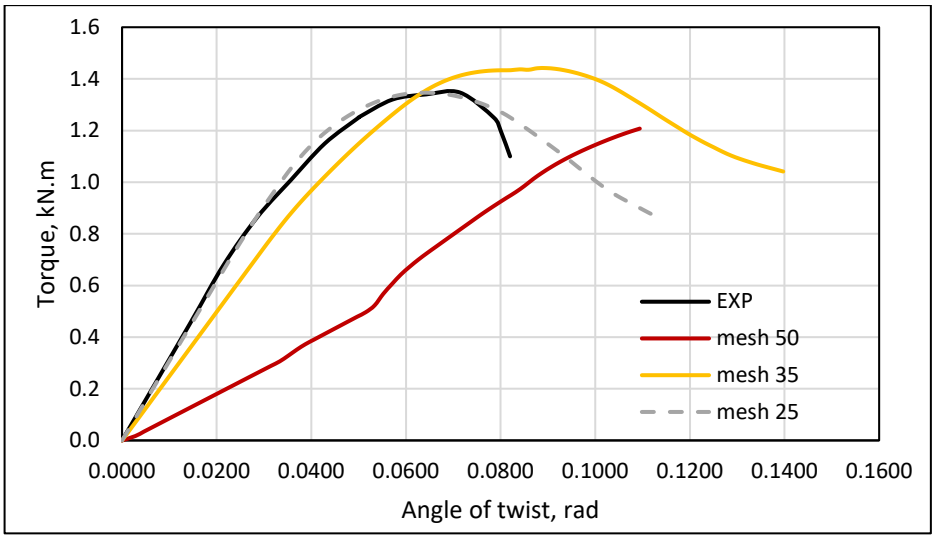

Figure 11. Meshing of the beam.

2.7. Loading and Boundary Conditions

In structural analysis, ABAQUS supports a variety of techniques and capabilities for applying mechanical, thermal, or a combination of the two. Automatic loading can generally be defined by forces, inertia forces (as gravity), pressures, and specified displacements. The load was applied in this process as a downward displacement (displacement/rotation) on the loading arm same as experimental program. The chosen approach is advised by many academics since it can solve the majority of these convergence issues. As shown in Fig. 12, to restrict beams, one types of supports are used pinned supports, which only permit rotation and restrict both vertical and longitudinal movement [21].

2.8. Type of Analysis

The static-general step analysis was used to apply loads. Only if the simulated system is not time-dependent can a static analysis be performed [22]. ABAQUS/Standard by default uses a period, in which "time" varies between 0.0 and 1.0 across the stage. To offer the program a greater range for picking the correct increment number, the maximum number of increments given was 10^4. This amount has no bearing on the analysis; it is just the maximum number of increments. The beginning and minimum increment sizes were chosen at 10^{-3} to avoid convergent issues. The maximum increment size was set to a value of 10^{-1}. The automated stabilization defined a dissipated energy percentage of 0.0002 to achieve static-general analysis.

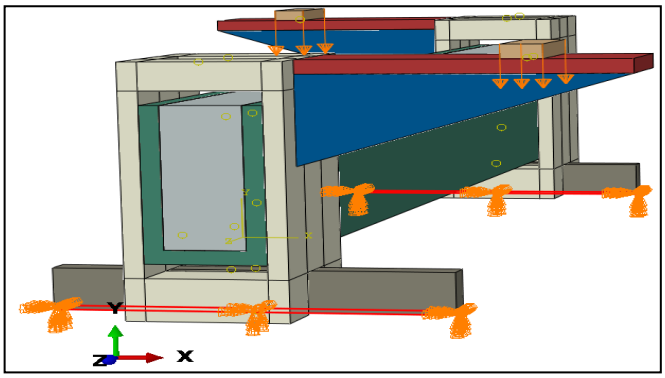

Figure 12. Beam boundary conditions and load.

3. Results and Discussion

3.1. Numerical Validation

The findings of the FE analysis are collated, organized, and presented for comparison with the experimental data, as shown in Table 4, and Figs. 13 and 14 comparisons between the ultimate torque and angle of twist finding from FE and the experimental test for the tested specimens. The values of the mean and coefficient of variations for [(Tu)FE/(Tu)Exp] were 0.998 and 0.247 %, respectively, for ultimate torque, while for the angle of twist [(Angle of twist) FE/(Angle of twist) Exp] were 0.945 and 3.823 %, respectively. The results indicate that when strengthening was used, the beam increased torsional capacity significantly.

Table 4. Numerical and experimental result.

Beams	Describe	FE		Exp. [9]		$T_u)_{FE}/T_u)_{Exp}$	$\phi)_{FE}/\phi)_{Exp}$
		T_u kN	ϕ Rad	T_u kN	ϕ Rad		
BN	Without torsional reinforcement	1.347	0.0635	1.347	0.07143	1.000	0.889
BW	With torsional reinforcement	2.410	0.0632	2.424	0.06429	0.994	0.983
BSSSFb	With strengthening SF 5%	5.957	0.1058	5.961	0.10909	0.999	0.970
BSSHFb	With strengthening HF (3 % + 2 %)	3.757	0.0799	3.756	0.08500	1.000	0.940
	Mean					0.998	0.945
	STDEV.					0.036148	0.002466
	C.V. %					0.247	3.823

$$C.V(\%) = \frac{\text{STDEV.}}{\text{Mean}} * 100. \quad (1)$$

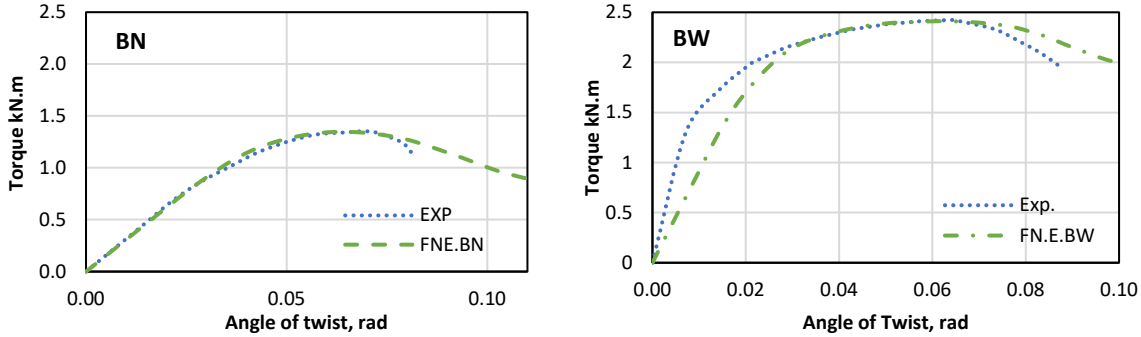

Figure 3. Numerical validation of BN and BW in ABAQUS.

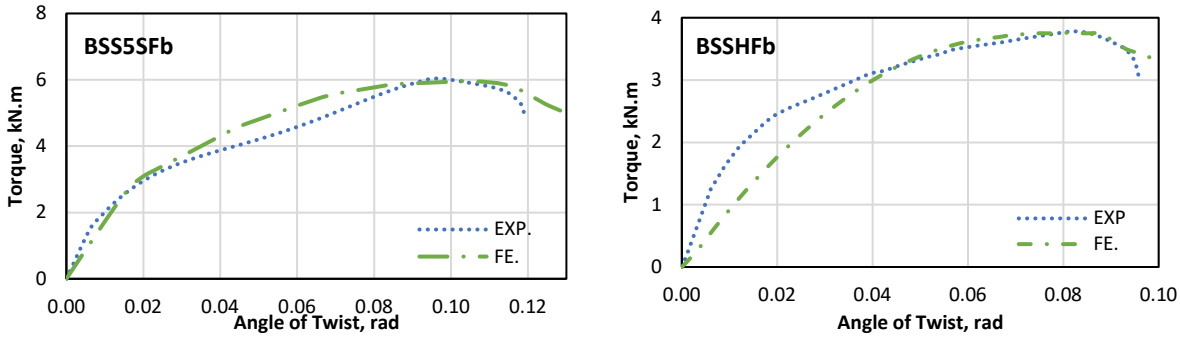

Figure 4. Numerical validation of BSS5SFb and BSSHFb in ABAQUS.

3.2. Parametric Study

3.2.1. Effect of Compressive strength of NC Beam

Three compressive strengths (CS) are chosen = 28, 38, and 48 MPa. The increase in CS led to an increase in the stiffness of beams, which led to an increase in the ultimate torque capacity. Figs. 15 to 17 show the effect of the CS of NC beams on the ultimate torque capacity and the torque and angle of twist relation. Table 5 illustrates that the increase in the ultimate torque capacity is 1 and 6 % for beams FE.BN-38 and FE.BN-48, respectively, related to beam FE.BN-28, while the percent of the increase in the ultimate torque capacity is 2 and 5 % for beams FE.BW-38 and FE.BW-48, respectively, related to FE.BW-28. The percent of the increase in the ultimate torque capacity is 0.17 and 4 % for beams FE.BSSSFb-38 and FE.BSSSFb-48, respectively, related to FE.BSSSFb-28, while the percent of the increase in the ultimate torque capacity is 1.84 and 7.13 % for beams FE.BSSHFb-38 and FE.BSSHFb-48, respectively, related to FE.BSSHFb-28. The effect was found to be marginal for the select CS range.

Table 5. Effect of compressive strength of the normal concrete beam.

Beams	Describe	T_u (kN.m)	Angle of twist	% increase in T_u
FE.BN28	Without torsional reinforcement and CS 28 MPa	1.347	0.0635	Ref1
FE.BN38	Without torsional reinforcement and CS 38 MPa	1.372	0.067	1.86
FE.BN48	Without torsional reinforcement and CS 48 MPa	1.434	0.0645	6.46
FE.BW28	With torsional reinforcement and CS 28 MPa	2.41	0.0632	Ref2
FE.BW38	With torsional reinforcement and CS 38 MPa	2.464	0.0597	2.24
FE.BW48	With torsional reinforcement and CS 48 MPa	2.55	0.0632	5.81
FE.BSSSFb28	Strengthening with 5 % SF and CS 28 MPa	5.957	0.1058	Ref3
FE.BSSSFb38	Strengthening with 5 % SF and CS 38 MPa	5.967	0.0858	0.17
FE.BSSSFb48	Strengthening with 5 % SF and CS 48 MPa	6.212	0.086	4.28
FE.BSSHFb28	Strengthening with (3 SF+2 GF)% and CS 28 MPa	3.757	0.0799	Ref4
FE.BSSHFb38	Strengthening with (3 SF+2 GF)% and CS 38 MPa	3.826	0.0742	1.84
FE.BSSHFb48	Strengthening with (3 SF+2 GF)% and CS 48 MPa	4.025	0.075	7.13

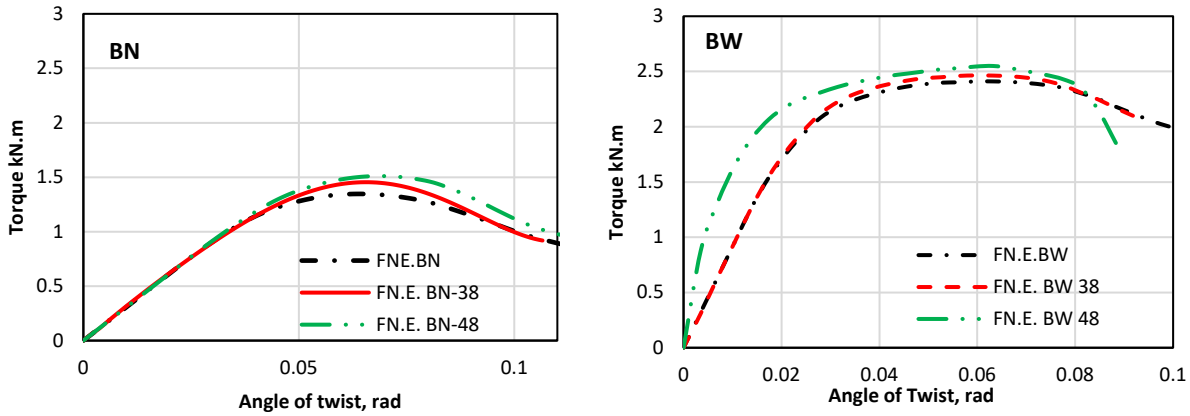

Figure 5. Torque and angle of twist relationship in ABAQUS for beams BN and BW with effect of compressive strength.

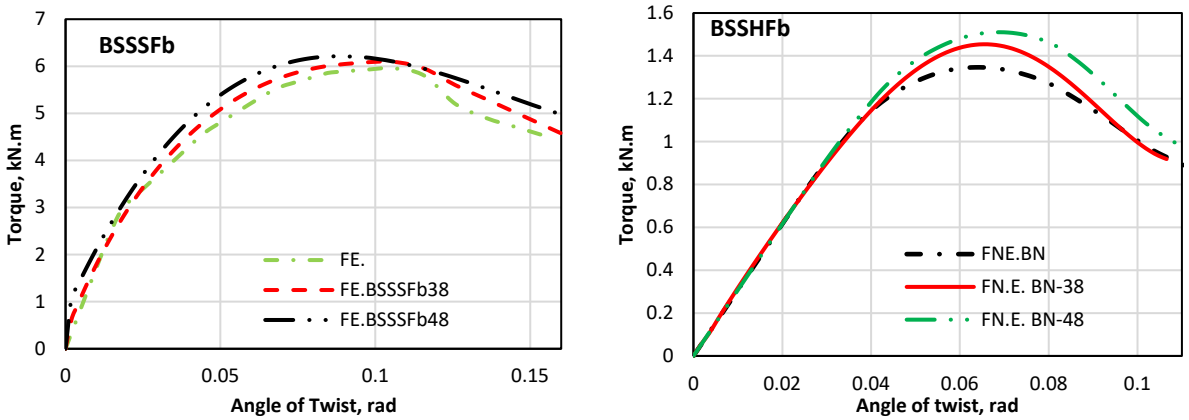

Figure 6. Torque and angle of twist relationship in ABAQUS for beams BSSSFb and BSSHFb with effect of compressive strength.

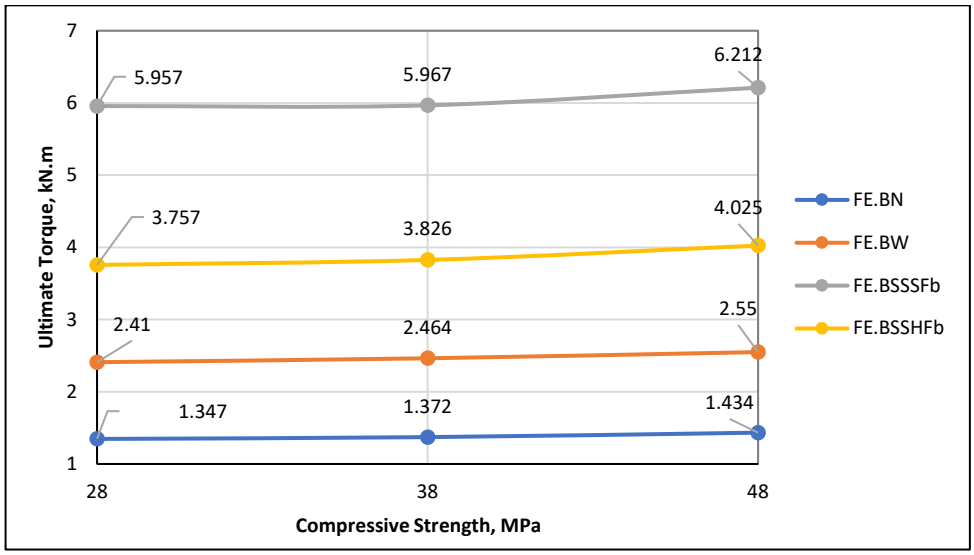

Figure 17. Effect of compressive strength on the ultimate torque capacity.

3.2.2. Effect of main reinforcement diameter – 8, 10, and 12 mm

Figs. 18 and 19 show the effect of reinforcement diameter on the ultimate torque capacity and the torque and angle of twist relative studied for beams. Three diameters were chosen = 8, 10, and 12 mm. The increase in reinforcement bar diameter led to a rise in the ultimate torque capacity. Table 6 illustrates that the increase in the ultimate torque capacity is about 8 and 12 % for beams FE.BN-10 and FE.BN-12, respectively, related to FE.BN, while the percent of the increase in the ultimate torque capacity is 4.02 and 11.66 % for beams FE.BW-10 and FE.BW-12, respectively, related to FE.BW. The percent of the increase

in the ultimate torque capacity is 1.93 and 4.45 % for beams FE.BSSSFb-10 and FE.BSSSFb-12, respectively, related to FE.BSSSFb, while the percent of the increase in the ultimate torque capacity is 2.66 and 5.32 % for beams FE.BSSHFb-10 and FE.BSSHFb-12, respectively, related to FE.BSSHFb. Fig. 20 shows the effect of reinforcement diameter on the ultimate torque capacity.

Table 6. Effect of reinforcement diameter (8, 10, and 12 mm).

Beams	Describe	T_u (kN.m)	Angle of twist (rad)	% increase in T_u
FE.BN8	Without torsional reinforcement and CS 28 MPa	1.347	0.0635	Ref1
FE.BN10	Without torsional reinforcement and CS 38 MPa	1.454	0.0653	7.94
FE.BN12	Without torsional reinforcement and CS 48 MPa	1.51	0.069	12.10
FE.BW8	With torsional reinforcement and CS 28 MPa	2.41	0.0632	Ref2
FE.BW10	With torsional reinforcement and CS 38 MPa	2.507	0.0632	4.02
FE.BW12	With torsional reinforcement and CS 48 MPa	2.691	0.0606	11.66
FE.BSSSFb8	Strengthening with 5 % SF and CS 28 MPa	5.957	0.1058	Ref3
FE.BSSSFb10	Strengthening with 5 % SF and CS 38 MPa	6.072	0.09983	1.93
FE.BSSSFb12	Strengthening with 5 % SF and CS 48 MPa	6.222	0.09982	4.45
BSSHFb8	Strengthening with (3 SF+2 GF) % and CS 28 MPa	3.757	0.0799	Ref4
FE.BSSHFb10	Strengthening with (3 SF+2 GF) % and CS 38 MPa	3.857	0.0818	2.66
FE.BSSHFb12	Strengthening with (3 SF+2 GF) % and CS 48 MPa	3.957	0.0799	5.32

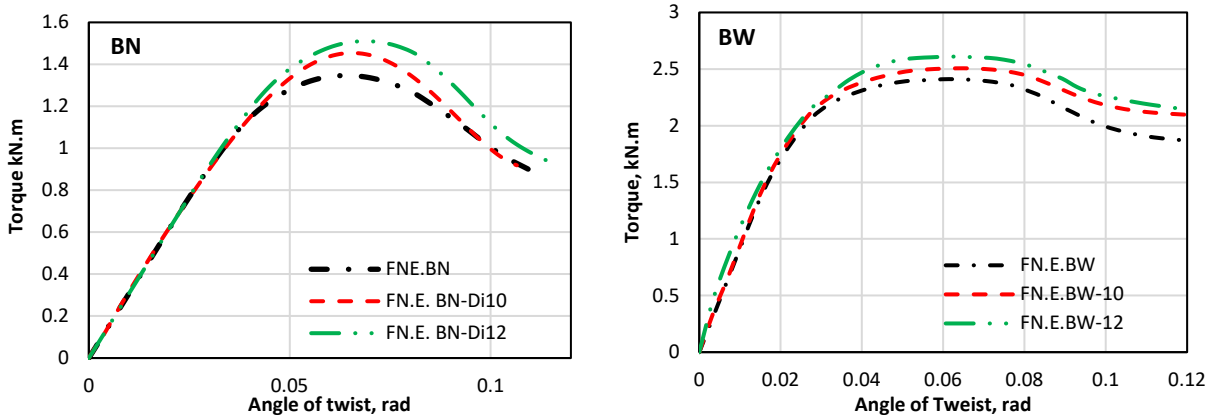

Figure 7. Torque and angle of twist relationship ABAQUS for beams BN and BW.

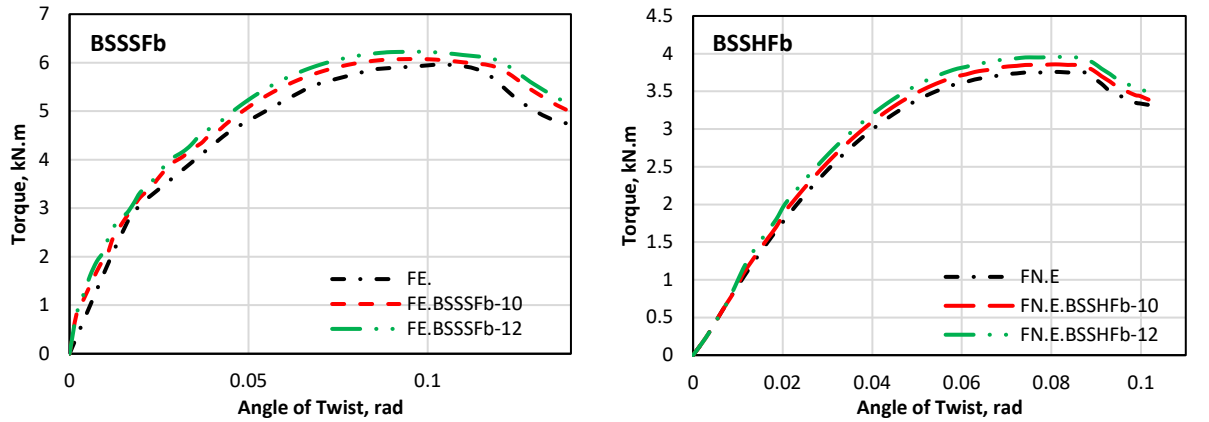

Figure 8. Torque and angle of twist relationship ABAQUS for beams BSSSFb and BSSHFb with variable reinforcement.

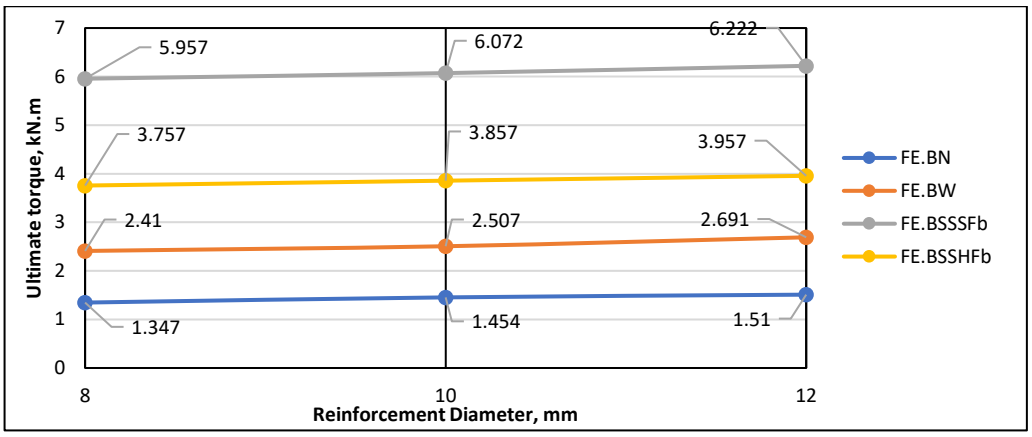

Figure 20. Effect reinforcement diameter on ultimate torque capacity.

3.2.3. Effect of thickness of the SIFCON layer (25, 15, and 35 mm)

Figs. 21 and 22 show the effect of thickness of the SIFCON layer on the ultimate torque capacity and the torque and angle of twist relation was studied for beams. Three thicknesses of the SIFCON layer values – 15, 25, and 35 mm. The increase in the thickness of the SIFCON layer leads to an increase in the ultimate torque capacity, while decreasing in the thickness of the SIFCON layer leads to a decrease in the ultimate torque capacity. Table 7 illustrates the increase and decrease in the ultimate torque capacity. When using the thickness of 35 mm percent the increase in the ultimate torque capacity is about 6, and 7 % for beams FE.BSSSFb-t35 and FE.BSSHFb-t35, respectively, while using the thickness of layet 15 mm, the ultimate torque decrease about 17, and 3 % related to beams FE.BSSSFb-t15 and FE.BSSHFb-t15, respectively. Figs.21 and 22 show the effect of thickness of the SIFCON layer on the ultimate torque capacity.

Table 7. Effect of thickness of the SIFCON layer (25, 15, and 35 mm).

Beams	Describe	T_u (kN.m)	Angle of twist (rad)	% increase in T_u
FE.BSSSFb-t25	Beam strengthening with 5 % SF and thickness 25 mm	5.957	0.1058	Ref1
FE.BSSSFb-t15	Beam strengthening with 5 % SF and thickness 15 mm	4.934	0.08583	–17.17
FE.BSSSFb-t35	Beam strengthening with 5 % SF and thickness 35 mm	6.288	0.0958	5.56
FE. BSSHFb-t25	Beam strengthening with (3SF+2GF) % and thickness 25 mm	3.757	0.0799	Ref2
FE.BSSHFb-t15	Beam strengthening with (3SF+2GF) % and thickness 15 mm	3.651	0.0732	–2.82
FE.BSSHFb-t35	Beam strengthening with (3SF+2GF) % and thickness 35 mm	4.001	0.0747	6.49

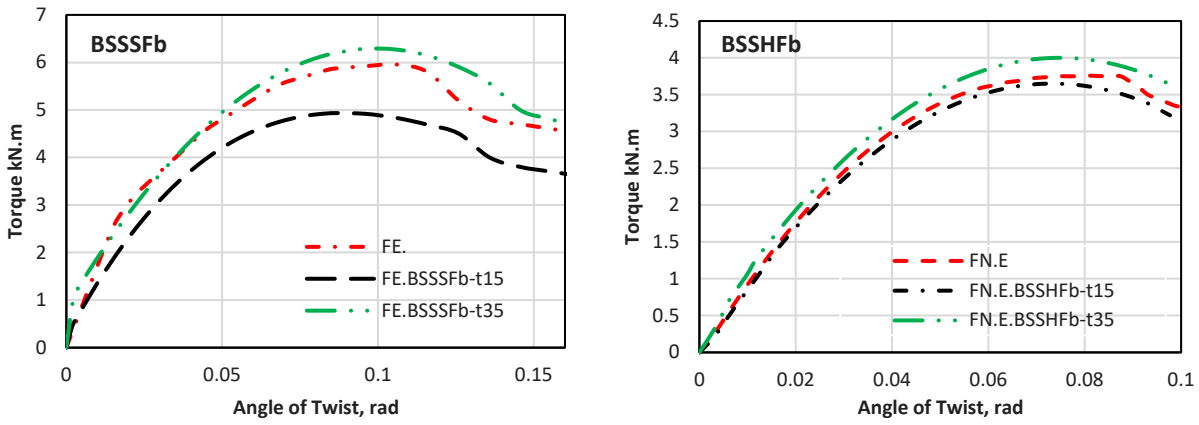

Figure 21 Torque and angle of twist relationship ABAQUS for beams BSSSFb and BSSHFb with variable SIFCON thickness.

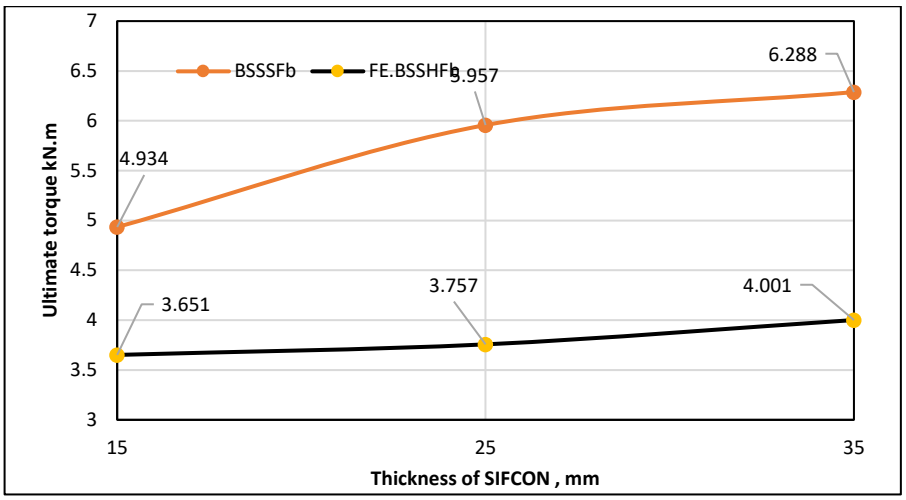

Figure 22. Effect of thickness of the SIFCON layer on the ultimate torque capacity.

3.2.4. Effect of hybrid fiber (SF + GF) (3 % + 2 %, 2.5 % + 2.5 %, and 2 % + 3%)

Fig. 23 shows the effect of HF of the SIFCON layer on the ultimate torque capacity and the torque and angle of twist relation studied for beams. Three HF of the SIFCON layer values (SF+GF) (3 % + 2 %, 2.5 % + 2.5 %, and 2 % + 3%). The decrease in SF in HF led to a decrease in the ultimate torque capacity. Table 8 shows that the decrease in the ultimate torque capacity is about 9 and 17 % for beams FE.BSSHFc and FE.BSSHFd, respectively.

Table 8. Effect of hybrid fiber.

Beams	Describe	Tu (kN.m)	Angle of twist (rad)	% increase of Tu
FE.BSSHFb	HF (3% SF + 2% GF)	5.957	0.0799	Ref1
FE.BSSHFc	HF (2.5% SF + 2.5% GF)	5.436	0.0958	8.75
FE.BSSHFd	HF (2% SF + 3% GF)	4.934	0.0858	17.17

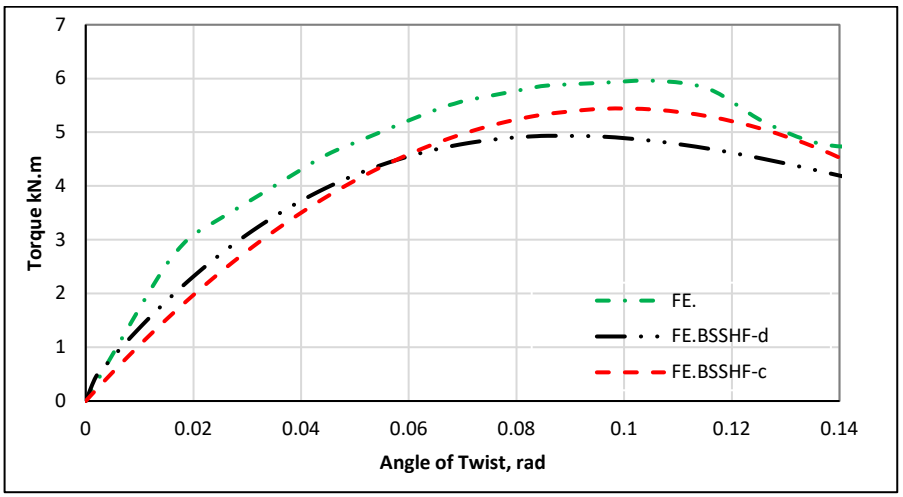

Figure 93. Torque and angle of twist relationship ABAQUS for beams BSSHFb with variable ratios of hybrid fiber.

3.2.5. Effect of length of the SIFCON layer (2 and 1.5 m)

Fig. 24 shows the effect of length of the SIFCON layer on the ultimate torque capacity and the torque and angle of twist relation was studied for beams. Two length of the SIFCON layer values = 2 and 1.5 m. The decrease in the length of the strengthening layer led to a decrease in the ultimate torque capacity. Table 9 shows that the decrease in the ultimate torque capacity is about 21 and 12 % for beams FE.BSSHFc and FE.BSSHFd, respectively.

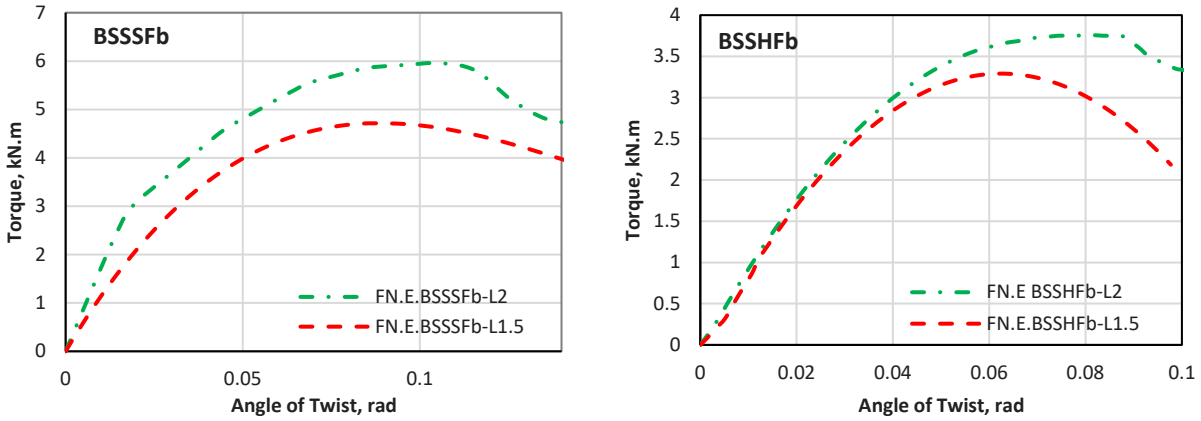

Figure 24. Torque and angle of twist relationship from ABAQUS for beams BSSSFb and BSSHFb.

Table 9. Effect of length of the SIFCON layer (2 and 1.5 m).

Beams	Describe	Tu (kN.m)	Angle of twist (rad)	% increase of Tu
F.E.BSSSFb-L2	Length of strengthening layer 2 m	5.957	0.1058	Ref1
FN.E.BSSSFb-L1.5	Length of strengthening layer 2 m	4.714	0.0858	–20.87
F.E.BSSHFb-L2	Length of strengthening layer 2 m	3.757	0.0799	Ref2
FN.E.BSSHFb-L1.5	Length of strengthening layer 2 m	3.29	0.0619	–12.43

3.3. Failure Mode

The failure mode in the torque is always cracks inclined at 45 degrees, appearing on both sides [23]. The cracks in the ABAQUS program are often more numerous and larger than they are experimentally because the program also shows invisible cracks as clear, as can be seen in Fig. 25.

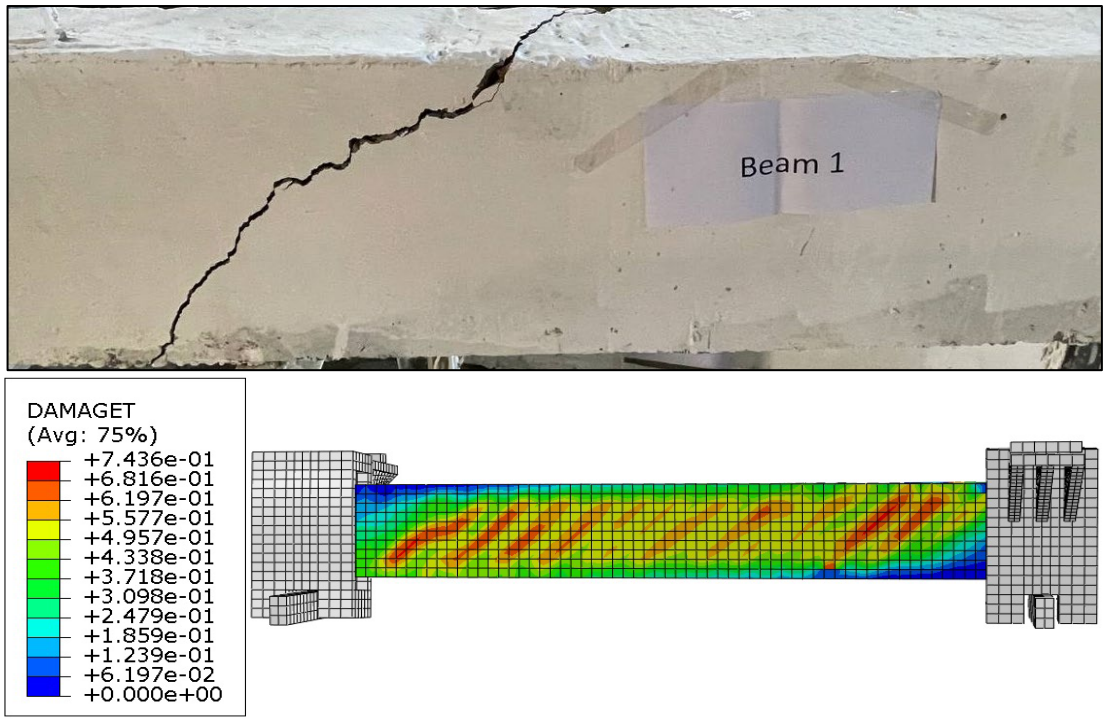

Beam BN

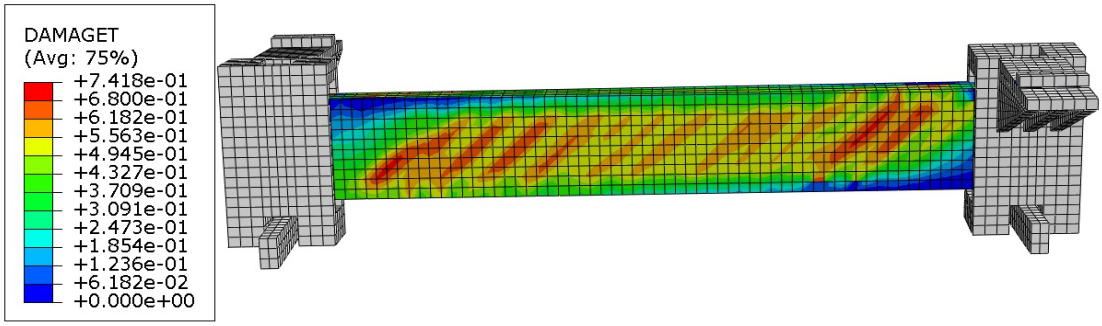

Beam BW

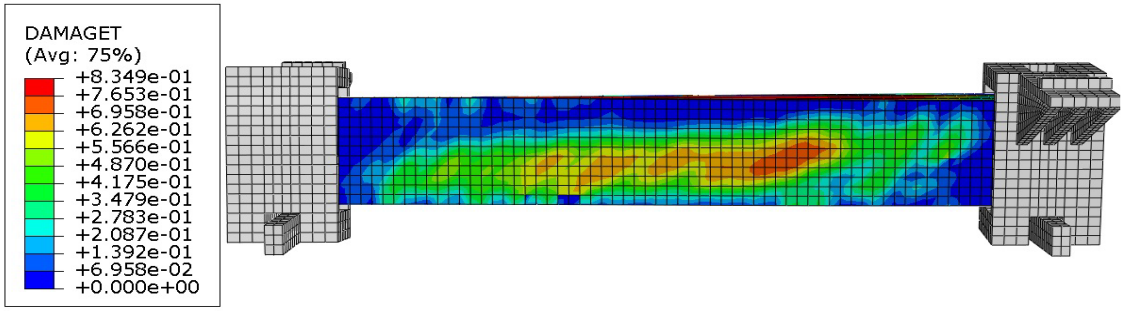

Beam BSSSFb

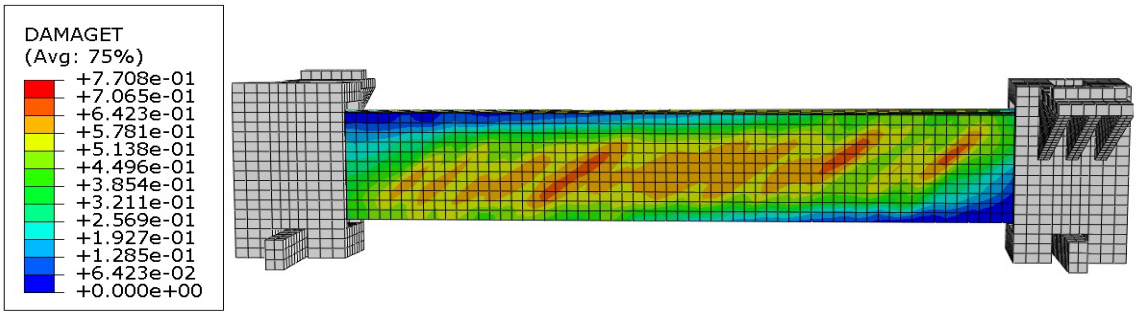

Beam BSSHFb

Figure 25. Damage tensile under pure torsion for tested beams.

4. Conclusions

The following conclusions are obtained from FE analysis:

1. Reasonable agreement was acquired between the ultimate torque and angle of twist of FE numerical models and found experimentally, in which the value of the mean and coefficient of variations were 0.998 and 0.247 %, respectively, for the ultimate torque, whilst, for the angle of twist, the value of the mean and coefficient of variation were 0.945 and 3.823 %, respectively.
2. The effect of CS on the ultimate torque capacity was studied numerically, the percentage of the increase in the ultimate torque capacity is 1 and 6 % for the reference beams without torsional reinforcement having the CSs of 38 and 48 MPa, respectively. The percent of the increase in the ultimate torque capacity is 2 and 5 % for the reference beams with torsional reinforcement having CSs of 38 and 48 MPa, respectively. The percent of the increase in the ultimate torque capacity is 0.17 and 4 % for three-sided SF SIFCON beams having CSs of 38 and 48 MPa, respectively. The percent of the increase in the ultimate torque capacity is 1.84 and 7.13 % for three-sided HF SIFCON beams having CSs of 38 and 48 MPa, respectively. The increase is marginal due to the selected range of CS.
3. The effect of increasing longitudinal reinforcement ratio is found to be higher for the torsionally unreinforced beam and marginal for the other beams for the selected range of reinforcement ratio or diameter (8 to 12 mm bar diameter).
4. The effect of thickness of the SIFCON layer on the behavior is found to be higher for SF SIFCON and lower for HF SIFCON jacketing.
5. The effect of HF on behavior is studied. It is clear that the decrease in SF content in HF SIFCON led to a decrease in the ultimate torque capacity. The decrease in the ultimate torque capacity is about 9 and 17 % for SIFCON beams with (2.5 SF + 2.5 GB) % and (2 SF + 3 GB) %, respectively.
6. It is clear that the decrease in the length of the SIFCON strengthening layer led to a decrease in the ultimate torque capacity. The decrease in the ultimate torque capacity is about 21 % for beams with strengthened SF SIFCON and 12 % for beams with HF SIFCON jacketing.
7. The increase depends on the type of parameter, whether it is primarily within the strengthening or secondary (parameter that effects on torsion not strengthening), as increasing the CS of the core beam is considered a secondary parameter, and the increase may be small. As for the primary parameters that affect the study of strengthening, for example, changing the thickness, percentage of fibers, and length of the reinforcement layer, they have a clear fundamental effect.

References

1. Andersen, P. Experiments with concrete in torsion. Transactions of the American Society of Civil Engineers. 1935. 100(1). Pp. 949–960.
2. Bentur, A., Cree, R. Cement reinforced with steel wool. International Journal of Cement Composites and Lightweight Concrete. 1987. 9(4). Pp. 217–223.
3. Ipek, M., Aksu, M. The effect of different types of fiber on flexure strength and fracture toughness in SIFCON. Constr. Build. Mater. 2019. 214. 207–218. DOI: 10.1016/j.conbuildmat.2019.04.055
4. Ali, M.I., Al-Azzawi, A.A. Finite element analysis of RC beams strengthened with near-surface mounted reinforcement bars under pure torsion. IOP Conference Series: Earth and Environmental Science. 2023. 1232(1). 12026. DOI: 10.1088/1755-1315/1232/1/012026
5. Le, K.B., Van Cao, V. Numerical Study of Circular Concrete Filled Steel Tubes Subjected to Pure Torsion. Buildings. 2021. 11(9). Article no. 397. DOI: 10.3390/buildings1109039
6. Majed, M.M., Tavakkolizadeh, M., Allawi, A.A. Finite element analysis of rectangular RC beams strengthened with FRP laminates under pure torsion. Structural Concrete. 2021. 22(4). Pp. 1946–1961. DOI: 10.1002/suco.202000291
7. Ganganagoudar, A., Mondal, T.G., Prakash Shanmugam, S. Analytical and finite element studies on behavior of FRP strengthened RC beams under torsion. Composite Structures. 2016. 153. Pp. 876–885. DOI: 10.1016/j.compstruct.2016.07.014
8. Jain, S., Chellapandian, M., Prakash Shanmugam, S. Emergency repair of severely damaged reinforced concrete column elements under axial compression: An experimental study. Construction and Building Materials. 2017. 155. 751–761. DOI: 10.1016/j.conbuildmat.2017.08.127
9. Mohammed, J.M. Torsional Performance of Reinforced Concrete Beams Strengthened with SIFCON Jacketing., MSc. Thesis, Department of Civil Engineering, College of Engineering, Al-Nahrain University, 2024.
10. Le Thanh, C., Minh, H.L., Sang-To, T. A nonlinear concrete damaged plasticity model for simulation reinforced concrete structures using ABAQUS. Frattura ed Integrità Strutturale. 2022. 16(59). Pp. 232–242. DOI: 10.3221/IGF-ESIS.59.17
11. ABAQUS. ABAQUS Analysis User's Manual Version 6.13. Rensselaer Polytechnic Institute, 2013.
12. Malm, R. Shear Cracks in Concrete Structures Subjected to In-Plane Stresses. Licentiate Thesis. KTH Royal Institute of Technology, 2006. 136 p.
13. ASTM A1064/A1064M-14. Standard Specification for Carbon-Steel Wire and Welded Wire Reinforcement, Plain and Deformed, for Concrete. ASTM International. West Conshohocken, PA, 2020.

14. ASTM A615/A615M-20. Standard Specification for Deformed and Plain Carbon-Steel Bars for Concrete Reinforcement. West Conshohocken, PA, 2020.
15. Padmarajaiah, S.K., Ramaswamy, A. A finite element assessment of flexural strength of prestressed concrete beams with fiber reinforcement. Cement and Concrete Composites. 2002. 24(2). Pp. 229–241. DOI: 10.1016/S0958-9465(01)00040-3
16. Wahalathantri, B., Thambiratnam, D., Chan, T., Fawzia, S. A material model for flexural crack simulation in reinforced concrete elements using ABAQUS. Proceedings of the First International Conference on Engineering, Designing and Developing the Built Environment for Sustainable Wellbeing. Queensland University of Technology. Brisbane, Qld, 2011. Pp. 260–264.
17. Khennane, A. Introduction to Finite Element Analysis Using MATLAB® and Abaqus. CRC Press, 2013. 453 p. DOI: 10.1201/b15042
18. Ali, M.I. Torsional Performance of Reinforced Concrete Beams Strengthened with Near-Surface Mounted Steel Bars. Al-Nahrain University, 2023.
19. Börgesson, L. Abaqus. Developments in Geotechnical Engineering. 1996. 79. Pp. 565–570. Pp. 10.1016/S0165-1250(96)80047-2
20. Barbero, E.J. Finite Element Analysis of Composite Materials using Abaqus®. CRC Press, 2023. 571 p. DOI: 10.1201/9781003108153
21. El-Mandouh, M.A., Hu, J.W., Shim, W.S., Abdelazeem, F., ELsamak, G. Torsional improvement of RC beams using various strengthening systems. Buildings 2022. 12(11). Article no. 1776. DOI: 10.3390/buildings12111776
22. Sun, Y. A Structural Optimization Scripted Software System. Virginia Tech, 2019. https://www.semanticscholar.org/paper/A-Structural-Optimization-Scripted-Software-System-Sun/e664ba6ccfe9fd30d3b4cfe142fd779958eb44ae
23. Hou, N., Ding, N., Qu, Sh., Guo, W., et al. Failure modes, mechanisms and causes of shafts in mechanical equipment. Engineering Failure Analysis. 2022. 136. Article no. 106216. DOI: 10.1016/j.engfailanal.2022.106216

Information about the authors:

Mohammed Mohammed,
E-mail: st.mohammed.g.m.f@nahrainuniv.edu.iq

Adel Al-Azzawi,
E-mail: dr_adel_azzawi@yahoo.com

Received 08.06.2024. Approved after reviewing 23.12.2025. Accepted 15.01.2026.

Magazine of Civil Engineering

ISSN 2712-8172

journal homepage: http://engstroy.spbstu.ru/

Research article

UDC 69.058.4

DOI: 10.34910/MCE.141.8

Dust atlas of construction works in point-pattern housing development

S.E. Manzhilevskaya ✉

Don State Technical University, Rostov-on-Don, Russian Federation

✉ *smanzhilevskaya@yandex.ru*

Keywords: point-pattern housing development, construction dust, dust atlas, dust protection measures

Abstract. With the development of megacities, active construction is becoming a key factor in the deterioration of atmospheric air quality due to the release of fine particulate matter, such as PM0.5–PM10. These particles pose a significant environmental risk. Given the increasing demand for dense urban development, issues of air purification and environmental stability are coming to the fore. A thorough understanding of the physical and chemical characteristics of dust is fundamental to developing and implementing dust protection measures on construction sites, including the selection of suitable dust collectors. A new approach has been developed for the analysis of dust particles generated by construction work at various urban sites. As part of this approach, a dust atlas has been created that organizes and classifies the diverse types of construction dust, detailing their physical and chemical characteristics. The atlas is based on a unique methodology that enables the identification and description of the main properties of each type of dust encountered during construction operations. Each type of dust studied in this research was assigned its own specification, which includes both the analysis methodology and the identified characteristics of the dust. Documentation related to dust testing contains all the necessary information, including the type of dust, the method of data collection, the time of measurement, the materials used, and the results of dust analysis. For the study, dust samples were taken from the air during construction processes. The study of dust on construction sites revealed that particle size varies significantly, a phenomenon that cannot be attributed solely to measurement errors. These variations in dust particle size can be attributed both to the specific nature of the work performed and to external conditions, including changes in humidity and wind intensity.

Citation: Manzhilevskaya, S.E. Dust atlas of construction works in point-pattern housing development. Magazine of Civil Engineering. 2026. 19(1). Article no. 14108. DOI: 10.34910/MCE.141.8

1. Introduction

Studies by Lumens & Spi [1] have shown an inextricable link between construction activity and dust formation. Dust particles in the air pose a serious threat to health, so their monitoring requires close attention [2]. At every stage of the construction process, whether it is the initial construction phase, its operation or dismantling, it is necessary to use resources efficiently and ensure personnel protection. An integrated approach to dust suppression plays a key role in ensuring environmental and industrial safety. From the start of preparatory work to the final cleaning of the site, it is critically important to comply with environmental regulations and safety requirements. The introduction of dust control methods is becoming a prerequisite for the protection of both humans and the ecosystem as a whole.

The construction industry makes a significant contribution to urban air pollution. Concreting, stone processing, preparation of building mixes and other operations on construction sites lead to the formation of microscopic dust particles. These particles, ranging in size from PM0.5 to PM10, pose a serious threat to health [3, 4]. They are particularly dangerous for construction workers and residents of the surrounding

areas because if they enter the respiratory tract, they can provoke the development of various lung diseases. Loading of materials, excavation, plastering, and delivery of building materials – all these processes exacerbate the problem of air pollution in urbanized areas [5].

In 2016, Deborah Dickerson identified that construction activities, including drilling, excavation, and loading and unloading operations, are a source of significant dust pollution [6]. Ming Hu has established the equivalent risks for office staff and construction personnel during construction activities [7]. In 2017, a scientific group led by Jiang Zuo documented the negative effects of atmospheric dust pollution on the health of both office workers and construction workers [8]. It is necessary to create and use comprehensive monitoring and management methods to ensure the security of workers on construction sites, where dust pollution is widespread [9].

Protecting the population from the negative effects of construction work is becoming a critically important task in modern cities [10, 11]. A team of researchers led by Zezhou Wu has developed innovative ways to control dust on construction sites, which is especially important when building in cramped urban environments [12]. Experiments by a group of scientists led by Qiming Luo have revealed a serious problem: during construction operations, such as mixing concrete, processing it and working with marble, large-scale air pollution occurs [13]. The most alarming situation is observed when cutting bricks – the concentration of fine particles PM2.5 and PM10 reaches values 60–100 times higher than the NAAQS (National Ambient Air Quality Standards) standards [14]. This problem is becoming particularly acute against the background of growing urbanization and increasing urban population density.

The problem of the spread of particulate matter in confined urban spaces has become the subject of close attention from the scientific community [15, 16]. A notable breakthrough in this area was made by a group led by Zhang Yisheng, who applied a combined research method: they combined computer simulations with experiments in a wind tunnel to study the behavior of dust on construction sites [17]. Successful results in solving the problem of air pollution caused by dust particles have been achieved by international scientific teams, including specialists from the USA, China, European countries, Korea, and the UK [18–21]. This innovative approach has allowed for a deeper understanding of the mechanisms of movement of construction dust in dense urban areas, which is especially important for megacities with high population density.

The problem of construction dust control has attracted the attention of many scientists who have proposed various solutions. Thus, a study by Sang-Woo Han and colleagues presented a hybrid model based on receptors for monitoring dust pollution [22]. Studying the characteristics of dust emissions during construction, the Bo Yu team analyzed their time parameters, intensity and concentration [23]. Optimization of the construction site layout using the MOPSO algorithm was proposed in Guowu Tao's work as a way to reduce dust pollution [24]. Special attention was paid to the protection of vulnerable groups of the population – Zachary M. Klaver and co-authors evaluated the effectiveness of HEPA PAF filters for air purification in the homes of elderly people living near construction sites [25].

The danger of construction dust to human health is confirmed by numerous scientific studies [26]. The Matthew Dietrich team has found that the chemical composition of dust particles entering the premises from construction sites poses serious risks to the public [27]. The specialists from the Russian Federation have also been actively studying this problem. A group of Russian scientists, including N. Sergina, D. Borovkov, V. Azarov, and A. Strelyaeva, discovered large-scale environmental violations during point-pattern housing development, especially in the context of air pollution by fine dust [28–31]. In densely populated urban areas, the problem of managing construction sites and controlling dust emissions is acute. The study revealed serious shortcomings in the implementation of anti-dust measures on construction sites.

The lack of a clear pollution control system in dense urban areas requires urgent measures and close attention from responsible authorities.

A deep understanding of the physical and chemical characteristics of dust from construction work is the basis for the development and implementation of dust suppression measures on construction sites, including the selection of suitable dust collectors. Solving this problem requires the development of a new approach to the analysis of dust particles generated as a result of construction work at various sites in the city. As part of this approach, a dust atlas has been created that systematizes and classifies various types of construction dust according to their physical and chemical characteristics.

2. Materials and Methods

Rostov-on-Don is a rapidly developing metropolis. The construction of new buildings and other structures is always an integral part of urban infrastructure development. Today, a large number of different residential complexes have been built in Rostov-on-Don, and this list is constantly growing. Rostov-on-Don is the largest city in southern Russia and the eleventh most populous city in the Russian Federation. In

recent years, the city has experienced an unfavorable environmental situation to breathe polluted air. Air pollution is often observed at construction sites, primarily caused by emissions of inorganic dust. This dust, containing up to 70 % silicon dioxide, is found in various materials such as chamotte and cement, as well as in industrial waste. Dust with a silicon dioxide content of more than 70 % was also found in dinas. There is also an environmental threat at construction sites from suspended particles and nitrogen dioxide released during the construction process. Sources of dust emissions into the atmosphere at construction sites include: construction machinery (e.g., transportation, loading, and unloading of bulk materials); building materials (e.g., gypsum, cement, sand); and construction processes (e.g., cutting gas blocks, mixing plaster, and mortar). The construction site of the 11-floor residential building (Fig. 1) is one of the typical examples of point-pattern housing development in a megacity.

Figure 1. Schemes of the research site: 1–3 – sampling points at the construction site.

This construction site was chosen as a research object because, according to the data from the developed map of the distribution of suspended matter concentrations near point-pattern housing development construction sites in Rostov-on-Don (Fig. 2), it was located in an area with the highest dust levels. Here, dust samples were taken at the construction site during construction. The construction dust sampling was carried out during excavation, foundation installation, and bulk materials handling.

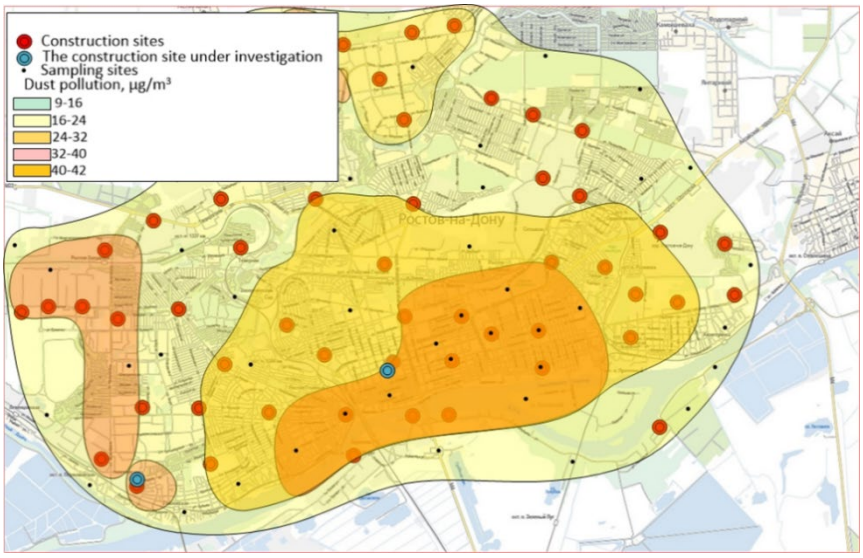

Figure 2. Distribution of suspended matter concentrations near point-of-construction facilities in Rostov-on-Don.

The study used two main devices to collect samples: a portable particle counter, Handheld 3016 by Lighthouse Worldwide Solutions (Medford, OR, USA), featuring 0.3 μm sensitivity, and a PU-3E/12 electric respirator by Ximko (Moscow, Russia). The respirator was used to detect dust and aerosol levels in the air with AFA VP aerosol filters having an active area of 10 cm^2 in both working and residential environments, as shown in Fig. 3.

(a) (b) (c)

Figure 3. Devices used in sampling: (a) Handheld 3016 particle counter; (b) PU-3E/12 electric respirator; (c) AFA aerosol filters by Krezol (Voronezh, Russia).

Dust particles filtered from various zones of the construction site were mixed to form a representative sample. The excess volume of the selected material was intensively homogenized, after which it was reduced to the required amount, thereby increasing the reliability of the analysis.

During sampling, special AFA filters were used to monitor aerosol particles in gaseous media and the atmosphere. Calibration and verification of measurement accuracy were carried out using the WIN-SFV32 v1.0 software package integrated with an electronic respirator. The filter elements were made using PVC-based fibers. The IRA-10 holders manufactured by the Russian company Krezol in Voronezh were used as retaining structures. The analysis of the collected samples was carried out using the methods for determining the concentration of pollutants in the air of the Russian Federation. According to the GOST R 58577-2019 standard [32], the sampling time for air samples to measure instantaneous concentrations at each control point was set to 20 minutes. The pretreatment of AFA type filters included their daily exposure in a desiccator containing calcium chloride as a moisture absorber. The filters were kept in open packages. After that, each sample was extracted using tweezers and weighed on a scale with a precision of 0.1 mg. The obtained weight data and the identification number were recorded on a paper package, into which the filter was then placed. An open filter holder was used to determine the dust concentration in the air. A filter, previously weighed to a constant weight, was placed in it. The prepared filters were stored in a room with a normal temperature, where there was no possibility of contamination. Before carrying out the weighing procedure, the filters delivered from the sampling site were left in the laboratory room for 24 hours. The process of weighing the dried samples was carried out several times until the weight became stable. During the dust particle sampling process, key characteristics of the air-dust mixture were measured, including humidity W (%), temperature t (°C), and flow rate V (cm/sec).

The dust concentration was determined by the following formula

$$C = \frac{m}{V_0}, \tag{1}$$

where m is the mass of dust trapped on the filter, determined by the gravimetric method as the difference between the mass of the filter after sampling and that of the clean filter before sampling, in milligrams; V_0 is the volume of the sample of air (gas) passed through the filter, in cubic meters.

The value of each sample was adjusted to normal conditions and calculated using the following formula

$$V_0 = \frac{V_1 \times 273 \times \left(P_i + \Delta P_{ac}\right)}{\left(273 + t\right) \times 101.325}, \tag{2}$$

where V_0 is the volume of the selected gas emissions sample, m^3; P_i is the atmospheric pressure during sampling, kPa; t is the gas temperature at the aspirator during sampling, °C; V_1 is the volume of the selected dust sample, m^3; ΔP_{ac} is the vacuum at the aspirator, kPa.

During sampling, the environment was characterized by moderate temperatures around 25 °C, with relatively dry air showing 30–40 % humidity. A steady 5-meter-per-second breeze was present, while no rain or artificial moisture sources were detected throughout the duration.

The selected samples were sent to a scientific laboratory to determine the physical and chemical characteristics of construction dust according to the following parameters: morphological analysis of particles, dispersion, specific surface area, density (bulk, free-state, and dense-packing densities),

surcharge angle, adhesion, abrasiveness, electrical resistivity, chemical composition, hygroscopicity, and wettability. The devices used to determine the physical and chemical characteristics of construction dust are shown in Fig. 4. Table 2 shows the device specifications.

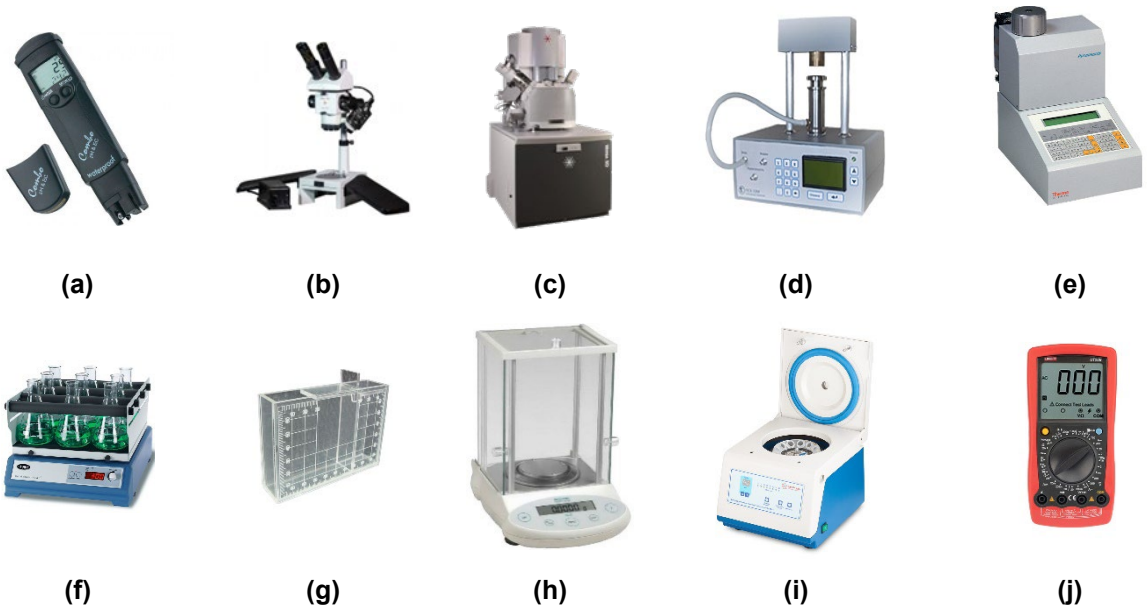

Figure 4. Devices used to determine the physico-chemical characteristics of construction dust: (a) TDS/pH-metr PH-986 analyzer by Hanna instruments (Germany); (b) MBS-10 stereoscopic microscope by LZOS (Moscow, Russia); (c) Versa 3D DualBeam electron-ion (bi-beam) microscope by FEI Company (Hillsboro, OR, USA); (d) PSKh-10 instrument by PSH (Moscow, Russia); (e) Pycnomatic Evo gas-weighing balloon by POROTEC (Germany); (f) SSL1 orbital shaker by Stual (Germany); (g) SWT-3M density analyzer by Emerging technologies corporate group (Russia); (h) ALC-80d4 digital weighing scale by Acculab (USA); (i) 80-2S sedimentator by Armed (Russia); (j) UT58B multimeter by UNI-T (China).

The process of studying the physical and chemical characteristics of construction dust took place in the following sequence.

1. Morphological analysis of construction dust particles was performed using an MBS-10 stereomicroscope equipped with a photodetector, which made it possible to obtain images magnified 200–2000 times. The resulting photographs were processed using the "Dust 1" software package, which made it possible to calculate the area occupied by the particles and determine their geometric shape based on these data. This technique relies on microscopic examination and photographic recording of dust particle sizes, followed by digital processing. The pH level in the dust samples was measured using a TDS/pH-meter PH-986 analyzer, which can measure pH and detect mineral particles.

2. The Versa 3D scanning electron microscope, which allows for detailed elemental analysis, was used to analyze the chemical state of construction dust. Using the software "STATISTICA 12.6," the data obtained during the analysis are visualized. The use of scanning transmission electron microscopy technology in combination with a suite of detectors (ETD, CBS, STEM) in high vacuum conditions made it possible to study the chemical elements in dust particles in detail and obtain their clear, highly detailed images. The mass percentage of component B for each chemical element was also determined.

3. The dispersion of construction dust was studied using a logarithmically normal distribution [33, 34]. Both theoretical models and experimental data were used to describe the characteristics of dust particles. In the presented results, the key parameters were the mass fraction percentage (g) of particles and their median diameter d_{50}, measured in microns. It is important to note that for cases of a logarithmically normal distribution, it is necessary not only to specify the median diameter of the particles but also to include the value of the standard deviation of the diameters

$$\delta = \frac{d_{50}}{d_{16}} = \frac{d_{84}}{d_{50}}, \tag{3}$$

where particles with sizes d_{16} and d_{84} represent the threshold values at which the total mass of small fractions reaches 16 % and 84 % of the total mass of the dust suspension, respectively. These patterns have been confirmed by studies [35, 36].

4. The specific surface area indicator S_{SS} (cm²/g) was determined using a PSKh-10 instrument. This indicator characterizes the specific surface area of the material, expressed in square centimeters per gram. The measurement is based on recording the time interval, during which a given amount of air passes through a sample of material.
5. The Pycnomatic Evo gas-type pycnometer was used to determine the density ρ (kg/m³). It is important to determine the mass-volume characteristics of construction dust. One of the key parameters is bulk density, an indicator that reflects the ratio of the mass of a substance to the space it occupies, including voids between individual elements. Measurements are carried out using two methods. The first method involves determining the density of the material in its free state (ρ_{FS}, kg/m³), where the sample is simply filled into a measuring container. The second method involves pre-compaction of the substance using special equipment – a laboratory SSL1 orbital shaker – which makes it possible to obtain the densest packing of particles (ρ_{DP}, kg/m³).
6. The surcharge angle (α_{SA}, degrees) of construction dust was measured using a SWT-3M density analyzer. When the dust sample is poured, a cone-shaped mound is formed. The phenomenon under study is characterized by a static angle of collapse (α_{STA}, degrees), an indicator that determines the slope between the base and the side surface of the formed figure. This angle was also measured during the experiment.
7. The breaking strength of the dust layer, adhesion (σ, Pa), was measured using a special technique with the aid of an ALC-80d4 digital weighing scale. The procedure begins by loading a dust sample into an air intake syringe, where the material is sealed at a pressure of 0.5 bar. The creation of a vacuum is ensured by hermetically closing the syringe. The breaking force (F_B, g) is determined at the moment the integrity of the dust layer is violated during the reverse movement of the piston. A quantitative estimate of the tensile strength of the layer (σ, g/cm²) is calculated using an appropriate mathematical expression that takes into account the experimentally obtained data

$$\sigma = \frac{F_B - M_{IN}}{S}, \tag{4}$$

where M_{IN} is the weight of the device with dust particles, g; S is the transverse square of the dust layer at its cut-off point, cm².

Information on the classification of dust in construction according to its adhesion properties is shown in Table 1.

Table 1. Adhesion degrees of construction dust.

Adhesion degree	The breaking strength, Pa
Non-stick	<60
Baseline	60–300
Average	300–600
Strong	> 600

8. A special technique utilizing a steel capsule is employed to measure the coefficient of abrasiveness, which characterizes the ability of dust to abrade materials. The experiment is based on determining the difference in weight of the test container before and after exposure to dust particles. The testing process comprises several stages: first, the test container with a screw cap is weighed using an ALC-80d4 digital scale, then the dust sample is filled into it. Next, the container is placed in a laboratory 80-2S sedimentator, where, during rotation, mechanical interaction occurs between the dust particles and the inner surface of the container. The final weighing enables the recording of a decrease in mass of the steel container, based on which the desired dust abrasiveness index is calculated using a specific formula

$$k_{AB} = k_{AB}^{AN} \Delta g, \tag{5}$$

where Δg is the reduction of capsule weight, kg; k_{AB}^{AN} is the constant that is established based on comparison k_{AB} with known materials that have the greatest similarity.

9. A special technique was used to determine the electrical resistivity ER (Ω×m) of dust particles. The UT58B multimeter was used to measure current and resistance in an electrical circuit. At the first stage, the base resistance between the copper conductors was recorded. The experiment was carried out with controlled temperature and voltage parameters. The key point was to find the distance between the conductors, at which the circuit was closed. After that, a sample of dusty material was inserted into the point, where the circuit was closed, and the resistance measurement procedure was repeated to obtain new measurements taking into account the influence of dust. After that, the electrical resistivity of dust particles was calculated using the appropriate mathematical expression.

After that, the electrical resistance of dust particles per unit volume was calculated using the appropriate mathematical expression

$$ER = R_{DUST} \times \frac{S}{l} = \frac{U}{I} \times \frac{S}{l}, \tag{6}$$

where R_{DUST} is the dust resistance, Ω; S is the conductor square, m²; I is the gap separating a pair of electrically conductive copper elements, m; U is set voltage, V; l is the electric current intensity, A.

10. Special measurements were conducted to study the ability of dust to absorb atmospheric moisture. The process involved sequential weighing of samples: first in a completely dry state, and then with a gradual increase in ambient humidity. The most important parameter of the study was the equilibrium humidity of the dust φ_{DUST} (%), which indicates the percentage of moisture contained in a substance at a given relative humidity φ_{AT} (%). This key indicator φ_{DUST} was calculated for each sample after all measurements using a special formula

$$\varphi_{DUST} = \frac{m_{WDUST} - m_{DUST}}{m_{DUST}} \times 100, \tag{7}$$

where m_{WDUST} is the volume of dust particles that have reached the point of equilibrium in moisture saturation, g; m_{DUST} is the weight of dried dust particles, g.

This method made it possible to study in detail the hygroscopic properties of dust particles – their ability to absorb water from the environment.

11. The ability to control pollution through humidification and wet dust collection largely depends on the wettability (*Wet*, %), which characterizes the interaction of particles with water. The film flotation method is used to measure this characteristic. The procedure includes several steps: first, identical amounts of dust samples are weighed, which are then placed in an aqueous medium. After light mixing, a part of the material settles. The final stage consists of filtration, drying, and weighing of the settled particles. The final wettability index is calculated as the ratio of the mass of the sediment to the mass of dust initially introduced. This parameter is crucial in assessing the effectiveness of hydraulic removal of dust pollution. Experimental measurements make it possible to classify dust particles according to their wettability. When 80–100 % of the particles settle, a high level of wettability is observed. An intermediate value in the range of 30–80 % indicates an average degree of interaction with moisture. If the amount of settled particles does not exceed 30 %, this indicates a low wettability of the dust.

3. Results

The dust particles produced during the construction of point-pattern development, not exceeding 150 microns, are divided into several categories.

The smallest elements belong to medium-dispersed particles of 0.5–10 microns in size, which have specific intermediate properties. The larger fractions are represented by fine dust (10–50 microns), which can be viewed with low magnification under a microscope due to its slow settling. The largest particles belong to coarse dust (50–150 microns) – they are easily distinguishable to the naked eye and are

characterized by rapid deposition in the air. This four-step classification covers the entire spectrum of dust pollution encountered during construction work.

Microscopic studies have shown interesting features of construction dust. Its particles are characterized by solidity and do not form clusters. They stand out for their black color and hardness, and their surface is distinguished by its brilliance. Externally, these opaque elements resemble stone fragments with pointed edges.

Dimensional characteristics make it possible to divide dust particles into categories. Electron microscopy is necessary to study the smallest particles (less than 0.1 microns) that constantly perform Brownian motion. However, larger particles (0.1–20 microns) can be viewed using a conventional microscope; this fine dust is characterized by slow settling.

The structure of dust particles shows a significant variety of shapes. The formation of construction dust is dominated by particles with a rough, irregular structure, which is typical for crushed solids, as shown in Fig. 5.

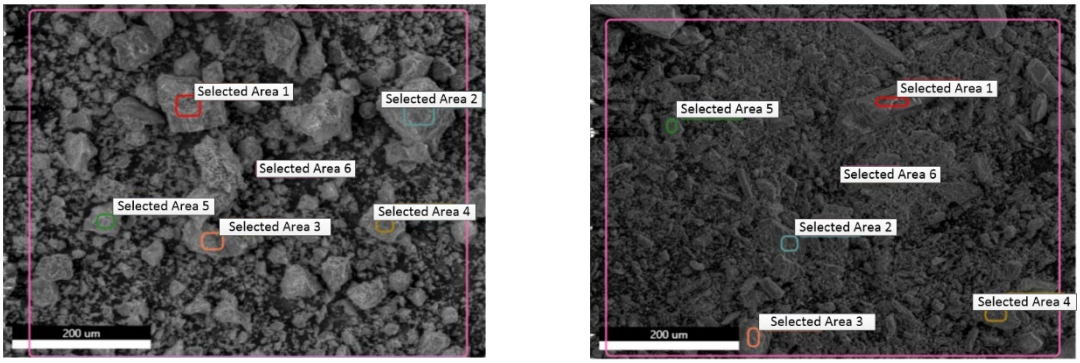

(a) **(b)**

Figure 5. Images of dust particles obtained by microscopic scanning: (a) cement dust; (b) gypsum dust.

However, it is also possible to detect elements in the dust that have a fibrous or lamellar structure due to their crystalline nature [37].

The morphological analysis of construction dust helped to distinguish three main categories of particles, differing in their spatial characteristics. Some of them are plate formations with predominant sizes in two planes. Another type includes particles with a uniform size distribution along all axes – they can have the shape of both ideal and deformed spheres or polyhedra. It is interesting to note that when such particles combine into larger formations, the resulting clusters exhibit significant morphological diversity. The latter category includes one-dimensional structures, which are elongated objects represented by fibrous, needle-like, and prismatic particle shapes.

Depending on the production method, the particles acquire different geometries. Grinding creates pointed elements, while attrition forms rounded edges. The most dangerous materials are those with cutting edges, whether it is hard quartz, glass, or metal dust. Plastic substances like clay, plaster, and cement carry less risk due to their soft structure.

A whole range of oxide compounds can be detected in the composition of the dust generated during the construction of point-pattern housing developments. It is based on substances such as sodium and potassium oxides, as well as sulfur compounds in the form of SO_2 and SO_3. A significant proportion is occupied by metal oxides – iron (Fe_2O_3), manganese (MnO), magnesium (MgO), and aluminum (Al_2O_3). In addition, phosphorus-containing components are present in the form of P_2O_5, silicon-containing components are SiO_2, and calcium compounds are CaO.

After analyzing the results obtained from studying the physical and chemical characteristics of construction dust from point-pattern housing developments in the laboratory, a compact dust atlas was created that systematizes dust particles of various sizes that occur in the construction industry. An individual specification has been compiled for each type of dust pollution, containing detailed information in tabulated form, shown in Figs. 6 and 7.

SPECIFICATION 1. CEMENT DUST

During the construction of a residential building, when carrying out work on the construction of a frame structure, a sample of pulverized cement was obtained, which is used to prepare a building mixture: t=20°C, C=79 mg/m³, V= 0.79 cm/sec, W=60%.

MORPHOLOGY OF DUST PARTICLES

The gray dust mass consists mainly of particles up to 25 micrometers in diameter. When illuminated, individual grayish-white inclusions are visible, reaching 40 microns in size. In general, the sample is characterized by a dark gray color scheme, dominated by fine gray elements.

PARTICLE SIZE DISTRIBUTION

d,μm	0.5	1	2.5	5	10
g,mass %	88	76	79	85	96
V, cm/sec	0.045	0.13	0.2	0.7	0.8

d_{50}=12 μm, δ=2.45, S_{SS} = 3545 cm²/g.

MECHANICAL CHARACTERISTICS OF DUST

ρ=2680 kg/m³	ρ_{FS}=972 kg/m³	ρ_{DP} =1083 kg/m³	k_{AB}=2.8×10⁻¹¹
α_{SA}=39°	α_{STA}=52°	σ=40Pa	Wet=98%

ELECTRICAL RESISTIVITY OF DUST AT VARIOUS TEMPERATURES

ER, Ω×m	1.5×10¹⁰	6×10¹⁰	4.3×10¹⁰	3.4×10¹⁰	2.1×10¹⁰	$max\ ER$ 6.1×10¹⁰
t,°C	50	100	150	200	250	118

ELEMENTAL COMPOSITION OF DUST

$Element$	CaO	MgO	P_2O_5	SiO_2	Al_2O_3	SO_3
B, mass %	48.2	1.4	1	27.2	3.2	19

pH=8

EQUILIBRIUM HUMIDITY OF THE DUST φ_{DUST} AT RELATIVE HUMIDITY φ_{AT}

φ_{DUST},%	0.7	1	1.3	1.4	2.9
φ_{AT},%	20	40	60	80	95

Figure 6. Specification of suspended particles formed during cement production and processing.

SPECIFICATION 2. CARBIDE RESIDUE DUST

During the construction of the frame structure of the building, a carbide residue dust sample of the material was taken, which belongs to calcareous substances.: t=23°C, C=79 mg/m³, V= 0.79 cm/sec, W=60%.

MORPHOLOGY OF DUST PARTICLES

In the passing light, you can see light beige specks of dust, although the bulk of the particles suspended in the air looks white. Dust particles are characterized by an asymmetric structure, with the largest of them reaching 40 micrometers. The predominant number of particles is white in color with a maximum size of up to 25 micrometers.

PARTICLE SIZE DISTRIBUTION

d,μm	0.5	1	2.5	5	10
g,mass %	75	79	81	84	96
V, cm/sec	0.045	0.14	0.2	0.2	0.7

d_{50}=12 μm, δ=2.45, S_{SS} = 3545 cm²/g.

MECHANICAL CHARACTERISTICS OF DUST

ρ=2480 kg/m³	ρ_{FS}=792 kg/m³	ρ_{DP} =1013 kg/m³	k_{AB}=3.1×10⁻¹¹
α_{SA}=40°	α_{STA}=52°	σ=38Pa	Wet=85%

ELECTRICAL RESISTIVITY OF DUST AT VARIOUS TEMPERATURES

ER, Ω×m	1.3×10¹⁰	5.8×10¹⁰	4.6×10¹⁰	3.4×10¹⁰	2.2×10¹⁰	$max\ ER$ 6.1×10¹⁰
t,°C	50	100	150	200	250	105

ELEMENTAL COMPOSITION OF DUST

$Element$	CaO	MgO	SO_3
B, mass %	95	3.4	1.6

pH=10

EQUILIBRIUM HUMIDITY OF THE DUST φ_{DUST} AT RELATIVE HUMIDITY φ_{AT}

φ_{DUST},%	0.2	0.3	0.65	1.8	2.05
φ_{AT},%	20	40	60	80	95

Figure 7. Specification of suspended particles formed during welding of the building frame.

The documentation includes information on sample collection methods, time parameters, materials involved, and a detailed analysis of dust characteristics. An important part of the project was the formation of a classifier of construction dust with a detailed description of its chemical and physical characteristics, as well as the methodology for their determination. All data are structured as a single information complex with a simple and intuitive navigation system.

Based on a comparative analysis of the data obtained in Rostov-on-Don and the data presented in the works of researchers [7, 14, 17, 18–21], it can be concluded that studies of the morphological and chemical parameters of dust from construction activities are often scattered. There is no systematic approach to capturing and structuring data on dust pollution, nor is there a consistent application of this data in practice to develop design and technical solutions for controlling pollution on construction sites for future construction projects. The advantage of the proposed system for determining dust pollution parameters on a construction site is its unified approach, as areas of concentrated development have their own climatic characteristics, and a dust atlas must be developed for each specific construction project.

4. Discussion

When participating in tenders and contractual prices for contractors involved in point-pattern housing development can gain significant advantages over competitors by applying data from the dust atlas of a model of a construction site or developing a dust atlas for a specific construction project. This can be achieved by including rational methods in projects of protecting the air environment from pollution and competent organization of construction work that minimizes the negative impact on the environment, knowing the list of works to be carried out on the urban area construction site and what building materials and mechanisms will be used [38].

Rationally selected dust collecting equipment helps not only to reduce costs but also to increase the profitability of point developments by reducing the environmental costs of combating and cleaning the territory and atmospheric air of the urban environment from dust pollution from point-pattern construction. The selection of dust collecting equipment requires a detailed analysis of the polluting components and their characteristics. Before installing a new dust collection system, it is important to conduct a comprehensive survey of the area, where point-pattern housing development will be implemented, including measurements of background concentrations of harmful substances, analysis of dust dispersion, assessment of temperature conditions and humidity levels, as well as dust pollution that will be generated during construction work.

It is difficult for an inexperienced contractor to independently choose the optimal solution that takes into account both the economic component and the cleaning efficiency. The physical and chemical characteristics and volume of pollutants directly affect the technical requirements for the equipment to be installed.

The proposed methodology for developing a dust atlas that takes into account the characteristics of dust for the construction of a specific point development facility will make it possible to optimize and control dust emissions at the construction site of an urban area located near the construction industry. Manufacturers often overestimate the efficiency of dust collection systems, especially when they claim performance above 98 %. It is necessary to conduct a full analysis of construction work with respect to dust before evaluating the declared characteristics of cleaning equipment and analyzing manufacturing companies' statements about their effectiveness. It is important to keep in mind that equipment testing is usually carried out on typical dust in the laboratory, so the actual efficiency may vary significantly when working with particles of different sizes and densities, as well as at different temperatures and humidity conditions.

There are many criteria to consider when choosing a cleaning system. Humidity parameters, temperature conditions of the gas environment, as well as spatial constraints for equipment installation, play a key role. It is necessary to take into account the consumption of water resources and wastewater disposal methods. The nature and characteristics of the pollutant are essential, including the resistance of particles to air flows, their dimensions and density in the medium. The difference between 99 % and 99.9 % efficiency indicators is minimal. However, if we consider this difference from the point of view of the ability to suppress and reduce the concentration of dust pollution, then the difference can be tenfold. When choosing equipment, its cost and installation location play a key role. These criteria are closely linked and require integrated assessment. In conditions of limited space, it is often necessary to give preference to compact but expensive installations, although there are equally efficient and more economical alternatives of a larger size. The specifics of the location of the facility also affect the choice – for hard-to-reach areas and cramped construction sites, more advanced and expensive equipment may be needed. There is no universal solution – each case requires individual consideration of all parameters. Making the best decision involves a thorough analysis of both technical characteristics and economic feasibility. It is necessary to study all aspects in detail, since the obvious choice at first glance may not be the most rational.

Choosing the most cost-effective dust control equipment requires an analysis of certain economic and technical indicators.

1. Equipment utilization rate K_U shows the ratio of the time of the actual operation of the machine for a certain period of time to the duration of this period

$$K_U = \frac{t_{ACTUAL}}{t_{OP}}, \tag{8}$$

where t_{ACTUAL} is the actual operation time of the dust control equipment on the construction site, months; t_{OP} is the overall time spent by the equipment on the construction site.

The value of the equipment utilization rate K_U for periodically used equipment in technological operations ranges from 0.05 to 0.1. The continuously operating installations have $K_U \le 1$, since part of the time is spent on maintenance and repair work. Under these conditions, the choice of equipment will depend on the actual parameters of the abrasiveness of the dust which will be deleted by this equipment.

1. Profitability of equipment P is the ratio of the useful return UR of the equipment for a certain period to the total cost of the equipment C_{EQ} for the same period

$$P = \frac{UR}{C_{EQ}}. \tag{9}$$

Let us consider the economic effect of the introduction of a wet dust collector at a construction site. Prior to its installation, the company incurred significant costs. They included expenses for dust control: regular humidification, cleaning, cleaning and updating of work clothes. In addition, the company was losing funds due to frequent sick leave. All these costs UR form a basic amount of money that can be saved after installing the dust collection equipment with the technical characteristics of dust collection that correspond to the data of the analysis of the physical and chemical characteristics of the dust, which will be deleted by this equipment.

2. The total costs C_{TOTAL} associated with the operation and maintenance of dust collection systems can be calculated by this expression

$$C_{TOTAL} = C_{EN} + C_{CS} + C_{ER} + C_{DE}, \tag{10}$$

where C_{EN} is the cost of consumed electricity; C_{CS} is he cost of consumables (for example, filter media that is periodically replaced, water); C_{ER} is the cost of equipment repair, payment of maintenance personnel for repairs, tools necessary for maintenance during operation of the equipment; C_{DE} is the costs of depreciation that reduce the cost of equipment due to its wear and tear.

When choosing efficient equipment, $P > 1$. The rational selection of equipment, taking into account the data of the dust atlas, reduces these costs.

3. Assessment of the financial benefits FB of upgrading the facility using technical means

$$FB = UR - C_{TOTAL} = UR\left(\frac{C_{TOTAL}}{UR}\right) = UR\left(1 - \frac{1}{P}\right). \tag{11}$$

4. The total economic benefit $\sum E$ accumulated over the entire period of operation of the technical means is

$$\sum E = t_{OP} \times \left[UR - \left(C_{EN} + C_{ER}\right)\right] - \sum C_{ER} - \sum C_{DE}. \tag{12}$$

5. The assessment of the economic efficiency of the equipment K_{EF} reflects the ratio between the total operating costs and the initial cost of the technical means and takes into account all costs during use

$$K_{EF} = \frac{\sum C_{TOTAL}}{C_{EQ}}, \tag{13}$$

where C_{EQ} is the cost of buying or renting equipment.

6. The equipment cost coefficient K_{EC} is the percentage ratio of the cost of the machine to the amount of costs

$$K_{EC} = \frac{C_{EQ}}{\sum C_{TOTAL}} \times 100. \tag{14}$$

As the service life of t_{OP} increases, there is a significant increase in the K_{EF} indicator, reflecting operating costs, which can reach values from 50 to 100. This leads to the fact that the share of depreciation charges C_{DE} in the structure of total expenses shows a tendency to decrease.

Based on the collected information on the physical and chemical characteristics of construction dust, presented in a dust atlas, the calculation and selection of optimal dust collection equipment for a point-pattern housing development facility – an 11-storey residential complex – was carried out. Tables 2 and 3 show the initial parameters and the final calculation results. The analysis included a comparison of several installations with identical cleaning and performance indicators, shown in Fig. 8, but differing in operational characteristics and maintenance costs. The information obtained on the dust composition made it possible to adjust the calculations and optimize the choice of equipment, taking into account technical and economic factors.

(a) **(b)**

Figure 8. Dust collecting equipment for the construction site: (a) vehicle-mounted water mist cannon atomizer sprayer Fog Elefante 70 by INDROBASE (Italy); (b) WLP 500 dust suppression system by WLP (Italy).

Table 2. Initial data and parameters for assessing the economic feasibility of using dust cleaning systems.

No.	Initial data	Units	Fog Elefante 70	WLP 500
1	K_U	USD	1 323.81	1 632.45
2	*UR*	USD	1 224.34	1 224.34
3	t_{OP}	Months	6	6
4	C_{EN}	USD	271.39	46.93
5	C_{ER}	USD	336.69	73.46
6	t_{ACTUAL}	Months	4	4
7	C_{CS}	USD	38.26	20.41
8	C_{DE}	USD	12.24	26.12

Table 3. The results of the calculation of the feasibility study.

No.	Indicators	Fog Elefante 70	WLP 500
1	K_U	0.67	0.67
2	C_{TOTAL}	658.59 USD	166.92 USD
3	*P*	1.85	7.3
4	*E*	563.19 USD	1 065.17 USD
5	K_{EF}	0.49	0.1
6	K_{EC}	201	977

When choosing dust-collecting equipment, the key role is played by its efficiency indicators, including productivity and durability, which in turn depends on the characteristics of the dust emissions, with which it operates. A rational decision on the purchase of equipment can be made by analyzing the total cost of transportation, maintenance, and repair during the entire period of use. An individual calculation of operating costs for a specific case allows us to assess the economic feasibility of introducing equipment into the production process and make the best choice in terms of financial costs.

A study of previous work on the formation of dust particles in construction sites [4, 39] revealed both common features and discrepancies with the data we obtained. Our work focused on a detailed study of the chemical composition and physical properties of dust pollutants that occur during construction work. The main goal was to find effective methods of controlling dust emissions to protect the ecology of urban airspace and protect the health of residents whose homes are located near point-pattern housing developments. In our study, we did not limit ourselves to the chemical analysis of construction dust but also

studied in detail its dispersed characteristics. In point-pattern housing developments, this analysis technique shows the most accurate results in determining the properties of dust particles, surpassing traditional methods for estimating dust emissions on construction sites. Of particular value is the fact that we measured the concentration of dust, its chemical composition, density, surcharge angle, adhesion, abrasiveness, electrical resistivity, hygroscopicity, and wettability for each individual type of construction work. Thanks to this, the created dust pollution atlases can be effectively used in a variety of situations – from the construction of new buildings to the reconstruction of existing facilities and even during repair activities. In this scientific work, the main focus was on the study of particulate matter, although the analysis of silica particles is equally important in assessing construction emissions. It is noteworthy that the degree of harmful effects of dust pollution on construction sites is largely determined by the concentration of silica in the dust. It is worth noting that the conducted research is not without certain drawbacks, and the study of the silica component remains a promising area for further scientific research in the field of construction dust pollution.

5. Conclusions

The physical and chemical characteristics of construction dust, including its size, shape, composition, and electrical charge, determine the degree of its impact on the environment and human health. Fine particles ranging in size from PM0.5 to PM10, which are formed during construction work, are particularly dangerous. Their influence extends to both workers and residents of the surrounding areas. The ability of particles to stay in the air for a long time and penetrate deep into the respiratory tract directly depends on their size. This parameter also determines their chemical activity and electrostatic properties. Therefore, measuring the size of dust particles on construction sites is crucial for assessing potential harm to health and developing protective measures.

In modern cities undergoing rapid development, it is critically important to control air quality, especially in the context of construction activities. Throughout the entire life cycle of a building, from construction to dismantling, there is a constant impact of dust pollution on the environment. The scientific community, both internationally and locally, pays increased attention to environmental degradation caused by dust pollutants. When designing new facilities, it is necessary to take into account research data on particulate emissions, which makes it possible to create a more environmentally friendly urban environment.

References

1. Lumens, M.E.G.L., Spee, T. Determinants of exposure to respirable quartz dust in the construction industry. The Annals of Occupational Hygiene. 2001. 45(7). Pp. 585–595. DOI: 10.1016/S0003-4878(01)00025-4
2. Xu, L., Pei, Z. Preparation and Optimization of a Novel Dust Suppressant for Construction Sites. Journal of Materials in Civil Engineering. 2017. 29(8). Article no. 04017051. DOI: 10.1061/(ASCE)MT.1943-5533.0001902
3. Meskhi, B.Ch., Evtushenko, A.I., Azarov, V.N., Zhukova, N. Comprehensive assessment of the dust environment at the construction industry enterprises. E3S Web of Conferences. 2021. 281. Article no. 09024. DOI: 10.1051/e3sconf/202128109024
4. Samaradiwakara, D.S., Pitawala, H.M.T.G.A. Extent of air pollution in Kandy area, Sri Lanka: morphological, mineralogical and chemical characterization of dust. Ceylon Journal of Science. 2021. 50(4). Pp. 475–486. DOI: 10.4038/cjs.v50i4.7946
5. Chen, X., Guo, C., Song, J., Wang, X., Cheng, J. Occupational health risk assessment based on actual dust exposure in a tunnel construction adopting roadheader in Chongqing, China. Building and Environment. 2019. 165(1). Article no. 106415. DOI: 10.1016/j.buildenv.2019.106415
6. Dickerson, D.E. Environmental relative burden index: A streamlined life cycle assessment method for facilities pollution prevention. J. Green Build. 2016. 11(1). Article no. 106415. DOI: 10.3992/jgb.11.1.95.1
7. Hu, M. Assessment of effective energy retrofit strategies and related impact on indoor environmental quality. Journal of Green Building. 2017. 12(2). Pp. 38–55. DOI: 10.3992/1943-4618.12.2.38
8. Zuo, J., Rameezdeen, R., Hagger, M., Zhou, Z., Ding, Z. Dust pollution control on construction sites: Awareness and self-responsibility of managers. Journal of Cleaner Production. 2017. 166(4). Pp. 312–320. DOI: 10.1016/j.jclepro.2017.08.027
9. Cheng, S., Chen, D., Li, J., Wang, H. An ARPS-CMAQ Modeling Approach for Assessing the Atmospheric Assimilative Capacity of the Beijing Metropolitan Region. Water, Air, and Soil Pollution. 2007. 181(1). Pp. 211–224. DOI: 10.1007/s11270-006-9294-8
10. Sarkar, A., Thakur, B., Gupta, A. Particulate pollution at construction sites of Kolkata and associated health burden for exposed construction workers. Urban Climate. 2023. 52(12). Article no. 101750. DOI: 10.1016/j.uclim.2023.101750
11. Kumi, L., Jeong, J., Jeong, J., Lee, J. Empirical Analysis of Dust Health Impacts on Construction Workers Considering Work Types. Buildings. 2022. 12(8). Article no. 1137. DOI: 10.3390/buildings12081137
12. Wu, Z., Zhang, X., Wu, M. Mitigating construction dust pollution: State of the art and the way forward. Journal of Cleaner Production. 2016. 112(2). Pp. 1658–1666. DOI: 10.1016/j.jclepro.2015.01.015
13. Luo, Q., Huang, L., Liu, Y., Xue, X., Zhou, F., Hua, J. Monitoring Study on Dust Dispersion Properties during Earthwork Construction. Sustainability. 2021. 13(15). Article no. 8451. DOI: 10.3390/su13158451
14. William Burgos, A. Ellwood. Regulatory Methods Used in Writing NPDES Permits for the Shipbuilding and Repair Industry. Naval Engineers Journal. 2009. 111(2). Pp. 91–97. DOI: 10.1111/j.1559-3584.1999.tb00758.x
15. Zuo, J., Rameezdeen, R., Hagger, M., Zhou, Z., Ding, Z. Dust pollution control on construction sites: Awareness and self-responsibility of managers. Journal of Cleaner Production. 2017. 166(4). Pp. 312–320. DOI: 10.1016/j.jclepro.2017.08.027
16. Cheriyan, D., Choi, J.-H. A review of research on particulate matter pollution in the construction industry. Journal of Cleaner Production. 2020. 254(2). Article no. 120077. DOI: 10.1016/j.jclepro.2020.120077

17. Zhang, Y., Tang, W., Li, H., Guo, J., Wu, J., Guo, Y. The Evaluation of Construction Dust Diffusion and Sedimentation Using Wind Tunnel Experiment. Toxics. 2022. 10(8). Article no. 412. DOI: 10.3390/toxics10080412
18. Karin, A.-D., Clifford, K., Hand, J. Dust Under the Radar: Rethinking How to Evaluate the Impacts of Dust Events on Air Quality in the United States. GeoHealth. 2023. 7(12). Article no. e2023GH000953. DOI: 10.1029/2023GH000953
19. Xing, J., Ye, K., Zuo, J., Jiang, W. Control Dust Pollution on Construction Sites: What Governments Do in China? Sustainability. 2018. 10(8). Article no. 2945. DOI: 10.3390/su10082945
20. Noh, H.-J., Lee, S.-K., Yu, J.-H. Identifying Effective Fugitive Dust Control Measures for Construction Projects in Korea. Sustainability. 2018. 10(4). Article no. 1206. DOI: 10.3390/su10041206
21. Stephanie, W., Alistair, S., Yongming, T., Marc, S., Andrew, Y., Eddy, R., Andy, W. The simulation of mineral dust in the United Kingdom Earth System Model UKESM1. Atmospheric Chemistry and Physics. 2022. 22(22). Article no. 14503. DOI: 10.5194/acp-22-14503-2022
22. Han, S.-W., Joo, H.-S., Kim, K.-C., Cho, J.-S., Moon, K.-J., Han, J.-S. Modification of Hybrid Receptor Model for Atmospheric Fine Particles (PM2.5) in 2020 Daejeon, Korea, Using an ACERWT Model. Atmosphere. 2024. 15(4). Article no. 477. DOI: 10.3390/atmos15040477
23. Yu, B., Lu, X., Fan, X., Fan, P., Zuo, L., Yang, Y., Wang, L. Analyzing environmental risk, source and spatial distribution of potentially toxic elements in dust of residential area in Xi'an urban area, China. Ecotoxicology and Environmental Safety. 2021. 208(6). Article no. 111679. DOI: 10.1016/j.ecoenv.2020.111679
24. Tao, G., Feng, J., Feng, H., Zhang, K. Reducing Construction Dust Pollution by Planning Construction Site Layout. Buildings. 2022. 12(531). Article no. 531. DOI: 10.3390/buildings12050531
25. Klaver, Z.M., Crane, R.C., Ziemba, R.A., Bard, R.L., Adar, S.D., Brook, R.D., Morishita M. Reduction of Outdoor and Indoor PM2.5 Source Contributions via Portable Air Filtration Systems in a Senior Residential Facility in Detroit, Michigan. Toxics. 2023. 11(12). Article no. 1019. DOI: 10.3390/toxics11121019
26. Chen, X., Guo, C., Song, J., Wang, X., Cheng, J. Occupational health risk assessment based on actual dust exposure in a tunnel construction adopting roadheader in Chongqing, China. Building and Environment. 2019. 165(1). Article no. 106415. DOI: 10.1016/j.buildenv.2019.106415
27. Dietrich, M., Barlow, C.F., Entwistle, J.A., Meza-Figueroa, D., Dong, C., Gunkel-Grillon, P., Jabeen, K., Bramwell, L., Shukle, J.T., Wood, L.R. et al. Predictive modeling of indoor dust lead concentrations: Sources, risks, and benefits of intervention. Environmental Pollution. 2023. 319(2-3). Article no. 121039. DOI: 10.1016/j.envpol.2023.121039
28. Azarov, V.N., Trokhimchyk, M.K., Sidelnikova, O.E. Research of dust content in the earthworks working area. Procedia Engineering. 2016. 150. Pp. 2008–2012. DOI: 10.1016/j.proeng.2016.07.282
29. Sergina, N.M. Issues of protection of atmospheric air against dust pollution in production of construction materials. IOP Conference Series: Materials Science and Engineering. 2019. 687(6). Article no. 066034. DOI: 10.1088/1757-899X/687/6/066034
30. Azarov, V., Lukanin, D., Borovkov, D., Redhwan, A. Experimental Study of Secondary Swirling Flow Influence on Flows Structure at Separation Chamber Inlet of Dust Collector with Counter Swirling Flows. International Review of Mechanical Engineering. 2014. 8(5). Article no. Pp. 851–856. DOI: 10.15866/ireme.v8i5.3455
31. Azarov, V.N., Batmanov, V.P., Strelyaeva, A.B. Aerodynamic characteristics of dust in the emissions into the atmosphere and working zone of construction enterprises. International Review of Civil Engineering. 2016. 7(5). Pp. 132–136. DOI: 10.15866/irece.v7i5.9869
32. GOST R 58577-2019. Regulation for establishment of permissible limits of pollutant emissions by economic entities being projected and in operation and methods of determination of the limits. Moscow, 2019.
33. Lapko, A., Vasiliy, L. Estimation of traditional numerical characteristics of lognormal distribution laws of a one-dimensional random variable in conditions of large volume statistical data. Measurement Techniques. 2024. 67(7). Pp. 23–29. DOI: 10.1007/s11018-024-02332-y
34. Huang, Y. Cascades and Kolmogorov's lognormal scaling in two-dimensional bacterial turbulence. Physics of Fluids. 2024. 36(6). Article no. 065149. DOI: 10.1063/5.0216209
35. Menzelintseva, N.V., Karapuzova, N.Y., Mikhailovskaya, Y.S., Redhwan, A.M. Efficiency of standards compliance for PM10 and PM2.5. International Review of Civil Engineering. 2016. 7(6). Pp. 192–195. DOI: 10.15866/irece.v7i6.9750
36. Evtushenko, A., Lupinogin, V., Kaluzgina, E., Strelyaeva, A., Sakharova, A. Investigation of air pollution with fine dust during repair and construction work inside premises. IOP Conference Series: Earth and Environmental Science. 2021. 937(2). Article no. 022082. DOI: 10.1088/1755-1315/937/2/022082
37. Lupinogin, V., Azarov, V., Gorshkov, E., Nikolenko, M. On the evaluation of storage facilities on the dustiness of the urban environment. E3S Web of Conferences. 2019. 126(5). Article no. 00073. DOI: 10.1051/e3sconf/201912600073
38. Mweendi, P., Shafodino, F., Munyaradzi, Z., Mwapagha, L. Assessment of Bacteria, Morphological Characteristics, and Elemental Composition of Dust Fallout. Journal of Geoscience and Environment Protection. 2023. 11(8). Pp. 114–130. DOI: 10.4236/gep.2023.118007
39. Evelyn, T.N., Simone, H., Ton, S., Judith, S., Friso, S., Mieke, L., Dick, H. Dust Control Measures in the Construction Industry. The Annals of Occupational Hygiene. 2003. 47(3). Pp. 211–218. DOI: 10.1093/annhyg/meg023

Information about the authors:

***Svetlana Manzhilevskaya**, PhD in Technical Sciences*
ORCID: https://orcid.org/0000-0001-7065-3726
E-mail: smanzhilevskaya@yandex.ru

Received 12.02.2025. Approved after reviewing 06.02.2026. Accepted 06.02.2026.

Magazine of Civil Engineering

ISSN 2712-8172

journal homepage: http://engstroy.spbstu.ru/

Research article

UDC 539.3

DOI: 10.34910/MCE.141.9

Comparison of single-field and three-field fem in nonlinear shell calculations

M.Yu. Klochkov[1], ***V.A. Pshenichkina***[1], ***A.P. Nikolaev***[2], ***Yu.V. Klochkov***[2], ***O.V. Vakhnina***[2] ✉

[1] *Volgograd State Technical University, Volgograd, Russian Federation*

[2] *Volgograd State Agrarian University, Volgograd, Russian Federation*

✉ *ovahnina@bk.ru*

Keywords: three-field finite element method, nonlinear mixed functional, kinematic unknowns, force unknowns, deformation unknowns

Abstract. On the basis of physical equations of deformation theory of plasticity using Kirchhoff–Lava hypothesis, matrix dependences between columns of forces and moments and columns of deformations and curvatures of the shell midface are determined at the loading step. As a finite element, a quadrilateral fragment of the shell midface with nodal unknowns in the form of: increments of displacements and their derivatives; increments of deformations and increments of curvatures; increments of forces and increments of moments were used. To approximate the required quantities, the following expressions are adopted: bicubic functions with elements of Hermite polynomials of the third degree for displacements; bilinear functions for deformation and force parameters. To obtain the stiffness matrix of the finite element, the nonlinear Lagrangian functional on the loading step was used with an additional condition: the real work of the difference of forces determined using their direct approximation and using approximating expressions for displacements, on deformations and curvatures of the loading step must be equal to zero. Minimisation of the functional by nodal unknowns provides three systems of equations, the solution of which determines the stiffness matrix of the finite element used to calculate the displacement fields. The force and deformation parameters at the discretisation nodes of the shell are determined from the displacements found. Case studies show the effectiveness of using a three-field finite element method (FEM) technique compared to using FEM in the displacement method formulation (single-field technique).

Citation: Klochkov, M.Yu., Pshenichkina, V.A., Nikolaev, A.P., Klochkov, Yu.V., Vakhnina, O.V. Comparison of single-field and three-field fem in nonlinear shell calculations. Magazine of Civil Engineering. 2026. 19(1). Article no. 14109. DOI: 10.34910/MCE.141.9

1. Introduction

Definition of the object of study. Structures consisting of shells and their fragments are now increasingly used in various fields. These include hangars, warehouses, domes and slabs, tanks, bunkers, cisterns, pipelines and others. The worldwide trend aimed at significant reduction of material intensity of systems and objects actualises the problem of determining the stress-strain state (SSS) of structures in the form of shells and their fragments in a physically nonlinear formulation.

Assumption within the regulated limits of the plastic stage of the applied material of structures allows to reduce the overall material intensity of structures, including those consisting of shells.

Literature review. The developed theory of solid body deformation [1–4] turned out to be theoretically unrealisable in the practice of engineering calculations of real structures, which led to the development of numerical methods for solving the equations of solid body deformation mechanics [5–9]. At the present stage of development of structural mechanics and computer science, the main tool for investigating the SSS of shell structures beyond the elastic limit is numerical finite element method (FEM). In spite of the considerable volume of publications on this subject [10–15] and the availability of foreign (ANSYS, ABAQUS, NASTRAN, etc.) and domestic (PRIIS, LIRA, etc.) finite element computational systems, the problem of finding the most optimal formulations of the FEM for the calculation of shell structures in a physically nonlinear setting remains quite relevant. It is known that the FEM in the form of the displacement method is the most widespread at present, but it does not lack the disadvantages associated with the use of only one field of unknowns – the displacement field. The mixed variant of the FEM with kinematic and force fields of unknowns [16–23], as well as the FEM variant with three fields of unknowns [24, 25], are becoming the most promising.

Purpose and objectives of the study. In this paper, the three-field variant of the mixed FEM is applied to the calculation of shells under elastic-plastic deformation and the finite element solutions obtained on its basis are compared with the solutions obtained using the FEM in the formulation of the displacement method in a physically nonlinear setting.

2. Materials and Methods

In order to realise the three-field variant of the mixed FEM in a physically nonlinear formulation, it is first of all necessary to formulate the corresponding nonlinear three-field functional. For this purpose, we introduce the following matrix notations: $\underset{1\times6}{\left\{S^{\alpha\beta}\right\}^T}=\left\{N^{11}N^{22}N^{12}M^{11}M^{22}M^{12}\right\}$; $\underset{1\times6}{\left\{\Delta S^{\alpha\beta}\right\}^T}=\left\{\Delta N^{11}\Delta N^{22}\Delta N^{12}\Delta M^{11}\Delta M^{22}\Delta M^{12}\right\}$ is matrix-string of longitudinal forces and bending moments and their increments at the loading step, respectively; $\underset{1\times6}{\left\{\Delta\varepsilon_{\alpha\beta}\right\}^T}=\left\{\Delta\varepsilon_{11}\Delta\varepsilon_{22}2\Delta\varepsilon_{12}\Delta\aleph_{11}\Delta\aleph_{22}2\Delta\aleph_{12}\right\}$ is matrix-string of deformation increments and curvature increments at the midpoint of the shell structure surface at the loading step; $\underset{1\times3}{\left\{\Delta U\right\}^T}=\left\{\Delta v^1\Delta v^2\Delta v\right\}$ is matrix-string of step increments of displacement vector components; $\underset{1\times3}{\left\{P\right\}^T}=\left\{p_1p_2p\right\}$; $\underset{1\times3}{\left\{\Delta P\right\}^T}=\left\{\Delta p_1\Delta p_2\Delta p\right\}$ are matrix-string of external surface load vector components and their step increments, respectively.

The increments of longitudinal forces $\Delta N^{\alpha\beta}$ and increments of bending moments $\Delta M^{\alpha\beta}$ at the loading step can be expressed through the increments of deformation and increments of curvature $\left\{\Delta\varepsilon_{\alpha\beta}\right\}$ using the following relations:

$$\underset{3\times1}{\left\{\Delta N^{\alpha\beta}\right\}}=\int\limits_{-\frac{h}{2}}^{\frac{h}{2}}\left\{\Delta\sigma^{\alpha\beta}\right\}d\zeta=\int\limits_{-\frac{h}{2}}^{\frac{h}{2}}\underset{3\times3}{\left[C_p\right]}\underset{3\times6}{\left[G\right]}d\zeta\underset{6\times1}{\left\{\Delta\varepsilon_{\alpha\beta}\right\}}=\underset{3\times6}{\left[\alpha_p\right]}\underset{6\times1}{\left\{\Delta\varepsilon_{\alpha\beta}\right\}};\tag{1}$$

$$\underset{3\times1}{\left\{\Delta M^{\alpha\beta}\right\}}=\int\limits_{-\frac{h}{2}}^{\frac{h}{2}}\left\{\Delta\sigma^{\alpha\beta}\right\}\zeta d\zeta=\int\limits_{-\frac{h}{2}}^{\frac{h}{2}}\underset{3\times3}{\left[C_p\right]}\underset{3\times6}{\left[G\right]}\zeta d\zeta\underset{6\times1}{\left\{\Delta\varepsilon_{\alpha\beta}\right\}}=\underset{3\times6}{\left[\beta_p\right]}\underset{6\times1}{\left\{\Delta\varepsilon_{\alpha\beta}\right\}},\tag{2}$$

where $\underset{1\times3}{\left\{\Delta N^{\alpha\beta}\right\}^T}=\left\{\Delta N^{11}\Delta N^{22}\Delta N^{12}\right\}$; $\underset{1\times3}{\left\{\Delta M^{\alpha\beta}\right\}^T}=\left\{\Delta M^{11}\Delta M^{22}\Delta M^{12}\right\}$; $\underset{3\times6}{\left[\alpha_p\right]}=\int\limits_{-\frac{h}{2}}^{\frac{h}{2}}\underset{3\times3}{\left[C_p\right]}\underset{3\times6}{[G]}d\zeta$ and $\underset{3\times6}{\left[\beta_p\right]}=\int\limits_{-\frac{h}{2}}^{\frac{h}{2}}\underset{3\times3}{\left[C_p\right]}\underset{3\times6}{[G]}\zeta d\zeta$ are matrices obtained by numerically finding definite integrals; $\underset{1\times3}{\left\{\Delta\sigma^{\alpha\beta}\right\}^T}=\left\{\Delta\sigma^{11}\Delta\sigma^{22}\Delta\sigma^{12}\right\}$ are the increments of the contravariant components of the stress tensor at the loading step.

The plasticity matrix included in (1) and (2) $\left[C_p\right]$ is composed on the basis of the relationships of the deformation theory of plasticity [4], represented in a curvilinear coordinate system by the expression:

$$E_{\alpha\beta}=\frac{3}{2}\cdot\frac{\varepsilon_i}{\sigma_i}T_{\alpha\beta}, \tag{3}$$

where $E_{\alpha\beta}=\varepsilon^{\varsigma}_{\alpha\beta}-\frac{1}{3}g_{\alpha\beta}P_{\varepsilon}$ are components of the deformation deviator; ε_i, σ_i are intensity of deformations and stresses; $T_{\alpha\beta}=\sigma_{\alpha\beta}-\frac{1}{3}g_{\alpha\beta}P_{\sigma}$ is stress deviator; $P_{\varepsilon}=g^{\alpha\beta}\varepsilon_{\alpha\beta}$, $P_{\sigma}=g_{\mu\nu}\sigma^{\mu\nu}$ are first invariants of strain and stress tensors; $g_{\alpha\beta}$, $g^{\alpha\beta}$ are covariant and contravariant components of the metric tensor.

The increments of deformations in an arbitrary layer at a loading step are determined by differentiating (3) in the following general form:

$$\Delta\varepsilon^{\varsigma}_{\alpha\beta}=\frac{\partial\varepsilon^{\varsigma}_{\alpha\beta}}{\partial\sigma^{\mu\nu}}\Delta\sigma^{\mu\nu}. \tag{4}$$

The partial derivatives included in (4) were determined by the relations:

$$\begin{aligned}\frac{\partial\varepsilon^{\varsigma}_{11}}{\partial\sigma^{11}}&=\frac{3}{2}\cdot\frac{\varepsilon_i}{\sigma_i}g_{11}g_{11}+\frac{3}{2}\left(g_{11}g_{11}\sigma^{11}+2g_{11}g_{12}\sigma^{12}+g_{12}g_{12}\sigma^{22}\right)\cdot\frac{\partial\left(\varepsilon_i/\sigma_i\right)}{\partial\sigma^{11}}+\\&+g_{11}g_{11}\left(\frac{1}{3}\cdot\frac{1-2\nu}{E}-\frac{1}{2}\cdot\frac{\varepsilon_i}{\sigma_i}\right)-\frac{1}{2}g_{11}P_{\sigma}\cdot\frac{\partial\left(\varepsilon_i/\sigma_i\right)}{\partial\sigma^{11}};\\\frac{\partial\varepsilon^{\varsigma}_{12}}{\partial\sigma^{12}}&=\frac{3}{2}\cdot\frac{\varepsilon_i}{\sigma_i}\left(g_{12}g_{22}+g_{12}g_{21}\right)+\\&+\frac{3}{2}\left(g_{11}g_{21}\sigma^{11}+\sigma^{12}\left(g_{11}g_{22}+g_{12}g_{21}\right)+g_{12}g_{22}\sigma^{22}\right)\cdot\frac{\partial\left(\varepsilon_i/\sigma_i\right)}{\partial\sigma^{12}}+\\&+2g_{12}g_{12}\left(\frac{1}{3}\cdot\frac{1-2\nu}{E}-\frac{1}{2}\cdot\frac{\varepsilon_i}{\sigma_i}\right)-\frac{1}{2}g_{12}P_{\sigma}\cdot\frac{\partial\left(\varepsilon_i/\sigma_i\right)}{\partial\sigma^{12}},\end{aligned} \tag{5}$$

where E is modulus of elasticity; ν is coefficient of transverse deformation.

The derivatives of the ratio of strain and stress intensities included in (5) are determined by the expressions:

$$\frac{\partial\left(\varepsilon_i/\sigma_i\right)}{\partial\sigma^{\mu\tau}}=\frac{\partial\left(\varepsilon_i/\sigma_i\right)}{\partial\sigma_i}\cdot\frac{\partial\sigma_i}{\partial\sigma^{\mu\tau}}=\left(\frac{\partial\varepsilon_i}{\partial\sigma_i}\sigma_i-1\cdot\varepsilon_i\right)\cdot\frac{1}{\sigma_i^2}=\psi\frac{\partial\sigma_i}{\partial\sigma^{\mu\tau}},\tag{6}$$

where $\psi=\frac{1}{\sigma_i}\left(\frac{1}{E_K}-\frac{1}{E_C}\right)$; E_K, E_C are tangent and secant modules of the deformation diagram;

$$\frac{\partial\sigma_i}{\partial\sigma^{11}}=\frac{3}{4}\cdot\frac{1}{\sigma_i}\left(\left(1-\frac{1}{3}g^{11}g_{11}\right)T_{11}+\frac{2}{3}g_{11}g_{11}T^{11}-\frac{1}{3}g^{22}g_{11}T_{22}+\right.$$

$$\left.+\left(g_{21}g_{21}-\frac{1}{3}g_{22}g_{11}\right)T^{22}-\frac{2}{3}g^{12}g_{11}\right)T_{12}+\frac{4}{3}g_{11}g_{21}T^{12}-\frac{1}{3}g^{33}g_{11}T_{33}-\frac{1}{3}g_{33}g_{11}T^{33}.$$

Using (4), (5), (6) a matrix dependence is formed:

$$\underset{3\times1}{\left\{\Delta\varepsilon\right\}}=\underset{3\times3}{\left[\omega\right]}\underset{3\times1}{\left\{\Delta\sigma^{\alpha\beta}\right\}},\tag{7}$$

where $\underset{1\times3}{\left\{\Delta\varepsilon^{\zeta}\right\}^T}=\left\{\Delta\varepsilon_{11}^{\zeta}\Delta\varepsilon_{22}^{\zeta}2\Delta\varepsilon_{12}^{\zeta}\right\}$.

Matrix $\underset{3\times3}{\left[C_p\right]}$ determined by matrix inversion $\underset{3\times3}{\left[\omega\right]}$.

Taking into account the above, the matrix relationship is written:

$$\underset{3\times1}{\left\{\Delta\sigma^{\alpha\beta}\right\}}=\underset{3\times3}{\left[C_p\right]}\underset{3\times1}{\left\{\Delta\varepsilon_{\alpha\beta}^{\zeta}\right\}}=\underset{3\times3}{\left[C_p\right]}\underset{3\times6}{\left[G\right]}\underset{6\times1}{\left\{\Delta\varepsilon_{\alpha\beta}\right\}},\tag{8}$$

where $\underset{1\times3}{\left\{\Delta\varepsilon_{\alpha\beta}^{\zeta}\right\}^T}=\left\{\Delta\varepsilon_{11}^{\zeta}\Delta\varepsilon_{22}^{\zeta}2\Delta\varepsilon_{12}^{\zeta}\right\}$; $\underset{3\times6}{\left[G\right]}=\begin{bmatrix}1&0&0&\zeta&0&0\\0&1&0&0&\zeta&0\\0&0&1&0&0&\zeta\end{bmatrix}$.

Taking into account (1) and (2), the following matrix relation can be composed as follows:

$$\underset{6\times1}{\left\{\Delta S_K^{\alpha\beta}\right\}}=\underset{6\times6}{\left[\gamma\right]}\underset{6\times1}{\left\{\Delta\varepsilon_{\alpha\beta}\right\}},\tag{9}$$

where $\underset{6\times6}{\left[\gamma\right]}=\begin{bmatrix}\underset{3\times6}{\left[\alpha_p\right]}\\\underset{3\times6}{\left[\beta_p\right]}\end{bmatrix}$.

If we use a four-node fragment of its midface [24] with nodes i, j, k, l as a discretisation element of the shell structure, the increments of longitudinal forces and increments of bending moments at the loading step can be expressed through their nodal values by means of bilinear relationships:

$$\Delta Q^{\alpha\beta}=\frac{1-\xi}{2}\cdot\frac{1-\eta}{2}\left(\Delta Q^{\alpha\beta}\right)^i+\frac{1+\xi}{2}\cdot\frac{1-\eta}{2}\left(\Delta Q^{\alpha\beta}\right)^j+\frac{1+\xi}{2}\cdot\frac{1+\eta}{2}\left(\Delta Q^{\alpha\beta}\right)^k+$$
$$+\frac{1-\xi}{2}\cdot\frac{1+\eta}{2}\left(\Delta Q^{\alpha\beta}\right)^l=\underset{1\times4}{\left\{\varphi\right\}^T}\underset{1\times4}{\left\{\Delta Q_u^{\alpha\beta}\right\}},\tag{10}$$

where $-1 \le \xi,\ \eta \le 1$ are local coordinates used to organise the procedure of numerical integration by Gauss quadrature; $\underset{1\times4}{\left\{\Delta Q_u^{\alpha\beta}\right\}^T} = \left\{\left(\Delta Q^{\alpha\beta}\right)^i \left(\Delta Q^{\alpha\beta}\right)^j \left(\Delta Q^{\alpha\beta}\right)^k \left(\Delta Q^{\alpha\beta}\right)^l\right\}$.

Here, $\Delta Q^{\alpha\beta}$ is understood as $\Delta N^{\alpha\beta}$ or $\Delta M^{\alpha\beta}$. On the basis of (10), a matrix dependence can be compiled:

$$\underset{6\times1}{\left\{\Delta S_a^{\alpha\beta}\right\}} = \underset{6\times24}{\left[H\right]} \underset{24\times1}{\left\{\Delta S_u^{\alpha\beta}\right\}}, \tag{11}$$

where $\underset{6\times24}{\left[H\right]}$ is a quasi-diagonal matrix, on the main diagonal of which the row matrices $\underset{1\times4}{\left\{\varphi\right\}^T}$; $\underset{1\times24}{\left\{\Delta S_u^{\alpha\beta}\right\}^T} = \left\{\underset{1\times12}{\left\{\Delta N_u^{\alpha\beta}\right\}^T} \quad \underset{1\times12}{\left\{\Delta M_u^{\alpha\beta}\right\}^T}\right\}$.

Taking into account the notations introduced above and (1)–(11), the nonlinear mixed functional can be written in the following form:

$$\begin{aligned}\Phi_S = \int_F \left[\underset{1\times6}{\left\{S^{\alpha\beta}\right\}^T} + \frac{1}{2}\underset{1\times6}{\left\{\Delta S_a^{\alpha\beta}\right\}^T}\right] \underset{6\times1}{\left\{\Delta\varepsilon_{\alpha\beta a}\right\}} dF - \\ -\int_F \underset{1\times3}{\left\{\Delta U\right\}^T} \left[\underset{3\times1}{\left\{P\right\}} + \frac{1}{2}\underset{3\times1}{\left\{\Delta P\right\}}\right] dF + \frac{1}{2}\int_F \left[\underset{1\times6}{\left\{\Delta S_K^{\alpha\beta}\right\}^T} - \underset{1\times6}{\left\{\Delta S_a^{\alpha\beta}\right\}^T}\right] \underset{6\times1}{\left\{\Delta\varepsilon_{\alpha\beta a}\right\}} dF.\end{aligned} \tag{12}$$

The column of increments of deformations and curvatures of the medial surface of the shell structure included in (12) can be expressed similarly to (11) through their nodal values:

$$\underset{6\times1}{\left\{\Delta\varepsilon_{\alpha\beta a}\right\}} = \underset{6\times24}{\left[H\right]} \underset{24\times1}{\left\{\Delta\varepsilon_{\alpha\beta u}\right\}}, \tag{13}$$

and can be represented by the Cauchy relations for thin shells [26] by a matrix product:

$$\underset{6\times1}{\left\{\Delta\varepsilon_{\alpha\beta K}\right\}} = \underset{6\times3}{\left[D\right]} \underset{3\times1}{\left\{\Delta U\right\}}. \tag{14}$$

The column of step increments of the components of the displacement vector of a point of the centre surface of the shell structure can be interpolated through the nodal values of the component increments by means of products of Hermite polynomials of the third degree:

$$\underset{3\times1}{\left\{\Delta U\right\}} = \underset{3\times36}{\left[A\right]} \underset{36\times1}{\left\{\Delta U^L\right\}} = \underset{3\times36}{\left[A\right]} \underset{36\times36}{\left[P_R\right]} \underset{36\times1}{\left\{\Delta U^G\right\}}, \tag{15}$$

where $\underset{3\times36}{\left[A\right]}$ is a quasi-diagonal matrix containing matrix-rows of polynomial Hermite functions; $\underset{36\times1}{\left\{\Delta U^L\right\}}$ and $\underset{36\times1}{\left\{\Delta U^G\right\}}$ are columns of kinematic nodal unknowns at the loading step in local and global coordinate systems, respectively, and $\underset{36\times36}{\left[P_R\right]}$ is the transition matrix from column $\underset{36\times1}{\left\{\Delta U^L\right\}}$ to column $\underset{36\times1}{\left\{\Delta U^G\right\}}$.

The relation (14) taking into account (15) will take the form:

$$\underset{6\times1}{\left\{\Delta\varepsilon_{\alpha\beta K}\right\}} = \underset{6\times3}{\left[D\right]} \underset{3\times36}{\left[A\right]} \underset{36\times36}{\left[P_R\right]} \underset{36\times1}{\left\{\Delta U^G\right\}} = \underset{6\times36}{\left[B\right]} \underset{36\times36}{\left[P_R\right]} \underset{36\times1}{\left\{\Delta U^G\right\}}, \tag{16}$$

where $\underset{1\times 36}{\left\{\Delta U^{L}\right\}^{T}}=\left\{\underset{1\times 12}{\left\{\Delta v^{1L}\right\}^{T}}\ \underset{1\times 12}{\left\{\Delta v^{2L}\right\}^{T}}\ \underset{1\times 12}{\left\{\Delta v^{L}\right\}^{T}}\right\}$; $\underset{1\times 36}{\left\{\Delta U^{G}\right\}^{T}}=\left\{\underset{1\times 12}{\left\{\Delta v^{1G}\right\}^{T}}\ \underset{1\times 12}{\left\{\Delta v^{2G}\right\}^{T}}\ \underset{1\times 12}{\left\{\Delta v^{G}\right\}^{T}}\right\}$;

$$\underset{1\times 12}{\left\{\Delta q^{L}\right\}^{T}}=\left\{\Delta q^{i}\ \ \Delta q^{j}\ \ \Delta q^{k}\ \ \Delta q^{l}\ \ \Delta q^{i}_{,\xi}\dots\Delta q^{l}_{,\xi}\ \ \Delta q^{i}_{,\eta}\dots\Delta q^{l}_{,\eta}\right\};$$

$$\underset{1\times 12}{\left\{\Delta q^{G}\right\}^{T}}=\left\{\Delta q^{i}\ \ \Delta q^{j}\ \ \Delta q^{k}\ \ \Delta q^{l}\ \ \Delta q^{i}_{,a}\dots\Delta q^{l}_{,a}\ \ \Delta q^{i}_{,\beta}\dots\Delta q^{l}_{,\beta}\right\}.$$

Here, Δq means Δv^{1}, Δv^{2} or Δv, and α and β are curvilinear global coordinates.

The functional (12) taking into account (8)–(11) and (13)–(16) can be transformed to the form:

$$\begin{aligned}\Phi_S=&\underset{1\times 36}{\left\{\Delta U^{G}\right\}^{T}}\underset{36\times 36}{\left[P_R\right]^{T}}\int\limits_{F}\underset{36\times 6}{\left[B\right]^{T}}\underset{6\times 1}{\left\{S^{\alpha\beta}\right\}^{T}}dF-\underset{1\times 36}{\left\{\Delta U^{G}\right\}^{T}}\underset{36\times 36}{\left[P_R\right]^{T}}\times\\ \times&\left(\int\limits_{F}\underset{36\times 3}{\left[A\right]^{T}}\underset{3\times 1}{\left\{P\right\}}dF-\frac{1}{2}\int\limits_{F}\underset{36\times 3}{\left[A\right]^{T}}\underset{3\times 1}{\left\{\Delta P\right\}}dF\right)+\frac{1}{2}\underset{1\times 24}{\left\{\Delta S^{\alpha\beta}_{u}\right\}^{T}}\int\limits_{F}\underset{24\times 6}{\left[H\right]^{T}}\underset{6\times 6}{\left[\gamma\right]^{-1}}\underset{6\times 24}{\left[H\right]}dF\underset{24\times 1}{\left\{\Delta S^{\alpha\beta}_{u}\right\}}+\\ +&\underset{1\times 24}{\left\{\Delta\varepsilon_{\alpha\beta u}\right\}^{T}}\frac{1}{2}\int\limits_{F}\underset{24\times 6}{\left[H\right]^{T}}\underset{6\times 6}{\left[\gamma\right]}\underset{6\times 36}{\left[B\right]}dF\underset{36\times 36}{\left[P_R\right]}\underset{36\times 1}{\left\{\Delta U^{G}\right\}}-\underset{1\times 24}{\left\{\Delta\varepsilon_{\alpha\beta u}\right\}^{T}}\frac{1}{2}\int\limits_{F}\underset{24\times 6}{\left[H\right]^{T}}\underset{6\times 24}{\left[H\right]}dF\underset{24\times 1}{\left\{\Delta S^{\alpha\beta}_{u}\right\}}.\end{aligned}\tag{17}$$

For convenience of further calculations, we introduce the following matrix notations:

$$\begin{aligned}&\underset{24\times 24}{\left[a\right]}=\int\limits_{F}\underset{24\times 6}{\left[H\right]^{T}}\underset{6\times 6}{\left[\gamma\right]^{-1}}\underset{6\times 24}{\left[H\right]}dF;\quad \underset{24\times 36}{\left[b\right]}=\frac{1}{2}\int\limits_{F}\underset{24\times 6}{\left[H\right]^{T}}\underset{6\times 6}{\left[\gamma\right]}\underset{6\times 36}{\left[B\right]}dF\underset{36\times 36}{\left[P_R\right]};\\ &\underset{24\times 24}{\left[c\right]}=\frac{1}{2}\int\limits_{F}\underset{24\times 6}{\left[H\right]^{T}}\underset{6\times 24}{\left[H\right]}dF;\quad \underset{36\times 1}{\left\{f_S\right\}}=\underset{36\times 36}{\left[P_R\right]^{T}}\int\limits_{F}\underset{36\times 6}{\left[B\right]^{T}}\underset{6\times 1}{\left\{S^{\alpha\beta}\right\}}dF;\\ &\underset{36\times 1}{\left\{f_p\right\}}=\underset{36\times 36}{\left[P_R\right]^{T}}\int\limits_{F}\underset{36\times 3}{\left[A\right]^{T}}\underset{3\times 1}{\left\{P\right\}}dF;\quad \underset{36\times 1}{\left\{f_{\Delta p}\right\}}=\underset{36\times 36}{\left[P_R\right]^{T}}\int\limits_{F}\underset{36\times 3}{\left[A\right]^{T}}\underset{3\times 1}{\left\{\Delta P\right\}}dF.\end{aligned}\tag{18}$$

The functional (17) taking into account (18) can be written in the following form:

$$\begin{aligned}\Phi_S=&\underset{1\times 36}{\left\{\Delta U^{G}\right\}^{T}}\underset{36\times 1}{\left\{f_S\right\}}-\underset{1\times 36}{\left\{\Delta U^{G}\right\}^{T}}\underset{36\times 1}{\left\{f_p\right\}}-\frac{1}{2}\underset{1\times 36}{\left\{\Delta U^{G}\right\}^{T}}\underset{36\times 1}{\left\{f_{\Delta p}\right\}}+\\ +&\frac{1}{2}\underset{1\times 24}{\left\{\Delta S^{\alpha\beta}_{u}\right\}^{T}}\underset{24\times 24}{\left[a\right]}\underset{24\times 1}{\left\{\Delta S^{\alpha\beta}_{u}\right\}}+\underset{1\times 24}{\left\{\Delta\varepsilon_{\alpha\beta u}\right\}^{T}}\underset{24\times 36}{\left[b\right]}\underset{36\times 1}{\left\{\Delta U^{G}\right\}}-\underset{1\times 24}{\left\{\Delta\varepsilon_{\alpha\beta u}\right\}^{T}}\underset{24\times 24}{\left[c\right]}\underset{24\times 1}{\left\{\Delta S^{\alpha\beta}_{u}\right\}}.\end{aligned}\tag{19}$$

By successively minimising (19) by $\left\{\Delta\varepsilon_{\alpha\beta u}\right\}^{T}$, $\left\{\Delta S^{\alpha\beta}_{u}\right\}^{T}$ and $\left\{\Delta U^{G}\right\}^{T}$, we can obtain the following system of matrix equations:

$$\begin{cases}\partial\Phi_S\Big/\partial\left\{\Delta\varepsilon_{\alpha\beta u}\right\}^{T}\equiv\underset{24\times 36}{\left[b\right]}\underset{36\times 1}{\left\{\Delta U^{G}\right\}}-\underset{24\times 24}{\left[c\right]}\underset{24\times 1}{\left\{\Delta S^{\alpha\beta}_{u}\right\}}=0;\\ \partial\Phi_S\Big/\partial\left\{\Delta S^{\alpha\beta}_{u}\right\}^{T}\equiv\underset{24\times 24}{\left[a\right]}\underset{24\times 1}{\left\{\Delta S^{\alpha\beta}_{u}\right\}}-\underset{24\times 24}{\left[c\right]^{T}}\underset{24\times 1}{\left\{\Delta\varepsilon_{\alpha\beta u}\right\}}=0;\\ \partial\Phi_S\Big/\partial\left\{\Delta U^{G}\right\}^{T}\equiv\underset{36\times 1}{\left\{f_S\right\}}-\underset{36\times 1}{\left\{f_p\right\}}-\underset{36\times 1}{\left\{f_{\Delta p}\right\}}+\underset{36\times 24}{\left[b\right]^{T}}\underset{24\times 1}{\left\{\Delta\varepsilon_{\alpha\beta u}\right\}}=0.\end{cases}\tag{20}$$

To solve the system (20), we can use the substitution method. For this purpose, from the first and second equations (20), it is necessary to express the force and deformation step nodal unknowns:

$$\underset{24\times1}{\left\{\Delta S_u^{\alpha\beta}\right\}} = \underset{24\times24}{\left[c\right]}^{-1} \underset{24\times36}{\left[b\right]} \underset{36\times1}{\left\{\Delta U^G\right\}}; \quad \underset{24\times1}{\left\{\Delta\varepsilon_{\alpha\beta u}\right\}} = \left[\underset{24\times24}{\left[c\right]}^{T}\right]^{-1} \underset{24\times24}{\left[a\right]} \underset{24\times1}{\left\{\Delta S_u^{\alpha\beta}\right\}}. \tag{21}$$

By substituting (21) into the third equation (20), the following matrix equation can be obtained:

$$\underset{36\times1}{\left\{f_S\right\}} - \underset{36\times1}{\left\{f_p\right\}} - \underset{36\times1}{\left\{f_{\Delta p}\right\}} + \underset{36\times24}{\left[b\right]}^{T} \left[\underset{24\times24}{\left[c\right]}^{T}\right]^{-1} \underset{24\times24}{\left[a\right]} \underset{24\times24}{\left[c\right]}^{-1} \underset{24\times36}{\left[b\right]} \underset{36\times1}{\left\{\Delta U^G\right\}} = 0, \tag{22}$$

or in a more convenient form:

$$\underset{36\times36}{\left[K\right]} \underset{36\times1}{\left\{\Delta U^G\right\}} = \underset{36\times1}{\left\{f_{\Delta p}\right\}} - \left(\underset{36\times1}{\left\{f_S\right\}} - \underset{36\times1}{\left\{f_p\right\}}\right), \tag{23}$$

where $\underset{36\times36}{\left[K\right]} = \underset{36\times24}{\left[b\right]}^{T} \left[\underset{24\times24}{\left[c\right]}^{T}\right]^{-1} \underset{24\times24}{\left[a\right]} \underset{24\times24}{\left[c\right]}^{-1} \underset{24\times36}{\left[b\right]}$ is the stiffness matrix of the used four-node discretisation element of the three-field variant of the mixed FEM at one of the successive loading steps; $\underset{36\times1}{\left\{f_{\Delta p}\right\}}$ is the column of step forces; $\left(\underset{36\times1}{\left\{f_S\right\}} - \underset{36\times1}{\left\{f_p\right\}}\right)$ is the Newton–Raphson correction at the loading step.

To obtain the stiffness matrix of the finite element at the loading step, a numerical integration procedure was applied using the Gauss method for the area of the mid-surface $\left(n=6\right)$ and the Simpson formula $\left(n=7\right)$ when integrating over the shell thickness.

The global stiffness matrix of the shell structure $\left[K\right]$ is composed of a four-node discretisation element by means of an index matrix formed according to the accepted boundary conditions of the calculated shell [27].

In order to verify the above algorithm for the calculation of shell structures in a physically nonlinear formulation, a comparative analysis of finite element solutions obtained using the developed variant of the mixed FEM with the solutions obtained on the basis of the FEM in the formulation of the displacement method was performed.

3. Results and Discussion

Example 1. As an example, a fragment of an elliptical cylinder made of duralumin alloy with the ratio of ellipse parameters of cross-section a/b = 5, loaded with internal pressure of intensity q = 6·10^{-3} MPa, was calculated. The calculation scheme of the shell is shown in Fig. 1. The following initial data were used: a = 1.5 m; b = 0.3 m; h = 0.01 m; L = 0.01 m; E = 7.49·10^4 MPa; ν = 0.32. The deformation diagram was assumed as a two-linked broken line defined by the formula:

$$\begin{cases} \sigma_i = tg\alpha \cdot \varepsilon_i; & \varepsilon_i \le 0.0023496; \\ \sigma_i = tg\beta \cdot \left(\varepsilon_i - 0.0023496\right) + 200; & \varepsilon_i > 0.0023496, \end{cases}$$

where $\mathrm{tg}\alpha = 85120.87;\ \mathrm{tg}\beta = 18087.03.$

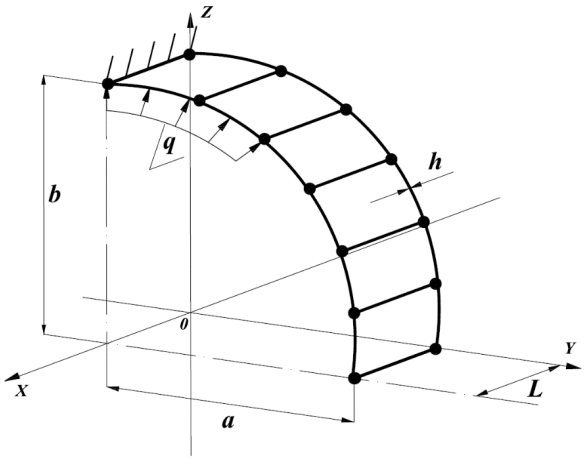

Figure 1. Calculation diagram of an elliptical cylinder.

The calculations were performed in two variants: in the first variant, the above three-field mixed FEM algorithm in a physically nonlinear formulation was implemented; in the second variant, the FEM algorithm in the formulation of the displacement method was used. The results of the variant calculations are presented in tabular form. The tables show the numerical values of normal stresses in the rigid embedment and at the free end of the shell, as well as the values of bending moment (for the first variant of calculation) when varying the degree of refinement of the discretisation grid and the number of loading steps.

Tables 1–3 present the results of the first variant of calculation at successive densification of the mesh of nodes 41×2, 51×2, and 61×2 depending on the number of stages of successive loading.

The selected design scheme allows to calculate the values of physical bending moment in the rigid embedment (Fig. 2):

$$M_{22} = \left(q_{\text{в}} b^2 / 2 + q_{\text{г}} c^2 / 2\right) L = \left(q/2\right)\left(b^2 + c^2\right) L =$$

$$= 3 \cdot 10^3 \ \text{N}/\text{m}^2 \cdot \left(\left(1.5\text{m}\right)^2 + \left(0.3\text{m}\right)^2\right) \cdot 10^{-2}\,\text{m} = 3 \cdot 10 \cdot 2.34 \ \text{N} \cdot \text{m} = 70.2 \ \text{N} \cdot \text{m}.$$

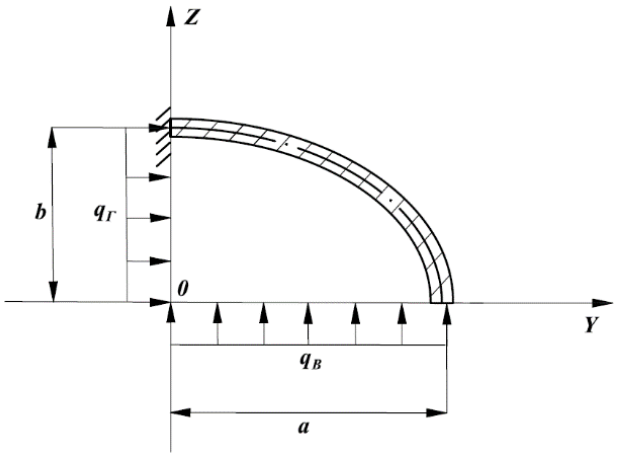

Figure 2. Section of the shell by the plane ZOY.

It is also obvious that the bending moment M_{22} at the free end of the elliptical cylinder, as well as the stresses, must be equal to zero.

The rightmost column of Tables 1–3 shows the above-mentioned analytical values of the controlled strength parameters of the shell SSS.

Table 1. Values of controlled SSS parameters at 41×2 node grid.

Point coordinates, *y*, m; *z*, m	Stress σ, MPa, moment, M_{22}, N·m	Number of loading steps				Analytical solution
		22	52	82	102	
0.0; 0.3	σ_{22}^{in}	347.3	347.5	347.6	347.6	–
	σ_{22}^{out}	-346.7	–347.1	–347.1	–347.1	–
	M_{22}	70.74	70.55	70.22	70.16	70.20
1.5; 0.0	σ_{22}^{in}	–0.192	–0.190	–0.190	–0.191	–
	σ_{22}^{out}	–0.137	–0.136	–0.136	–0.136	–
	σ_{22}^{midl}	0.0687	0.0681	0.0681	0.0685	0.000
	M_{22}	0.0005	0.0005	0.0005	0.0005	0.000

Table 2. Values of controlled SSS parameters at 51×2 node grid.

Point coordinates, *y*, m; *z*, m	Stress σ, MPa, moment, M_{22}, N·m	Number of loading steps				Analytical solution
		22	52	82	102	
0.0; 0.3	σ_{22}^{in}	347.4	347.6	347.6	347.6	–
	σ_{22}^{out}	–346.7	–347.1	-347.2	–347.2	–
	M_{22}	70.87	70.36	70.32	70.29	70.20
1.5; 0.0	σ_{22}^{in}	–0.0708	–0.0682	–0.0679	–0.0683	–
	σ_{22}^{out}	–0.0533	–0.0514	–0.0511	–0.0515	–
	σ_{22}^{midl}	0.0273	0.0266	0.0265	0.0266	0.000
	M_{22}	0.0004	0.0004	0.0004	0.0004	0.000

Table 3. Values of controlled SSS parameters at 61×2 node grid.

Point coordinates, *y*, m; *z*, m	Stress σ, MPa, moment, M_{22}, N·m	Number of loading steps				Analytical solution
		22	52	82	102	
0.0; 0.3	σ_{22}^{in}	347.5	347.6	347.7	347.7	–
	σ_{22}^{out}	–346.7	–347.1	–347.2	–347.2	–
	M_{22}	71.03	70.50	70.37	70.33	70.20
1.5; 0.0	σ_{22}^{in}	–0.0295	–0.0298	–0.0299	–0.0297	–
	σ_{22}^{out}	–0.0223	–0.0225	–0.0225	–0.0224	–
	σ_{22}^{midl}	0.0119	0.0120	0.0120	0.0120	0.000
	M_{22}	0.0003	0.0003	0.0003	0.0003	0.000

As follows from the analysis of the data given in Tables 1–3, the three-field version of the mixed FEM in the physically nonlinear formulation demonstrates stable convergence of the computational process, both when the discretisation grid is reduced and when the number of successive loading stages is increased. In addition, the numerical values of the bending moment M_{22} in the rigid embedment and at the free end practically coincide with their analytical values, which is also a proof of the correctness and high degree of

accuracy of finite element solutions obtained by using the developed three-field mixed FEM in the physically nonlinear formulation.

If the classical FEM formulation of the displacement method is applied to the solution of this problem, the results of finite element solutions will be quite different from the above-mentioned ones. For example, Table 4 shows the results of the FEM calculation of an elliptical cylinder in the form of the displacement method with a 61×2 node grid.

Table 4. Stress values of elliptical cylinder FEM in the form of displacement method with 61×2 node grid.

Point coordinates, *y*, m; *z*, m	Stress σ_{22}, MPa	Number of loading steps				Analytical solution
		22	52	82	102	
0.0; 0.3	σ_{22}^{in}	304.1	274.6	120.3	276.0	–
	σ_{22}^{out}	–303.8	–274.3	–112.7	–275.8	–
1.5; 0.0	σ_{22}^{in}	–76.44	–66.17	–140.8	–62.41	–
	σ_{22}^{out}	358.4	323.2	330.2	319.4	–
	σ_{22}^{midl}	270.7	250.8	246.4	248.9	0.000

As follows from the analysis of Table 4, there is no convergence of the computational process when the number of successive loading steps is increased. In addition, the stresses at the free end of the shell reach unacceptably high values, although they should be equal to zero.

Obviously, when using the FEM in the formulation of the displacement method in physically nonlinear calculations of shells with significant curvature of the medial surface, a much more significant refinement of the discretisation grid is required. Tables 5–7 show the results of elliptical cylinder calculations with 81×2, 101×2, and 121×2 node grids, respectively.

Table 5. Stress values of elliptical cylinder FEM in the form of displacement method with 81×2 node grid.

Point coordinates, *y*, m; *z*, m	Stress σ_{22}, MPa	Number of loading steps				Analytical solution
		22	52	82	102	
0.0; 0.3	σ_{22}^{in}	343.9	302.9	369.0	264.1	–
	σ_{22}^{out}	–343.4	–302.2	–370.4	–263.0	–
1.5; 0.0	σ_{22}^{in}	–66.74	–59.54	–32.91	–56.99	–
	σ_{22}^{out}	278.5	259.7	253.6	248.7	–
	σ_{22}^{midl}	213.8	178.8	176.7	156.3	0.000

Table 6. Stress values of elliptical cylinder FEM in the form of displacement method with 101×2 node grid.

Point coordinates, *y*, m; *z*, m	Stress σ_{22}, MPa	Number of loading steps				Analytical solution
		22	52	82	102	
0.0; 0.3	σ_{22}^{in}	345.0	345.2	344.2	341.6	–
	σ_{22}^{out}	–344.5	–344.8	–343.8	–341.2	–
1.5; 0.0	σ_{22}^{in}	–47.34	–47.49	–47.21	–46.41	–
	σ_{22}^{out}	227.5	227.7	227.2	225.6	–
	σ_{22}^{midl}	114.9	115.2	114.6	112.9	0.000

Table 7. Stress values of elliptical cylinder FEM in the form of displacement method with

121×2 node grid.

Point coordinates, *y*, m; *z*, m	Stress σ_{22}, MPa	Number of loading steps				Analytical solution
		22	52	82	102	
0.0; 0.3	σ_{22}^{in}	346.3	346.6	346.6	346.6	–
	σ_{22}^{out}	–345.8	–346.1	–346.1	–346.1	–
1.5; 0.0	σ_{22}^{in}	–37.30	–37.41	–37.43	–37.44	–
	σ_{22}^{out}	145.1	145.6	145.7	145.8	–
	σ_{22}^{midl}	69.49	69.74	69.80	69.81	0.000

Analysing the tabulated values of normal stresses in Table 5 shows that for 81×2 node grid, there is also no convergence of the computational process as the number of sequential loading steps increases and the stresses at the free end have unacceptably high values.

For 101×2 node grid in rigid embedment (Table 6), satisfactory convergence of the computational process is observed. However, the stresses at the free end have unacceptably high values.

With a 121×2 node grid (Table 7), the values of stresses in the rigid embedment remain almost unchanged and coincide with the values of stresses in the rigid embedment obtained using the three-field version of mixed FEM (Tables 1–3). However, at the free end, the normal stresses still remain very far from zero values, which requires further refinement of the discretisation grid.

Table 8 shows the calculation results of the elliptical cylinder at 201×2 node grid. As can be seen from the analysis of the tabular data, a steady convergence of the computational process is observed in the rigid termination as the number of successive loading steps increases. At the free end of the shell, the stress values have decreased but still remain quite far from zero values.

Table 8. Stress values of elliptical cylinder FEM in the form of displacement method with 201×2 node grid.

Point coordinates, *y*, m; *z*, m	Stress σ_{22}, MPa	Number of loading steps				Analytical solution
		22	52	82	102	
0.0; 0.3	σ_{22}^{in}	347.2	347.5	347.6	347.6	–
	σ_{22}^{out}	–346.8	–347.0	–347.1	–347.1	–
1.5; 0.0	σ_{22}^{in}	–17.44	–17.49	–17.50	–17.51	–
	σ_{22}^{out}	40.28	40.41	40.44	40.45	–
	σ_{22}^{midl}	16.31	16.37	16.38	16.38	0.000

In addition, it should be noted that when using the traditional formulation of the FEM in the form of the displacement method, the problem of obtaining the numerical value of the bending moment in the rigid embedment arises. To solve this problem, a graphical method can be applied to calculate the bending moment value from the normal stress epiphysis in the rigid embedment, plotted at fixed points of vertical coordinate along the normal to the medial surface of the shell.

Fig. 3 shows the normal stress epiphysis in the rigid embedment with a 201×2 node grid plotted at 9 node points along the surface normal. For convenience of further calculations, the epyure was divided into elementary figures and the centres of gravity in each figure were found. Then, the forces $\vec{T}_i \left(i = 1,\ldots,10\right)$ were calculated as the areas of each of the figures. Moments were calculated as products of forces by the corresponding arms $\vec{M}_i = \vec{T}_i \cdot d_i \left(i = 1,\ldots,10\right)$.

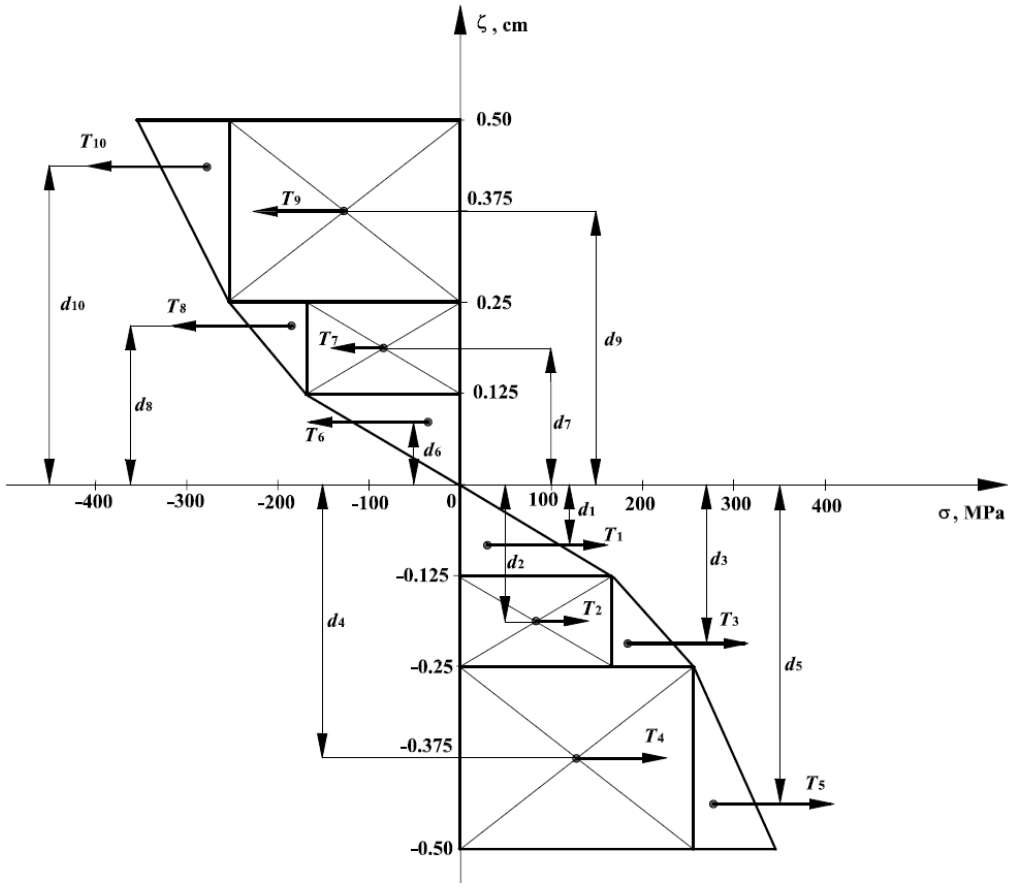

Figure 3. Normal stress diagram in a rigid termination.

The resultant moment can be obtained by summing the moments $\vec{M}_i$:

$$M_{22} = \sum_{i=1}^{10} \left| \vec{M}_i \right|.$$

After performing the above calculations, the resultant torque is obtained as follows:

$$M_{22} = 69.554 \text{ N} \cdot \text{m}.$$

The calculation error was:

$$\delta = \frac{70.2 - 69.554}{70.2} \cdot 100\% = 0.92\%.$$

Obviously, when building a more detailed stress diagram, for example, by dividing it by height into 17 points, the calculation error can be reduced. However, the error of 0.92 % obtained by dividing the stress diagram into 9 points along the section height is quite acceptable for engineering calculations.

Calculation example 2: A fragment of an elliptical ring with the ratio of ellipse parameters a/b = 6, loaded on the right side with a linear load of intensity q = 25 kN/m uniformly distributed along the formations and having a hinged support on the left side, was calculated (Fig. 4). The following initial data were used: a = 1.2 m; b = 0.2 m; h = 0.008 m; L = 0.01 m. The physical characteristics of the material and the deformation diagram were taken from the previous calculation example. A reactive force equal to the applied nodal load occurs at the hinge points $R = Q$. Thus, the normal stresses σ_{22} at points K and M must be equal. The equality of the normal stresses σ_{22} at points K and M can serve as an additional criterion for the correctness of the numerical values of the normal stresses obtained as a result of the solution.

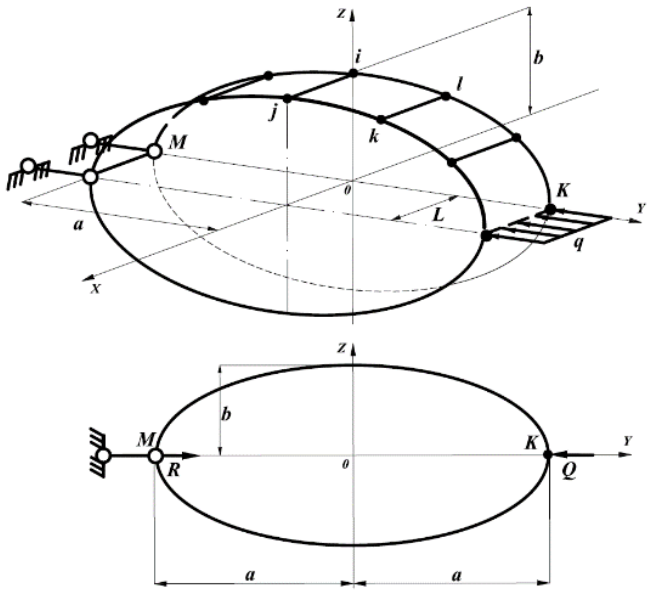

Figure 4. Calculation diagram of an elliptical ring.

The calculations, as in the previous example, were performed in two variants: the first variant used the developed three-field mixed four-node discretisation element; the second variant used a finite element whose stiffness matrix was composed in the formulation of the displacement method. The results of the first variant of the calculation are summarised in Tables 9 and 10. Table 9 shows the values of normal stresses on the inner and outer surfaces of the shell at the points of application of a given load and at the points of hinge support depending on the density of the discretisation grid at a fixed number of loading steps equal to 22.

Table 9. Stress values of the first calculation variant depending on the size of the discretisation grid.

Point coordinates, *y*, m; *t*, m	Stress σ_{22}, MPa	Sampling grid			
		51×2	61×2	81×2	101×2
1.2; π/2	σ_{22}^{in}	303.5	304.0	305.2	305.5
	σ_{22}^{out}	–270.1	–270.4	–271.0	–271.2
–1.2; π/2	σ_{22}^{in}	303.0	304.0	305.2	305.5
	σ_{22}^{out}	–269.6	–270.3	–271.0	–271.1

Analysis of the data shown in Table 9 indicates the stable convergence of the computational process as the discretisation grid thickens and the values of normal stresses at points K and M practically coincide, which should be the case with the selected design scheme.

Table 10 shows the results of the shell calculation with a fixed discretisation grid of 61×2 and a sequential increase in the number of sequential loading stages.

Table 10. Stress values of the first variant depending on the number of loading steps.

Point coordinates, *y*, m; *t*, m	Stress σ_{22}, MPa	Number of loading steps			
		22	52	82	102
1.2; π/2	σ_{22}^{in}	304.0	304.7	304.8	304.8
	σ_{22}^{out}	–270.4	–270.5	–270.6	–270.55
–1.2; π/2	σ_{22}^{in}	304.0	304.7	304.8	304.8
	σ_{22}^{out}	–270.3	–270.4	–270.4	–270.4

As follows from the analysis of the data in Table 10, a stable convergence of the computational process is observed. The numerical values of normal stresses change very slightly when the number of loading steps increases from 22 to 102, which is also a necessary condition for the reliability of the numerical values of stresses obtained as a result of the calculation.

The results of calculations for the second variant, in which the FEM algorithm in the classical formulation of the displacement method was implemented, are presented in Tables 11 and 12. Table 11 contains the results of calculations with a fixed number of loading steps equal to 22 and successive densification of the discretisation grid from 61×2 to 201×2.

Table 11. Stress values of the second calculation variant depending on the size of the discretisation grid.

Point coordinates, *y*, m; *t*, m	Stress σ_{22}, MPa	Sampling grid					
		61×2	81×2	101×2	121×2	151×2	201×2
1.2; π/2	σ_{22}^{in}	711.6	528.7	442.5	394.8	357.8	334.4
	σ_{22}^{out}	–284.7	–320.9	–319.0	–309.5	–297.7	–287.5
–1.2; π/2	σ_{22}^{in}	276.9	301.7	301.1	302.9	305.9	305.7
	σ_{22}^{out}	–250.1	–269.1	–268.1	–269.5	–271.6	–271.4

The analysis of Table 11 shows a very slow convergence of the computational process as the discretisation grid of the calculated shell becomes denser. It can also be noted that the normal stresses σ_{22} at the load application points q and the hinge points do not match. Fig. 5 shows a plot of the variation of the stress ratio $k = \left(\sigma_{22}^{in}\right)_K \Big/ \left(\sigma_{22}^{in}\right)_M$ at the K and M points of the shell as a function of the density of the discretisation grid in the two computational formulations of the FEM.

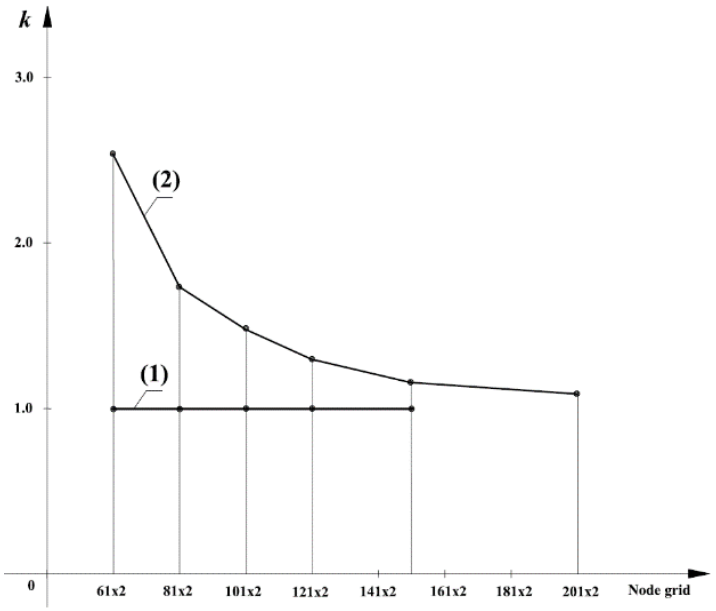

Figure 5. Plots of coefficient *k* variation depending on the size of the sampling grid for the first (1) and second (2) variants of calculation for the first (1) and the second (2) calculation variants.

As can be seen from Fig. 5, the developed three-field mixed FEM algorithm allows to have a coefficient k equal to 1 at any, even very sparse, discretisation grid, whereas the FEM in the formulation of the displacement method does not allow to achieve such a result, despite a very significant densification of the discretisation grid. Further densification of the mesh is also not reasonable, as it leads to the accumulation of rounding errors at the size of the discretisation element comparable to its thickness, which does not meet the criteria of a thin shell.

Table 12 shows the results of the second variant of calculation at a fixed 201×2 discretisation grid depending on the number of stages of sequential loading.

Table 12. Stress values of the second variant depending on the number of loading steps.

Point coordinates, *y*, m; *t*, m	Stress σ_{22}, MPa	Number of loading steps			
		22	52	82	102
1.2; π/2	σ_{22}^{in}	334.4	313.1	318.5	311.7
	σ_{22}^{out}	–287.5	–271.6	–276.4	–271.1
–1.2; π/2	σ_{22}^{in}	305.7	295.1	285.7	282.4
	σ_{22}^{out}	–271.4	–263.4	–256.6	–254.1

As follows from the analysis of the data in Table 12, satisfactory convergence of the computational process is observed, but the difference between the stress values at points K and M remains almost constant within 10 %, which should not be the case with the selected design scheme.

Calculation example 3. A calculation was made of a truncated ellipsoid of revolution under the action of internal pressure of intensity q = 6.5 MPa (Fig. 6). The left end was rigidly clamped, the right end was free. The geometric dimensions of the ellipsoid were taken to be: a = 1.3 m; b = 0.8 m; h = 0.02 m; coordinate x was determined by inequality $0 \le x \le 1.2$ m. The physical properties of the shell material were taken from the previous example. Considering that the right free end of the ellipsoid is in a momentless state, the value of the normal stress in the hoop stress can be found using the Laplace formula [28]

$$\sigma_{xx}/R_x + \sigma_{tt}/R_t = q/h.$$

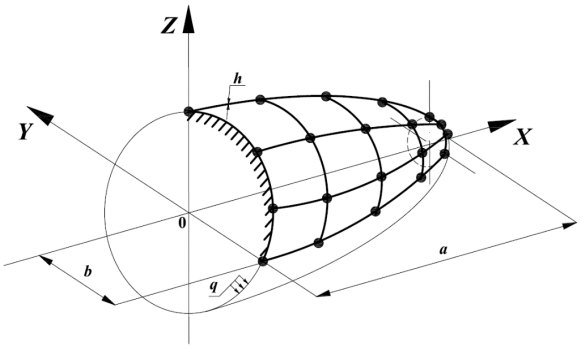

Figure 6. Calculation scheme of an ellipsoidal shell.

Taking into account that on the free end σ_{xx} should be equal to zero, σ_{tt}^{midl} will be equal:

$$\sigma_{tt}^{midl} = (q/h)\cdot R_t = (6.5\ \text{MPa}/0.02\ \text{m})\cdot 0.5488\ \text{m} = 178.36\ \text{MPa}.$$

During the solution process, the convergence of the computational process was monitored both as the mesh density increased and as the number of loading steps increased. Table 13 presents the stress values on the internal σ^{in}, external σ^{out} and median σ^{midl} the ellipsoid surfaces at the supporting and free ends, depending on the degree of mesh density for a fixed number of loading steps equal to 22.

The stress calculated using the Laplace formula is included in the far right column of Table 13.

Table 13. Stress values depending on the discretization grid size.

Shell cross-section	Stress σ, MPa	Sampling grid				Analytical solution
		201×21	301×21	361×21	401×21	
Support, *x* = 0.0 m	σ_{xx}^{in}	322.3	327.2	324.2	326.1	–
	σ_{xx}^{out}	–232.4	–236.5	–233.8	–233.9	–
	σ_{xx}^{midl}	162.7	164.4	163.4	165.1	–

Shell cross-section	Stress σ, MPa	Sampling grid				Analytical solution
		201×21	301×21	361×21	401×21	
Free end, x = 1.2 m	σ_{xx}^{in}	0.073	0.035	0.033	0.034	–
	σ_{xx}^{out}	0.068	0.033	0.030	0.031	–
	σ_{xx}^{midl}	0.062	0.025	0.022	0.024	0.00
	σ_{tt}^{in}	182.7	183.0	184.2	185.4	–
	σ_{tt}^{out}	169.9	170.2	171.4	172.6	–
	σ_{tt}^{midl}	176.14	176.44	177.61	178.86	178.36

Analyzing the data presented in Table 13, we can confirm stable convergence of the calculations and consider a 201×21 node grid to be entirely sufficient.

Table 14 shows the values of the controlled parameters of the ellipsoid SSS for a 201×21 node grid depending on the number of loading steps.

Table 14. Stress values depending on the number of loading steps.

Shell cross-section	Stress σ, MPa	Number of loading steps				Analytical solution
		22	32	42	52	
Support, x = 0.0 m	σ_{xx}^{in}	322.3	320.3	320.1	320.4	–
	σ_{xx}^{out}	–232.4	–231.1	–231.0	–230.9	–
	σ_{xx}^{midl}	162.7	161.3	161.1	161.8	–
Free end, x = 1.2 m	σ_{xx}^{in}	0.073	0.074	0.082	0.083	–
	σ_{xx}^{out}	0.068	0.068	0.075	0.076	–
	σ_{xx}^{midl}	0.062	0.062	0.070	0.071	–
	σ_{tt}^{in}	182.7	182.8	183.5	183.6	–
	σ_{tt}^{out}	169.9	170.0	170.7	170.8	–
	σ_{tt}^{midl}	176.14	176.21	176.92	177.02	178.36

Table 14 shows that as the number of loading steps increases, the stress values change only slightly. Therefore, the stability of the computational process convergence is ensured. The numerical stresses at the free end of the ellipsoid correspond to their analytical values with an acceptable error of 0.75 %.

The multipolic end-element approach to the analysis of the elastoplastic deformation was used in works [25, 28–31], in which in addition to the fields of displacements and stresses, additional fields of plastic factors were used in expressions to determine the speeds of plastic deformations.

In this work, in the mixed formulation of the FEM, they are used as the desired fields of unknown quantities: increment of movements, deformations and curvatures of the midlife, as well as increment of efforts and moments.

To obtain a plasticity matrix, a deformation theory of plasticity [4] is realized in a step of loading, which made it possible to exclude an additional field of unknowns – the field of plastic factors.

4. Conclusions

1. A nonlinear mixed functional with three fields of step unknowns: kinematic, force and strain is proposed.
2. Based on the proposed nonlinear mixed functional, an algorithm for forming the stiffness matrix of a curvilinear four-node discretisation element at a loading step is developed.

3. A comparative analysis of finite element solutions obtained using the developed algorithm and solutions obtained on the basis of single-field FEM in the formulation of the displacement method has been performed.
4. The analysis of the results of the comparative analysis proved the significant advantages of the developed three-field FEM in the calculation of shell structures in the physically nonlinear formulation in comparison with the single-field FEM in the form of the displacement method.

References

1. Sedov, L.I. Mekhanika sploshnoy sredy [Mechanics of a continuous medium]. 1. Moscow: Nauka, 1976. 536 p.
2. Zubchaninov, V.G. Mekhanika sploshnykh deformiruyemykh sred [Mechanics of continuous deformable media]. Tver: TSTU, 2000. 703 p.
3. Petrov, V.V., Krivoshein, I.V. Metody rascheta konstruktsiy iz nelineyno deformiruyemogo materiala [Methods for calculating structures made of nonlinearly deformable material]. Moscow: ASV Publishing House, 2009. 208 p.
4. Malinin, N.N. Prikladnaya teoriya plastichnosti i polzuchesti [Applied theory of plasticity and creep]. Moscow: Yurayt Publishing House, 2024. 402 p.
5. Paimushin, V.N. Nonlinear Theory of Sandwich Shells with a Transversely Soft Core Containing Delamination Zones and Edge Support Diaphragm. Mechanics of Solids. 2018. 53(1). Pp. 76–87. DOI: 10.3103/S0025654418030111
6. Bazhenov, V.G., Kazakov, D.A., Osetrov, S.L., Osetrov, D.L., Ryabov, A.A. Analysis of the Limiting States of Cylindrical Elastic-Plastic Shells under Tension and Combined Loading by Internal Pressure and Tension. PNRPU Mechanics Bulletin. Mechanics. 2022. 2. Pp. 39–48. DOI: 10.15593/perm.mech/2022.2.04
7. Bazhenov, V.G., Kazakov, D.A., Kibets, A.I., Nagornykh, E.V., Samsonova, D.A. Formulation and Numerical Solution of the Stability Loss Problem of Elastic-Plastic Shells of Revolution with an Elastic Filler under Combined Axisymmetric and Torsional Loadings. PNRPU Mechanics Bulletin. 2022. 3. Pp. 95–106. DOI: 10.15593/perm.mech/2022.3.10
8. Levin, V.A., Vershinin, A.V. Nelineynaya vychislitel'naya mekhanika prochnosti [Nonlinear computational strength mechanics]. 2: Numerical methods [Chislennyye metody]. Moscow: Fizmatlit, 2015. 544 p.
9. Levin, V.A. Nelineynaya vychislitel'naya mekhanika prochnosti [Nonlinear computational strength mechanics]. 1: Modeli i metody [Models and methods]. Moscow: Fizmatlit, 2015. 456 p.
10. Madeo, A., Liguori, F., Zucco, G., Fiore, S. An efficient isostatic mixed shell element for coarse mesh solution. International Journal for Numerical Methods in Engineering. 2021. 122(1). Pp. 82–121. DOI: 10.1002/nme.6526
11. Cavalcante, E., Neto, E.L. A pseudo-equilibrium finite element for limit analysis of Reissner-Mindlin plates. Applied Mathematical Modelling. 2021. 96. P. 336–354. DOI: 10.1016/j.apm.2021.03.004
12. Sagdatullin, M.K. Numerical Modeling of Nonlinear Deformation Processes for Shells of Medium Thickness. Structural mechanics of engineering constructions and buildings. 2023. 19(2). Pp. 130–148. DOI: 10.22363/1815-5235-2023-19-2-130-148
13. Sultanov, L.U. Analysis of Finite Elasto-Plastic Strains: Integration Algorithm and Numerical Examples. Lobachevskii Journal of Mathematics. 2018. 39(9). Pp. 1478–1483. DOI: 10.1134/S1995080218090056
14. Golovanov, A.I., Tyuleneva, O.N., Shigabutdinov, A.F. Metod konechnykh elementov v statike i dinamike tonkostennykh konstruktsiy [Finite element method in the statics and dynamics of thin-walled structures]. Moscow: Fizmatlit., 2006. 391 p.
15. Khairullin, F.S., Sakhbiev, O.M. Calculation of the Elastoplastic Deformations by the Variational Method Based on Functions with Finite Carriers. Herald of Technological University. 2021. 24(4). Pp. 102–106.
16. Klochkov, Yu.V., Pshenichkina, V.A., Nikolaev, A.P., Marchenko, S.S., Vakhnina, O.V., Klochkov, M.Yu. Calculation of Shells of Revolution with the Use of a Mixed FEM with a Vector Approximation Procedure. Journal of Machinery Manufacture and Reliability. 2024. 52(1). Pp.10–21. DOI: 10.1134/S1052618824010059
17. Cervera, M., Chiumenti, M., Codina, R. Mixed stabilized finite element methods in nonlinear solid mechanics: Part I: Formulation. Computer Methods in Applied Mechanics and Engineering. 2010. 199(37–40). Pp. 2559–2570. DOI: 10.1016/j.cma.2010.04.006
18. Nodargi, N.A., Bisegna, P. A novel high-performance mixed membrane finite element for the analysis of inelastic structures. Computers & Structures. 2017. 182. Pp. 337–353. DOI: 10.1016/j.compstruc.2016.10.002
19. Liguori, F.S., Madeo, A., Garcea, G. A mixed finite-element formulation for the elasto-plastic analysis of shell structures. Materials Research Proceedings. 2023. 26. Pp. 227–232. DOI: 10.21741/9781644902431-37
20. Liguori, F.S., Madeo, A., Garcea, G. A dual decomposition of the closest point projection in incremental elasto-plasticity using a mixed shell finite element. International Journal for Numerical Methods in Engineering. 2022. 123(24). Pp. 6243–6266. DOI: 10.1002/nme.7112
21. Bilotta, A., Garcea, G., Leonetti, L. A composite mixed finite element model for the elasto-plastic analysis of 3D structural problems. Finite Elements in Analysis and Design. 2016. 113. Pp. 43–53. DOI: 10.1016/j.finel.2016.01.002
22. Mendes, L.A.M., Castro, L.M.S.S. Hybrid-mixed stress finite element models in elastoplastic analysis. Finite Elements in Analysis and Design. 2009. 45(12). Pp. 863–875. DOI: 10.1016/j.finel.2009.06.021
23. Madeo, A., Liguori, F., Zucco, G. et al. An efficient isostatic mixed shell element for coarse mesh solution. International Journal for Numerical Methods in Engineering. 2021. 122(1). Pp. 82–121. DOI: 10.1002/nme.6526
24. Klochkov, Yu., Nikolaev, A., Pshenichkina, V., Vakhnina, O., Klochkov, M. Three-field FEM for analysis of thin elastic shells. Magazine of Civil Engineering. 2024. 3(127). Article no. 12710. DOI: 10.34910/MCE.127.10
25. Bilotta, A., Leonetti, L., Garcea, G. Three field finite elements for the elastoplastic analysis of 2D continua. Finite Elements in Analysis and Design. 2011. 47(10). Pp. 1119–1130. DOI: 10.1016/j.finel.2011.05.002
26. Novozhilov, V.V. Teoriya tonkikh obolochek [Theory of thin shells]. St. Petersburg: Publishing House of the St. Petersburg University, 2010. 378 p.
27. Postnov, V.A., Kharkhurim, I.Ya. Metod konechnykh elementov v raschetakh sudovykh konstruktsiy [Finite element method in calculations of ship structures]. Leningrad: Sudostroyeniye, 1974. 342 p.
28. Belyaev, N.M. Soprotivleniye materialov [Strength of materials]. Moscow: Nauka, 1976. 607 p.

29. Nodargi, N.A. An Overview of Mixed Finite Elements for the Analysis of Inelastic Bidimensional Structures. Archives of Computational Methods in Engineering. 2019. 26. Pp. 1117–1151. DOI: 10.1007/s11831-018-9293-0
30. Simo, J.C, Kennedy, J.G, Taylor, R.L. Complementary mixed finite element formulations for elastoplasticity. Comput. Methods Appl Mech Eng. 1989. 74(2). Pp. 177–206. DOI: 10.1016/0045-7825(89)90102-3
31. Arnold, D.N., Boffi, D., Falk, R.S. Approximation by quadrilateral finite elements. Mathematics of Computation. 2002. 71(239). Pp. 909–922. DOI: 10.1090/S0025-5718-02-01439-4

Information about the authors:

Mikhail Klochkov,
ORCID: https://orcid.org/0000-0001-6751-4629
E-mail: m.klo4koff@yandex.ru

Valeria Pshenichkina, *Doctor of Technical Sciences*
ORCID: https://orcid.org/0000-0001-9148-2815
E-mail: vap_hm@list.ru

Anatoly Nikolaev, *Doctor of Technical Sciences*
ORCID: https://orcid.org/0000-0002-7098-5998
E-mail: anpetr40@yandex.ru

Yuri Klochkov, *Doctor of Technical Sciences*
ORCID: https://orcid.org/0000-0002-1027-1811
E-mail: klotchkov@bk.ru

Olga Vakhnina, *PhD in Technical Sciences*
ORCID: https://orcid.org/0000-0001-9234-7287
E-mail: ovahnina@bk.ru

Received 17.05.2025. Approved after reviewing 03.02.2026. Accepted 03.02.2026.

Magazine of Civil Engineering

ISSN 2712-8172

journal homepage: http://engstroy.spbstu.ru/

Research article

UDC 666.972:004.8

DOI: 10.34910/MCE.141.10

Adaptive cost-constrained optimization of concrete mixtures using machine learning-guided genetic algorithms

M.B. Beigi ✉

Islamic Azad University, Semnan, Iran

✉ *mohsenbeigi59@gmail.com*

Keywords: concrete mix optimization, machine learning, genetic algorithm, compressive strength prediction, cost constraint, android application

Abstract. This study presents an adaptive framework for optimizing high-performance concrete mixtures by integrating machine learning with a genetic algorithm under cost constraints. An experimental dataset was used to train an XGBoost model, which accurately predicts 28-day compressive strength. The trained machine learning model was embedded as the objective function within the genetic algorithm to maximize compressive strength while incorporating cost limitations defined by user-provided unit prices and budget. Unlike most previous studies that treat cost and strength as two separate objectives in multi-objective formulations, this work introduces cost as a constraint and strength as the sole optimization objective, thereby simplifying the decision-making process. To bridge the gap between theory and practice, an Android application was developed. The application enables users to input real-time material prices and budget limits, which are transmitted to a server hosting the machine learning model and genetic algorithm. The server computes optimized mix proportions and returns both the predicted compressive strength and the optimal design to the user interface. The proposed adaptive optimization framework was shown to effectively adjust to market price fluctuations and varying budget scenarios, providing a practical and flexible solution for real-world applications. Furthermore, the single-objective formulation ensures a unique optimal solution, avoiding the complexity of selecting among multiple Pareto-optimal alternatives.

Citation: Beigi, M.B. Adaptive cost-constrained optimization of concrete mixtures using machine learning-guided genetic algorithms. Magazine of Civil Engineering. 2026. 19(1). Article no. 14110. DOI: 10.34910/MCE.141.10

1. Introduction

Concrete is one of the most widely used construction materials due to its versatility, durability, and cost-effectiveness. It is a composite material composed primarily of cement, aggregates, water, and chemical admixtures. Cement acts as the binding agent, holding the mixture together, while aggregates contribute to bulk and significantly influence the mechanical and durability properties of both fresh and hardened concrete. Water facilitates the hydration of cement and affects the porosity, strength, and durability of the hardened material. Chemical admixtures are employed to regulate physical properties and improve workability and performance [1, 2].

The 28-day compressive strength of concrete is a critical performance indicator in both research and practice. It is affected by multiple factors including mix proportions, water-to-cement ratio, curing conditions, and the properties of individual components. Accurate prediction of this property is essential for ensuring safety, performance, and compliance with standards [3, 4].

Cost is another significant factor in concrete production. Raw material expenses, such as cement, aggregates, and admixtures, can constitute more than half of the total production cost. Rising material

prices, particularly for cement, can substantially impact project budgets. Optimizing concrete mixtures with supplementary materials like fly ash or slag can reduce costs while maintaining or enhancing performance [5, 6].

However, compressive strength and production cost are generally conflicting objectives, since an increase in strength is often associated with higher costs, and vice versa. In many studies, this trade-off has been addressed through multi-objective optimization approaches, where compressive strength and cost are treated as two separate objectives to be optimized simultaneously [7–17].

Predicting concrete compressive strength is a complex task due to nonlinear relationships between input variables, such as mix proportions and curing conditions, and output variables. Traditional empirical models often fall short in capturing these interactions. Machine learning techniques, such as extreme gradient boosting and artificial neural networks, have demonstrated high accuracy in estimating compressive strength, effectively managing complex datasets and improving prediction reliability [18, 19].

Integrating genetic algorithms with machine learning models has proven highly effective for optimizing concrete mix designs to achieve maximum compressive strength under specified constraints. Genetic algorithm explores vast solution spaces and identifies optimal solutions by mimicking natural selection. When combined with machine learning models predicting compressive strength, genetic algorithms can fine-tune mix proportions for enhanced performance. Studies have demonstrated that integrating machine learning estimators with genetic algorithms enables optimization of concrete mixtures, balancing strength, cost, and durability under quality constraints [20, 21].

In this study, an experimental dataset was employed to develop a machine learning model for predicting the 28-day compressive strength of concrete. The trained model was subsequently coupled with a genetic algorithm to optimize concrete mixture proportions subject to both technical and economic constraints. In contrast to previous studies, construction cost is not formulated as a secondary optimization objective; instead, it is explicitly imposed as a constraint. This formulation allows market price fluctuations to be flexibly incorporated into the optimization framework. By enabling users to specify material unit prices and a maximum allowable budget, the proposed approach ensures that compressive strength is maximized while strictly satisfying the prescribed cost limitation.

The novelty of this work lies in two main aspects. First, the optimization problem is formulated as a single-objective genetic algorithm, where the objective function is the compressive strength predicted by the machine learning model, while cost and proportional limitations are treated as constraints. This design offers a more flexible and practical framework compared to traditional multi-objective approaches. Second, to facilitate real-world application, an Android application was developed that allows users to input unit prices and budget information. These inputs are transmitted to a server hosting the machine learning model and genetic algorithm, which computes the optimal mixture proportions and returns the results to the application (Fig. 1). This user-oriented design makes the framework not only technically innovative but also highly accessible for practical decision-making in concrete mix design.

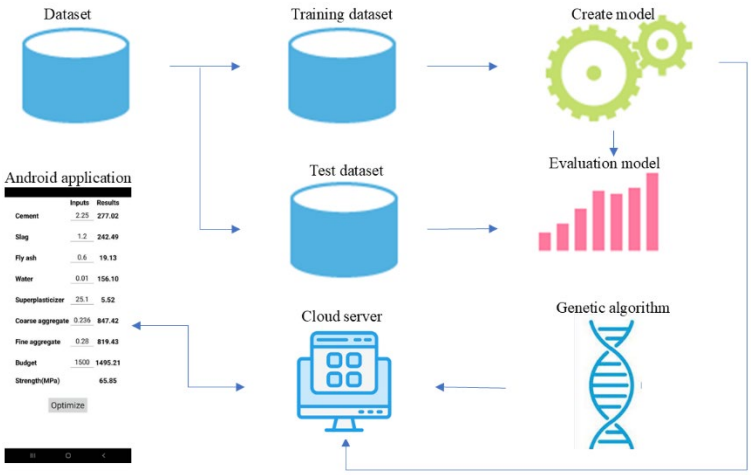

Figure 1. Schematic representation of the developed framework.

2. Materials and Methods

2.1. Problem Formulation

The present study addresses the optimization of high-performance concrete mixture proportions using a single-objective genetic algorithm. The objective function (cost function) is to maximize the 28-day compressive strength predicted by a trained machine learning model:

$$f\left(X_1, X_2, \ldots, X_7\right) = \hat{f}_{ML}\left(X_1, X_2, \ldots, X_7\right), \tag{1}$$

where $\hat{f}_{ML}$ represents the output of the machine learning model and the input variables X_i (all in kg/m^3) the concrete constituents as defined in Table 1.

Table 1. Concrete components, specific gravities, and constraint ratios.

Component	Symbol	Specific Gravity (kg/m³)	Min Ratio	Max Ratio	Notes / Constraint Type
Cement	X_1	3.15	—	—	Part of binder
Slag	X_2	2.80	0	0.61	Slag-to-binder ratio
Fly Ash	X_3	2.50	0	0.61	Fly Ash-to-binder ratio
Water	X_4	1.00	0.23	0.90	Water-to-binder ratio
Superplasticizer	X_5	1.35	0	0.13	SP-to-cement ratio
Coarse Aggregate	X_6	2.50	1.18	5.62	Coarse-to-binder ratio
Fine Aggregate	X_7	2.65	0.35	0.54	Fine-to-total aggregate ratio

The genetic algorithm aims to determine the optimal mixture proportions under a set of general, proportional, and cost constraints.

2.1.1. Volume constraint

The total volume of the concrete mixture must equal 1 m^3, enforced using the specific gravities G_i of each component:

$$\sum_{i=1}^{7} \frac{X_i}{G_i} = 1000. \tag{2}$$

This ensures that the genetic algorithm-generated mixture corresponds to a physically feasible 1 m^3 concrete volume.

2.1.2. Ratio constraints

To maintain logical and practical mixture proportions, the ratio constraints listed in Table 1 are imposed [16].

2.1.3. Cost constraint

A user-defined budget constraint is introduced as an innovative aspect of this study. The user specifies the unit price P_i (per kg) for each material and the maximum allowable budget $\sum_{i=1}^{7} P_i X_i \leq Budget$ is ensures that the optimized mixture maximizes compressive strength without exceeding the user's budget.

2.2. Implementation

2.2.1. Framework description

As illustrated in Fig. 2, the proposed framework operates as follows. The user, through an Android application, inputs the unit prices of the concrete constituents (cement, slag, fly ash, water, superplasticizer, coarse aggregate, and fine aggregate) along with the maximum allowable budget. This information is

transmitted to a web server via an API. On the server, a machine learning model – trained on an experimental dataset – is hosted to predict the 28-day compressive strength of concrete for given inputs X_1 through X_7. Simultaneously, a genetic algorithm is implemented on the server, where the output of the machine learning model serves as the fitness function to be maximized. The genetic algorithm searches for optimal mixture proportions while satisfying the volume constraint, ratio constraints (e.g., water-to-binder ratio, slag-to-binder ratio, fly ash-to-binder ratio, coarse-to-total aggregate ratio, fine-to-binder ratio, and superplasticizer-to-cement ratio), and the budget.

Finally, the genetic algorithm computes the optimal values of $X_1,\ldots,X_7$ that maximize the predicted compressive strength while ensuring that all constraints are satisfied. The optimized mix proportions are then returned to the Android application, enabling the user to conveniently view and utilize the results without requiring advanced knowledge of optimization methods.

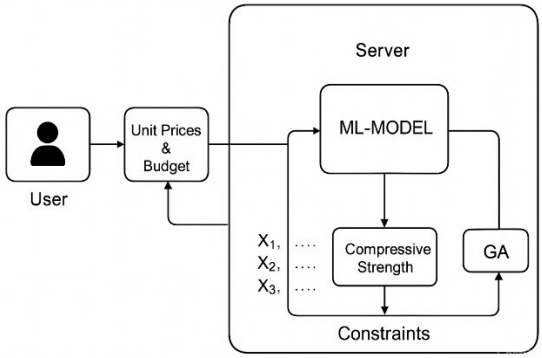

Figure 2. Framework of the proposed methodology.

2.2.2. Modeling

In this study, a dataset of 425 samples of high-performance concrete was employed for developing the machine learning model. The input features consisted of seven variables – cement, slag, fly ash, water, superplasticizer, coarse aggregate, and fine aggregate – while the output variable was the 28-day compressive strength. The experimental data were originally obtained from the program reported by Yeh [22], in which ASTM Type I Portland cement was used. Aggregate properties were described qualitatively, indicating that the coarse aggregate consisted of crushed natural stone with a maximum size of 10 mm, whereas the fine aggregate was washed river sand with a fineness modulus of approximately 3 mm. This dataset provided sufficient diversity to capture the variability in mixture proportions and their influence on compressive strength.

To incorporate economic considerations, an additional column representing the cost of each mixture was computed using unit prices ($/kg) for all constituents: cement (0.11), slag (0.06), fly ash (0.055), water (0.000024), superplasticizer (2.94), coarse aggregate (0.01), and fine aggregate (0.006). Descriptive statistics for the dataset used in this study are presented in Table 2. The distributions of the input variables compressive strength and cost are shown in Fig. 3, illustrating the range and variability of the experimental data.

Table 2. Descriptive statistics for the concrete dataset.

	mean	std	min	25 %	50 %	75 %	max
Cement	265.44	104.67	102.00	160.20	261.00	323.70	540.00
Slag	86.29	87.83	0.00	0.00	94.70	160.50	359.40
Fly Ash	62.80	66.23	0.00	0.00	60.00	120.00	200.10
Water	183.06	19.33	121.80	171.00	185.00	193.30	247.00
Superplasticizer	7.00	5.39	0.00	0.00	7.80	10.30	32.20
Coarse Aggregate	956.06	83.80	801.00	882.60	953.20	1013.20	1145.00
Fine Aggregate	764.38	73.12	594.00	712.00	769.30	811.50	992.60
Compressive Strength	36.75	14.71	8.54	26.23	33.76	44.39	81.75
Cost	72.55	19.05	34.93	59.24	72.07	83.67	166.86

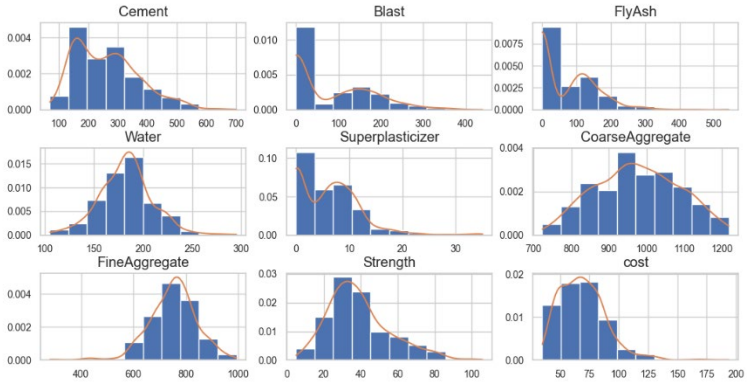

Figure 3. Histograms of input and output variables used in the study.

The correlation map (Fig. 4) displays the pairwise Pearson correlation coefficients between the main concrete mix variables and cost. Strong positive correlations are observed between superplasticizer and cost, compressive strength and cement, and compressive strength and cost, indicating that higher amounts of superplasticizer and cement lead to increased compressive strength and higher overall cost [23–26].

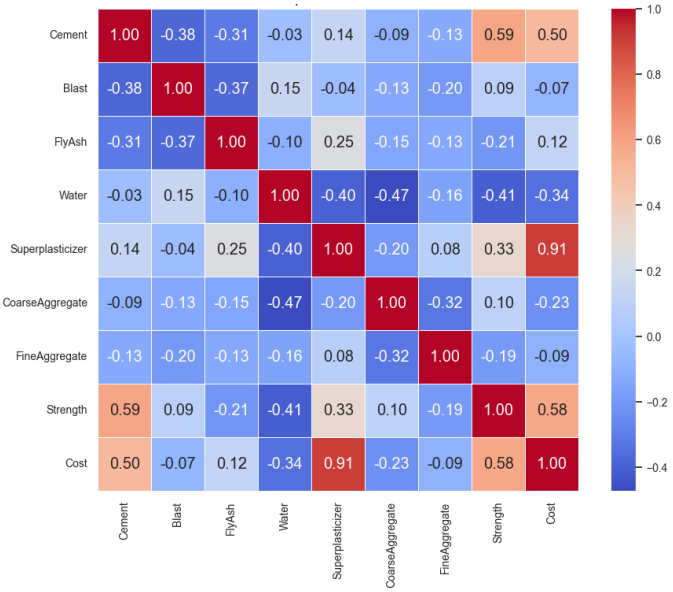

Figure 4. Correlation map of concrete mix variables and cost.

Three different machine learning models were considered: extreme gradient boosting [19], multilayer perceptron neural network [27], and random forest [28]. To ensure robust evaluation, a 10-fold cross-validation approach was employed during training. Model performance was compared using the mean squared error metric.

2.2.3. Optimization

Genetic algorithm is an evolutionary optimization technique inspired by the process of natural selection [29]. It operates by encoding potential solutions, known as chromosomes, and evolving them over successive generations to find the optimal solution. In the present study, each chromosome represents a possible concrete mixture, defined by the seven input variables $X_1 - X_7$ (cement, slag, fly ash, water, superplasticizer, coarse aggregate, and fine aggregate). The fitness of each chromosome is evaluated using the trained machine learning model, which predicts the 28-day compressive strength, while budget and proportional constraints are simultaneously enforced. As illustrated in Fig. 5, the genetic algorithm applies selection to retain high-performing chromosomes, crossover to recombine parent solutions, and mutation to introduce diversity and avoid premature convergence. Through iterative search of the solution space, the genetic algorithm gradually improves the population until the optimal mix proportions that maximize compressive strength without exceeding the budget are obtained.

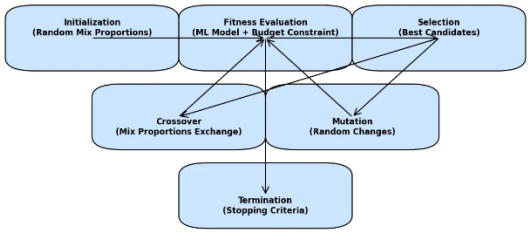

Figure 5. Schematic representation of the genetic algorithm framework.

2.2.4. Implementation and deployment

After the machine learning model was trained and saved, it was deployed on the PythonAnywhere hosting platform. Along with the trained model, the genetic algorithm code was also implemented on the same host. To enable practical use, an Android application was developed using App Inventor, through which users could provide unit prices of concrete components and the maximum allowable budget. These inputs were transmitted via an API to the server. The Flask framework was employed to handle communication, ensuring efficient transfer of requests and responses between the application and the server. On the server side, the genetic algorithm utilized the user-provided information together with the trained machine learning model to compute the optimal mix proportions $\left(X_1 - X_7\right)$. The optimization process was carried out with the objective of maximizing compressive strength without exceeding the specified budget. Finally, the computed optimal proportions and the corresponding compressive strength were returned to the Android application through the API, enabling the user to conveniently access and interpret the results.

3. Results and Discussion

3.1. Modeling Results

The experimental dataset was divided into two subsets: 75 % for training and 25 % for testing. The training data were further used in a 10-fold cross-validation scheme to ensure robust model evaluation. Three different machine learning models were considered: Extreme gradient boosting (XGBoost), random forest, and a multi layer perceptron neural network. After training, the models were tested on the 25 % test set, and their predictive performances were compared using the mean squared error as the evaluation criterion. The results demonstrated that XGBoost achieved the best performance with a mean squared error of 17.56 MPa^2, followed by random forest with a mean squared error of 17.90 MPa^2, and the multi layer perceptron with a mean squared error of 18.22 MPa^2. These findings indicate that XGBoost provides superior predictive accuracy for 28-day compressive strength compared to the other tested models. Previous studies have also confirmed the strong capability of XGBoost in predicting the compressive strength of concrete [19, 30–55].

The specifications of the XGBoost model are summarized in Table 3. This table highlights the model's performance with the hyperparameters set to a maximum depth of 4 and the number of estimators set to 500. The maximum depth parameter, fixed at 4, was selected to balance model complexity and mitigate overfitting. Meanwhile, the use of 500 decision trees (estimators) was chosen to improve predictive accuracy. The results demonstrate that the model achieved high predictive performance, with low error values in estimating the 28-day compressive strength of concrete.

Table 3. Performance metrics and hyperparameters of the optimized XGBoost model.

Metrics and hyperparameters	Value
max_depth	4
n_estimators	500
Mean Squared Error	17.56
Root Mean Squared Error	4.19
Mean Absolute Error	2.82
R-squared	0.93

3.2. Genetic Algorithm

In this study, the implementation of the genetic algorithm was designed within an adaptive framework to account for varying unit prices of materials and budget limitations provided by the user. Unlike traditional

static optimization approaches, the proposed genetic algorithm incorporates economic constraints in an adaptive manner during the optimization process. The cost function, defined as the 28-day compressive strength predicted by the trained machine learning model, is maximized while simultaneously satisfying proportional mixture constraints and the user-defined budget constraint. Since unit prices and budget vary depending on market conditions and project-specific requirements, the optimization problem is adaptively solved for each input scenario. The trained machine learning model, deployed on the server, evaluates candidate solutions during the genetic algorithm search, ensuring that only feasible mixtures are explored. This integration of genetic algorithm with machine learning and adaptive cost constraints enables flexible and practical optimization, making the approach suitable for real-world applications where cost and material availability fluctuate.

The pseudocode shown in Fig. 6 represents the implementation of the genetic algorithm on the server. First, a Flask application is initialized to handle communication between the Android client and the optimization framework. The pre-trained machine learning model, which predicts the 28-day compressive strength of concrete, is loaded into memory. Feature names and all associated constraints are then defined, including both proportional mixture rules and the user-defined budget constraint.

The core of the algorithm is the objective function. This function accepts input parameters (mixture proportions), validates them by checking for invalid values, such as NaN or infinity, and predicts compressive strength using the machine learning model. It also calculates the total cost of the mixture and applies the budget constraint. Any violations of the ratio constraints are penalized, ensuring that only feasible solutions are promoted. The genetic algorithm therefore aims to maximize the predicted compressive strength while minimizing penalties due to constraint violations.

Next, an API route /optimize is defined within the Flask application. This route receives input data from the Android application, including the maximum budget and unit prices of concrete components. After validating the inputs, the genetic algorithm-based optimization problem is solved. If optimization is successful, the algorithm extracts the optimal mixture proportions and the corresponding predicted compressive strength, and returns these results in JSON format to the client. If optimization fails, an appropriate error message is generated. Finally, the Flask application is launched, enabling real-time interaction between the client and the optimization framework.

```
Initialize Flask application
Load pre-trained model
Define feature names and constraints

Define objective function:
    - Accept input parameters
    - Validate inputs (check for NaN and infinity)
    - Use model to predict compressive strength
    - Calculate total cost and apply budget constraint
    - Apply ratio and physical constraints with penalties
    - Return predicted compressive strength minus penalties

Define API route '/optimize':
    - Receive input data (budget and unit prices)
    - Validate inputs
    - Define optimization problem using genetic algorithm
    - If optimization succeeds:
        - Extract optimal parameters and predicted compressive strength
        - Return results in JSON format
    - If optimization fails:
        - Return error message

Start Flask application
```

Figure 6. Pseudocode of the server-side implementation of the genetic algorithm integrated with the trained machine learning model and Flask framework.

3.3. Practical Implementation

To bridge the gap between theoretical research and practical implementation, an Android application was developed using the App Inventor platform. Considering the rapid advancement of smart technologies and the widespread use of smartphones in daily life, deploying an Android-based solution provides an effective means of operationalizing the outcomes of this study. The application receives user inputs, such as unit costs of raw materials and the available budget, and communicates with a server hosting the pre-trained machine learning model and the implemented genetic algorithm. Based on these inputs, it computes the optimal mixture proportions and the maximum achievable compressive strength within the specified budget and presents the results to the user. In this way, the theoretical contributions of the research are translated into a practical tool with direct applicability in the concrete industry.

Fig. 7 illustrates the overall architecture of the developed framework. On the left, a screenshot of the Android application (designed in MIT App Inventor) is shown. The application interface consists of three main columns: (i) labels indicating input parameters, such as cement, aggregate, and budget, (ii) input

fields for entering unit prices and the allowable budget, and (iii) result fields that display the optimized mix design and predicted compressive strength returned from the server. An “Optimize” button allows the user to send the entered data to the server. On the right, an icon representing the PythonAnywhere hosting platform is illustrated, where the trained machine learning model, the genetic algorithm code, and the Flask framework are deployed. The Android app sends a request (containing unit prices and budget) to the server, and in return, the server sends a response (optimized mix proportions and compressive strength), which is displayed in the application interface.

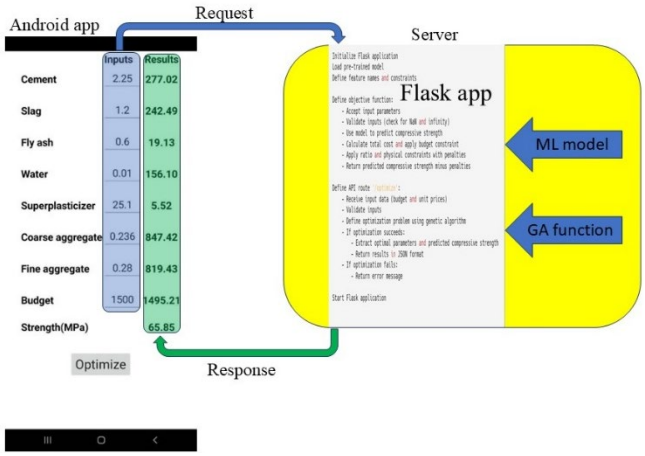

Figure 7. Schematic representation of the developed framework integrating the Android application with the Flask-based server on PythonAnywhere.

In Fig. 8, the essential App Inventor blocks required for developing the Android application are illustrated. Two groups of blocks can be observed. The blocks on the left are responsible for sending the input information provided by the user – including the unit prices of concrete components and the maximum allowable budget – to the server. The blocks on the right handle the response received from the server, which contains the optimized mixture proportions of the seven components within the specified budget. Additionally, these blocks display the corresponding 28-day compressive strength predicted by the trained machine learning model for the optimized mixture design.

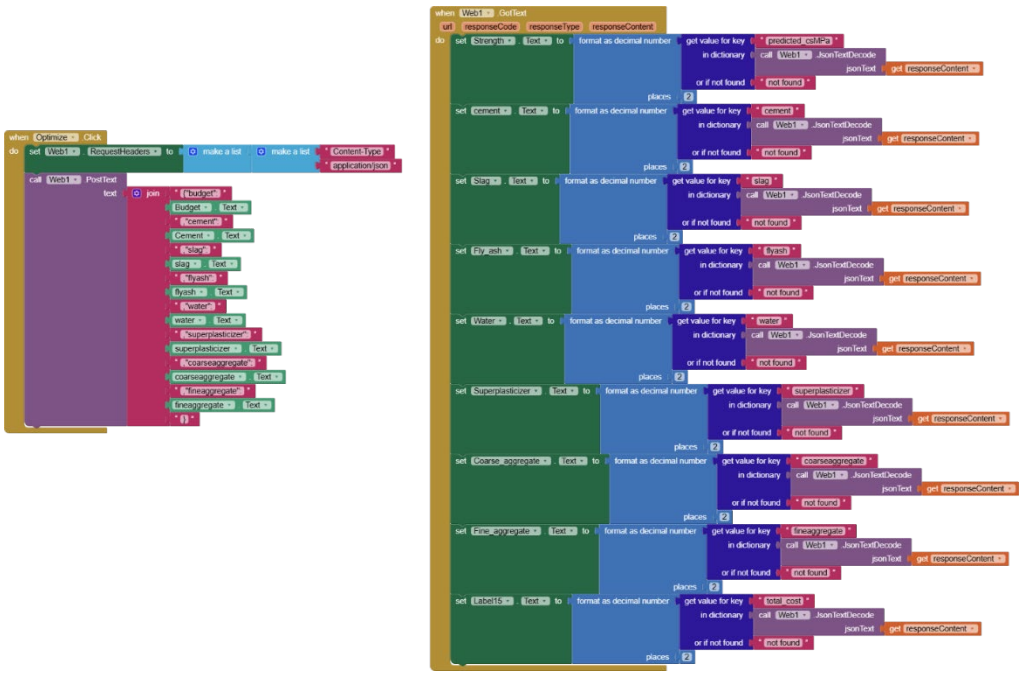

Figure 8. App Inventor blocks used in the Android application.

4. Conclusion

In this study, a machine learning-guided optimization framework was developed to design cost-effective and high-performance concrete mixtures. An XGBoost model was trained on an experimental dataset of 425 samples to accurately predict the 28-day compressive strength of concrete. The trained model was then integrated with a genetic algorithm to optimize mixture proportions under adaptive cost

constraints, allowing flexible consideration of varying market conditions. Unlike conventional multi-objective approaches that simultaneously optimize strength and cost, this study formulated the problem as a single-objective optimization with compressive strength maximization, while cost was incorporated as a constraint. This approach enables practical adaptability while ensuring budget limits are not exceeded.

To bridge the gap between theory and practice, an Android application was developed using App Inventor. The application allows users to input unit prices of components and defines budget limits, which are then transmitted to a server hosting the machine learning model and genetic algorithm implemented via Flask. The server computes optimized mixture proportions and returns both the mix design and predicted compressive strength to the user interface. This practical implementation demonstrates the usability of the framework even for non-expert users, supporting data-driven decision-making in construction material design.

An important advantage of the proposed framework lies in its adaptability to real-world economic conditions. In scenarios where market prices of materials fluctuate, the system can seamlessly adjust optimization results according to updated unit prices. Similarly, when project budgets vary – ranging from generous allocations to highly cost-sensitive cases – the framework can readily adapt to provide optimized designs that meet the specified financial constraints. This flexibility makes the proposed approach highly practical and valuable for real construction applications where both material costs and budget availability are inherently dynamic.

Moreover, unlike multi-objective approaches that typically generate a large set of non-dominated solutions (Pareto front), which may cause confusion for practitioners in selecting the most suitable mix design, the single-objective formulation adopted here provides a unique optimal solution. This simplifies the decision-making process by directly identifying the best mix design under the specified budget, thereby enhancing the usability of the framework in practical scenarios.

Workability, commonly quantified by slump, is a critical performance requirement for concrete mixtures, as it directly affects placing, compaction, and overall constructability, particularly in high-strength concrete. Future work may extend the proposed framework by incorporating concrete workability as a constraint rather than as an additional optimization objective. This can be achieved by developing a dedicated machine learning model to predict slump based on mixture proportions. During the optimization process, the objective function would remain the maximization of compressive strength, while a minimum target slump value would be imposed as a constraint. Such a constrained optimization strategy would ensure that the optimized concrete mixtures achieve high strength while maintaining adequate workability, thereby enhancing the practical applicability of the proposed framework.

References

1. Neville, A.M. Properties of concrete. 4th edn. Longman. Essex, 1995. 844 p.
2. Mehta, P.K., Monteiro, P.J. Concrete microstructure, properties, and materials.: McGraw-Hill. 3rd edn. McGraw-Hill. New York, 2006. 684 p.
3. Abolpour, B., Afsahi, M.M., Hosseini, S.G. Statistical analysis of the effective factors on the 28 days compressive strength and setting time of the concrete. Journal of Advanced Research. 2015. 6(5). Pp. 699–709. DOI: 10.1016/j.jare.2014.03.005
4. Abd Elaty, M.A.A. Compressive strength prediction of Portland cement concrete with age using a new model. HBRC Journal. 2014. 10(2). Pp. 145–155. DOI: 10.1016/j.hbrcj.2013.09.005
5. Amin, M.N., Iftikhar, B., Kaffayatullah, Kh., and Qadir, M.T. Analyzing the compressive strength, eco-strength, and cost–strength ratio of agro-waste-derived concrete using advanced machine learning methods. Reviews on Advanced Materials Science. 2025. 64(1). Article no. 20250091. DOI: 10.1515/rams-2025-0091
6. Ramseyer, C.C., Kiamanesh, R. Optimizing Concrete Mix Designs to Produce Cost Effective Paving Mixes. Oklahoma Department of Transportation. 2009. 122 p.
7. Zheng, W., Zheng, W., Shui, Zh., Xu, Zh., Gao, Xu, Zhang, Sh. Multi-objective optimization of concrete mix design based on machine learning. Journal of Building Engineering. 2023. 76. Article no. 107396. DOI: 10.1016/j.jobe.2023.107396
8. Tipu, R.K., Panchal, V., Pandya, K. Multi-objective optimized high-strength concrete mix design using a hybrid machine learning and metaheuristic algorithm. Asian Journal of Civil Engineering. 2023. 24(3). Pp. 849–867. DOI: 10.1007/s42107-022-00535-8
9. Wang, M., Wang, M., Du, M., Zhuang, X., x Lv, X., Wang, Ch., Zh. Multi-objective optimization of ultra-high performance concrete based on life-cycle assessment and machine learning methods. Frontiers of Structural and Civil Engineering. 2025. 19(1). Pp. 143–161. DOI: 10.1007/s11709-025-1152-0
10. Zhang, F., Wen, B., Niu, D., Li, A., & Guo, B. Optimized Design of Low-Carbon Mix Ratio for Non-Dominated Sorting Genetic Algorithm II Concrete Based on Genetic Algorithm-Improved Back Propagation. Materials. 2024. 17(16). Article no. 4077. DOI: 10.3390/ma17164077
11. DeRousseau, M., Kasprzyk, J., Srubar III, W. Multi-objective optimization methods for designing low-carbon concrete mixtures. Frontiers in Materials. 2021. 8. Article no. 680895. DOI: 10.3389/fmats.2021.680895
12. Wei, J., Zhang, H., Yang, Y., Zhang W., Liu, X. Multi-objective optimization of compressive strength and slump in MPCM-integrated concrete using machine learning. Materials Today Communications. 2025. 46. Article no. 112619. DOI: 10.1016/j.mtcomm.2025.112619

13. Gu, Y., Fan, R., Li, Y., Zhao, J., Song, Z., Chu, H. Multi-Objective Optimization for Nano-Silica-Modified Concrete Based on Explainable Machine Learning. Nanomaterials. 2025. 15(18). Article no. 1423. DOI: 10.3390/nano15181423
14. Chen, F., Xu, W., Wen, Q., Zhang, G., Xu, L., Fan, D., Yu, R. Advancing concrete mix proportion through hybrid intelligence: A multi-objective optimization approach. Materials. 2023. 16(19). Article no. 6448. DOI: 10.3390/ma16196448
15. Fan, M., Li, Y., Shen., J., J., Kaikai, Shi, J. Multi-objective optimization design of recycled aggregate concrete mixture proportions based on machine learning and NSGA-II algorithm. Advances in Engineering Software. 2024. 192. Article no. 103631. DOI: 10.1016/j.advengsoft.2024.103631
16. Zhang, J., Huang, Y., Wang, Y., Ma, G. Multi-objective optimization of concrete mixture proportions using machine learning and metaheuristic algorithms. Construction and Building Materials. 2020. 253. Article no. 119208. DOI: 10.1016/j.conbuildmat.2020.119208
17. Tipu, R.K., Rathi, P., Pandya, K., Panchal, V.R. Optimizing sustainable blended concrete mixes using deep learning and multi-objective optimization. Scientific Reports. 2025. 15(1). Article no. 16356. DOI: 10.1038/s41598-025-00943-1
18. Paudel, S., Pudasaini, A., Shrestha, R.K., Kharel, E. Compressive strength of concrete material using machine learning techniques. Cleaner Engineering and Technology. 2023. 15. Article no. 100661. DOI: 10.1016/j.clet.2023.100661
19. Abbas, Y.M., Khan, M.I. Robust Machine Learning Framework for Modeling the Compressive Strength of SFRC: Database Compilation, Predictive Analysis, and Empirical Verification. Materials. 2023. 16(22). Article no. 7178. DOI: 10.3390/ma16227178
20. Oviedo, A.I., Londoño, J.M., Vargas, J.F., Zuluaga, C., Gómez, A. Modeling and Optimization of Concrete Mixtures Using Machine Learning Estimators and Genetic Algorithms. Modelling. 2024. 5(3). Article no. 642–658. DOI: 10.3390/modelling5030034
21. Zuo, S., Liu, B. Optimization design of concrete mix proportion based on support vector machine regression and enhanced genetic algorithm. Discover Applied Sciences. 2025. 7(3). Article no. 200. DOI: 10.1007/s42452-025-06603-3
22. Yeh, I.-C. Design of high-performance concrete mixture using neural networks and nonlinear programming. Journal of Computing in Civil Engineering. 1999. 13(1). Pp. 36–42.
23. Ma, M., Tam, V.W., Le, Kh.N., Osei-Kyei, R. Analysing the impacts of key factors on the price of recycled concrete: A system dynamics model. Journal of Building Engineering. 2023. 80. Article no. 108123. DOI: 10.1016/j.jobe.2023.108123
24. Khan, A., Do, J., Kim, D. Cost effective optimal mix proportioning of high strength self compacting concrete using response surface methodology. Computers and Concrete. 2016. 17(5). Pp. 629–638. DOI: 10.12989/cac.2016.17.5.629
25. Cavusoglu, I. Superplasticizer Dosage Effect on Strength, Microstructure and Permeability Enhancement of Cementitious Paste Fills. Minerals. 2024. 14(12). Article no. 1242. DOI: 10.3390/min14121242
26. Alsadey, S., Omran, A. Effect of superplasticizers to enhance the properties of concrete. Design, Construction, Maintenance. 2022. 2. Pp. 84–91. DOI: 10.37394/232022.2022.2.13
27. Asteris, P.G., et al. AI-powered GUI for prediction of axial compression capacity in concrete-filled steel tube columns. Neural Computing and Applications. 2024. 36(35). Article no. 22429–22459. DOI: 10.1007/s00521-024-10405-w
28. Li, H., Lin, J., Lei, X., Wei, T. Compressive strength prediction of basalt fiber reinforced concrete via random forest algorithm. Materials Today Communications. 2022. 30. Article no. 103117. DOI: 10.1016/j.mtcomm.2021.103117
29. Holand, J.H. Adaptation in Natural and Artificial Systems: An Introductory Analysis with Applications to Biology, Control, and Artificial Intelligence. The University of Michigan Press. Ann Arbor, MI, 1975. 232 p.
30. Nukah, P.D., Abbey, S.J., Booth, C.A. Development of a learner model tool for predicting strength and embodied carbon for lightweight concrete production. Journal of Building Engineering. 2024. 95. Article no. 110330. DOI: 10.1016/j.jobe.2024.110330
31. Abdennaji, T.S., Tipu, R.K., Alassaf, Y. Predicting compressive and tensile strength of concrete with different sand types using machine learning. Ain Shams Engineering Journal, 2025. 16(8). Article no. 103474. DOI: 10.1016/j.asej.2025.103474
32. Golafshani, E., Khodadadi, N., Ngo, T., Nanni, A., Behnood, A. Modelling the compressive strength of geopolymer recycled aggregate concrete using ensemble machine learning. Advances in Engineering Software. 2024. 191. DOI: 10.1016/j.advengsoft.2024.103611
33. Fathy, I.N., Dahish, H.A., Alkharisi, M.K., Mahmoud, A.A., Fouad, H.E.E. Predicting the compressive strength of concrete incorporating waste powders exposed to elevated temperatures utilizing machine learning. Scientific Reports. 2025. 15(1). Article no. 25275. DOI: 10.1038/s41598-025-11239-9
34. Shaaban, M., Amin, M., Selim, S., Riad, I.M. Machine learning approaches for forecasting compressive strength of high-strength concrete. Scientific Reports. 2025. 15(1). Article no. 25567. DOI: 10.1038/s41598-025-10342-1
35. Chou, J.-S., Chen, L.-Y., Liu, C.-Y. Forensic-based investigation-optimized extreme gradient boosting system for predicting compressive strength of ready-mixed concrete. Journal of Computational Design and Engineering. 2023. 10(1). Pp. 425–445. DOI: 10.1093/jcde/qwac133
36. Cihan, M.T., Cihan, P. Bayesian-Optimized Ensemble Models for Geopolymer Concrete Compressive Strength Prediction with Interpretability Analysis. Buildings. 2025. 15(20). Article no. 3667. DOI: 10.3390/buildings15203667
37. Philip, S., Nidhi, N. Compressive strength prediction and feature analysis for GGBS-Based geopolymer concrete using optimized XGBoost and SHAP: A comparative study of optimization algorithms and experimental validation. Journal of Building Engineering. 2025. 108. Article no. 112879. DOI: 10.1016/j.jobe.2025.112879
38. Khan, M.I., Abbas, Y.M., Fares, G., Alqahtani, F. Strength prediction and optimization for ultrahigh-performance concrete with low-carbon cementitious materials – XG boost model and experimental validation. Construction and Building Materials. 2023. 387. Article no. 131606. DOI: 10.1016/j.conbuildmat.2023.131606
39. Tabani, A., Sharma, A., Biswas, R., Sivenas, T., Asteris, P.G. Revealing the nature of Ultra-High-Performance concrete using computational intelligence. Construction and Building Materials. 2025. 492. Article no. 143082. DOI: 10.1016/j.conbuildmat.2025.143082
40. Al-Naghi, A.A., Ahmad, A., Amin, M.N., Algassem, O., Alnawmasi, N. Sustainable optimisation of GGBS-based concrete: De-risking mix design through predictive machine learning models. Case Studies in Construction Materials. 2025. 23. Article no. e04900. DOI: 10.1016/j.cscm.2025.e04900

41. Cakiroglu, C., Batool, F., Sangi, A.J., Fatima, B., Nehdi, M.L. Explainable machine learning predictive model for mechanical strength of recycled ceramic tile-based concrete. Materials Today Communications. 2025. 44. Article no. 112139. DOI: 10.1016/j.mtcomm.2025.112139
42. Ehsan, K., Mohamed, A.H., Inqiad, W.B., Javed, M.A., Iqbal, I. Multi expression programming and interpretable machine learning for determining compressive strength of coral sand aggregate concrete. Materials Today Communications. 2025. 45. Article no. 112370. DOI: 10.1016/j.mtcomm.2025.112370
43. Hamed, A.K., Elshaarawy, M.K., Alsaadawi, M.M. Stacked-based machine learning to predict the uniaxial compressive strength of concrete materials. Computers and Structures. 2025. 308. Article no. 107644. DOI: 10.1016/j.compstruc.2025.107644
44. Abushanab, A., Vimonsatit, V. Compressive strength, flexural strength, and slump of recycled aggregate fibre-reinforced fly ash concrete using explainable extreme gradient boosting machine learning model with prediction tool. Powder Technology. 2025. 469(1). Article no. 121710. DOI: 10.1016/j.powtec.2025.121710
45. Alahmari, T.S., Arif, K. Machine learning approaches to predict the strength of graphene nanoplatelets concrete: Optimization and hyper tuning with graphical user interface. Materials Today Communications. 2024. 40. Article no. 109946. DOI: 10.1016/j.mtcomm.2024.109946
46. Kapil, A., Jadda, K., Jee, A.A. Developing machine learning models to predict the fly ash concrete compressive strength. Asian Journal of Civil Engineering. 2024. 25(7). Article no. 5505–5523. DOI: 10.1007/s42107-024-01125-6
47. Javed, M.F., Fawad, M., Lodhi, R., Najeh, T., Gamil, Y. Forecasting the strength of preplaced aggregate concrete using interpretable machine learning approaches. Scientific Reports. 2024. 14(1). Article no. 8381. DOI: 10.1038/s41598-024-57896-0
48. Khatoon, S., K, K.A., Sapkota, S.C. Experimental insights and hybridized ensemble machine learning validation of fiber reinforced geopolymer concrete strength. Asian Journal of Civil Engineering. 2026. 27. Pp. 1289–1312. DOI: 10.1007/s42107-025-01562-x
49. Li, T., Yang, J., Jiang, P., Abuhussain, M.A., Zaman, A., Fawad, M., Farooq, F. Forecasting the strength of nanocomposite concrete containing carbon nanotubes by interpretable machine learning approaches with graphical user interface. Structures. 2024. 59. Article no. 105821. DOI: 10.1016/j.istruc.2023.105821
50. Liu, X., Mei, Sh., Wang, X., Li, X. Estimation of compressive strength of concrete with manufactured sand and natural sand using interpretable artificial intelligence. Case Studies in Construction Materials. 2024. 21. Article no. e03840. DOI: 10.1016/j.cscm.2024.e03840
51. Nguyen, N.H., Abellán-García, J., Lee, S., Garcia-Castano, E, Vo. Th.P. Efficient estimating compressive strength of ultra-high performance concrete using XGBoost model. Journal of Building Engineering. 2022. 52. Article no. 104302. DOI: 10.1016/j.jobe.2022.104302
52. Sun, Y. Explainable Prediction of Compressive Strength and Elastic Modulus for Concrete Containing Waste Foundry Sand Using Bayesian-Optimized XGBoost with 10-Fold Cross-Validation. Journal of Sustainable Metallurgy. 2024. 10(1). Pp. 335–359. DOI: 10.1007/s40831-024-00790-w
53. Singh, S., Patro, S.K., Parhi, S.K. Evolutionary optimization of machine learning algorithm hyperparameters for strength prediction of high-performance concrete. Asian Journal of Civil Engineering. 2023. 24(8). Pp. 3121–3143. DOI: 10.1007/s42107-023-00698-y
54. Sun, Y. Estimation of compressive strength for spiral stirrup-confined circular concrete column using optimized machine learning with interpretable techniques. Mechanics of Advanced Materials and Structures. 2024. 31(28). Pp. 10839–10858. DOI: 10.1080/15376494.2023.2298232
55. Ullah, A., Yang,Y., Ullah, W., Ayub, B., Alzlfawi, A., Iqbal, I. Toward transparent AI: Predicting strength of fly ash foam composite concrete using explainable ML models. Structural Concrete. 2025. 27(1). Pp. 595–624. DOI: 10.1002/suco.70302

Information about the authors:

Mohsen Beigi,
ORCID: https://orcid.org/0000-0002-0644-2657
E-mail: mohsenbeigi59@gmail.com

Received 29.09.2025. Approved after reviewing 05.02.2026. Accepted 05.02.2026.